BULGARIAN CHEMICAL COMMUNICATIONS

Hydrogen sorption and electrochemical hydriding of $Mg_{2.1}Ni_{0.7}V_{0.3}$

E. Grigorova[1*], S. Todorova[2], P. Tzvetkov[1], T. Spassov[2*]

[1]*Institute of General and Inorganic Chemistry, Bulgarian Academy of Sciences, Acad. G. Bonchev Str., Bl. 11, 1113 Sofia, Bulgaria*
[2]*Faculty of Chemistry and Pharmacy, Sofia University "St. Kliment Ohridski", 1 James Bourchier Blvd., 1164 Sofia, Bulgaria*

Mixture of metals with overall composition corresponding to $Mg_{2.1}Ni_{0.7}V_{0.3}$ is prepared by ball milling under Ar atmosphere. Hydrogen sorption characteristics of the mixture are determined at different temperatures in a volumetric Sievert-type apparatus. Hydrogenation at 300^0C and 1MPa results in 3.8 wt. % H_2 absorption capacity with improved hydriding kinetics, explained by the refined particle size attained by appropriate milling. Hydrogen desorption at 300^0C and 0.15 MPa is found to proceed with high rate as well. Slower, but still relatively fast desorption rate compared to this at 300^0C is registered at 280^0C. After hydriding, the sample is characterized by X-ray diffraction analysis and SEM, revealing the phase composition of the powder mixture- orthorhombic and monoclinic Mg_2NiH_4 as main phases and small amounts of MgH_2, Ni and VH_x. The electrochemical hydrogen charge/discharge behavior of this material is studied as well, but because of rapid corrosion the electrochemical capacity drops down after the first cycle only.

Keywords: hydrogen storage; Mg_2NiH_4 hydride; ball milling; NiMH battery

INTRODUCTION

A detailed review of magnesium-based alloys, compounds, and composites for hydrogen energy storage is published by Yartys *et al.*, with a conclusion that they can be very attractive not only as solid-state hydrogen storage media but also for storage of concentrated solar heat and in the future as novel type magnesium batteries replacing lithium ones [1]. One of these promising materials is the intermetallic Mg_2Ni, forming Mg_2NiH_4 hydride with improved hydriding kinetics in comparison to Mg and theoretical hydrogen storage capacity of 3.6 wt. %. Mg_2NiH_4 has some interesting properties related to its polymorphs – different color, structure, and electric properties. Some authors as Gavra *et al.* [2], Rönnebro *et al.* [3], Li *et al.* [4], Cermak *et al.* [5, 6], Orimo *et al.* [7], Varin *et al.* [8, 9] and other [10-17] carried out studies on the formation and decomposition of this hydride. The polymorphs of Mg_2NiH_4 are two low-temperature phases – monoclinic with metal-like electrical conductivity and orthorhombic crystal structures with orange-rust color and insulator properties and a high-temperature one with a cubic structure [4, 5]. For the synthesis of Mg_2NiH_4 different methods are applied as combustion synthesis [4] or ball milling of Mg and Ni and hydrogenation [5], or reactive ball milling under hydrogen of MgH_2 and Ni [6, 9, 13]. A review on different intermetallic compounds

including Mg_2Ni and its hydrides, prepared by mechanical alloying is published recently by Liu *et al.* [18].

The Mg_2Ni-type intermetallics have shown potential as an anode material in Ni-MH batteries as well. The development of high capacity and low-cost anode material is of great importance for the extensive production and application of these batteries. The theoretical electrochemical capacity of Mg_2Ni is reported to be close to 1000 mAh/g. However, the electrochemical cycle characteristics of Mg-based materials fail to meet the requirements for practical application, because they are easily oxidized in alkaline solution electrolyte used in the battery leading to much lower experimental discharging capacities than the theoretical ones [19-25]. Some authors proved that partial substitution of Ni in Mg_2Ni by La or Cu and melt-spinning as a preparation technique improve the electrochemical characteristics [22, 23].

Main subject of the present work is the synthesis of the ternary hydride Mg_2NiH_4 applying an easier and faster approach at lower temperature and pressure and optimized ball milling conditions compared to previously reported [12-14]. Both, gas-solid hydrogen absorption-desorption properties at different temperatures and electrochemical charge/discharge behavior of the prepared material were studied. In general, this study extended our recently published results on $Mg_{2.1}Ni_{0.7}V_{0.3}$

---

* To whom all correspondence should be sent:
E-mail: egeorg@svr.igic.bas.bg;
    tspassov@chem.uni-sofia.bg

hydriding [26]. The novelties in the present work are the extended ball milling time with the aim to obtain a more active material with increased number of defects and level of amorphization and to investigate the hydrogen sorption properties in gas phase and electrochemically in the absence of carbon additive.

EXPERIMENTAL

Ni powder sized less than 150 μm with a 99.99% purity and V powder 325 mesh with a 99.5% purity purchased from Sigma Aldrich (Munich, Germany) were used for the preparation of the mixture. Mg powders with purity 99% and 50 mesh were purchased from Strem Chemicals (Newburyport, MA, USA). Mg$_{2.1}$Ni$_{0.7}$V$_{0.3}$ composite was synthesized by ball milling under Ar atmosphere, followed by annealing in hydrogen atmosphere. High-purity argon (99.999%) and hydrogen (99.99%) purchased from Messer were used for the experiments. The mixture was ball milled under argon in a planetary mono mill Pulverisette 6 Fritsch (Thuringia, Germany) using the following conditions: ball-to-sample weight ratio of 10:1, stainless steel balls with diameter of 10 mm, vial volume of 80 cm^3, rotation speed of 200 rpm and duration of 6 and 10 h. After 6 and 10 h of ball milling, the vial was opened in a glove box under argon and a small portion was taken for X-ray diffraction analysis. Also, the powder was manually removed from the wall of the vial and the balls. Hydrogen absorption-desorption characteristics were studied at various temperatures using self-constructed Sievert type apparatus. After milling and hydrogenation, the sample was characterized by X-ray diffraction phase analysis using powder X-ray diffractometer Bruker D8 Advance with a LynxEye detector and Cu Kα radiation.

The electrochemical hydrogen charge/discharge of the composite was performed in a three-electrode cell and 6 mol/dm^3 KOH electrolyte, permitting accurate control of the electrodes' geometry. The working electrode with an area of 1 cm^2 and a thickness of about 2 mm was prepared by mixing 100 mg of the synthesized alloys with 70 mg of teflonized carbon, adding a few droplets of heptane. NiO(OH)/Ni(OH)$_2$ was used as the counter-electrode, and the reference electrode was Ag/AgCl. The charge (charge time of 4h) and discharge current densities were 50 mA/g and 20 mA/g, respectively, and the voltage to which the electrodes were discharged was 0.5 V. For the hydrogen diffusion coefficient determination two electrodes were prepared – the first one with gas phase hydrided

alloy and the second one electrochemically hydrided after one charge/discharge cycle. Both were discharged under potentiostatic conditions at a potential of 0.6 V.

RESULTS AND DISCUSSION

Figure 1 presents X-ray diffraction patterns of a Mg-Ni-V mixture with a composition corresponding to the formula Mg$_{2.1}$Ni$_{0.7}$V$_{0.3}$ after two different ball milling times, as well as of a sample ball-milled (10 h) and then hydrogenated at 300^{0}C and 1 MPa. Even after ten hours of milling no newly formed phases were observed, but just the diffraction lines of unreacted Mg, Ni and V metals. Some very small increase of the background and the intensity of nickel diffraction lines could only be detected.
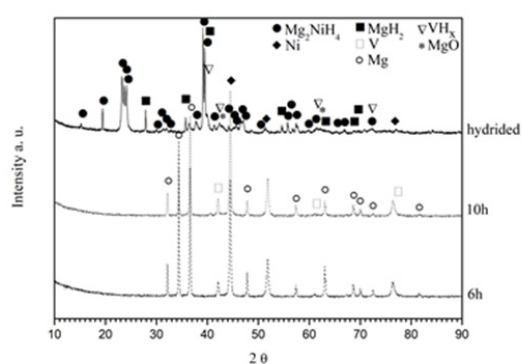

Figure 1. X-ray diffraction patterns of Mg-Ni-V mixture after 6 and 10 h of ball milling and of a sample ball milled (10 h) and then hydrided.
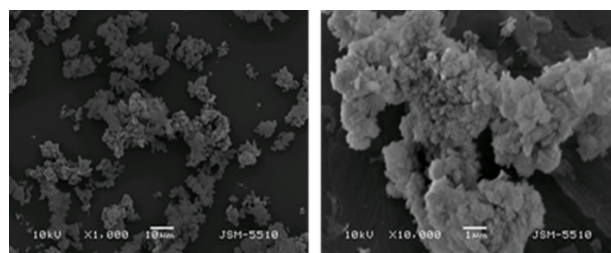

Figure 2. SEM micrograph of a Mg-Ni-V mixture, ball milled for 10 h and hydrided.

Milling for 10 h and hydriding produces fine metallic particles, the largest ones close to 1000 nm (Figure 2). Particles' agglomerations (soldering) are also observed due to the softness of the main metal (Mg) in the mixture. Obviously, the absence of anti-sticking agent in the composite, as for example activated carbon [26], leads to material agglomeration and sticking to the milling balls and walls.

During hydrogenation, the ball-milled composite transforms into Mg$_2$NiH$_4$ with monoclinic and orthorhombic polytypes as main phases, as well as VH$_x$ and a small amount of unreacted Ni and MgH$_2$.

Comparison with previously published results by the authors [26] shows less visible X-ray diffraction lines of unreacted Ni, revealing that more complete transformation to Mg_2NiH_4 is achieved in the current study. A semiquantitative phase analysis for the composite $Mg_{2.1}Ni_{0.7}V_{0.3}$ was made by using DiffracPlus EVA program [27] and RIR (reference intensity ratio) method, showing: MgH_2 - 13%, Mg_2NiH_4 - 81%, VH_x - 2-3% and MgO - 2-3 %. Hydrogen absorption curves are presented in Figures 3 and 4. In Figure 3 hydrogen absorption curves of $Mg_{2.1}Ni_{0.7}V_{0.3}$ ball milled for 10 h with different hydrogenation cycles at 300^0C and 1 MPa are presented. It is shown that only after the first hydriding/dehydriding cycle the hydriding kinetics is noticeably improved. Almost complete hydriding was reached for less than 10 min and the absorption capacity was 3.3 wt. % H_2 after only 3 min of hydrogenation. This is a very promising result for this type of material. The maximum absorption capacity of 3.8 wt. % H_2 was measured for the composite after 7 cycles. It should also be mentioned that except for the first activation cycle, all other hydrogenation cycles showed similar hydrogen absorption kinetics and capacity (Figure 3). Similar hydrogen storage capacity value, 3.76 wt. % H_2 for $Mg_2Ni_{0.75}Cu_{0.25}$ at 300^0C, but at higher pressure of 2.8 MPa has been shown by M. V. Simicič *et al.* [25].
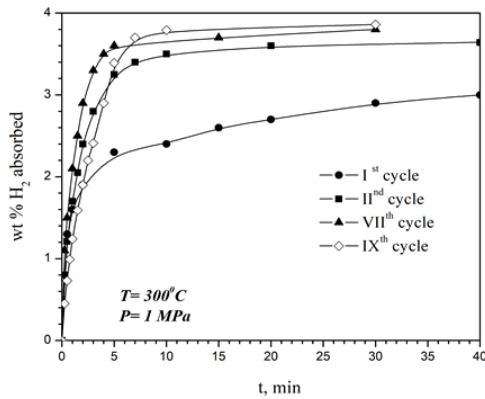
Figure 3. Hydrogen absorption curves of $Mg_{2.1}Ni_{0.7}V_{0.3}$ at different cycles.

In Figure 4 the hydrogen absorption curves at 300^0C and 200^0C for composites of the same type, but milled for a different time with and without activated carbon are compared. As it was mentioned in the Introduction part of this study, the ball milling duration is longer, e.g., 10 h with the idea to obtain more active material with introduction of an increased number of defects. Longer ball milling leads to particles' size refinement, more defects,

better contacts between the metallic particles, and also larger fresh non-oxidized surface.
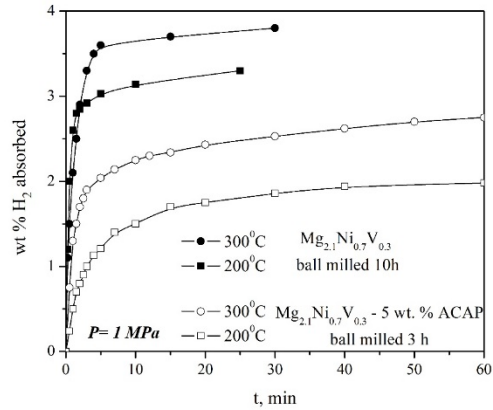
Figure 4a. Hydrogen absorption curves of $Mg_{2.1}Ni_{0.7}V_{0.3}$ and $Mg_{2.1}Ni_{0.7}V_{0.3}$ - 5 wt. % ACAP [26] at 300^0C and 200^0C.
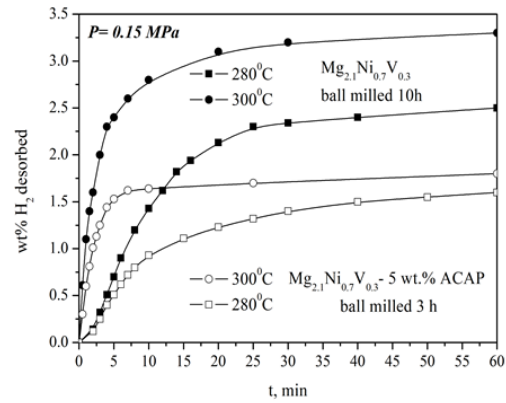
Figure 4b. Hydrogen desorption curves of $Mg_{2.1}Ni_{0.7}V_{0.3}$ and $Mg_{2.1}Ni_{0.7}V_{0.3}$ - 5 wt. % ACAP [26] at 300^0C and 280^0C.

All these effects cause improved absorption kinetics and increased hydrogen absorption capacity. After hydrogenation at 300^0C and 1 MPa of $Mg_{2.1}Ni_{0.7}V_{0.3}$ milled for 10 h under argon we could also confirm the change in the color of the composite (orange-rust reddish); an effect which other authors have also observed [2, 3].

The desorption curves at 300^0C and 280^0C for the two composites - the current one $Mg_{2.1}Ni_{0.7}V_{0.3}$ ball milled for 10 h and $Mg_{2.1}Ni_{0.7}V_{0.3}$ - 5 wt% ACAP ball milled for 3 h [26], are also compared, Figure 4b. Improved hydrogen desorption kinetics and increased desorption capacity was detected for $Mg_{2.1}Ni_{0.7}V_{0.3}$ ball milled for 10 h at both temperatures. Other authors have shown that Mg_2Ni-type materials with partial substitution of Ni by Cu

or V can desorb hydrogen at 200⁰C, but under vacuum [25].

The hydrogen-sorption properties of the alloy were also electrochemically characterized.
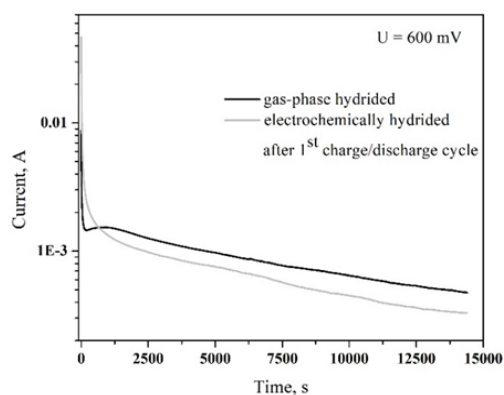

Figure 5. Charge-discharge curve (a) and cycle stability of $Mg_{2.1}Ni_{0.7}V_{0.3}$ ball milled for 10 h (b).
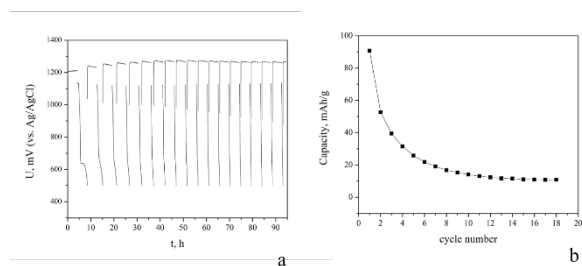

Figure 6. Current *vs.* time during H-discharge of the hydrided Mg_2Ni-based material.

Figure 5 shows hydrogen charge/discharge curves of the obtained composite, applying relatively low current densities of charge and discharge. In contrast to the very good hydrogen sorption characteristics of the composite from a hydrogen gas phase, at electrochemical hydrogenation the discharge capacity is low. Compared to the capacities of other similar Mg_2Ni based compositions our results are between measured lower or close [19, 20, 22, 32] and higher [20, 22 - 24, 25, 29, 31, 32] capacity values. The rapid reduction of the discharge capacity is clearly visible, which can be explained by the chemical corrosion of the alloy. An additional reason for the low corrosion stability of the alloy is its fine-particle nature formed during prolonged grinding at a sample-to-ball mass ratio of 1:10, as well as the high intensity of the grinding process.

In order to shed light on the factors determining the improved gas-phase hydriding kinetics, additional electrochemical experiments were performed to determine the diffusion coefficient of hydrogen in the alloy. Figure 6 shows a potentiostatic discharge of the fully gas-phase hydrided sample and of a sample electroche-

mically hydrided after one charge/discharge cycle. This analysis allows to obtain the diffusion coefficients of hydrogen, DH, calculated according to a methodology described by Zheng *et al.* [28]. Due to the difficulty of determining the average particle size (because of agglomeration), we can indicate here only the interval of the diffusion coefficient, 4.10^{-12} m²/s - 4.10^{-10} m²/s, taking particle diameters of 1 and 10 μm, respectively. DH values in the range of 4.10^{-11} m²/s - 4.10^{-10} m²/s are also reported by other authors for Mg_2Ni based materials [29-32].

It is well known that the hydrogen sorption characteristics of Mg_2Ni-based materials from a hydrogen gas phase surpass those obtained by electrochemical hydrogen for charge/discharge [24, 25], as the most probable reason is the higher sensitivity of these materials toward oxidation in alkaline water solutions. In agreement, it was already reported that longer ball milling could result in distributed electrocatalytic active sites, larger interface, smaller particle size, and higher reactivity due to higher defects density, but on the other hand, excessive milling damages the crystal lattice and causes a sharp drop in electrochemical capacity [20].

CONCLUSIONS

A mixture of metals with general composition $Mg_{2.1}Ni_{0.7}V_{0.3}$ was milled under an argon atmosphere at more energetic/intensive milling conditions and its hydriding properties were studied both in a hydrogen gas atmosphere and electrochemically. The capacity and kinetics of hydriding were found to be noticeably improved compared to a material with the same composition but milled with carbon additives. As expected, during electrochemical hydriding/dehydriding this alloy suffers from significant corrosion, which limits its hydrogen storage capacity and cycling stability. The present study shows that improved hydriding properties of the synthesized material are most probably a result of both the suitable combination of crystalline phases forming hydrides under the conditions applied, and reduced particle size.

REFERENCES

1. V. A. Yartys, M. V. Lototskyy, E. Akiba, R. Albert, V. E. Antonov, J. R. Ares, M. Baricco, N. Bourgeois, C. E. Buckley, J. M. von Colbe Bellosta, J.-C. Crivello, F. Cuevas, R. V. Denys, M. Dornheim, M. Felderhoff, D. M. Grant, B. C. Hauback, T. D. Humphries, I. Jacob, T. R. Jensen, P. E. de Jongh, J.-M. Joubert, M. A. Kuzovnikov, M. Latroche, M. Paskeviciusi, L. Pasquini, L. Popilevsky, V. M. Skripnyuk, E. Rabkin, M. V. Sofianos, A. Stuart, G. Walker, H. Wang, C. J. Webb, M. Zhu, *Int. J. Hydrog. Energy,* **44**, 7809 (2019).
2. Z. Gavra, G. Kimmel, Y. Gefen, M. H. Mintz, *J. Appl. Phys.*, **57**, 4548 (1985).
3. E. Rönnebro, D. Noréus, *Appl. Surf. Sci.,* **228**, 115 (2004).
4. L. Li, T. Akiyama, J. Yagi, *Int. J. Hydrog. Energy,* **26**, 1035 (2001).
5. J. Cermak, B. David, *Int. J. Hydrog. Energy*, **36**, 13614 (2011).
6. J. Cermak, K. Kral, *J. Alloys Compds.,* **546**, 129 (2013).
7. S. Orimo, K. Ikeda, H. Fujii, Y. Fujikawa, Y. Kitano, K. Yamamoto, *Acta Mater.*, **45**, 2271 (1997).
8. R. A. Varin, T. Czujko, J. Mizera, *J. Alloys Compds.*, **354**, 281 (2003).
9. R. A. Varin, T. Czujko, *Mater. Manuf. Process*, **17**, 129 (2002).
10. P. Tessier, H. Enoki, M. Bououdina, E. Akiba, *J. Alloys Compds.*, **268**, 285 (1998).
11. F. C. Gennari, M. R. Esquivel, *J. Alloys Compds.*, **459**, 425 (2008).
12. M. Polanski, T. K. Nielsen, I. Kunce, M. Norek, T. Płociński, L. R. Jaroszewicz, C. Gundlach, T. R. Jensen, J. Bystrzycki, *Int. J. Hydrog. Energy*, **38**, 4003 (2013).
13. R. Martínez-Coronado, M. Retuerto, B. Torres, M. J. Martínez-Lope, M. T. Fernández-Díaz, J. A. Alonso, *J. Hydrog. Energy*, **38**, 5738 (2013).
14. X. Hou, R. Hu, T. Zhang, H. Kou, W. Song, J. Li, *Int. J. Hydrog. Energy*, **39**, 19672 (2014).
15. A. Baran, M. Polański, *Materials*, **13**, 1936 (2020).
16. X. Q. Tran, S. D. McDonald, Q. Gu, T. Yamamoto, K. Shigematsu, K. Aso, E. Tanaka, S. Matsumura, K. Nogita, *J. Power Sources*, **341**, 130 (2017).
17. Y. Fu, Z. Ding, S. Ren, X. Li, S. Zhou, L. Zhang, W. Wang, L. Wu, Y. Li, S. Han, *Int. J. Hydrog. Energy*, **45**, 28154 (2020).
18. Y. Liu, D. Chabane, O. Elkedim, *Energies*, **14**, 5758 (2021).
19. N. Cui, B. Luan, H. K. Liu, H. J. Zhao, S. X. Dou, *J. Power Sources*, **55**, 263 (1995).
20. N. Cui, P. He, J. L. Luo, *Acta Mater.*, **47**, 3737 (1999).
21. N. Cui, J. L. Luo, *Electrochimica Acta*, **45**, 3973 (2000).
22. Y.-H. Zhang, D.-L. Zhao, B.-W Li, H.-P. Ren, Sh.-H. Guo, X.-L. Wang, *J. Alloys Compds.*, **491**, 589 (2010).
23. X. Hou, R. Hu, T. Zhang, H. Kou, W. Song, J. Li, *Mater. Charact.*, **106**, 163 (2015).
24. H. Shao, X. Li, *J. Alloys Compd.*, **667**, 191 (2016).
25. M. V. Simičić, M. Zdujić, R. Dimitrijević, Lj. Nikolić-Bujanović, N. H. Popović, *J. Power Sources*, **158**, 730 (2006).
26. E. Grigorova, P. Tzvetkov, S. Todorova, P. Markov, T. Spassov, *Materials*, **14**, 1936 (2021).
27. Eva Software Bruker. Available online: https://www.bruker.com/products/x-ray-diffraction-and-elemental-analysis/x-ray-diffraction/xrd-software/eva.html.
28. G. Zheng, B. N. Popov, R. E. White, *J. Electrochem. Soc.*, **143**, 834 (1996).
29. O. Reiko, L. Chao-Ho, H. Chii-Shyang, *J. Alloys Compds.*, **580**, S368 (2013).
30. N. Cui, J. L. Luo, K. T. Chuang, *J. Electroanal. Chem.*, **503**, 92 (2001).
31. Y.-H. Zhang, K. Lü, D.-H. Zhao, Sh.-H. Guo, Y. Qi, X.-L.Wang, *Trans. Nonferrous Met. Soc. China*, **21**, 502 (2011).
32. N. Cui, J. L. Luo, *Int. J. Hydrog. Energy*, **24**, 37 (1999).

Enhanced iodide uptake from aqueous solutions by silver-modified mesoporous SBA-15

F. Zahakifar[1], N. Karkhanei[2], J. Fasihi[1], H. Sepehrian[1*]

[1]Nuclear Science and Technology Research Institute, Tehran, Iran
[2]Chemistry Department, Islamic Azad University, Saveh Branch, Saveh, Iran

In this work, mesoporous Ag-SBA-15 was prepared and its iodide adsorption from aqueous solutions was examined. The synthesized adsorbent was characterized by powder X-ray diffraction (XRD) and nitrogen adsorption-desorption. The impacts of several parameters such as pH, agitation time, temperature, initial iodide concentration, and competing anions have been also scrutinized in batch experiments. The adsorption capacity at pH=2.0 was high which decreased with increasing the pH value. The kinetics of iodide adsorption was in good agreement with the pseudo-first-order and second-order models. $\Delta H°$, $\Delta\Delta S°$, and $\Delta\Delta G°$ were 16.7 kJ.mol^{-1}, 0.11 J.mol^{-1}.k^{-1}, and -17.3 kJ.mol^{-1}, respectively. The results illustrated that the experimental data of the adsorption isotherm can be well described by the Langmuir model. The maximum adsorption capacity of Ag-SBA-15 was 312.5 mg.g^{-1}. The results indicated the high ability of Ag-SBA-15 to adsorb iodide.

Keywords: Mesoporous SBA-15; Surface modification, Impregnation, Silver; Iodide; Adsorption

INTRODUCTION

Today, environmental concerns arising from nuclear power plants have become a serious threat [1, 2]. The uranium fission in nuclear reactors may result in fission fragments which are usually unstable and radioactive [3-5]. These elements are easily soluble in the water, posing adverse effects on human health [6-8].

The 1986 Chernobyl nuclear disaster in Ukraine has raised concerns about releasing these elements. After the nuclear accident in Fukushima, the leakage of nuclear waste has become a serious concern [9].

Iodine is one of the crucial fission elements. Iodide isotopes have a half-life of 8 days to 1.6×10^7 years [10]. The thyroid collects iodide and there is a risk of damage to the body by radioactive iodide. Ref. [11] highlights the urge for the treatment of radioactive iodide in nuclear waste and its removal from water sources [12]. Iodide removal by adsorption methods is one of the effective techniques. In this regard, various adsorbents such as activated carbons [13], silver-impregnated sorbents [9], anion-exchange resins [14, 15], and activated carbon fibers [13] have been used to remove iodide from the aqueous solutions. However, most of these adsorbents have disadvantages such as small and irregular pore size, inaccessible pores, and low surface area which limits their use [16].

Mesoporous molecular sieves have gained increasing attention owing to their specific characteristics such as large pore size, high specific surface area, and excellent thermal and mechanical stability [17]. So far, mesoporous materials such as MCM-41, MCM-48, CMK-3, and CMK-5 have been employed to remove ions from wastewater [18].

Compared to the mentioned materials, the SBA-15 has a larger pore size and a thicker wall, which can significantly enhance thermal stability [19]. Therefore, SBA-15 can be a promising adsorbent for iodide. Functionalization can further increase the adsorption ability of SBA-15 toward ions.

Using functionalized SBA-15, several elements such as uranium [20], copper [21], and lead [22-24] have been adsorbed from aqueous solutions. Moreover, previous studies have shown that silver can well adsorb iodide [25-28]. Therefore, silver is expected to be a suitable material for functionalizing SBA-15 for better iodide uptake.

The main purpose of this paper was to prepare an SBA-15 impregnated with silver atoms and to use it as a novel iodide adsorbent. The impacts of several parameters such as pH, temperature, agitation time, initial concentration of iodide, ionic strength, and competing anions were also scrutinized in batch experiments. Iodide equilibrium adsorption data were analyzed using adsorption isotherms such as Langmuir, Freundlich and Temkin isotherms.

---

* To whom all correspondence should be sent:
E-mail: Hsepehrian@aeoi.org.ir

EXPERIMENTAL

Materials

The materials used to produce the Ag-SBA-15 adsorbents were all of analytical grade and purchased from Merck. P123 copolymer was obtained from Sigma-Aldrich. Sodium iodide was utilized to make the iodide-containing feed solution.

Apparatus

The prepared Ag-SBA-15 was characterized by powder X-ray diffraction (XRD) and nitrogen adsorption-desorption. The X-ray studies were performed using the Philips X'pert powder diffractometer system operating by Cu-Kα (λ = 1.541 Å) radiation. XRD analysis was performed from 1.5° to 100° (2θ) at a scan rate of 0.02° (2θ) s^{-1}. The nitrogen adsorption-desorption analysis was conducted by the Quantachrome NOVA model 2200e to measure specific surface area, total pore volume, and pore size. The concentration of iodide in the solutions was measured with an inductively coupled plasma-atomic emission spectrometer (ICP-AES, Varian, Liberty 150ax Turbo, Australia).

The zero charge point was determined by the pH drift method [29, 30]. A 0.01 mol.L^{-1} KNO$_3$ was used as the inert electrolyte. The pH of test solutions was adjusted in the range of 2-10 using 0.01 mol.L^{-1} HNO$_3$ and 0.01 mol.L^{-1} KOH. 0.2 g of Ag-SBA-15 adsorbents was added to 50 mL of test solutions in glass tubes and equilibrated for 24 h. The final pH (pH$_f$) was measured after 24 h and plotted against the initial pH (pH$_i$). The point where the curve intersects the line pH$_i$ = pH$_f$ was taken as the pH$_{pzc}$. The pH was measured by Schott CG841 pH-meter (Germany), which was calibrated before every measure.

Preparation of mesoporous silica SBA-15

According to the reported synthesis methods [16, 31-33], 0.8 g of P123 copolymer was added to 60 g of distilled water and 160 g of HCl (2 mol.L^{-1}) and stirred for 15 min at a rate of 130 rpm. Then, 3 g of tetraethyl orthosilicate (TEOS) was gradually added to the mixture and stirred for 20 h.

The produced precipitate was then placed in a Teflon container and kept at 90 °C for 24 h. After this time, a filtration operation was carried out on the precipitate using a Büchner funnel followed by rinsing with distilled water. The filtered precipitate was dried for 24 h in an oven at 50 °C. Finally, the precipitated sample was calcined in a furnace at 540 °C for 6 h to remove residual surfactants.

Preparation of mesoporous silica Ag-SBA-15

To impregnate the prepared adsorbent with silver, 1 g of SBA was added to 3 mL of a 1.20 mmol.L^{-1} silver nitrate solution and stirred. It was then placed in an oven at 105 °C for 12 h to dry. Then 10 mL of 10 mol.L^{-1} hydrazine hydrate was added to 1 g of product to convert silver ions to silver atoms. After one hour, the adsorbent was filtered and washed with sufficient distilled water and dried in an oven at 50 °C. The SBA-15 silicon porous adsorbent containing silver particles was named Ag-SBA-15.

Procedure of adsorption experiments

Batch experiments were carried out to investigate the iodide adsorption utilizing Ag-SBA-15 adsorbent. In these experiments, 25 mg of the adsorbent was mixed with 25 mL of iodide solution. The mixture of solution and adsorbent was shaken at the rate of 150 rpm utilizing a water bath shaker. The solution was filtered after the adsorption process. The iodide concentration in the solution was measured by ICP-AES. The adsorption percentage, adsorption capacity (q), and distribution coefficient (K$_d$) were calculated using the following equations:

$$\text{Adsorption (\%)} = \frac{(C_i - C_f)}{C_i} \times 100 \qquad (1)$$

$$q = \left(C_i - C_f \right) \times \frac{V}{m} \qquad (2)$$

$$K_d = \frac{(C_i - C_f)}{C_f} \times \frac{V}{m} \qquad (3)$$

where C$_i$ and C$_f$, V, and m are the initial and final concentrations of iodide (mg L^{-1}), solution volume (mL), and the mass of the adsorbent (g), respectively.

RESULTS AND DISCUSSION

Characterization of modified mesoporous adsorbent

The prepared Ag-SBA-15 adsorbent was characterized by XRD and BET techniques.

Nitrogen adsorption and desorption isotherms of SBA-15 and Ag-SBA-15 samples were investigated at 77 °K. Specific surface area and pore size distribution of adsorbent were obtained from BET and BJH equations, respectively [34-36]. The pore size distribution of samples is illustrated in Figure 1. This Figure confirms the mesoporosity of the adsorbent. The pore size distribution curve demonstrates a mean pore size of ~4 nm.

The pore size distribution curve also shows that the pore size distribution of Ag-SBA-15 was shifted to

slightly larger values since silver atoms filled the SBA-15 micro-pits.

The physical properties of SBA-15 and Ag-SBA-15 are presented in Table 1. The surface area, pore volume, and size of SBA-15 changed from 816 $m^2.g^{-1}$, 0.84 $cm^3.g^{-1}$, and 4.9 nm to 513 $m^2.g^{-1}$, 0.73 $cm^{-3}.g^{-1}$, and 4.61 nm upon silver impregnation. These changes are due to the entrance of silver atoms into the SBA-15 pores**.**
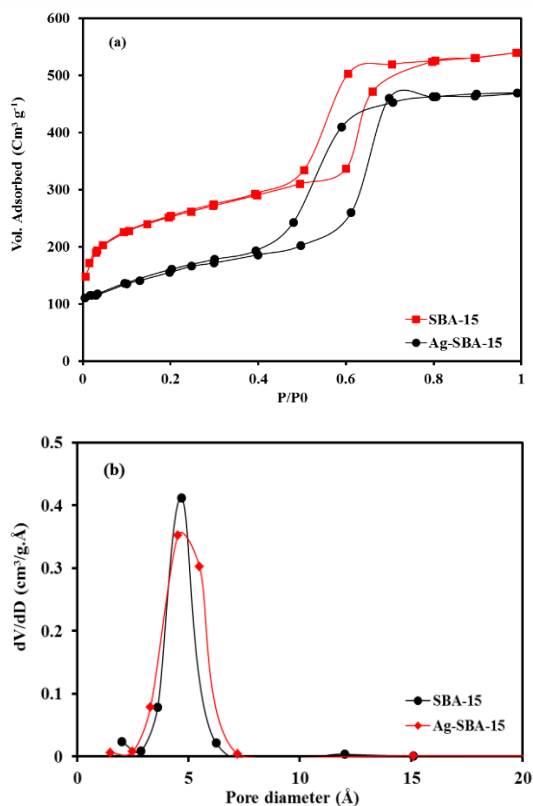

Figure 1. (a) Nitrogen adsorption and desorption isotherm and (b) Pore size distribution curve of SBA-15 and Ag-SBA-15 adsorbents

Table 1. Physical properties of SBA-15 and Ag-SBA-15 adsorbents

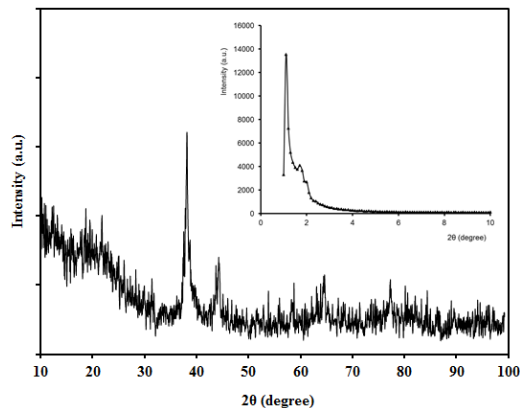| Sample	Pore volume (cm^{-3} g^{-1})	Specific surface area (m^2 g^{-1})	Average pore size (nm)
SBA-15	0.84	816	4.09
Ag-SBA-15	0.73	513	4.61

Figure 2. XRD pattern of Ag-SBA-15 adsorbent
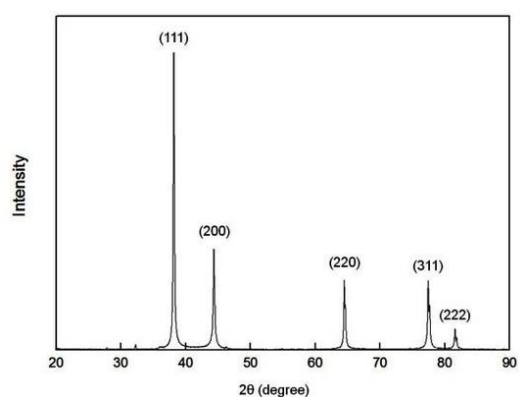
Figure 3. XRD pattern of silver nanoparticles [36]

The X-ray diffraction pattern of the Ag-SBA-15 is demonstrated in Fig. 2. As shown, its XRD pattern in $2\theta = 2\text{-}10$ is similar to that of mesoporous SBA-15, while the pattern in $2\theta = 10\text{-}100$ confirms the presence of silver particles in the Ag-SBA-15 pores. The XRD pattern of silver nanoparticles prepared by Park *et al.* is in complete agreement with that of the Ag-SBA-15 (Fig. 3) [36]. Therefore, it is confirmed that silver atoms are present in the pores of the mesoporous SBA-15 without disturbing the structure of the mesoporous adsorbent.

Effect of acidity

The effect of acidity on iodide adsorption was studied in the pH range of 1-8. The results are demonstrated in Figure 4. At acidities less than 3, the iodide adsorption was favorable, while maximum iodide adsorption was obtained at pH = 2.

At low pH (pH<3), metallic silver is oxidized to silver ions on the adsorbent surface (Eq. 4). With the production of silver ions, the adsorbent surface becomes positively charged [37].

$O_2(aq) + 4H^+(aq) + 4Ag^0(s) \rightarrow 4Ag^+(aq) + 2H_2O(l)$ (4)
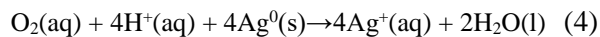
The pH_{pzc} of the Ag-SBA-15 was 4.0. At pH values lower than pH_{pzc}, the adsorbent possesses a positive surface charge. This behavior explains the higher adsorption of Ag-SBA-15 at pH <4.0. As the pH of the solution increased, the iodide adsorption decreased due to the rise in OH ions and their competition with iodide. Adsorption experiments were continued at an initial pH of 2.0.
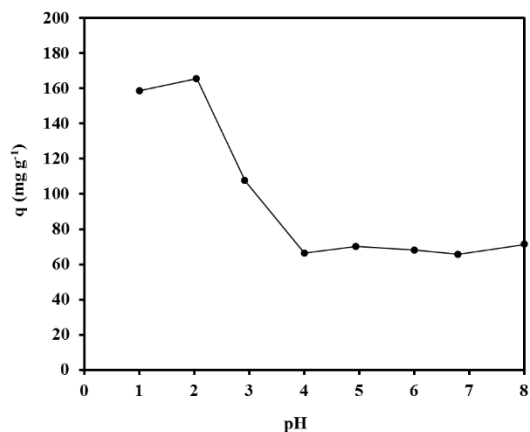
Figure 4. Effect of initial pH on iodide adsorption with Ag-SBA-15 (nitial pH: 1-8, agitation time 5 h, temperature: 25 °C, adsorbent: 25 mg, concentration: 1.2×10^{-2} M NaI, and solution volume: 25 mL).

Study of adsorption kinetics

The impact of agitation time on the iodide adsorption by Ag-SBA-15 was studied at 25 °C, as shown in Figure 5 (a). According to the results, iodide adsorption is a slow process and the adsorption rate increases with increasing time up to 24 hours and then reaches equilibrium. Other tests were performed for 48 h to achieve equilibrium.

Figures 5 (b) and 5 (c) show the graphs of pseudo-first-order and pseudo-second-order kinetics, respectively. The adsorption kinetics study demonstrated that the process agrees with the mentioned kinetic models. This means that the adsorption depends on the adsorbent surface and the concentration of iodide.

Figure 5. (a) Effect of agitation time on iodide adsorption with Ag-SBA-15; (b) pseudo-first-order kinetics (c) pseudo-second-order kinetics (initial pH: 2, temperature: 25 °C, adsorbent: 25 mg, concentration: 1.2×10^{-2} M NaI, and solution volume: 25 mL).

191

Effect of temperature

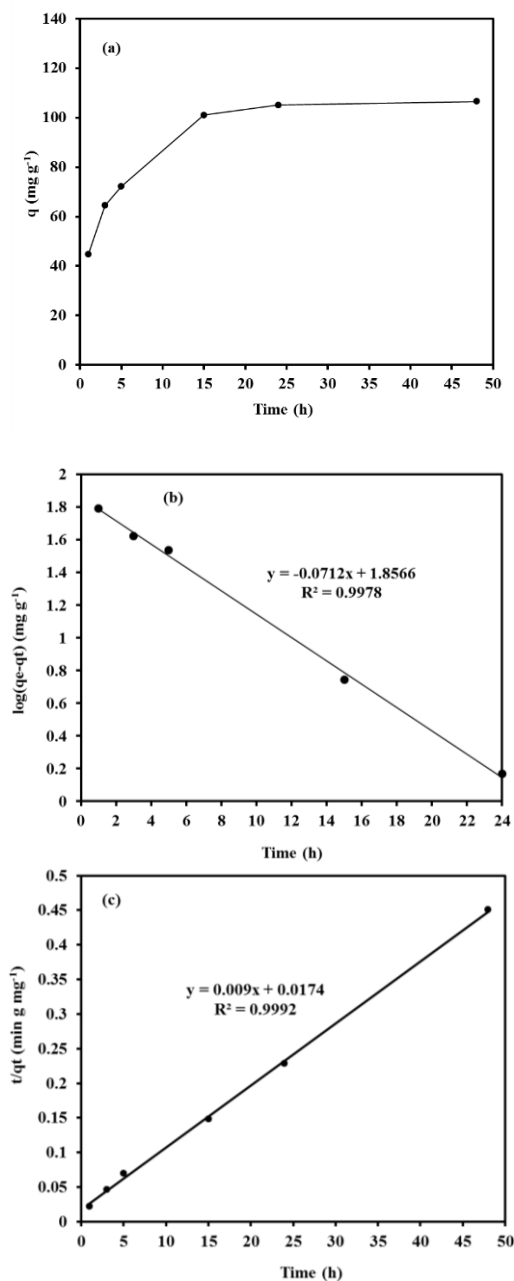The impact of temperature on the iodide adsorption rate of Ag-SBA-15 was studied at 25 to 65 °C, as illustrated in Figure 6.
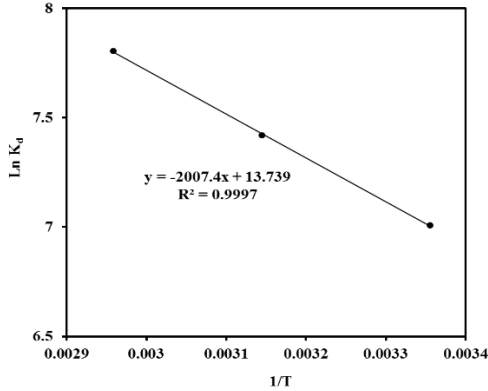

Figure 6. Effect of temperature on iodide adsorption with Ag-SBA-15 (initial pH:2, agitation time 48 h, adsorbent: 25 mg, concentration: 1.2×10^{-2} M NaI, and solution volume: 25 mL).

The mechanism of iodide adsorption can be determined by thermodynamic values. The thermodynamic values such as the change in Gibbs free energy (ΔG^o), adsorption enthalpy (ΔH^o), and entropy (ΔS^o) were obtained from the Van't Hoff equations [38, 39]:

$$\Delta G^0 = -RT \operatorname{Ln} K_d \qquad (5)$$

$$\operatorname{Ln} K_d = \frac{\Delta H^0}{-(RT)} + \frac{\Delta S^0}{R} \qquad (6)$$

where R and T (K) are the gas constant (8.314 J.mol^{-1}.K^{-1}) and the absolute temperature, respectively.

ΔH^o, ΔS^o, and ΔG^o were obtained, 16.7 kJ.mol^{-1}, 0.11 J.mol^{-1}.k^{-1}, and -17.3 kJ.mol^{-1}, respectively, implying an endothermic and spontaneous adsorption process. Therefore, with increasing temperature, the adsorption of iodide on the adsorbent will increment.

Iodide adsorption isotherm

The isotherm experiments were performed with an initial concentration of iodide between 5 and 300 mg L^{-1} at pH 2 for 48 h. Langmuir, Freundlich, and Temkin are common isotherm models that describe the nature and mode of adsorption of ions onto the adsorbent. The mathematical expressions of these models are expressed in the following equations [40-43]:

$$q_e = \frac{q_L K_L C_e}{1 + K_L C_e} \qquad (7)$$

$$q_e = K_F C_e^{1/n} \qquad (8)$$

$$q_e = \frac{RT}{b_T} \ln(K_T C_e) \qquad (9)$$

where q_e and q_L are adsorption capacity at equilibrium and Langmuir maximum adsorption capacity, respectively. K_L, K_F, and b_T are Langmuir, Freundlich, and Temkin model constants. K_T is the Temkin isotherm equilibrium binding constant. The n denotes the deviation from the linearity of adsorption, and C_e is the equilibrium concentration of ions.

Experiments were performed with various concentrations of iodide to study the adsorption isotherm. Figure 7 (a) demonstrates the iodide adsorption isotherms on the Ag-SBA-15 adsorbent. The Langmuir, Freundlich and Temkin linear adsorption models are illustrated in Figures 7 (b) and 7 (d), respectively. The parameters of these models are shown in Table 2. As seen, the experimental data of the adsorption isotherm are well described by the Langmuir model. Therefore, uniform and homogeneous adsorption on the Ag-SBA-15 adsorbent can be considered [44-47].

The K_F and 1/n in the Freundlich model are indicators of adsorption capacity and adsorption power. A less than one 1/n value shows normal adsorption [48]. The maximum adsorption capacity of iodide on Ag-SBA-15 adsorbent was calculated as 312.5 mg g^{-1}.

Effect of coexisting anions

The impact of coexisting anions on iodide adsorption with Ag-SBA-15 was also investigated as shown in Figure 8. For this purpose, a solution of 1.2 mol.L^{-1} sodium iodide was prepared containing different concentrations of fluoride and chloride. The results demonstrated that iodide adsorption decreased with raising the concentration of the fluoride and chloride which declined the adsorption capacity to about 65 mg g^{-1}.

So far, several studies have been performed on iodide adsorption using various adsorbents [37, 49-51], as summarized in Table 3. It is observed that the amount of iodide adsorbed by the present adsorbent is much higher than by other adsorbents, and the q_{max} value increased to 312.5 mg g^{-1}. The high adsorption efficiency is probably due to the high affinity of silver and the top surface area of Ag-SBA-15 adsorbent compared to other adsorbents.
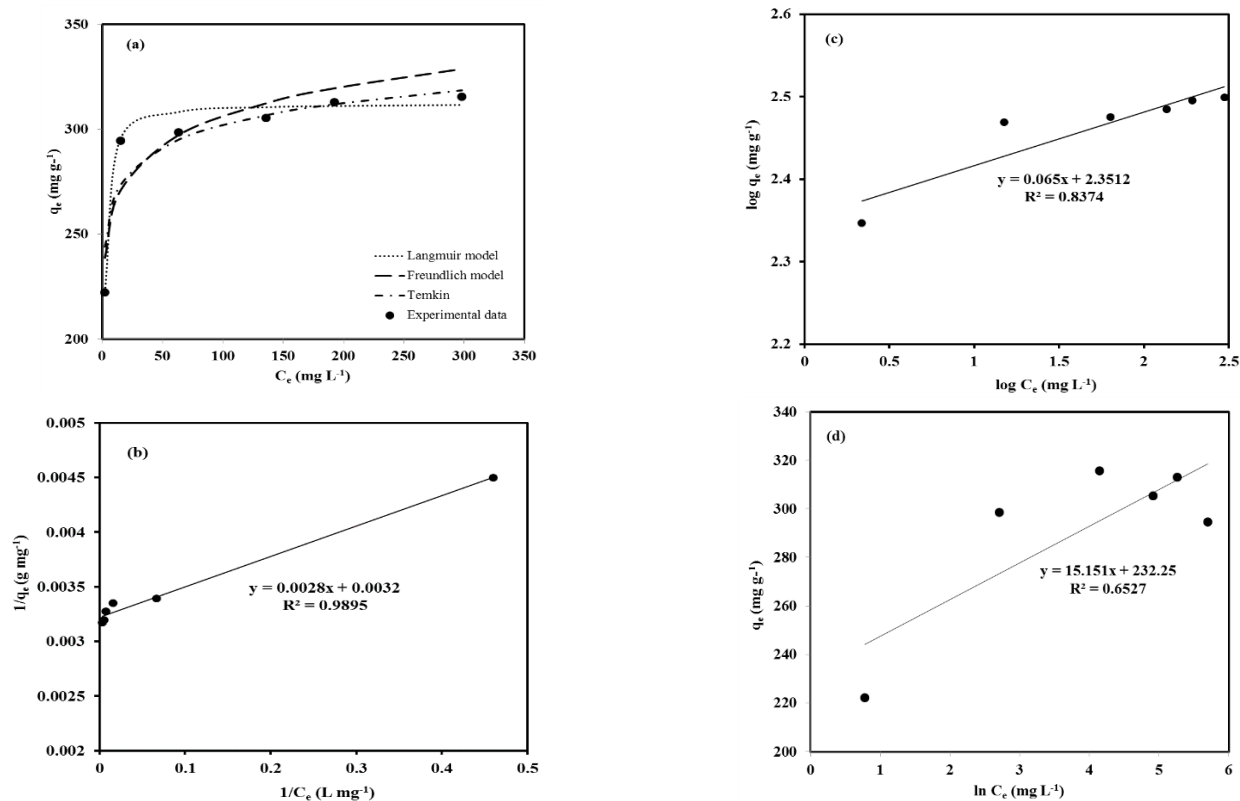
Figure 7. (a) Iodide adsorption isotherms on Ag-SBA-15; (b) Langmuir, (c) Freundlich; (d) Temkin linear model (initial pH: 2, agitation time 48 h, temperature: 65 °C, adsorbent: 10 mg, solution volume: 20 mL

Table 2. Parameters of the Langmuir, Freundlich and Temkin models for iodide adsorption

Model	Parameters		
Langmuir	R^2	K_L(L mg^{-1})	q_{max}(mg g^{-1})
	0.989	1.14	312.5
Freundlich	R^2	K_F (mg g^{-1} mg^m L^m)	$1/n$
	0.837	224.49	0.065
Temkin	R^2	b_T	K_T (L g^{-1})
	0.65	163.53	4591359

Table 3. Comparison of iodide adsorption by Ag-SBA-15 with other adsorbents

Adsorbent	Initial iodide conc. (mg L^{-1})	Iodide adsorption		Ref.
		%	mg g^{-1}	
Duolite A-116	510	50	-	[49]
Mg-Al-(NO$_3$) LHD[a]	342	59	-	[50]
CaALG-AgCl composite[b]	-	-	139.7	[51]
AgAC[c]	1-200	-	18.2-19.5	[37]
Ag-MCM-41	88-352	34-95	166.7-238.1	[52]
Ag-SBA-15	113-445	33-98	222.3-312.5	This work

[a]Layered double hydroxide
[b]Calcium alginate-silver chloride composite
[c]Silver-impregnated granular activated carbon

Figure 8. Effect of concentration of fluoride and chloride ions on iodide adsorption on Ag-SBA-15 adsorbent (initial pH: 2, agitation time 48 h, temperature: 25 °C, adsorbent: 25 mg, solution volume: 25 mL).

CONCLUSIONS

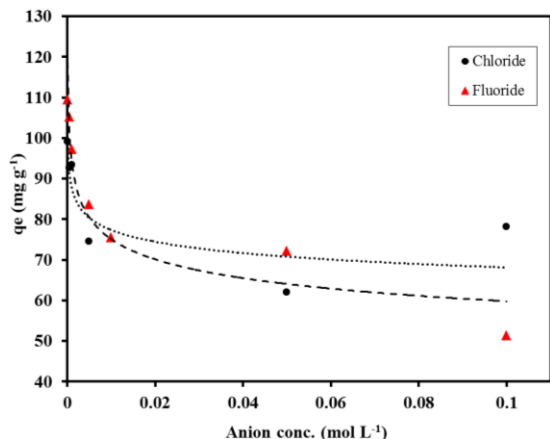In this research, a new adsorbent (Ag-SBA-15) was prepared by impregnating SBA-15 with silver atoms and its adsorption behavior for iodide was studied. The adsorbent was characterized by powder XRD and nitrogen adsorption-desorption. The results indicated the loading of silver nanoparticles on the mesoporous SBA-15.

The adsorption behavior of iodide on Ag-SBA-15 was also examined. The adsorption capacity was very high at pH=2.0 and decreased with enhancing pH value. The results illustrated that the adsorption reaction is endothermic and spontaneous and follows the pseudo-first-order and second-order kinetic models. Also, experimental data were well described by the Langmuir model. The maximum adsorption capacity of iodide onto Ag-SBA-15 was found to be 312.5 mg g^{-1}. These results illustrated that Ag-SBA-15 has the appropriate ability for adsorption of iodide from aqueous solutions.

Data Availability: Some or all data, models, or codes that support the findings of this study are available from the corresponding author upon reasonable request.

REFERENCES!

1. M. Sadiq, F. Wen, *Nuclear Engineering and Technology,* **54** (10), 3672 (2022).
2. S. Venturi, *Juvenis Scientia,* **8** (2), 5 (2022).
3. F. Zahakifar, A. Charkhi, M. Torab-Mostaedi, R. Davarkhah, *Journal of Radioanalytical and Nuclear Chemistry* **316** (1), 247 (2018).
4. F. Zahakifar, A. Charkhi, M. Torab-Mostaedi, R. Davarkhah, *Radiochimica Acta,* **106** (3), 181 (2018).
5. F. Zahakifar, A. Charkhi, M. Torab-Mostaedi, R. Davarkhah, A. Yadollahi, *Journal of Radioanalytical and Nuclear Chemistry,* **1** (2018).
6. P. Kumar, B. Kumar, D. Singh, in: Hazardous Waste Management, Elsevier, 2022, p. 289.
7. T. S. Rao, S. Panigrahi, P. Velraj, in: Microbial biodegradation and bioremediation, Elsevier, 2022, p. 419.
8. F. Zahakifar, A. Keshtkar, E. Nazemi, A. Zaheri, *Radiochimica Acta,* **105** (7*),* 583 (2017).
9. A. Bo, S. Sarina, Z. Zheng, D. Yang, H. Liu, H. Zhu, *Journal of Hazardous Materials,* **246**, 199 (2013).
10. J. Livingood, G. Seaborg, *Physical Review,* **54** (10), 775 (1938).
11. M. Eisenbud, Y. Mochizuki, A. S. Goldin, G. R. Laurer, *Science,* **136** (3514), 370 (1962).
12. L. Szente, É. Fenyvesi, J. Szejtli, *Environmental Science & Technology,* **33** (24), 4495 (1999).
13. O. B. Yang, J. C. Kim, J. S. Lee, Y. G. Kim, *Industrial & Engineering Chemistry Research,* **32** (8), 1692 (1993).
14. N. Hiromichi, K. Hiroshi, M. Nobuaki, S. Hiroshi, S. Akira, N. Masashi, D. Yuu, Google Patents, 1967.
15. S. K. Glenn,(ed.), Google Patents, 1960.
16. X. Wang, G. Zhu, F. Guo, *Annals of Nuclear Energy,* **56**, 151 (2013).
17. C. Kresge, M. Leonowicz, W. J. Roth, J. Vartuli, J. Beck, *Nature,* **359** (6397), 710 (1992).
18. M. Gao, G. Zhu, C. Gao, *Energy and Environment Focus,* **3**, 219 (2014*).*
19. D. Zhao, J. Feng, Q. Huo, N. Melosh, G. H. Fredrickson, B. F. Chmelka, G. D. Stucky, *Science,* **279**, 5350 (1998).
20. Y. Liu, L. Yuan, Y. Yuan, J. Lan, Z. Li, Y. Feng, Y. Zhao, Z. W. Chai, , *Journal of Radioanalytical and Nuclear Chemistry,* **292** (2), 803 (2012).
21. Da'na, A. Sayari, *Chemical Engineering Journal,* **166** (1), 445 (2011).
22. S. Wang, K. Wang, C. Dai, H. Shi, J. Li, *Chemical Engineering Journal,* **262**, 897 (2015).
23. Y. Liu, Z. Liu, J. Gao, J. Dai, J. Han, Y. Wang, J. Xie, Y. Yan*, Journal of Hazardous Materials,* **186** (1), 197 (2011).
24. V. Hernández-Morales, R. Nava, Y. Acosta-Silva, S. Macías-Sánchez, J. Pérez-Bueno, B. Pawelec, *Microporous and Mesoporous Materials,* **160**, 133 (2012).
25. F. Forstmann, W. Berndt, P. Büttner, *Physical Review Letters,* **30** (1), 17 (1973).
26. K. W. Chapman, P. J. Chupas, T. M. Nenoff, *Journal of the American Chemical Society,* **132** (26), 8897 (2010).
27. C. Mathew, M. Majali, S. Balakrishnan, *Applied Radiation and Isotopes,* **57** (30), 359 (2002).

28. T. R. Thomas, B. A. Staples, L. P. Murphy, (eds.), Google Patents, 1978.
29. Y. Yang, Y. Chun, G. Sheng, M. Huang, *Langmuir,* **20** (16), 6736 (2004).
30. A. Aziz, M. S. Ouali, E. H. Elandaloussi, L. C. De Menorval, M. Lindheimer, *Journal of Hazardous Materials,* **163** (1), 441 (2009).
31. M. Kruk, M. Jaroniec, C. H. Ko, R. Ryoo, *Chemistry of Materials,* **12** (7), 1961 (2000).
32. S. Vashnia, H. Tavakoli, R. Cheraghali, H. Sepehrian, *Desalination and Water Treatment,* **55** (5), 1220 (2015).
33. Y. Wang, B. Zibrowius, C.-M. Yang, B. Spliethoff, F. Schüth, *Chemical Communications,* **1**, 46 (2004).
34. M. Hayati-Ashtiani, *Particle & Particle Systems Characterization,* **28** (3-4), 71 (2011).
35. E. P. Barrett, L. G. Joyner, P. P. Halenda, *Journal of the American Chemical Society,* **73** (1), 373 (1951).
36. E. J. Park, S. W. Lee, I. C. Bang, H. W. Park, *Nanoscale Research Letters,* **6** (1), 223 (2011).
37. J. S. Hoskins, T. Karanfil, S. M. Serkiz, *Environmental Science & Technology,* **36** (4), 784 (2002).
38. X. Huang, N.-Y. Gao, Q.-l. Zhang, *Journal of Environmental Sciences,* **19** (11), 1287 (2007).
39. M. Sekar, V. Sakthi, S. Rengaraj, *Journal of Colloid and Interface Science,* **279** (2), 307 (2004).
40. S. Chen, Y. Qi, J. J. Cossa, S. I. D. S. Dos, *Progress in Nuclear Energy,* **117**, 103 (2019).
41. I.-K. Jung, Y. Jo, S.-C. Han, J.-I. Yun, Science of the Total Environment, 2019, p. 135814.
42. A. Yusoff, M. Salimi, S. Gopinath, M. Abdullah, E. Samsudin, *Materials Chemistry and Physics,* **241**, 122337 (2020).
43. A. Mehdinia, S. Heydari, A. Jabbari, *Materials Chemistry and Physics,* **239**, 121964 (2020).
44. F. Zahakifar, A. R. Keshtkar, M. Talebi, *Progress in Nuclear Energy,* **134**, 103642 (2021).
45. F. Zahakifar, A. R. Keshtkar, M. Talebi, *Journal of Radioanalytical and Nuclear Chemistry,* **327** (1), 65 (2021).
46. F. Vaziri Alamdarlo, G. Solookinejad, F. Zahakifar, M. Rezvani Jalal, M. Jabbari, *Journal of Water and Wastewater; Ab va Fazilab (in Persian),* 2021.
47. F. V. Alamdarlo, G. Solookinejad, F. Zahakifar, M. R. Jalal, M. Jabbari, *Journal of Radioanalytical and Nuclear Chemistry,* **329** (2), 1033 (2021).
48. A. Dada, A. Olalekan, A. Olatunya, O. Dada, *IOSR Journal of Applied Chemistry,* **3** (1), 38 (2012).
49. R. Lokhande, P. Singare, S. Parab, *Radiochemistry,* **50** (6), 642 (2008).
50. L. Kentjono, J. Liu, W. Chang, C. Irawan, *Desalination,* **262** (1-3), 280 (2010).
51. H. Zhang, X. Gao, T. Guo, Q. Li, H. Liu, X. Ye, M. Guo, Z. Wu, Colloids and Surfaces A: Physicochemical *and Engineering Aspects,* **386**, (1-3), 166 (2011).
52. N. Karkhanei, H. Sepehrian, R. Cheraghali, *Desalination and Water Treatment,* **56** (11), 3096 (2015).

Synthesis, characterization, cytotoxicity, DFT calculations, and DNA interaction studies of new Schiff base metal (II) complexes

E. Abdalrazaq[1][*], R. K. R. Al-Shemary[2], A. A. Q. Jbarah[1]

[1]*Al-Hussein Bin Talal University, Faculty of Science, Department of Chemistry, P.O. Box 20, Ma'an, Jordan*
[2]*Department of Chemistry, College of Education for Pure Sciences, Ibn -Al-Haitham, University of Baghdad, Iraq*

SYNOPSIS

New Schiff base metal (II) complexes were synthesized and characterized. The cytotoxicity efficiency of the complexes was tested. Molecular docking analysis of the Schiff base ligands and of the Cu (II) complexes was reported. Optimized structures, electronic structures, and HOMO-LUMO gaps of the complexes were investigated using DFT calculations. The study included thermal analysis, fluorescence studies, and DNA-binding assays of the synthesized complexes.
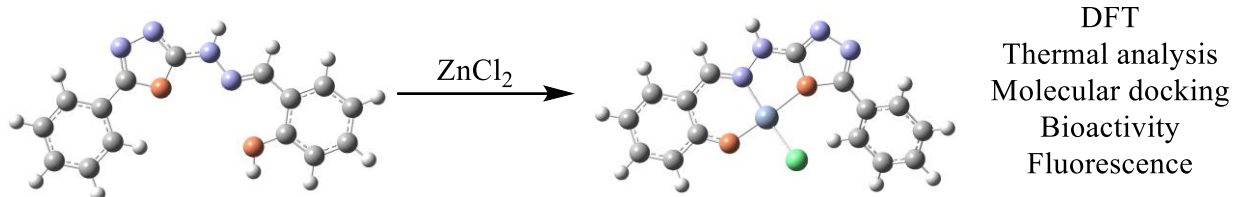
Mononuclear complexes of the type [M(L1-H)Cl], [M(L2-H)Cl], and [M(L3-H)Cl], where M = Ni^{2+}, Cu^{2+} or Zn^{2+}, L1 = (E)-2-((2-(5-phenyl-1,3,4-oxadiazol-2-yl) hydrazineylidene)methyl)phenolate, L2 = (E)-2-((2-(5-(4-hydroxyphenyl)-1,3,4-oxadiazol-2-yl) hydrazineylidene)methyl)phenolate and L3 = (E)-2-((2-(5-(4-chlorophenyl)-1,3,4-oxadiazol-2-yl) hydrazineylidene)methyl)phenolate, were synthesized and identified. The synthesized complexes were characterized by microelement analyses of metal content, Fourier transform infrared spectroscopy (FTIR), molar conductance, mass spectroscopy, magnetic measurements, thermal analysis, ^{13}C, and ^{1}H NMR, and UV–visible spectroscopy. Recorded FTIR data were supported by density functional theory (DFT) calculations. The vibrational frequencies of the molecules were computed using the optimized geometry obtained from the DFT calculations. According to the elemental analysis data and spectroscopic measurements tetrahedral structures were designated for all the complexes whilst Ni^{2+} complexes had a specified square planar structure. Cu^{2+} complex shows effective DNA cleavage in the non-attendance of factors of the exterior. Cu^{2+} complexes IC50 data explained the higher cytotoxicity efficiency compared to the other complexes. All the complexes react with CT–DNA by a groove system linking with DNA. Cytotoxicity efficacy was tested with cell lines of cancer like HCT–15, HeLa, and A549 where the Cu complex appears the most effective with HCT-15. Molecular docking analysis of Cu^{2+} complexes and ligands with human DNA topoisomerase was performed.

INTRODUCTION

The studies of the coordination chemistry of biological ligands and their complexes significantly impact bioinorganic chemistry. Schiff bases are compounds that have many applications [1]. These compounds can be used in biological [2], photochemical [3], electrochemical [4], and catalytic activities [5].

The ligands and their metal complexes are also used as patterns to better understand biological modes [6]. The variable geometries of the Schiff base complexes make them substantial models of anthropomorphic chemical structures [7]. Transition metal complexes can cleave and link double-standard DNA [8], altering cancer cell expansion and DNA recurrence; this is the foundation for developing more effective anti-tumor

---

* To whom all correspondence should be sent:
E-mail: eidalzooby@yahoo.com

drugs [9, 10]. Understanding the different non-covalent DNA bonding patterns with these complexes [11], such as linking along outside the helix [12], linking along major or minor grooves [13, 14], planar aromatic ring intercalation, or forming planar molecules between pairs of bases, is critical for improving this type of anticancer drugs [15]. The flatness, chelation system [16], and type of donor atom in the ligands all play a role in calculating the complexes' intermediate ability to link with DNA [17]. Also, the secondary grooves are of interest for being free and able to carry enough room to link little molecules [18]. Most anticancer and antibiotic drugs are small molecules; hence, the major linking site is in the secondary DNA groove [19, 20].

In this study, we synthesized and characterized a chain of Zn(II), Cu(II), and Ni(II) complexes with Schiff base ligands. The efficacy of cytotoxicity was tested with cell lines of cancer like HCT–15, HeLa, and A549. Density functional theory (DFT) calculations, including geometry optimization, vibrational frequency analysis, and electronic structures, were reported for the synthesized molecules using B3LYP functional with the 6-31+G(d,p) basis set for C, H, O, N, and Cl atoms and the LANL2DZ basis set for metal atoms. In addition, molecular docking was performed for the ligands and complexes to investigate their interactions with the human DNA topoisomerase I (70 Kda) (PDB ID: 1SC7).

EXPERIMENTAL

Materials and physical measurements

All chemicals, reagents, and solvents used were of analytical grade and were used as received with no further purification. The materials were supplied by Sigma-Aldrich (St. Louis, MO, USA) and Merck (Darmstadt, Germany). ^1H and ^{13}C NMR spectra were recorded on 400 and 100 MHz Bruker NMR spectrometers, respectively. Elemental analysis (C, H, and N) was carried out using Thermoscientific Flash 2000. Infrared spectra were obtained with an Agilent Technologies Cary 630 FTIR spectrophotometer from 4000 to 600 cm^{-1} using the KBr disk method. Mass spectra were recorded on an LC Premier micro-mass spectrometer, and UV–Vis spectra were recorded on a Perkin-Elmer Lambda 25 UV–Vis spectrophotometer. The melting points of the ligands and complexes were measured by Stuart's SMP3 digital melting point apparatus using melting point capillary tubes. The molar conductivity measurements of the 10^{-3} mol L^{-1}

complexes in dimethylformamide (DMF) were performed using a device of the digital conductivity series Ino.Lab.720. Magnetic measurements of the complexes were performed by using a Johnson Matthey balance. The fluorescence emission spectra were recorded using a Fluorolog-3, ISA (Jobin-Yvon-Spex, Edison, NJ, USA).

Synthesis of B1*,* B2 *and* B3

A 0.01 mol solution of benzoic acid (1.220 g), 4-hydroxybenzoic acid (1.381 g), or 4-chlorobenzoic acid (1.566 g) in 25 mL of ethanol was mixed with 5 mL of 98% H$_2$SO$_4$ and refluxed for 7 h. The solution was distilled under vacuum. The product was collected and washed with a solution of sodium carbonate (Scheme 1). A solution of 0.01 mol (0.50 mL) of 90% NH$_2$NH$_2$·H-H$_2$O in 50 ml of ethanol was added dropwise to the mixtures and refluxed with stirring for 5 h, then left to cool at room temperature. The solid products **B1**, **B2,** and **B3** were collected. The products were washed and recrystallized from the solvent (Scheme 1) [2, 3].

B1 compound: yellow solid; yield 76%; m.p. 158°C to 160°C; IR (v_{max}, cm^{-1}):3342 cm^{-1} (v N-H$_{asym.}$), 3392 cm^{-1} (v N-H $_{sym.}$), 3294(v NH $_{amide}$), 1618(v C=O; EI-MS (m/z): 136.15 [M]$^+$; ^{1}H NMR(400 MHz, DMSO-d$_6$): δ 4.57 (d,2H, NH$_2$), 9.60 (s,1H, N-H), 7.48 to 8.00 (m,5H, aromatic protons), ^{13}C NMR (100 MHz, DMSO-d$_6$): δ176.86 (C=O), 126.65, 128.34, 130.78, 132.67, (aromatic carbons); Anal. % Found: C, 60.87; H, 5.43; N, 20.11; % Calcd.: C, 61.75;H, 5.92; N, 20.58%.

B2 compound: light yellow solid; yield 70%; m.p. 162°C to 164°C; IR (v_{max}, cm^{-1}): 3421 cm^{-1} (v OH$_.$), 3338 cm^{-1} (v N-H$_{asym.}$), 3389 cm^{-1} (v N-H $_{sym.}$), 3290 (v NH $_{amide}$), 1616 (v C=O); EI-MS (m/z): 152.15 [M]$^+$; ^{1}H NMR(400 MHz, DMSO-d$_6$): δ 4.53 (d, 2H, NH$_2$), 9.64 (s, 1H, N-H), 7.43 to 8.01 (m,4H, aromatic protons), 9.69 (s, 1H, OH), ^{13}C NMR (100 MHz, DMSO-d$_6$): δ169.34 (C=O), 139.32 (COH), 121.32, 125.98, 129.76, (aromatic carbons); Anal. % Found: C, 56.34; H, 5.98; N, 19.17; %. Calcd.: C, 55.26; H, 5.30; N, 18.41%.

B3 compound: dark yellow solid; yield 88%; m.p. 167 °C to 169°C; IR (v_{max}, cm^{-1}): 33427 cm^{-1} (v N-H$_{asym.}$), 3386 cm^{-1} (v N-H $_{sym.}$), 3288(v NH $_{amide}$), 1615 (v C=O), 830 (v C-Cl); EI-MS (m/z): 170.02 [M]$^+$; ^{1}H NMR (400 MHz, DMSO-d$_6$): δ 4.64 (d, 2H, NH$_2$), 9.54 (s, 1H, N-H), 7.40 to 8.12 (m,4H, aromatic protons);^{13}C NMR (100 MHz, DMSO-d$_6$): δ169.43 (C=O), 137.75 (C-Cl), 126.32, 126.78, 129.65,

(aromatic carbons); Anal. % Found: C, 49.82; H, 4.58; N, 16.68; %. Calcd.: C, 49.28; H, 4.14; N, 16.42%.

Synthesis of **E1**, **E2** *and* **E3**

A 0.01 mol solution of D1 (1.78 g), D2 (1.94 g), or D3 (2.13 g) and 0.01 mol (0.50 mL) of $NH_2NH_2.H_2O$ in 20 mL of absolute ethanol was refluxed for 7 hours. The products were filtered, washed, and dried under vacuum (Scheme 1).

E1 compound: brown solid; yield 77%; m.p. 210 °C to 212°C; IR (v_{max}, cm^{-1}): 3423 cm^{-1} (v N-H$_{asym.}$), 3385 cm^{-1} (v N-H $_{sym.}$), 3084 (v CH $_{aromatic}$), 1663 (v C=N $_{endo.}$); EI-MS (m/z): 176.18 [M]$^+$; ^{1}H NMR (400 MHz, DMSO-d$_6$): δ 4.60 (d, 2H, NH$_2$), 8.90 (s, 1H, N-H), 6.97 to 7.82 (m, 5H, aromatic protons); ^{13}C NMR (100 MHz, DMSO-d$_6$): δ 173.12 (C=N), 125.98, 127.75, 129.54, 130.63 (aromatic carbons); Anal. %Found: C, 53.78; H, 4.21; N, 32.98; %Calcd.: C, 54.54; H, 4.58; N, 31.80.

E2 compound: dark brown solid; yield 75%; m.p. 208 °C to 211°C; IR (vmax, cm^{-1}): 3343 cm^{-1} (v OH.), 3475cm^{-1} (v N-H$_{asym.}$), 3380 cm^{-1} (v N-H $_{sym.}$), 3079 (v CH $_{aromatic}$), 1668 (v C=N $_{endo.}$); EI-MS (m/z): 192.18 [M]$^+$; ^{1}H NMR(400 MHz, DMSO-d$_6$): δ 4.60 (d, 2H, NH$_2$), 8.94 (s, 1H, N-H), 7.61 to 7.82(m,4H, aromatic protons), 9.58 (s,1H, OH);^{13}C NMR (100 MHz, DMSO-d$_6$): δ 167.43 (C=N), 125.54, 127.23, 129.87, 130.54, (aromatic carbons), 159.43 (COH); Anal. %Found: C, 50.65; H, 4.43; N, 29.87; %Calcd.: C, 50.00; H, 4.20; N, 29.15.

E3 compound: light brown solid; yield 70%; m.p. 200 °C to 202°C; IR (v_{max}, cm^{-1}): 3423 cm^{-1} (v N-H$_{asym.}$), 3385 cm^{-1} (v N-H $_{sym.}$), 3084 (v CH$_{aromatic}$), 1663 (v C=N $_{endo.}$), 827 (v C-Cl); EI-MS (m/z): 210.03 [M]$^+$; ^{1}H NMR (400 MHz, DMSO-d$_6$): δ 4.62 (d, 2H, NH$_2$), 8.97 (s, 1H, N-H), 7.61 to 7.82 (m,4H, aromatic protons); ^{13}C NMR (100 MHz, DMSO-d$_6$): δ170.12 (C=N), 134.23 (C-Cl), 124.76, 128.82, 125.98, 130.32, (aromatic carbons); Anal. %Found: C,45.67; H, 2.47; N, 26.54; %Calcd. C, 45.45; H, 2.35; N, 26.60.
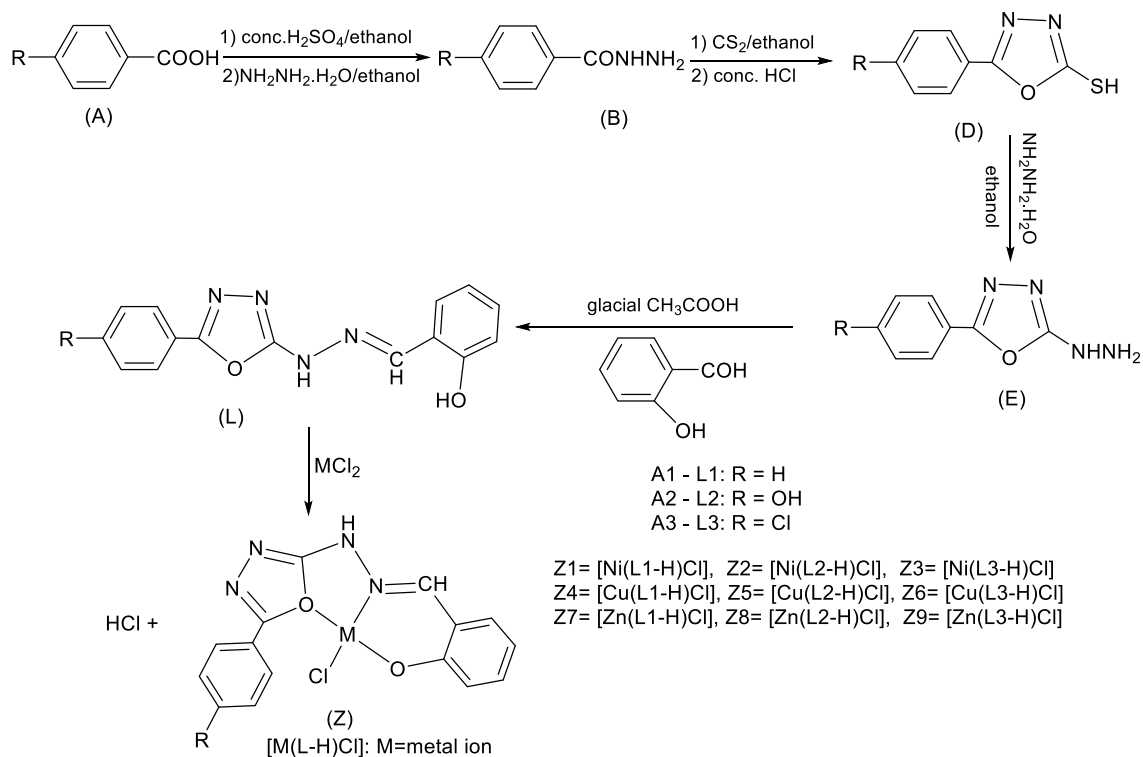
Scheme 1. Synthesis of L1-L3 Schiff bases and Z1-Z9 complexes

Preparation of Schiff base ligands **L1**, **L2,** *and* **L3**

A 0.001 mol solution (0.122 g) of 2-hydroxybenzaldehyde and some drops of glacial acetic acid were added to a 0.001 mol solution of E1 (0.176 g), E2 (0.192 g), or E3 (0.21 g) in 20 mL of absolute ethanol. The mixture was stirred and refluxed for 5 hours. The products were filtered, washed with ethanol, and dried under vacuum (Scheme 1).

L1 compound: green crystals; yield 80%; m.p. 129°C to 131 °C; IR (v_{max}, cm^{-1}): 3325 cm^{-1} (v OH.), 3320 (v NH $_{amide}$), 3150, 3087 (v CH $_{aromatic}$), 2931 (v CH $_{azomethine}$), 1678 (v C=N imine), 1625 (v C=N $_{oxadiazole}$ ring), 1262 (v(C-O) oxadiazole ring; EI-MS 280.29 (m/z): 280, 263, 187 111, 112, 94, 42; ^{1}H NMR (400 MHz, DMSO-d$_6$): 10.54 (s, 1H, N-H), 8.23 (s, 1H, HC=N), 6.78 to 8.30 (m, 9H, aromatic protons), 11.12 (s, 1H, OH); ^{13}C NMR (100 MHz, DMSO-d$_6$): δ 170. 9(C-O), 123.45, 124.56, 125.98, 130.98, (aromatic carbons), 144.54 (C=N), 159.21 (COH); Anal. %Found: C, 63.76; H, 4.65; N, 19.76; %Calcd.: C, 64.28; H, 4.32; N, 19.99.

L2 compound: light green crystals; yield 70%; m.p. 119°C to 121 °C; IR (v_{max}, cm^{-1}): 3343, 3330 (v OH.), 3313 (v NH $_{amide}$), 3158, 3090 (v CH $_{aromatic}$), 2937 (v CH $_{azomethine}$), 1674 (v C=N $_{imine}$), 1629 (v C=N $_{oxadiazole}$), 1268 (v(C-O) oxadiazole ring); EI-MS 296.29 (m/z): 296, 279, 203, 111, 112, 42; ^{1}H NMR(400 MHz, DMSO-d$_6$): 9.74 (s, 1H, OH), 10.52 (s,1H, N-H), 8.52 (s,1H, HC=N), 7.24 to 8.35 (m, 8H, aromatic protons),11.60 (s, 1H, OH); ^{13}C NMR (100 MHz, DMSO-d$_6$): δ 159.30 (OH), 170.67(C-O), 123.45, 124.76, 128.82, 125.98, 130.32 (aromatic carbons) 143.89 (C=N), 157.54 (COH); Anal. %Found: C, 60.56; H, 4.23; N, 18.78; %.Calcd.: C, 60.81; H, 4.08; N, 18.91.

L3 compound: yellowish green crystals; yield 77%; m.p. 112°C to 114 °C; IR (v_{max}, cm^{-1}):⁻ 3347 cm^{-1} (v OH.); 3319 (v NH amide), 3155, 3091 (v CH $_{aromatic}$), 2936 (v CH $_{azomethine}$), 1677 (v C=N $_{imine}$), 1629 (v C=N $_{oxadiazole}$), 1270 (v(C-O) oxadiazole ring), 830 (v C-Cl); EI-MS (m/z): 314, 232, 204, 187, 122, 112, 94, 70, 42; ^{1}H NMR (400 MHz, DMSO-d$_6$): 10.51 (s,1H, N-H), 8.45 (s,1H, HC=N), 7.30 to 8.32 (m, 8H, aromatic protons), 11.23 (s, 1H, OH); ^{13}C NMR (100 MHz, DMSO-d$_6$): δ 171.34(C-O), 124.0, 124.76, 128.82, 125.98, 130.32 (aromatic carbons), 134.23 (C-Cl) 144.12 (C=N), 156.98 (COH); Anal. %Found: C, 57.76; H, 11.34; N, 17.12; %.Calcd.: C, 57.24; H, 3.52; N, 17.80.

Synthesis of complexes

Z1 nickel (II) complex [Ni(L1-H)Cl]: brown solid; yield 74%; m.p. 179°C to 181°C; conductance (ΔM, Ω^{-1} cm^2 mol^{-1}; DMF) =19; μ$_{eff}$ = 0.24 BM at 298 K; IR (v_{max}, cm^{-1}): 3318 (v NH $_{amide}$), 3148, 3089 (v CH $_{aromatic}$), 2954 (v CH $_{azomethine}$), 1658 (v C=N $_{imine}$), 1620 (v C=N $_{oxadiazole}$), 1260 (v(C-O) oxadiazole ring), 465 (v Ni-N), 554 (v Ni-O) 431 (v Ni-Cl); EI-MS (m/z): 373.42, Anal. %Calcd. for C$_{15}$H$_{11}$ClN$_4$NiO$_2$: C, 48.25; H, 2.97; Cl, 9.49; N, 15.00; Ni, 15.72; % Found C, 46.26; H, 2.85; Cl, 9.10; N, 14.39; Ni, 15.07.

Z2 nickel (II) complex [Ni(L2-H)Cl]: brown solid; yield 67 %; m.p. 176°C to 179°C; conductance (ΔM, Ω^{-1} cm^2 mol^{-1}; DMF) = 24; μ$_{eff}$ = 0.12 BM at 298 K; IR (v_{max}, cm^{-1}): 3340 (v OH.),3310 (v NH $_{amide}$), 3155, 3094 (v CH $_{aromatic}$), 2933 (v CH $_{azomethine}$), 1656 (v C=N $_{imine}$), 1625 (v C=N $_{oxadiazole\ ring}$), 1249 (v(C-O) oxadiazole ring), 445 (v Ni-N) 521(v Ni-O) 427 (v Ni-Cl); EI-MS (m/z): 389.42, Anal. %Calcd. for C$_{15}$H$_{11}$ClN$_4$NiO$_3$: C, 46.26; H, 2.85; Cl, 9.10; N, 14.39; Ni, 15.07; %Found: C, 46.65; H, 2.43; Cl, 9.08; N, 14.39; Ni, 15.32.

Z3 nickel (II) complex [Ni(L3-H)Cl]: greenish-brown; yield 82%; m.p. 165°C to 167°C; conductance (ΔM, Ω^{-1} cm^2 mol^{-1}; DMF) =18; μ$_{eff}$ = 0.16 BM at 298 K; IR (v_{max}, cm^{-1}): 3313 (v NH amide), 3150, 3089 (v CH $_{aromatic}$), 2933 (v CH $_{azomethine}$), 1660 (v C=N $_{imine}$), 1624 (v C=N oxadiazole ring), 1259 (v(C-O) oxadiazole ring), 843(v C-Cl), 456 (v Ni-N) 567 (v Ni-O) 421 (v Ni-Cl); EI-MS (m/z): 407.86, Anal. %Calcd. for C$_{15}$H$_{10}$Cl$_2$N$_4$NiO$_2$: C, 44.17; H, 2.47; Cl, 17.38; N, 13.74; Ni, 14.39; % Found: C, 43.87; H, 2.98; Cl,16.78; N, 13.87; Ni, 14.67.

Z4 copper(II) complex [Cu(L1-H)Cl]: reddish – brown solid; yield 79%; mp. 175°C to 177°C; Conductance (ΔM, Ω^{-1} cm^2 mol^{-1}; DMF) =20; μeff=1.76 BM at 298 K; IR (vmax, cm^{-1}): 3310 (v NH $_{amide}$), 3140, 3084 (v CH $_{aromatic}$), 2950 (v CH $_{azomethine}$), 1656 (v C=N $_{imine}$), 1621 (v C=N $_{oxadiazole}$ ring), 1261 (v(C-O) oxadiazole ring), 462 (v Cu-N), 550 (v Cu-O) 436 (v Cu-Cl); EI-MS (m/z): 378.28, Anal. %Calcd. for C$_{15}$H$_{11}$ClCuN$_4$O$_2$: C, 47.63; H, 2.93; Cl, 9.37; Cu, 16.80; N, 14.81; % Found: C, 47.43; H,2.11; Cl, 8.87; Cu, 16.43; N, 14.23.

Z5 copper(II) complex [Cu(L2-H)Cl]: brown solid; yield 76%; m.p. 170°C to 172°C; conductance (ΔM, Ω^{-1} cm^2 mol^{-1}; DMF) =17; μeff=1.79 BM at 298 K; IR (v_{max}, cm^{-1}): 3337 (v OH.), 3309 (v NH $_{amide}$), 3152, 3090 (v CH $_{aromatic}$), 2930 (v CH $_{azomethine}$), 1661 (v C=N $_{imine}$), 1622 (v C=N $_{oxadiazole}$ ring), 1255 (v(C-

O) oxadiazole ring), 543 (v Cu-O), 432 (v Cu-N), 412 (v Cu-Cl); EI-MS (m/z): 394.27, Anal. %Calcd. for $C_{15}H_{11}ClCuN_4O_3$ C, 45.70; H, 2.81; Cl, 8.99; Cu, 16.12; N, 14.21; %Found: C, 45.65; H, 2.43; Cl, 8.12; Cu, 15.76; N, 14. 09.

Z6 copper(II) complex [Cu(L3-H)Cl]: dark brown solid; yield 76%; m.p. 180°C to 182°C; UV-Vis (DMF, λ_{max}, nm (abs)): 367 (0.045), 279 (1.451), 783 (12,771); conductance (ΔM, Ω^{-1} cm^2 mol^{-1}; DMF) = 22; μeff =1.75 BM at 298 K; IR (v_{max}, cm^{-1}): 3317 (v NH amide), 3145, 3089 (v CH aromatic), 2943 (v CH azomethine), 1658 (v C=N imine), 1620 (v C=N oxadiazole ring), 1250 (v(C-O) oxadiazole ring), 830 (v C-Cl), 563 (v Cu-O), 456 (v Cu-N), 412 (v Cu-Cl); EI-MS (m/z): 412.72, Anal. %Calcd. for $C_{15}H_{10}Cl_2CuN_4O_2$: C, 43.65; H, 2.44; Cl, 17.18; Cu, 15.40; N, 13.58; %Found: C, 43.11; H, 2.87; Cl, 17.54; Cu, 15.22; N, 13.89.

Z7 zinc(II) complex [Zn(L1-H)Cl]: brown solid; yield 68%; m.p. 179°C to 181°C; UV-Vis (DMF, λ_{max}, nm (Abs)): 367 (0.045), 279 (1.451), 275 (1.530); Conductance (ΔM, Ω^{-1} cm^2 mol^{-1}; DMF) = 21; IR (v_{max}, cm^{-1}): 3314 (v NH amide), 3144, 3082 (v CH aromatic), 2956 (v CH azomethine), 1657 (v C=N imine), 1624 (v C=N oxadiazole ring), 1252 (v(C-O) oxadiazole ring), 466 (v Zn -N), 560 (v Zn -O) 438 (v Zn-Cl); EI-MS (m/z): 343.21; ^{1}H NMR(400 MHz, DMSO-d$_6$): 10.54 (s,1H, N-H), 7.65 (s,1H, HC=N), 6.78 to 8.30 (m,9H, aromatic protons),11.45 (s,1H, OH); ^{13}C NMR (100 MHz, DMSO-d$_6$): δ155.4 (C-N), 124.43, 124.58, 125.96, 130.93, (aromatic carbons), 144.54 (C=N); Anal. %Calcd. for $C_{15}H_{11}ClN_4O_2Zn$: C, 47.40; H, 2.92; Cl, 9.33; N, 8.42; Zn, 17.20; % Found: C, 47.54; H, 2.43; Cl, 9.78; N, 14.74, Zn, 17.87.

Z8 zinc(II) complex [Zn(L2-H)Cl]: brown solid; yield 68%; m.p. 175°C to 177°C; UV-Vis (DMF, λ_{max}, nm (Abs)): 367 (0.045), 279 (1.451), 275 (1.530); Conductance (ΔM, Ω^{-1} cm^2 mol^{-1}; DMF) = 23; IR cm^{-1}): 3335 (v OH), 3319 (v NH amide), 3162, 3094 (v CH aromatic), 2932 (v CH azomethine), 1655 (v C=N imine), 1621 (v C=N oxadiazole ring), 1251 (v(C-O) oxadiazole ring), 837 (v M-O), 567 (v Zn-O), 476 (v Zn-N), 432 (v Zn-Cl); EI-MS (m/z):396.11; ^{1}H NMR(400 MHz, DMSO-d$_6$): 9.74 (s, 1H, OH), 10.52 (s,1H, N-H), 7.70 (s,1H, HC=N), 7.24 to 8.35 (m, 8H, aromatic protons); ^{13}C NMR (100 MHz, DMSO-d$_6$): δ 159.30 (C-O), 156.8 (C-O), 123.46, 124.76, 128.84, 125.97, 130.34 (aromatic carbons) 143.89 (C=N), 157.54 (COH); Anal. %Calcd. for $C_{15}H_{11}ClN_4O_3Zn$: C, 45.48; H, 2z.80; Cl, 8.95; N, 14.14; Zn, 16.51. %Found: C, 45.78; H, 2.34; Cl, 8.12; N, 14.65; Zn, 16.22.

Z9 zinc (II) complex [Zn(L3-H)Cl]: brown solid; yield 68%; m.p. 185°C to 187°C; UV-Vis (DMF, λ_{max}, nm (Abs)): 367 (0.045), 279 (1.451), 275 (1.530); Conductance (ΔM, Ω^{-1} cm^2 mol^{-1}; DMF) = 25; IR (v_{max}, cm^{-1}): 3318 (v NH amide), 3147, 3082 (v CH aromatic), 2936 (v CH azomethine), 1659 (v C=N imine), 1625 (v C=N oxadiazole ring), 1256 (v(C-O) oxadiazole ring), 840 (v C-Cl), 564 (v Zn-O), 467(v Zn-N), 422 (v Zn-Cl); ^{1}H NMR (400 MHz, DMSO-d$_6$): 10.51 (s,1H, N-H), 7.57 (s,1H, HC=N), 7.30 to 8.32 (m, 8H, aromatic protons); ^{13}C NMR (100 MHz, DMSO-d$_6$): δ 157.2 (C-O), 124.0, 124.76, 128.82, 125.98, 130.32 (aromatic carbons), 134.23 (C-Cl) 144.12 (C=N), 156.98 (COH); EI-MS (m/z): 414.55; Anal. %Calcd. for $C_{15}H_{10}Cl_2N_4O_2Zn$: C, 43.46; H, 2.43; Cl, 17.10; N, 13.52; O, 7.72; Zn, 15.77; %Found: C, 43.65; H, 2.43; Cl, 17.11; N, 13.67; Zn, 15.43.

DNA interaction studies

The studies of DNA cleavage and binding with complexes were carried out in Tris–HCl/NaCl buffer solutions [17].

Computational details

Gaussian 09 software [21] was used to perform the DFT calculations. All the structures of the compounds were optimized at the B3LYP level using the 6-31+G(d,p) basis set for C, H, O, N, and Cl atoms and the LANL2DZ basis set [22] for metal atoms. Several researchers used the LANL2DZ as a basis set in DFT calculations of systems that included metal atoms [23, 24]. GaussView 5.0, which is supported by Gaussian Inc. [21], was used to create the input files for the DFT calculations. The GaussView 5.0 software is used to visualize and analyze the data obtained from Gaussian09 output results. A frequency calculation was performed to identify the most stable structures of the synthesized compounds. The absence of the imaginary frequencies in the calculated vibrational modes indicates that the corresponding optimized structure of the molecule is the most stable one. The obtained values of the vibrational modes from the DFT calculations were scaled by a factor of 0.966 [25]. The energies and electron densities of the frontiers' molecular orbitals were calculated using the B3LYP level of theory and the LANL2DZ as a basis set. The excited states were computed for all compounds at the same level of theory using the TD-DFT (Time-Dependent Density Functional Theory) method [26]. The TD-DFT calculations were performed in DMSO solvent using the CPCM

solvation model (conductor-like polarizable continuum model) [27]. The projected density of states (PDOS) was obtained through the calculated orbital populations for all compounds at the same level of theory, using the GAUSSUM 3.0 program [28]. *lecular docking*

The structures of the ligands and their complexes were obtained by using DFT calculations using GaussView 5.0. A molecular docking study was done using topoisomerase I (70 kDa) (PDB ID: 1SC7) which was obtained from the RCSB protein data bank (http://www.rcsb.org/pdb). AutoDock Tool 4.2 [29] was used for the preparation of protein, grid, and missed atoms. The polar hydrogen atoms were added to the ISC7 receptor structure.

The Kollman charge was computed and added to the structures. A PDBQT file of protein structures was created by loading the receptor ISC7 into AutoDock Tool 4.2. A grid box with X: 60 Y: 60 Z: 60 Å, with a grid spacing of 0.5 Å, centered on X: 99.50. Y:1.82 Z: 11.35 Å was established to define the docking site on the protein. The Discovery Studio 4.0 client [30] was used to analyze the interactions of the compounds with ISC7.

RESULTS AND DISCUSSION

Synthesis of the compounds

Three types of ligands, L1, L2, and L3, have been synthesized in this work in four steps, beginning with a reaction of benzoic acid, 4-hydroxybenzoic acid, or 4-chlorobenzoic acid with an equimolar amount of $NH_2NH_2.H_2O$ and 98% H_2SO_4 (B products). In the second step, the reaction of the B product with CS_2 and KOH was in a 1:1 molar ratio. Third step: a solution of $NH_2NH_2.H_2O$ was mixed with a solution of the D product. Finally, equimolar amounts of 2-hydroxybenzaldehyde and E products from the previous step and some drops of glacial acetic acid were mixed to give L1, L2, and L3 ligands, according to Scheme 1, with a percentage yield of 80%, 70%, and 77%, respectively. The synthesized ligands are stable and soluble in THF, DMF, DMSO, dichloromethane, and chloroform. The complexes were prepared as shown in Scheme 1 by reaction of the ligand of $MCl_2.6H_2O$, or $ZnCl_2$, M is Ni or Cu, in a molar ratio of 1:1 (M:L) to give [M(L1-H)Cl], [M(L2-H)Cl], [M(L3-H)Cl] where M is Ni^{2+}, Cu^{2+}, or Zn^{2+}, with yields in the range of 67% - 82%. The obtained complexes are air-stable and soluble in

DMSO, DMF, and dichloromethane. Mass spectrometry gave ion peaks M^+ at 373.42, 389.42, 407.86, 378.28, 394.27, 412.72, 343.21, 396.11, and 414.55 m/z, respectively, for Z1-Z9 complexes [14 .15]. The molecular masses correlate to the proposed structures and confirm the molar ratio of metal: ligand of 1:1 in all complexes.

FTIR spectral studies

Selected vibrational frequencies of the infrared spectra of the complexes (Z1-Z9) and the ligands (L1-L3) are given in Table S3. The assignments for the observed infrared bands were based on the calculated vibrational modes and the literature data [31-33]. The FTIR spectra of the ligands (L1-L3) show bands in the range 1678-1674 and 1270-1262 cm^{-1} are attributed to ν(C=N) imine and ν(C-O) oxadiazole, respectively. These modes were detected in the FTIR spectra of the complexes (Z1-Z9) in the ranges 1655-1662 cm^{-1} for ν(C=N) imines and 1249-1261 cm^{-1} for ν(C-O) oxadiazole. The chelation through the nitrogen atom of the imine group and the oxygen atom of the oxadiazole ring with the metal ion in complexes is supported by the downshifting of the vibrational frequencies of the (C=N) imine and (C-O) oxadiazole in the IR spectra of the complexes compared to those of the ligand [11]. In the FTIR spectra (Figures S1 and S2, see the ESI) of the ligands (L1-L3), a band appeared in the range of 3325-3347 cm^{-1} and was assigned to the stretching vibration of the hydroxyl group (ν(OH)) [12]. This band is absent in the FTIR spectra (Figures S3, S4, and S5) of the Z1, Z3, Z4, Z6, Z7, and Z9 complexes. This result is an indication of the coordination of the L1, L2, and L3 ligands *via* the oxygen atom of the hydroxyl group with the metal ion and the deprotonation of the hydroxyl group upon the complexation process. The ν(OH) appeared in the FTIR spectra (Figures S6, S7, and S8) of the Z2, Z5, and Z8 complexes, contrary to what was observed in the spectra of other complexes (Z1, Z3, Z4, Z6, Z7, and Z9). This result is due to the presence of two hydroxyl groups in the L2 ligand, which is coordinated with the metal ion via the oxygen atom of one hydroxyl group to form the Z2, Z5, and Z8 complexes. The coordination of the L1, L2, and L3 ligands *via* oxygen and nitrogen atoms is further supported by the observation of the bands in the ranges 476–432 and 521–567 cm^{-1} which are assigned to ν(M-N) and ν(M-O), respectively [13]. The above-mentioned observations are also concluded from the

calculated IR spectra for the ligands and complexes that are given in Table S3.

¹H NMR and ¹³C NMR spectra

The ¹H NMR spectra (Figures S9, S10, and S11) of the ligands, L1, L2, and L3, show peaks as singlet signals for N-H, HC=N, OH, and C=NH groups at 10.51- 10.54, 8.23-8.52 ppm, 11.23-11.60 and 7.70–7.45 ppm, respectively [14]. Also in the spectra, peaks appeared at 6.78 to 8.32 ppm as multiplet signals and were assigned to aromatic protons. The ¹³C NMR spectra (Figures S12 and S13) of the ligands showed peaks at 123.45–130.32 ppm and were assigned to aromatic carbon. The chemical shifts of the C signals of the C-O ring (155.4-157.2 ppm) in the zinc (II) complex spectra [15].

Mass spectral studies

The composition of the compound was characterized by mass spectra. The ligands L1, L2, and L3 showed peaks at m/z 280, 296, and 314, respectively. The molecular ions are confirmed by the peaks that appeared at m/z 378 (30%), 394 (25%), and 412 (70%). The observed molecular masses of the complexes were evidenced by ESI mass spectra peaks at m/z 378 (13%) and 412 (46%), coinciding with the molecular weights of complexes Z4 and Z6, respectively. They showed a base peak of L2 and L3 at 378 (80%) and 412 (90%) and identified the molecular weight of these ligands [16].

Geometry optimization of the complexes

Full geometry optimization of the Z1-Z9 complexes was performed using the DFT/B3LYP (exchange-correlation functional [34-36]) with the 6-31+G(d,p) basis set for C, H, O, N, and Cl atoms and the effective core potential LANL2DZ basis set for metal atoms. The optimized structures of the Z1, Z2, and Z3 (Ni²⁺ complexes) according to the B3LYP/LANL2DZ level of theory are displayed in Figure 1. The selected bond distances and angles of these complexes' optimized structures are listed in Table 1. The calculated geometries of Z1, Z2, and Z3 indicated a distorted square-planar environment around the central Ni atom. The result is obtained according to the calculated Cl-Ni-O and O-Ni-N angles of these complexes, which are close to 90° as listed in Table 1. The other features of Figure 1 that support the distorted square-planar environment around the central Ni atom are the calculated values

of the Cl-Ni-N and O-Ni-O angles, which are close to 180°.

Figure 1. Optimized structures of Z1, Z2, and Z3 complexes according to DFT calculations using B3LYP functional with the 6-31+G(d,p) basis set for C, H, O, N, and Cl atoms and LANL2DZ basis set for the Ni atom.

Figure 2. Optimized structures of Z4, Z5, and Z6 complexes according to DFT calculations using B3LYP functional with the 6-31+G(d,p) basis set for C, H, O, N, and Cl atoms and LANL2DZ basis set for the Cu atom.

The selected bond distances and angles of these complexes' optimized structures are listed in Table 2. The calculated geometries of Z4, Z5, and Z6 indicated a distorted tetrahedral environment around the central Cu atom. This conclusion is made from the calculated Cl-Cu-O and O-Cu-N angles of these complexes, which are listed in Table 2.

The optimized structures of Z7, Z8, and Z9 (Zn^{2+} complexes) according to the B3LYP/LANL2DZ level of theory are displayed in Figure 3. The selected bond distances and angles of these complexes' optimized structures are listed in Table 3. The calculated geometries of Z7, Z8, and Z9 indicated a distorted tetrahedral environment around the central Zn atom.

The optimized structures of Z7, Z8, and Z9 (Zn^{2+} complexes) according to the B3LYP/LANL2DZ level of theory are displayed in Figure 3. The selected bond distances and angles of these complexes' optimized structures are listed in Table 3. The calculated geometries of Z7, Z8, and Z9 indicated a distorted tetrahedral environment around the central Zn atom.
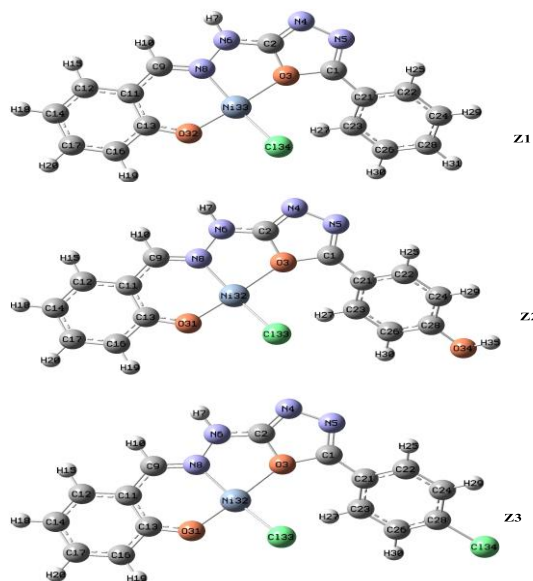
Figure 3. Optimized structures of Z7, Z8, and Z9 complexes according to DFT calculations using B3LYP functional with the 6-31+G(d,p) basis set for C, H, O, N, and Cl atoms and LANL2DZ basis set for the Zn atom.
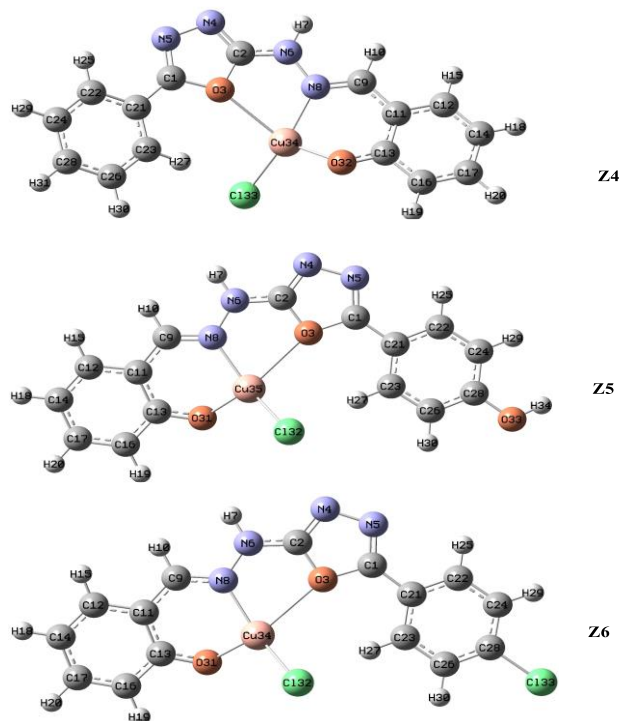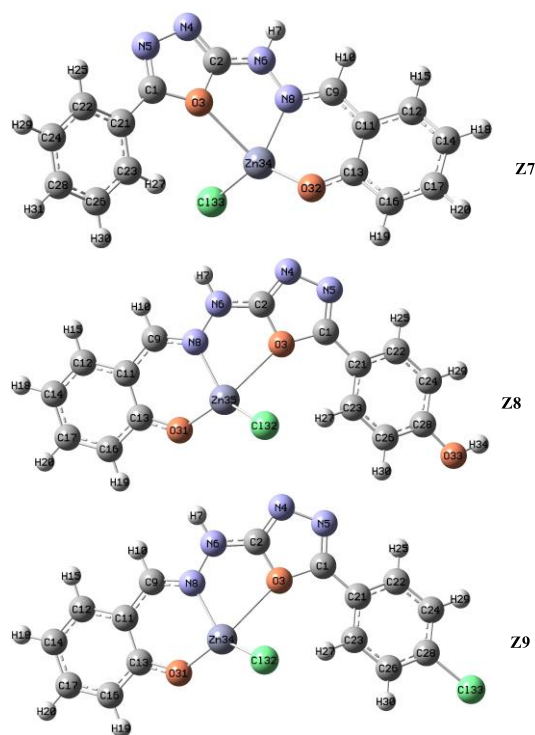
Table 1. Selected bond lengths (Å) and bond angles (°) of the computed structures of the Z1, Z2, and Z3 according to DFT calculations[*].

Bond lengths (Å) of Z1		Bond lengths (Å) of Z2		Bond lengths (Å) of Z3	
Ni33-Cl34	2.210	Ni32-Cl33	2.211	Ni32-Cl33	2.211
O32-Ni33	1.823	O31-Ni32	1.823	O31-Ni32	1.821
N8-Ni33	1.922	N8-Ni32	1.922	N8-Ni32	1.921
O3-Ni33	2.067	O3-Ni32	2.068	O3-Ni32	2.074
N6-N8	1.404	N6-N8	1.404	N6-N8	1.404
N8-C9	1.321	N8-C9	1.321	N8-C9	1.321
Angles (°) of Z1		Angles (°) of Z2		Angles (°) of Z3	
Cl34-Ni33-O32	90.7	Cl33-Ni32-O31	90.6	Cl33-Ni32-O31	90.7
Cl34-Ni33-N8	168.9	Cl33-Ni32-N8	169.0	Cl33-Ni32-N8	168.7
Cl34-Ni33-O3	95.4	Cl33-Ni32-O3	95.4	Cl33-Ni32-O3	95.6
O32-Ni33-N8	93.5	O31-Ni32-N8	93.5	O31-Ni32-N8	93.5
O32-Ni33-O3	170.8	O31-Ni32-O3	170.8	O31-Ni32-O3	170.3
N8-Ni33-O3	81.8	N8-Ni32-O3	81.8	N8-Ni32-O3	81.8

[*]The DFT calculations are performed using B3LYP functional with the 6-31+G(d,p) basis set for C, H, O, N, and Cl atoms and LANL2DZ basis set for Ni atom.

Table 2. Selected bond lengths (Å) and bond angles (°) of the computed structures of the Z4, Z5, and Z6 according to DFT calculations[*].

Bond lengths (Å) of Z4		Bond lengths (Å) of Z5		Bond lengths (Å) of Z6	
Cl33-Cu34	2.215	Cl32-Cu35	2.216	Cl32-Cu34	2.214
O32-Cu34	1.927	O31-Cu35	1.927	O31-Cu34	1.927
N8-Cu34	2.026	N8-Cu35	2.028	N8-Cu34	2.028
O3-Cu34	2.548	O3-Cu35	2.542	O3-Cu34	2.571
N8-C9	1.322	N8-C9	1.323	N8-C9	1.323
N6-N8	1.392	N6-N8	1.391	N6-N8	1.393
Angles (°) of Z4		Angles (°) of Z5		Angles (°) of Z6	
Cl33-Cu34-O32	108.3	Cl32-Cu35-O31	108.4	Cl32-Cu34-O31	108.7
Cl33-Cu34-N8	152.4	Cl32-Cu35-N8	152.3	Cl32-Cu34-N8	152.9
Cl33-Cu34-O3	100.8	Cl32-Cu35-O3	100.6	Cl32-Cu34-O3	99.9
O32-Cu34)-N8	90.4	O31-Cu35-N8	90.1	O31-Cu34-N8	90.2
O32-Cu34)-O3	141.7	O31-Cu35-O3	142.1	O31-Cu34-O3	142.5
N8-Cu34-O3	73.5	N8-Cu35-O3	73.6	N8-Cu34-O3	73.2

[*]The DFT calculations are performed using B3LYP functional with the 6-31+G(d,p) basis set for C, H, O, N, and Cl atoms and LANL2DZ basis set for Cu atom.

Table 3. Selected bond lengths (Å) and bond angles (°) of the computed structures of the Z7, Z8, and Z9 according to DFT calculations[*].

Bond lengths (Å) of Z7		Bond lengths (Å) of Z8		Bond lengths (Å) of Z9	
Cl33-Zn34	2.252	Cl32-Zn35	2.252	Cl32-Zn34	2.249
O32-Zn34	1.920	O31-Zn35	1.920	O31-Zn34	1.916
N8-Zn34	2.069	N8-Zn35	2.068	N8-Zn34	2.065
O3-Zn34	2.559	O3-Zn35	2.569	O3-Zn34	2.652
N8-C9	1.328	N8-C9	1.328	N8-C9	1.330
N6-N8	1.406	N6-N8	1.406	N6-N8	1.407
Angles (°) of Z7		Angles (°) of Z8		Angles (°) of Z9	
Cl33-Zn34-O32	125.6	Cl32-Zn35-O31	125.7	Cl32-Zn34-O31	126.5
Cl33-Zn34-N8	135.5	Cl32-Zn35-N8	135.7	Cl32-Zn34-N8	136.5
Cl33-Zn34-O3	92.8	Cl32-Zn35-O3	92.3	Cl32-Zn34-O3	90.2
O32-Zn34-N8	90.5	O31-Zn35-N8	90.5	O31-Zn34-N8	91.0
O32-Zn34-O3	136.3	O31-Zn35-O3	136.4	O31-Zn34-O3	137.2
N8-Zn34-O3	70.5	N8-Zn35-O3	70.4	N8-Zn34-O3	69.3

[*]The DFT calculations were performed using B3LYP functional with the 6-31+G(d,p) basis set for C, H, O, N, and Cl atoms and LANL2DZ basis set for Zn atom.

UV-Vis results

The UV-Vis electronic absorption spectra (Figures S14–S21) of the ligands (L1-L3) and complexes (Z1-Z9) were experimentally recorded in the region of 200-1100 nm at ambient temperature in DMSO solvent with a concentration of 1 mM. Time-Dependent Density Functional Theory (TD-DFT [37-39]) calculations approach for the optimized geometry has been used to examine the electronic absorption behaviors of the studied compound in solvent media. In these calculations, we used B3LYP functional (exchange-correlation functional [34-36]) with the 6-31+G(d,p) basis set for C, H, O, N, and Cl atoms and the effective core potential LANL2DZ basis set for metal atoms.

The UV-vis spectra of the ligands show two absorption peaks. The first peaks for L1, L2, and L3 ligands appeared at 231, 225, and 231 nm, respectively, and were assigned to charge transfer transition ($\pi \rightarrow \pi^*$) [16]. The second peak appeared at 356, 350, and 363 nm for L1, L2, and L3 ligands, respectively, and is assigned to the charge transfer transition ($n \rightarrow \pi^*$) [16]. The UV-Vis spectra of the Z1, Z2, and Z3 complexes (Ni^{2+} complexes) show two bands. The bands that appeared at 465, 459, and 455 nm in the UV-Vis spectra of Z1, Z2, and Z3 complexes, respectively, are assigned to 2A1g → 2B1g transitions. The calculated value for this band is obtained at 471, 449, and 457 nm for Z1, Z2, and Z3, respectively, according to the TD-DFT results. The other band appeared at 645, 651, and 660 nm in the UV-Vis spectra of Z1, Z2, and Z3 complexes, respectively, and was assigned to 2A1g → 2A2g transitions. The calculated value of this band is observed at 655, 658, and 670 nm for Z1, Z2, and Z3, respectively. These results indicated a square planer environment around the central Ni atom, as evidenced by the calculated structures for these complexes (Figure 1).

The UV-Vis spectra of the Z4, Z5, and Z6 complexes (Cu^{2+} complexes) show a band in the range of 609–632 nm. The shape of this band is unsymmetrical, seeming to encompass several overlapping transitions. This band is similar to the reported absorption maximum for distorted tetrahedral Cu(II) complexes [40]. The TD-DFT calculation shows that these complexes (Z4, Z5, and Z6) exhibit two absorption bands that are very close to each other in the range of 600–640 nm. These two bands are separated by 15 to 18 nm. The result further supports that the Cu^{2+} complexes have two overlapped transitions in this range.

The UV-Vis spectra of the Z7, Z8, and Z9 complexes (Zn^{2+} complexes) exhibit two bands in the range of 374–280 and 465–490 nm. These bands are attributed to the C.T. transition. The absence of a band > 400 nm may be due to the MLCT of the d10 geometry of the zinc (II) ion [18]. The corresponding calculated UV-Vis spectra for the Z7, Z8, and Z9 complexes show three absorption bands for these complexes. The two bands are located very close to each other and in the range of 325–350 nm. The third band is observed in the range of 400–485 nm. A theoretical study of zinc(II) interactions with amino acid models and peptide fragments concluded that the zinc complexes prefer a tetrahedral geometry [41]. In

our study, the calculated structures of the Z7, Z8, and Z9 complexes are found to have a distorted tetrahedral geometry.

The energy profiles of the HOMO, LUMO, and HOMO-LUMO gaps for Z4, Z5, and Z6 (Cu^{2+} complexes) are shown in Figure 5, using B3LYP functional with the 6-31+G(d,p) basis set for C, H, O, N, and Cl atoms and the LANL2DZ basis set for the Cu atom in DMSO solvent. Figure 5 shows the HOMO-LUMO energy gaps of Cu^{2+} complexes which are higher than those of Ni^{2+} complexes (Figure 4). The contribution of copper ions (Cu^{2+}) in the HOMO and LUMO orbitals in complexes Z4, Z5, and Z6 is very small (1-2%) which is contrary to nickel complexes (Figure 4). The imine group (N8=C9−H10) is the major contributor in the LUMO orbital of the Z4, Z5, and Z6 with 44, 46, and 42%, respectively. In the HOMO orbitals of the Z4, Z5, and Z6 The contributions of the imine group are 9, 7, and 9%, respectively. Also, the ortho-disubstituted benzene rings of the Z4, Z5, and Z6 notably contribute to the LUMO orbitals of these complexes with 31, 33, and 30%, respectively. A remarkable contribution of the disubstituted benzene rings of the Z4, Z5, and Z6 to the HOMO orbitals of these complexes is 39, 25, and 36%, respectively. The contribution of the oxadiazole ring is also 15, 20, and 17% to the HOMO orbitals of Z4, Z5, and Z6, respectively. While in the LUMO orbitals the contribution of the oxadiazole rings of Z4, Z5, and Z6, are 14, 12, and 15%, respectively.

Figure 6 shows the energy profile of the HOMO's, LUMO's, and HOMO-LUM-O gaps for the Zn^{2+} complexes Z7, Z8, and Z9, which are calculated at the B3LYP function with the 6-31+G(d,p) basis set for C, H, O, N, and Cl atoms and LANL2DZ basis set for zinc atom in DMSO solvent. The energy gaps of HOMO-LUMO in zinc complexes are higher than that of nickel complexes (Figure 4) and very close to copper complexes (Figure 5). In the HOMO and LUMO orbitals, the contribution of the zinc metal ion in the complexes Z7, Z8, and Z9 is very small (0–1%) as observed in the case of Cu^{2+} complexes. A remarkable contribution in the LUMO orbitals of the Z7, Z8, and Z9 is observed for the imine group (N8=C9−H10) with 42, 45, and 37%, respectively. The contribution of the imine group in the HUMO orbital is only 8% in the case of Zn^{2+} complexes. Also, the ortho-disubstituted benzene rings of the Z7, Z8, and Z9 notably contribute to the LUMO orbitals of these complexes with 29, 32, and 26%, respectively.

The major contributions of the HOMO orbitals of the Z7, Z8, and Z9 are observed for the disubstituted benzene ring at 48, 41, and 50%, respectively. The oxadiazole ring also contributed 15, 12, and 18% to the LUMO orbitals of Z7, Z8, and Z9, respectively. It was observed that the contribution of the oxadiazole ring in the HOMO orbitals of Z7, Z8, and Z9, is 10, 13, and 9%, respectively.

Electronic structures

The calculated energies and electron densities of the frontier's molecular orbitals were used to confirm the electronic properties of the complexes.

The energy profiles of the highest occupied molecular orbitals, HOMOs, lowest unoccupied molecular orbitals, LUMOs, and HOMO-LUMO gaps for Z1, Z2, and Z3 (Ni^{2+} complexes) are shown in Figure 4. The B3LYP functional with the 6-31+G(d,p) basis set is used to calculate the energies for C, H, O, N, and Cl atoms and the LANL2DZ basis set for Ni atoms using DMSO solvent. The Z1 complex explores the higher HOMO-LUMO energy gap. In complexes Z1, Z2, and Z3, the percent composition of the selected frontier-occupied and the virtual molecular orbitals are obtained based on the results of the projected density of states (PDOS) calculations.

The LUMO orbitals in the complexes Z1, Z2, And Z3 are mostly localized on Ni^{2+} ions in order of 66, 66, and 65%, respectively. Figure 4 does not show the contribution of the phenyl ring, phenol group, and chlorobenzene in Z1, Z2, and Z3 in the HOMO and LUMO orbitals.

The contribution of the imine group (N8=C9-H10) in HOMO and LUMO orbitals of the complexes Z1, Z2, and Z3 is only 7%. The HOMO orbital of these complexes (Z1, Z2, and Z3) is mostly localized on the ortho-disubstituted benzene ring with 48, 42, and 49%, respectively. The contribution of oxygen atoms to the HOMO orbitals in Z1, Z2, and Z3 complexes are 20, 17, and 20%, respectively.

The energy profiles of the HOMOs, LUMOs, and HOMO-LUMO gaps for Z4, Z5, and Z6 (Cu^{2+} complexes) are shown in Figure 5, using B3LYP functional with the 6-31+G(d,p) basis set for C, H, O, N, and Cl atoms and the LANL2DZ basis set for the Cu atom in DMSO solvent. Figure 5 shows the HOMO-LUMO energy gaps of Cu^{2+} complexes which are higher than that of Ni^{2+} complexes (Figure 4). The contribution of copper ions (Cu^{2+}) in the HOMO and LUMO orbitals in complexes Z4, Z5, and Z6 is very small (1-2%) which is contrary to nickel complexes

(Figure 4). The imine group (N8=C9−H10) is the major contributor in the LUMO orbital of the Z4, Z5, and Z6 with 44, 46, and 42%, respectively. In the HOMO orbitals of the Z4, Z5, and Z6 The contributions of the imine group are 9, 7, and 9%, respectively. Also, the ortho-disubstituted benzene rings of the Z4, Z5, and Z6 notably contribute to the LUMO orbitals of these complexes with 31, 33, and 30%, respectively. A remarkable contribution of the disubstituted benzene rings of the Z4, Z5, and Z6 to the HOMO orbitals of these complexes is 39, 25, and 36%, respectively. The contribution of the oxadiazole ring is also 15, 20, and 17% to the HOMO orbitals of Z4, Z5, and Z6, respectively. While in the LUMO orbitals the contribution of the oxadiazole rings of Z4, Z5, and Z6, are 14, 12, and 15%, respectively.

Figure 6 shows the energy profile of the HOMO's, LUMO's, and HOMO-LUMO gaps for the Zn^{2+} complexes Z7, Z8, and Z9, which are calculated at the B3LYP function with the 6-31+G(d,p) basis set for C, H, O, N, and Cl atoms and LANL2DZ basis set for zinc atom in DMSO solvent. The energy gaps of HOMO-LUMO in zinc complexes are higher than that of nickel complexes (Figure 4) and very close to copper complexes (Figure 5). In the HOMO and LUMO orbitals, the contribution of the zinc metal ion in the complexes Z7, Z8, and Z9 is very small (0–1%) as observed in the case of Cu^{2+} complexes. A remarkable contribution in the LUMO orbitals of the Z7, Z8, and Z9 is observed for the imine group (N8=C9−H10) with 42, 45, and 37%, respectively. The contribution of the imine group in the HUMO orbital is only 8% in the case of Zn^{2+} complexes. Also, the ortho-disubstituted benzene rings of the Z7, Z8, and Z9 notably contribute to the LUMO orbitals of these complexes with 29, 32, and 26%, respectively. The major contributions of the HOMO orbitals of the Z7, Z8, and Z9 are observed for the disubstituted benzene ring at 48, 41, and 50%, respectively. The oxadiazole ring also contributed 15, 12, and 18% to the LUMO orbitals of Z7, Z8, and Z9, respectively. It was observed that the contribution of the oxadiazole ring in the HOMO orbitals of Z7, Z8, and Z9, is 10, 13, and 9%, respectively.

Measurement of molar conductivity

The measurements of molar conductivity (ΔM) for the Z1–Z9) complexes of mononuclear metal (II) were performed in DMF solvent, according to the conductance data (17–25 Ω^{-1} cm^2 mol^{-1}) of the

complexes, which is the non-electrolytic behavior of these complexes [19].

Magnetic properties

The corrected magnetic moments of metal (II) complexes (Z1–Z9) were measured and calculated using Pascal's constants. The magnitudes of the magnetic moments (1.75–1.79 BM) for Cu(II) complexes (Z4–Z6) are assigned to the spin only of the d^9 environment with one unpaired electron, confirming the tetrahedral environment around Cu(II) metal ions complexes. The magnetic moments of Ni(II) complexes (Z1-Z3) are in the 0.12 – 0.24 BM range and are attributed to a square planar environment, which agrees with the electronic transitions in the UV-vis spectra [20]. The Zn(II) complexes, (Z7–Z9), exhibit diamagnetic properties which are attributed to the d10 environment, as predictable. The electronic transitions in UV-Vis, magnetic susceptibility, and sensitivity values confirm a distorted tetrahedral environment for Zn(II) complexes (Z7-Z9) and Cu(II) complexes (Z4-Z6), and a distorted square planar environment for Ni²⁺ complexes (Z1-Z3).
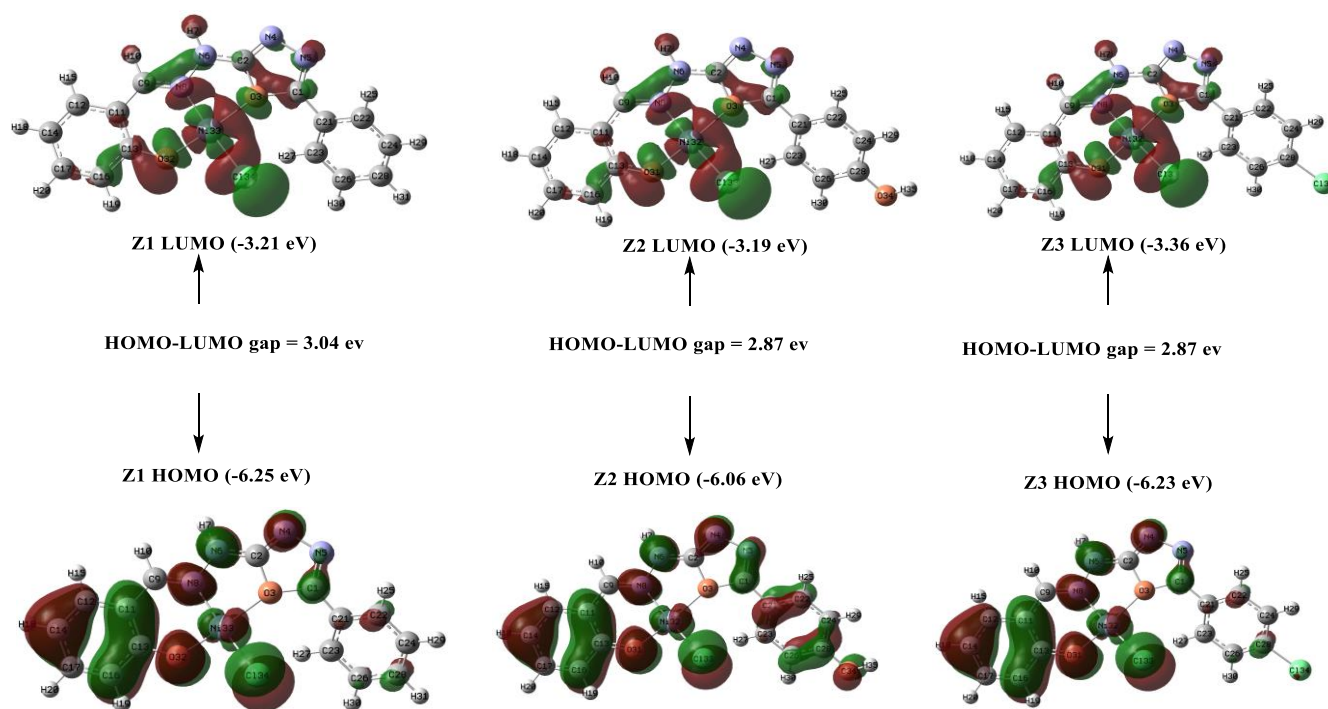

Figure 4. Energy profile of the frontier orbitals HOMO and LUMO, and HOMO-LUMO gaps for Z1, Z2, and Z3, calculated at the B3LYP functional with the 6-31+G(d,p) basis set for C, H, O, N, and Cl atoms and LANL2DZ basis set for Ni atom in DMSO as solvent.

Z4 LUMO (-2.80 eV)   **Z5 LUMO (-2.76 eV)**   **Z6 LUMO (-2.92 eV)**

HOMO-LUMO gap = 3.56 ev   **HOMO-LUMO gap = 3.42 ev**   **HOMO-LUMO gap = 3.56 ev**

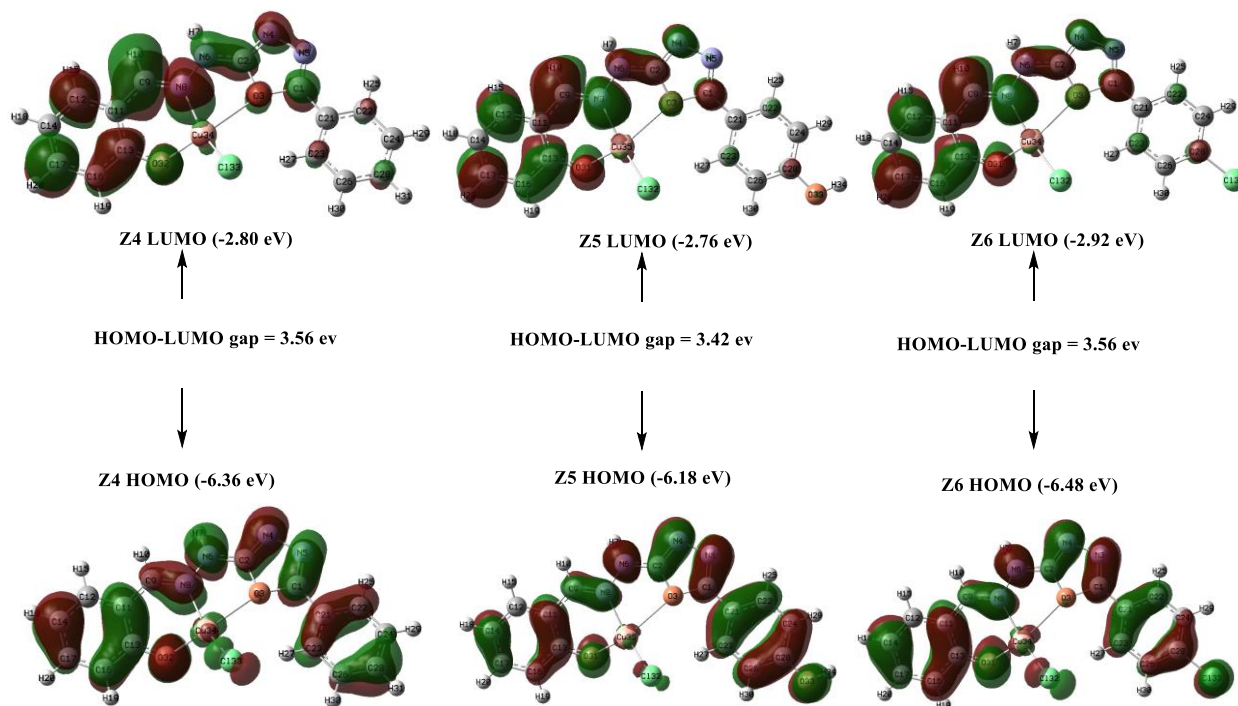**Z4 HOMO (-6.36 eV)**   **Z5 HOMO (-6.18 eV)**   **Z6 HOMO (-6.48 eV)**

Figure 5. Energy profile of the frontier orbitals HOMO and LUMO, and HOMO-LUMO gaps for Z4, Z5, and Z6, calculated at the B3LYP functional with the 6-31+G(d,p) basis set for C, H, O, N, and Cl atoms and LANL2DZ basis set for Cu atom in DMSO as solvent.

Z7 LUMO (-2.69 eV)   **Z8 LUMO (-2.66 eV)**   **Z9 LUMO (-2.83 eV)**

HOMO-LUMO gap = 3.55 ev   **HOMO-LUMO gap = 3.50 ev**   **HOMO-LUMO gap = 3.54 ev**

Z7 HOMO (-6.24 eV)   **Z8 HOMO (-6.16 eV)**   **Z9 HOMO (-6.37 eV)**
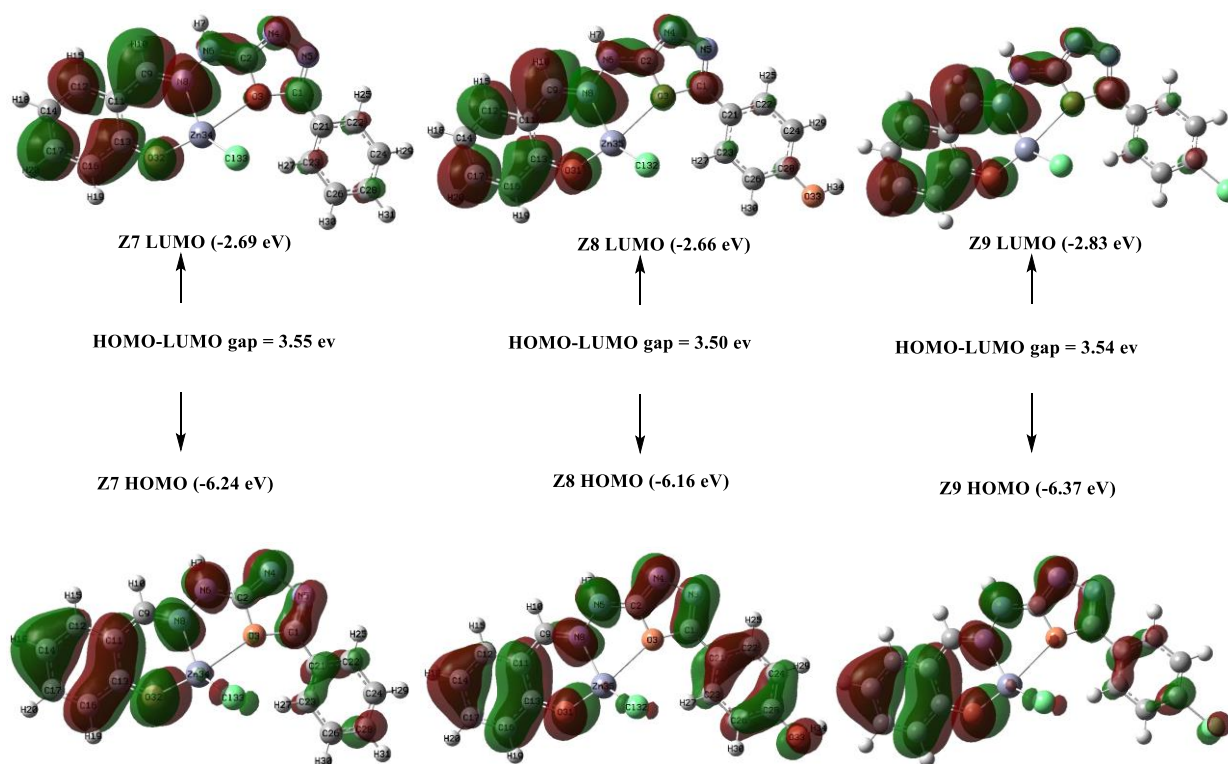
Figure 6. Energy profile of the frontier orbitals HOMO and LUMO, and HOMO-LUMO gaps for Z7, Z8, and Z9, calculated at the B3LYP functional with the 6-31+G(d,p) basis set for C, H, O, N, and Cl atoms and LANL2DZ basis set for Zn atom in DMSO as solvent.

Thermal analysis

All the complexes (Z1–Z9) appeared in an analogous decomposition style, with mass lacking in all four steps. The curves of DSC and TG for complexes Z7–Z9 appeared at the first stage; complexes offer an exothermic peak between 175 and 280 °C (obs. 34%, calc. 30%) attributed to the removal of Cl from the complex. The 2nd and 3rd stages form the ligand decomposition (350–410 °C, obs. 62.87%, calc. 60.23%) and depart from the metal atom that is then oxidized to obtain the definitive remains as a MO at 500.43–550.76 °C [42].

DNA-binding assays

Because DNA interactions were carried out in a Tris–HCl/NaCl buffer, the complexes' stability had to be tested. After 96 hours, no significant change in the absorbance or emission spectra was observed. Therefore, the lack of significant absorbance/emission changes without a significant wavelength shift predicted the stability of complexes in this buffer.

Electronic absorption titration

Electronic spectroscopy investigates the change in spectral profiles during the titration of complexes with CT–DNA. Although there was no discernible shift in the position of the intra-ligand band as CT–DNA concentrations increased, there was a strong hyperchromic effect. The complexes may interact with DNA via groove binding [43]. The presence of synergic non-covalent interactions such as external contact (electrostatic binding), hydrogen bonding, and groove surface binding (major or minor) outside the DNA helix has been linked to hyperchromic. The data for the binding constant (Kb) for complexes (Z1–Z9) is determined to be in the range of 0.85–2.82X10^3 M^{-1}, corresponding to the obtained arrangement of hyperchromic [44]. The complex Z5 appears to have the highest affinity for linking with CT–DNA. Complex linking intensities decrease in the following order: Z5 > Z4 > Z6 > Z3 > Z7 > Z8 > Z9 > Z2 > Z1. Kb data indicate that DNA was strongly bound to the complex Z5 due to the (–OH) substituent connected to the aromatic ring (Table S4) [45].

Fluorescence studies

Fluorescence titration (EB) is used to investigate the mode of interaction between the complexes (Z1-Z9) and CT–DNA (EB). The induced emission intensity at 432-445 nm was reduced when complexes were added to DNA pretreated with EB [46]. The observed quenching is due to the photoelectron transfer mechanism. These complexes bind to DNA via non-covalent groove binding modes. Therefore, the extent of the reduction in emission intensity is used to determine the relative binding of these complexes to CT–DNA. For complexes (Z1-Z9), the Stern-Volmer quenching constant value Ksv was calculated as a slope of Io/I against [DNA]/[complex] and observed to be between 0.38 and 1.76 X 10^{-2} M^{-1} (Figure 7). As a result of the findings, it was determined that Z6 has the highest Ksv values with CT–DNA. At the same time, the linking strength of the other complexes reduces in the arrangement Z5> Z4> Z6> Z2> Z1> Z3> Z8> Z7> Z9. The trend of DNA binding affinities obtained from spectral absorption studies is reflected in the binding capacity for DNA in complexes in the arrangement Cu(II)>Ni(II)>Zn(II) [46].

Properties of viscosity

Viscosity measurements on CT–DNA were performed to confirm the groove mode of binding complexes (Z1-Z9) with CT–DNA. Complexes bind to CT–DNA with a minor change in relative viscosity, demonstrating that these complexes preferentially bind to CT–DNA via minor grooves. Complexes' ability to increase the viscosity of CT-DNA varies in the following order: Z5> Z4>Z6> Z2> Z1> Z3> Z8> Z7> Z9. Z5 caused the most significant increase in DNA viscosity, indicating a better interaction with DNA, according to the findings of this study. As a result, the viscosity measurements agree with the absorption and emission results.

Studies of DNA cleavage

As shown in Figure S23, the DNA linking products show that the Cu(II) (Z4-Z6) complexes have a higher DNA linking characteristic [47]. No distinct cleavage was observed in the control, but it was observed in all the complexes. The cleavage of the complexes Z4-Z6 is visible in lanes 6–9. The variation in DNA cleavage activity was caused by the influence of substituents in complexes that interact with DNA very actively [48]. The arrangement in which DNA interacts with complexes is Z5>Z4>Z6 (Figure 2) [49]. The central metal ion may interact with the P-O bond of DNA *via* electrostatic interaction or/and Chalet linkage. As a result of the charge neutralization, a P-atom of DNA is stimulated, and one of the bonds of the P–O ester of DNA is cleaved. The results showed that the complex Z6 actively cleaves the pBR322 plasmid DNA [50].
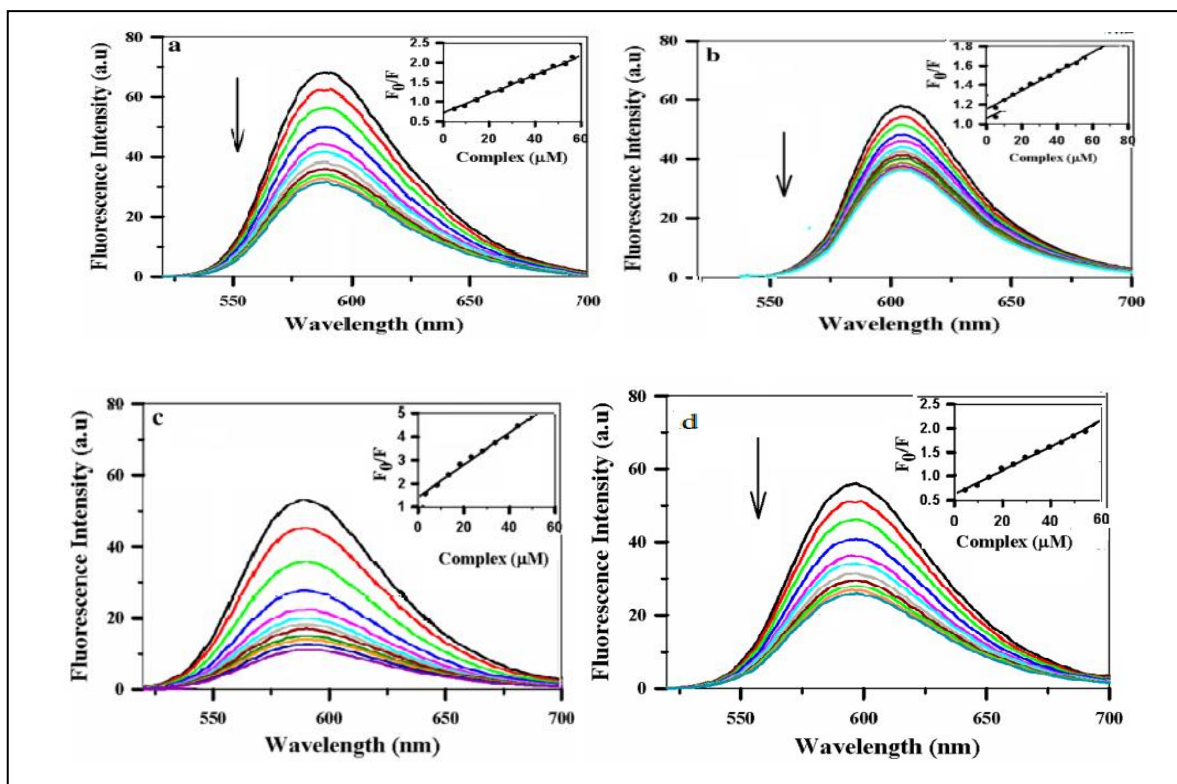
Figure 7. Fluorescence emission spectra of (50 μM) CT-DNA (2 μM) EB bound to non-attendance and existence of complexes, Z4-Z6, at diverse concentrations buffer (pH 7.9) in 10 mM Tris–HCl

Molecular docking analysis

The molecular docking analysis was used to understand the interactions of the synthesized Schiff base ligands (L1, L2, and L3) and their respective Cu^{2+} complexes (Z4, Z5, and Z6) with biotargets like DNA and protein molecules. Schiff base ligands (L1, L2, and L3) and their Cu^{2+} complexes Z4, Z5, and Z6 were docked into human DNA topoisomerase I (70 Kda) (PDB ID: 1SC7). According to the docking results, the binding energy and inhibition constant (Ki) that correspond to the interaction of Schiff base ligands (L1, L2, and L3) with 1SC7 are listed in Table S1. The interaction of the Schiff base ligands with 1SC7 is due to hydrogen bonding, pi-pi stacking (hydrophobic), and, pi-halide (hydrophobic), as shown in Figure 8. Pi-pi stacking (also known as - stacking) in chemistry refers to attractive, non-covalent interactions between aromatic rings that contain pi bonds. These interactions are important in nucleobase stacking within DNA and RNA molecules, protein folding, template-directed synthesis, materials science, and molecular recognition [51, 52]. Based on the binding energies listed in Table S1, the strongest interaction with 1SC7 was observed for the L3 ligand.
210

The binding energy and inhibition constant (Ki) that correspond to the interaction of Z4, Z5, and Z6 complexes with 1SC7 are listed in Table S2. The interaction of these complexes with 1SC7 is due to hydrogen bonding, pi-pi stacked (hydrophobic), pi-halide (hydrophobic), and pi-cation (electrostatic), as shown in Figure 9. Based on the binding energies listed in Table S2, the strongest interaction with 1SC7 was observed for the Z6 complex.

Cytotoxicity (in vitro) of compounds

The MTT test was used to compare complexes (Z1-Z9) versus cisplatin and two non-cancer cell lines, (PBMC) mononuclear cells of peripheral blood and (HEK) kidney of human embryonic, and three cancer cell lines, (A549) lung, (HCT-15) colon, and (HeLa), human cervical. Four various concentrations of prepared compounds (1000, 500, 250, and 100 nM) and cisplatin for 48 h were examined in triplicate, and the outcomes are evidenced by the mean ± standard perversion of two separate trials of cytotoxic [53,54]. Complexes were dissolved in DMSO, and blank specimens were taken as controls included with similar DMSO volume in experiences of cytotoxicity

to calculate solvent efficacy. IC50 concentrations were obtained from the doses that appear in studies of molecular anchorage with human topoisomerase l DNA. The presence of Cu (II) complexes (Z4-Z6) demonstrated that DNA linking is a better slope binding than other compounds, according to the results of DNA linking and molecular linking analysis [55]. IC50 concentrations were obtained from the doses that appear in studies of molecular anchorage with human topoisomerase l DNA (Table S5, Figure S24) [56, 57].
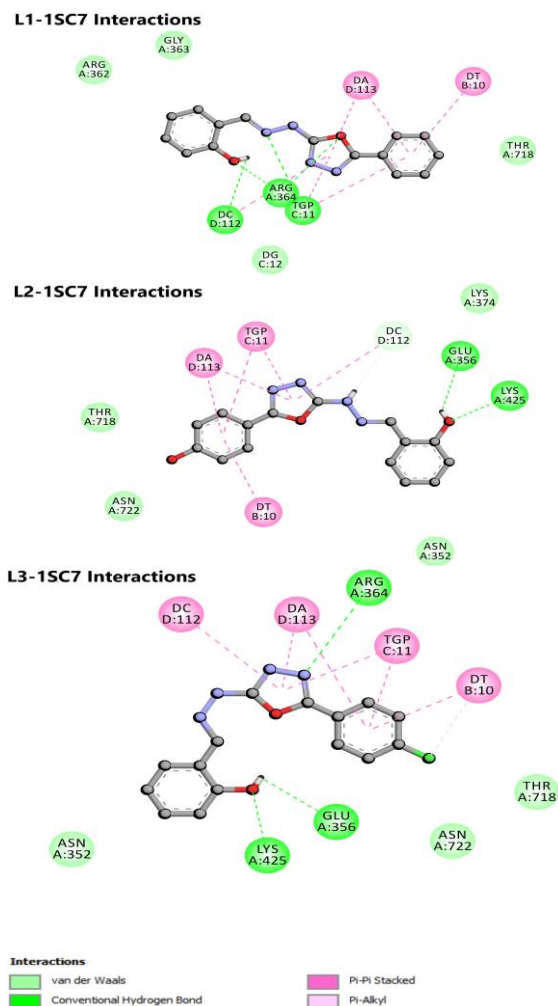

Figure 8. 2D plot of interaction between L1, L2, and L3 ligands with the human DNA topoisomerase I (70 Kda) (PDB ID: 1SC7) receptor.

complexes (Z1, Z2, Z3, Z4, Z5, Z6, Z7, Z8, and Z9) are tetrahedral environments complexes around the central metal ions. CT– DNA appears in the groove, linking the system with all the complexes. The complex Z6 shows active cleavage of plasmid DNA from the other complexes in the absence of any external factors. The Cu(II) complexes showed greater activity in cytotoxicity than the other complexes based on the data of IC50. The cell death technique demonstrates apoptosis, but proof of the apoptosis technique is required. The strongest interaction with 1SC7 was observed for the L3 ligand and the Z6 complex according to our molecular docking results.
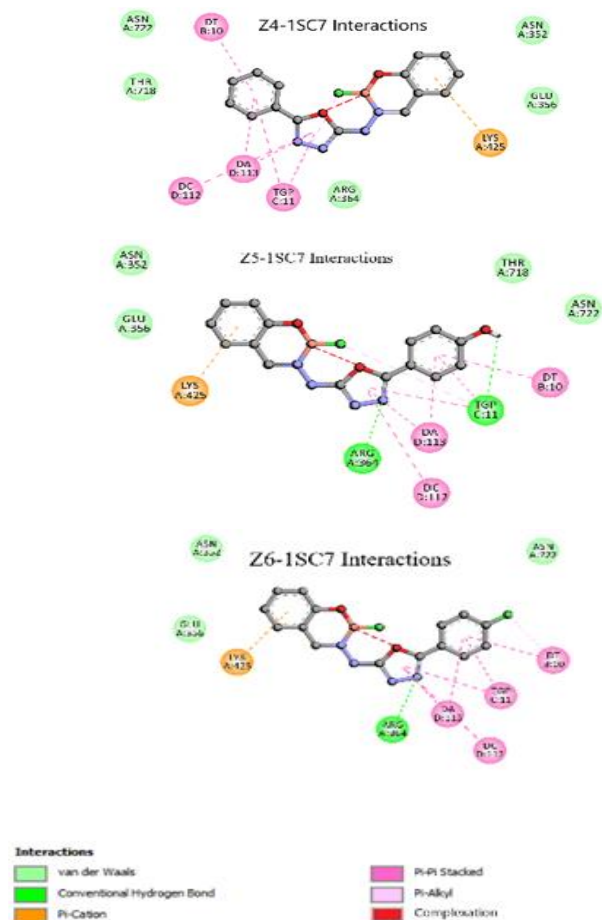

Figure 9. 2D plot of interaction between Z4, Z5, and Z6 complexes with the human DNA topoisomerase I (70 Kda) (PDB ID: 1SC7) receptor.

CONCLUSIONS

Mononuclear Schiff base complexes of Zn (II), Cu (II), and Ni (II) have been synthesized and characterized. The complexes Z1, Z2, and Z3 adopted square planar complexes around the nickel metal ions, based on the spectral data. The Cu (II) and Zn (II)

REFERENCES

1. Y. Nakamura, Y. Taruno, M. Sugimoto, Y. Kitamura, H.-L. Seng, S. Kong, M. Chikira, *J. Chem. Soc., Dalton Trans.*, **42**, 3745 (2013), https://doi.org/10.1039/C2DT32709

2. D. Amarante, C. Cherian, E. Megehee, *Inorganica Chim. Acta*, **461**, 239 (2472}. https://doi.org/10.1016/j.ica.2017.02.011

3. C. Rajarajeswari, L. Rangasamy, P. Mallayan, S. Eringathodi, A. Riyasdeen, M A. Akbarsha, *J. Chem. Soc., Dalton Trans.*, **42** 8347 (2013), https://doi.org/10.1039/C3DT32992E

4. Y. Nie, Z. Dai, F. Lal, G. Zhao, J. Jiang, X. Xu, M. Ying, Y. Wang, Z. Hu, H. Xu, *J. Phys. Chem. B*, **126**, 4787 (2022). https://doi.org/10.1021/acs.jpcb.2c02104

5. E. Marco, F. Gago, *Mol. Pharmacol.*, **68**. 1559 (2006), https://doi.org/10.1124/mol.105.015685

6. E. Scherbinina, D. Dar'in, P. Lobanov, *Chem. Heterocycl. Compd.*, **46**, 1109 (2010). https://doi.org/10.1007/s10593-010-0634-7

7. S.M. Basavarajaiah, B.H.M. Mramyunjayaswamy, *Indian J. Chem. B.*, **57**, 390 (2018).

8. A. Abdallah, G. Elgemeie, *Drug Des. Devel. Ther.*, 12, 1785 (2018). https://doi.org/10.2147/DDDT.S159310

9. P. Nunes, T. Pinheiro, A. Matos, I. Correia, J. Pessoa, *Ann. Med.*, **51**, 36 (2019), https://doi.org/10.1080/07853890.2018.156007*9

10. A. Haleel, P. Arthi, N.D. Reddy, V. Veena, N. Sakthivel, Y. Arun, P.T. Perumald, A.K. Rahiman, *RSC Adv.*, **4**, 60816 (2014). https://doi.org/10.1039/C4RA11197D

11. S. Voitekhovich, A. Lyakhov, L. Ivashkevich, V. Matulis, Y. Grigoriev, J. Klose, B. Kersting, O. Ivashkevich, *Z. Anorg. Allg. Chem.*, **648**, e202200213 (2022), https://doi.org/10.1002/zaac.202200213

12. W.L.F. Armarego, D.D. Perrin, Purification of Laboratory Chemicals, 4th edn., Oxford, Pergamon Press, 1996.

13. A. Haleel, D. Mahendiran, V. Veena, N. Sakthivel, A. K. Rahiman, *Mater. Sci. Eng.C*, **68**, 366 2016, https://doi.org/10.1016/j.msec.2016.05.120

14. D. Padhorny, A. Kazennov, B. Zerbe, K. Porter, B. Xia, S. Mottarella, Y. Kholodov, D. Ritchie, S. Vajda, D. Kozakov, *Proc. Natl. Acad. Sci.*, **113**, E4286 (2016), https://doi.org/10.1073/pnas.1603929113

15. L. Zeng, Y.-M. Ren, C. Cai, *ChemInform Abstract*, **43** (2012), https://doi.org/10.1002/chin.201218186.

16. S. Betanzos-Lara, C. Gómez-Ruiz, L.R. Barrón-Sosa, I. Gracia-Mora, M. Flores-Álamo, N. Barba-Behrens, *J. Inorg. Biochem.*, **114**, 82 (2012), https://doi.org/10.1016/j.jinorgbio.2012.05.001

17. , M. Sobiesiak, T. Muziol, M. Rozalski, U. Krajewska, E. Budzisz, *New J. Chem.*, **38**, 5349 (2014), https://doi.org/10.1039/C4NJ00977K

18. A.B.P. Lever, Inorganic Electronic Spectroscopy, 2nd edn., Elsevier, Amsterdam, 1984, p. 18.

19. B. Naskar, R. Modak, D.K. Maiti, S.K. Mandal, J.K. Biswas, T.K. Mondal, S. Goswami, *Polyhedron*, **117**, 834 (2016), https://doi.org/10.1016/J.POLY.2016.07.018

20. J. Ravichandran, P. Gurumoorthy, C. Karthick, A. K. Rahiman, *J. Mol. Struct.*, 1062, 147 (2014), https://doi.org/10.1016/j.molstruc.2014.01.026

21. M. J. Frisch et al., *Gaussian*, Inc., Wallingford CT, 2009.

22. E. A. Al-Razaq, N. Buttrus, W. Al-Kattan, A.A. Jbarah, M. Almatarneh, *J. Sulfur Chem.*, **32**, 159 (2011), https://doi.org/10.1080/17415993.2010.550617

23. T. Tüğsüz, F. Sevin, *J. Mol. Struct. Theochem.*, **775**, 29 (2006), https://doi.org/10.1016/j.theochem.2006.07.004

24. M. Zhang, Y. Wang, X. Wang, B. Zhao, W. Ruan, *J. Phys. Chem. C*, **125**, 17125 (2021), https://doi.org/10.1021/acs.jpcc.1c02058

25. M.K. Assefa, J.L. Devera, A.D. Brathwaite, J.D. Mosley, M.A. Duncan, *Chem. Phys. Lett.*, **640**, 175 (2015), https://doi.org/10.1016/j.cplett.2015.10.031

26. J. Tölle, M. Böckers, J. Neugebauer, *J. Chem. Phys.*, **150**, 181101 (2019), https://doi.org/10.1063/1.5097124

27. M. Cossi, N. Rega, G. Scalmani, V. Barone, *J. Comput. Chem.*, **24**, 669 (2003).

28. A. Peraza, V. Sojo, F. Ruette, M. Sánchez, , A. Eleonora, *J. Comput. Methods Sci. Eng.*, **12**, 397 (2012), https://doi.org/10.3233/JCM-2012-0428.

29. P. A. Ravindranath, S. Forli, D. Goodsell, A. Olson, M. Sanner, *Comput. Biol.*, **11**, e1004586 (2015), https://doi.org/10.1371/journal.pcbi.1004586.

30. BIOVIA, Dassault Systèmes, Discovery studio 4.0 client, 21.1.00, San Diego, Dassault Systèmes, 2021.

31. F.R. Dollish, W.G. Fateley, F.F. Bentley, Characteristic Raman Frequencies of Organic Compounds, Wiley, 1974.

32. D. Lin-Vien, N.B. Colthup, W.G. Fateley, J.G. Grasselli, The Handbook of Infrared and Raman Characteristic Frequencies of Organic Molecules, Academic Press. San Diego, 199l.

33. G. Socrates, Infrared and Raman Characteristic Group Frequencies: Tables and Charts, NewYork, Wiley, 1980.

34. A.L. Baskerville, M. Targema, H. Cox, *R. Soc. Open Sci.*, **9**, 211333 (2022), https://doi.org/10.1098/rsos.211333

35. T. Culpitt, K. Brorsen, M. Pak, S. Hammes-Schiffer, *J. Chem. Phys.*, **145**, 044106 (2016), https://doi.org/10.1063/1.4958952

36. A. Becke, *J. Chem. Phys.*, **150**, 241101 (2019) ,https://doi.org/10.1063/1.5109675.

37. V. Saheb, F. Rezaei, S. Hosseini, *Comput. Theor. Chem.*, 1051, **123** (2014), https://doi.org/10.1016/j.comptc.2014.10.027

38. M. Mosquera, *Phys. Rev. A.*, **88**, 022515 (2013), https://doi.org/10.1103/PhysRevA.88.022515.

39. K. Pernal, *J. Chem. Phys.*, **136**, 184105 (2012), https://doi.org/10.1063/1.4712019

40. R. Al-Shemary, B. Zaidan, N. Al-marsomy, *Diyala Journal for Pure Science*, **13**, 21 (2017), https://doi.org/10.24237/djps.1303.189C

41. R. Friedman, E. Ahlstrand, K. Hermansson, *J. Phys. Chem. A.*, **121**., 2643 (2017), https://doi.org/10.1021/acs.jpca.6b12969

42. S. Al-Ashqar, *Open J. Inorg. Chem.*, **6** 195 (2016), https://doi.org/10.4236/ojic.2016.63015

43. P. Deepika, H.M. Vinusha, M. Begum, R. Ramu, P. Shirahatti, M.N.N. Prasad, *Heliyon*, **8**, e09648. (2022), https://doi.org/10.1016/j.heliyon.2022.e09648

44. D. Moon, S. Jeon, M. Mazúr, M. Valko, J.-H. Choi, *J. Mol. Struct.*, 1231, 129897 (2021), https://doi.org/10.1016/j.molstruc.2021.129897

45. M. Manjunath, A. Kulkarni, G. Bagihalli, S. Malladi, S. Patil, *J. Mol. Struct.*, **1127**, 314 (2016), https://doi.org/10.1016/j.molstruc.2016.07.123

46. B. Lombardi, R. Brown, C. Gendy, C. Chang, T. Chivers, R. Roesler, *Organometallics*, **36**, 3250 (2017), https://doi.org/10.1021/acs.organomet.7b00396

47. S. Kou, K. Zhou, Z. Lin, Y. Lou, J. Shi, Y. Liu, *J. Mol. Liq.*, **328**, 115491 (2021), https://doi.org/10.1016/j.molliq.2021.115491

48. X. Chen, B. Wang, K. Zhou, Y. Lou, S. Kou, Z. Lin, J. Shi, *ChemistrySelect*, **4**, 3774 (2019), https://doi.org/10.1002/slct.201900089

49. F. Shahri, A. Niazi, A. Akrami, *Iranian Journal of Mathematical Chemistry*, **7**, 47 (2016), https://doi.org/10.22052/IJMC.2016.11869

50. D.M. Suresh, D. Sajan, Y.-P. Diao, I. Nemec, I.H. Joe, V. Jothy, *Spectrochim. Acta A Mol.*, **110**, 157 (2013), https://doi.org/10*.1016/j.saa.2013.01.067

51. N. Tidjani-Rahmouni, N.H. Bensiradj, S. Djebbar, O.\ Benali-Baitich, *J. Mol. Struct.*, **1075**, 254 (2014), https://doi.org/10.1016/j.molstruc.2014.06.067

52. A. Gubendran, G.G.V. Kumar, M.P. Kesavan, G. Rajagopal, P. Athappan, J. Rajesh, *Appl. Organomet. Chem.*, **32**, e4128 (2018), https://doi.org/10.1002/aoc.4128

53. C.R. Martinez, B.L. Iverson, *Chem. Sci.*, **3**, 2191 (2012), https://doi.org/10.1039/C2SC20045G

54. A. Campo, E. Cabaleiro-Lago, J. Carrazana-García, J. Rodriguez-Otero, *J. Comput. Chem.*, **35**, 1290 (2014), https://doi.org/10.1002/jcc.23623.

55. H.H. Alkam, W.M. Alwan, R.K.R. Alshemary, *Int. J. Pharm. Res.*, **14**, 3370 (2021), https://doi.org/10.31838/ijpr/2021.13.01.429

56. N.M. Majeed, S.A. Al-Sahab, R.K. Al-Shemary, *Int. J. Pharm. Res.*, **13**, (2021), https://doi.org/10.31838/ijpr/2021.13.01.428

57. E.M. Mohammed, R.K R. Al-Shemary, *Int. J. Pharm. Res.*, **13**, (2021), https://doi.org/10.31838/ijpr/2021.13.01.427

Improving of rheological and mechanical properties of natural and EPDM rubbers *via* multi-walled carbon nanotubes (MWCNTs) reinforcement

K. Gündoğan[*], M. Gitmiş

Department of Materials Science and Nanotechnology Engineering, Faculty of Engineering, University of Uşak, Uşak, Turkey

In this study, natural rubber and EPDM rubber were reinforced with multi-walled carbon nanotubes (MWCNTs) by three different methods. These methods are homogenous mixing, spraying and hand laying methods. The rheological and mechanical properties of two different rubbers produced by the three different methods were examined. As a result, six samples of nano composite material with different rheological properties were produced. The maximum torque (MH), the minimum torque (ML), the start time (tc10), the time of vulcanization (tc90) and the time of early scorch were calculated from the rheological properties. The mechanical behavior of MWCNTs reinforced rubber samples was determined by tensometer test in two different ways in tensile and compression directions. As a result of this experiment, it was observed that the difference in tensile and compressive load is that the rubber has a hysteretic structure and doesn't lose elasticity. Torsional stiffness (Kt) torque - angle (N rad^{-1}) values were found. Although torsion joint of EPDM rubber differs in three methods, this difference hasn't been observed in natural rubber. The hardness values of MWCNTs reinforced mixtures were tested in shore form and it was stated that these values could not be related to torsional stiffness. The natural frequency test was performed with a hammer and natural frequencies of the system (without rubber) and variable natural frequencies in the system when EPDM and natural rubber were observed. It was determined that the vibration damping of nano-particle reinforced EPDM rubber is different from that of natural rubber.

Keywords: EPDM rubber, Multi-walled carbon nanotubes, Natural rubber.

INTRODUCTION

Rubber is a remarkable engineering material found in every aspect of our daily lives. It is preferred because of its viscoelastic structure, being an alternative to metals, and providing ease of use. Its usage areas increase each day in many sectors such as work environments, home applications, games, sports, automotive industry, aircraft industry, railway transportation, and construction.

Elastomers, which have a structure between a linear polymer and a spatial polymer, consist of long molecular chains that are twisted and entangled in the form of pellets. These materials are called elastomers because they show a highly reversible behavior (elastic deformation) as a result of the opening of the lumps and bond rotation under the effect of force. In industry, elastomers are divided into two groups as "thermoplastic" and "thermoset" in terms of behavior under the effect of temperature [1]. Thermoplastic elastomers are linear polymers that soften when the temperature is increased, harden when cooled, and tend to soften again when reheated. Thermoset elastomers are materials that tend to soften when heated. All of them are called plastic because of this reason. The difference between elastomers and thermoset plastics is due to

their mechanical properties. For example, if an elastomer material is subjected to a certain tension in both directions, the material begins to elongate, and when the stretching process is released, it tends to take its former shape. This situation is called elasticity. Thermosets, on the other hand, maintain their elasticity up to a certain limit (yield limit). After this limit, the material breaks and undergoes deformation. This condition is permanent and irreversible. However, elastomers have less elastic modulus and tensile strength than thermosets. Because of this situation, although elastomers start to elongate immediately, thermoplastics cause elongation under higher load [2].

The average molecular weight of natural rubber is 68.12 g mol^{-1} and varies in a wide range. Due to its structure, it crystallizes when stress is applied or at low temperatures. The crystallization has some positive effects on natural rubber, resulting in its characteristics. It has very good tensile and tear resistance, elasticity, and fatigue properties. During the vulcanization process, the sulfur molecule, which is a ring with eight atoms, is opened.

Cross-linking occurs by linking the sulfur molecules to the polyisoprene chains [3].

Ethylene-propylene diene monomer is formed as a result of the chemical combination of ethylene and

* To whom all correspondence should be sent:
E-mail: kadir.gundogan@usak.edu.tr

propylene monomers. By combining two monomers, an amorphous, semi-crystalline, and crystalline elastomer is obtained. EPM, which has a saturated structure, is produced as a result of the copolymerization of ethylene and polypropylene. EPDM is obtained by adding diene to the chemical structure obtained from EPM. Today, it has become an engineering material that can be widely used in the industrial field.

Nanotechnology is the most important and rapidly developing technology of the 21st century, it is in a key position for many researchers and has managed to attract attention in this regard. The rapid increase in global competition causes this science to have strategic importance among the countries. With the developing technology in the production techniques of rubber and nanomaterials, different approaches are being made every day. Because of this situation, many researchers have tried to bring these two different structures together with new methods. With the emergence of new composite materials, the view of manufacturing methods has reached a very important point. The physical and chemical effects on the material are investigated.

In a study supported by the National Natural Science Foundation of China and the Postdoctoral Science Foundation of China, nanoparticles were added to the rubber to reduce vibration and noise in tubes operating under water, and tribological and mechanical properties were investigated. As a result of the study, it was observed that the friction coefficient of nano-particle reinforced NBR rubber decreased at critical speeds, and besides, the damping ability of its mechanical properties improved [4].

Ramzan *et al.,* in their study, obtained a composite material by reinforcing elastomers with nanomaterials. The damping capabilities of natural rubber by throwing nanoparticles into it were investigated and as a result, design parameters were determined in different variations. They proposed nanocomposites for their strong damping capabilities [5]. In another study, Ramzan and Kumar prepared a test setup and demonstrated the damping ability with this test method [6]. Ziraki e*t al.* added silica nanoparticles and polypropylene fibers to the silicone rubber matrix. They examined the viscoelastic behavior and mechanical properties of the samples they took from this nanoparticle reinforced rubber. As a result, they proved that silica particles increase the effect on the elastic modulus on rubber and reach higher hardness [7]. Huang and Tsai characterized the vibration damping response of composite layers containing silica nanoparticles and

rubber particles. They compared the experimental results they obtained with their study with the finite element method. These results showed that the reduction of flexural stiffness of fiber composites, especially for (90/10) layers, decreased as the damping properties of the layers were improved. Vibration damping responses of composite layers obtained using micrometric analysis were shown to be compatible with experimental data together with modal analysis [8].

Muhammad *et al.* have designed a new nanocomposite vibration damper. They used NR rubber and alumina zirconium as test specimens. Modal analysis and natural frequency results were compared with analytical and finite element methods. Then they revealed the first five modes. They proved that the vibration amplitude was reduced by 25% [9].

Azizli *et al.* have prepared a series of elastomeric nanocomposites based on NR/EPDM rubber blends. It was determined that with the addition of graphene oxide to the samples, the mechanical properties increased with fatigue resistance, hardness, tensile strength, and elongation at break. At the end of all analyses, they found a good coherence between the experimental and theoretical results [10]. Ruksakulpiwat *et al.* used natural rubber NR and EPDM rubber with various contents as impact modifiers for composites. The composites were prepared using injection molding. The rheological, morphological, and mechanical properties of the composites were investigated. They observed a significant increase in impact resistance and elongation when NR or EPDM was added to the composites. They also explained the effect of NR and EPDM rubbers on the mechanical properties of PP composites. They stated that composites with EPDM rubber showed slightly higher tensile strength and impact resistance than composites with NR [11]. Enew *et al.* investigated the mechanical properties of the effect of aramid fiber in Kevlar (KP), carbon mono fiber (CMF), and nano-carbon black (NCB) pulp form as filler for Trilene liquid polymers on EPDM rubber. They found that EPDM rubber improved its mechanical properties such as thermal insulation, tensile strength, elongation, and hardness [12]. In this work, MWCNTs reinforced natural and EPDM rubbers were developed to investigate their rheological and mechanical properties by using three different methods. The aim of this study is to determine the most suitable method and MWCNTs reinforced rubber which can be added to the literature as a remarkable engineering materials.

Table 1. Ratios of homogeneously mixed NR and EPDM mixture raw materials.

Raw Materials	%	phr		Raw Materials	%	phr
NR Rubber	100	40.88		EPDM Rubber	100	29.03
MWCT Nano material	50	20.44		MWCT Nano material	50	14.51
N330 (Carbon black)	76	31.07		N550 (Carbon black)	120	34.83
Oil	4	1.64		Oil	45	13.06
Plasticizer	2	0.82		Plasticizer	4	1.16
Stearic acid ($CH_3(CH_2)16COOH$)	3	1.23		Calcium carbonate ($CaCO_3$)	19	5.52
Zinc oxide (ZnO)	6	2.45		Zinc oxide (ZnO)	5	1.45
Sulfur (S)	1.7	0.70		Sulfur (S)	0.1	0.03
Antiozonants	0.9	0.37		Antiozonants	0.4	0.12
Antioxidants	0.2	0.08		Antioxidants	0.1	0.03
Accelerators	0.8	0.33		Accelerators	0.9	0.26
Total	244.6	100.00		Total	344.5	100.00

MATERIALS AND TEST METHODS

While preparing the test samples, MWCT reinforcement to NR and EPDM rubbers was handled by three methods. These methods are homogeneous mixing, hand-laying, and spraying methods, respectively. The ratios of homogeneously mixed NR and EPDM mixture raw materials are given in Table 1.

MWCNTs were applied to natural rubber and EPDM rubber by spray gun with the help of 3 – 4 bar air pressure. In this method, MWCNTs are permeated to rubber by making a special solution out of them. 5 mg of MWCNTs and 20 ccs of a special solution were used in this mixture. MWCNTs were spread on the sample rubbers with the help of a roller. As in the spray method, the solution and the nanomaterial were made at the same scale. The MWCNTs reinforced natural (NR) and EPDM rubbers produced by three different methods are presented in Figure 1.
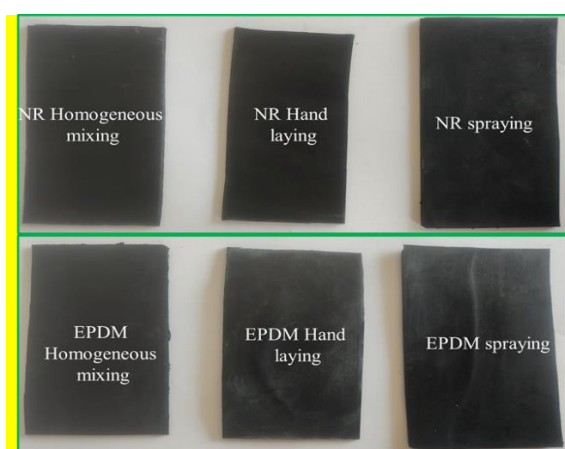

Fig. 1. MWCNTs reinforced natural (NR) and EPDM rubbers produced with homogeneous mixing, hand laying and spraying methods.

Rubber is formed by the combination of many raw materials such as carbon black, oil, accelerators, resins, fillers. Before the curing of this mixture, it was tested in rheometer test devices to see the results such as curing time and scorch time. Experimental samples (GOTECH Moving Die Rheometer M2000 A) were tested with boundary conditions of 150 ºC for 15 minutes. Both tensile and compressive behavior of metals in the elastic region show the same properties. This can be expressed by Hooke's laws. Features such as Poisson's ratio and modulus of elasticity can easily be found. However, the same statements are not true for elastic materials such as rubber. It is aimed to make the measurements easier by subjecting the rubber sample to deformation by a force that will provide homogeneous distribution. Thus, it was found to be a simpler method since the forces applied to the sample would cause the same deformation and elongation at all points [13].

There are two types of tensile test methods: uniaxial and multi-axis. Due to the different behavior of rubber in the tensile and compression regions, it is insufficient to determine only the mechanical properties. Due to the accumulation of knowledge on this subject, standards such as ASTM D412, DIN 53 504, and ISO 37 have emerged [14-16]. Mechanical properties of rubber-type materials change with the rate of deformation applied to the material. For the test samples, rubbers were designed according to ASTM D412 – C sample and subjected to uniaxial tensile and compression test (LLOYD LR50KPlus) according to different preloading speeds.

Elastomer materials such as rubber have similar characteristic properties as a metal spring and a viscous liquid. This viscoelastic behavior is defined as deformation and energy-absorbing. Crank pulleys, which are used as automotive parts, are an

important test of torsional stiffness, and their resistance to torsion is a torsional behavior. The rubber structure on the crank pulleys is determined by the torsional stiffness (kt). Torsional stiffness is an important parameter because it affects the natural frequency of the crank pulley. The test specimens were subjected to tests in the DEVOTRANS Torque Life Test device at room temperature, providing angles of 1 º – 30 º.

Many researchers have developed test methods for natural frequency and vibration measurements. In the modern automotive industry, natural frequency measurements are made according to modal test methods. For crank pulleys, it is available as torsional (torsion) frequency. A modal test on the rotating component takes place by actuation by mounting accelerometers in a constant tangential fashion to both inertial masses in the same direction. Therefore, frequency functions (FRF) are formed here. These FRFs form a theory in finding physical properties [17]. Known as the current theory, it is known as the hysteretic damping of the rubber, dissipating the input energy and accelerating the system without resonating [18]. Natural frequency measurements are generally measured with the hammer method because it is cheap and easy. The vibration frequency distribution of the force is found in the test performed with the hammer in the modal test setup. With these distributions, natural frequency, damping, and modal shapes can be determined [19, 20]. Experimental samples were measured between two sheet metal plates, using a bedding element to dampen the vibrations coming from the ground, and data collector DEWESoft DAQ with the help of a hammer.

RESULTS

Figure 2 (a, b, c, d) shows the SEM image of the EPDM sample, MWCNTs blended EPDM sample, NR sample and MWCNTs blended NR sample, respectively. The SEM image of the EPDM sample obtained by the homogeneous mixing method displayed a rough surface morphology. After adding of 0.5 wt% MWCNTs to EPDM, the composite materials showed that MWCNTs were placed as nanotube groups in the composite material. The mechanical test results indicated the enhancement after MWCNT addition, as mentioned above. According to the SEM results, the dispersion of CNT groups was not completely homogeneous and if it could be provided the enhancement of mechanical properties also could be increased. By functionalization of CNTs or using a different method the homogeneity could be increased and

will be the subject of future studies. SEM image of the NR and MWCNTs blended NR sample obtained by homogeneous mixing method displayed a rough surface morphology like EPDM samples.
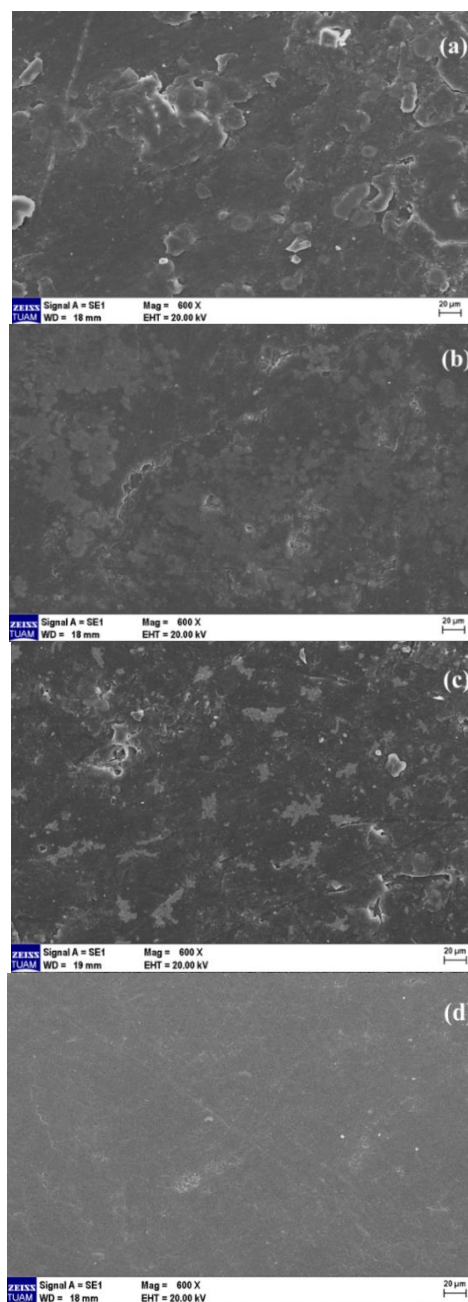

Fig. 2. SEM image of EPDM (a), MWCNTs blended EPDM sample (b), NR sample (c), MWCNTs blended NR sample (d).

Rheometer test results of MWCNTs reinforced natural rubber and EPDM rubber produced *via* homogeneous mixing method are given in Figure 3. The MWCNTs reinforced natural and EPDM rubbers produced *via* other two methods are given in Table 2 for hand-laying and spraying methods, respectively.
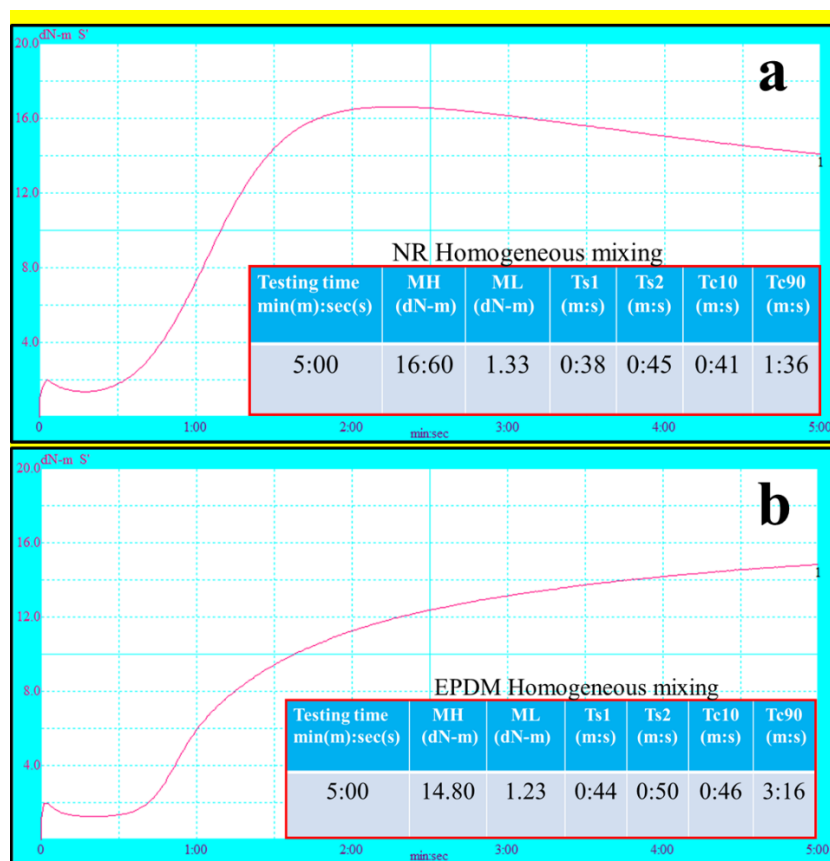
Fig. 3. Rheometer test results of MWCTs reinforcement (a) natural rubber (b) EPDM rubber produced *via* homogeneous mixing method.

Table 2 Rheometer test results of MWCNTs reinforced natural and EPDM rubbers produced *via* hand-laying and spraying methods.

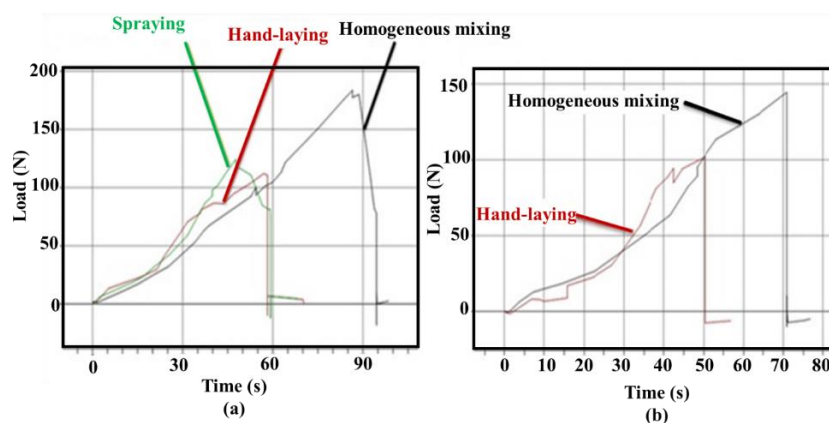| Materials/Method	Testing time min(m):sec(s)	MH (dN-m)	ML (dN-m)	Ts1 (m:s)	Ts2 (m:s)	Tc10 (m:s)	Tc90 (m:s)
NR Hand laying method	5:00	15.06	0.32	0:20	0:28	0:23	1:23
EPDM/Hand laying method	5:00	16.30	1.26	0:53	1:02	0:57	3:29
NR Spraying	5:00	17.22	1.74	0:40	0:48	0:43	1:45
EPDM Spraying	5:00	14.87	1.17	1:00	1:09	1:02	3:16

Fig. 4. MWCT reinforced (a) natural rubber (b) EPDM rubber rupture test results

According to the tensile test of MWCT reinforced composite specimens, the preload stress and velocities are equally given in Figure 4. In Table 3, tensile and compression results according to different sample types with preload stress velocities (50 – 100 – 200 mm/min) are shown. In addition, the hardness values of nanocomposite materials were measured in shore – A hardness measuring device (HUATEC).

Torsional stiffness graphs for two different rubbers, angle – torque graphs between 1º – 30º (0.0174 – 0.523 radian) with three different methods are given in Figures 5 and 6.
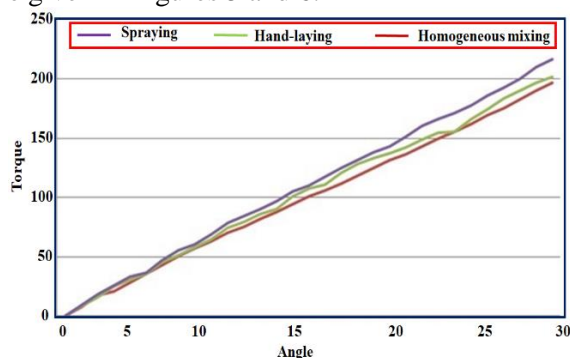

Fig. 5. MWCTs reinforced NR rubber angle-torque graph

Fig. 6. EPDM rubber angle-torque graph with MWCTs reinforcement

Natural frequency measurements were made and the test results of MWCT reinforced NR and EPDM rubbers are given in Figures 7, 8 and 9. The chart data of Figure 7 is given in the inset of Figure 7. The chart data of Figure 8 and 9 are given in Table 4 and Table 5, respectively.

As the preload stress rate increases, the difference between the tensile and compressive loads of the sample mixtures increases. For MWCNTs-reinforced NR, the highest load was with the spraying method, while the least load was formed in the homogeneous mixing method. In EPDM rubber, while the highest load is in the homogeneous mixing method, the least load is seen in the hand laying method. Due to this situation, three different methods that are subjected to the highest load are given in Figure 10 below.

DISCUSSION

The rheological and mechanical properties of natural rubber and EPDM rubber with MWCTs reinforcement were experimentally investigated. In the tests, it was observed that the nano-material reinforcement had different effects on the material and different nano-composite materials emerged due to the different methodological processes.

The data on the rheological properties of MWCTs reinforced natural rubber and EPDM rubber are shown in Figure 3, where they differ. From the rheometer curve, it was observed that the nanocomposites produced by the homogeneous mixing and spraying method for natural rubber were the same. In the hand lay-up method, which has different firing start times (tc10) and maximum torque (MH), it was observed that the rubber cooked later than other methods. The curing time (tc90) time was taken as the same value for all methods of natural rubber. It is seen that MH and ML of EPDM rubber vary. When the rheometer curves were examined, it was observed that the cooking additive used the same raw material in both rubbers and the firing condition was stable.

When the mechanical properties were examined, the effect of nanomaterial reinforcement for the NR mixture (Figure 4) on the tensile strength and maximum elongation amount, the highest tensile strength and elongation amount were obtained by the homogeneous mixing method. while the tensile direction is subjected to more load in general, the compression direction is subjected to less load due to the hysteretic nature of the rubber (Table 3). It was determined that the method that affects the hardness value the most among the nanocomposite samples is the hand lay-up method. Torsional stiffness of MWCTs reinforced NR and EPDM rubber was tested and is given in Figures 5 and 6. For NR and EPDM rubber, the same torsion is observed in all methods up to 7º. The torque values after this degree are ordered as spraying, hand-laying, and homogeneous mixing for NR rubber and for EPDM rubber, homogeneous mixing, spraying, and hand-laying are listed from the largest to the smallest. For EPDM rubber, homogeneous mixing, spraying, and hand-laying are listed from the largest to the smallest.

It was observed that the MWCTs reinforcement has little effect on the torsional stiffness in natural rubber, but differences occur in EPDM rubber.

Natural frequency test results are given in Figs. 7, 8 and 9.

Table 3. Tensile and compression results of reinforced NR and EPDM rubber. Tensile – compression test results of nano composite materials

Test Conditions				NR Rubber			EPDM Rubber		
Sample Type/ Method	Method	Preload Stress (N)	Preload Stress Rate (mm/min)	Hardness (Shore A)	Max. Load (N)	Max. Elonga-tion (mm)	Hardness (Shore A)	Max. Load (N)	Max. Elonga-tion (mm)
Spraying	Tensile	100	50	63	79.876	100.76	67	71.075	100.04
Spraying	Compression	100	50	63	72.727	84.548	67	59.061	69.965
Spraying	Tensile	100	100	63	88.775	101.49	67	60.094	96.007
Spraying	Compression	100	100	63	82.189	82.829	67	58.647	100.8
Spraying	Tensile	100	200	63	102.75	118.06	67	88.792	144.79
Spraying	Compression	100	200	63	35.619	105.48	67	20.704	63.297
Hand Lay	Tensile	100	50	68	72.081	94.694	69	64.066	78.063
Hand Lay	Compression	100	50	68	61.478	91.86	69	-	-
Hand Lay	Tensile	100	100	68	667.553	96.016	69	37.566	46.182
Hand Lay	Compression	100	100	68	53.806	79.5	69	-	-
Hand Lay	Tensile	100	200	68	73.09	107.26	69	39.351	108.42
Hand Lay	Compression	100	200	68	39.351	103.42	69	-	-
Homogeneous Mixing	Tensile	100	50	61	52.07	103.03	63	73.212	99.342
Homogeneous Mixing	Compression	100	50	61	38.333	102.58	63	63.553	71.39
Homogeneous Mixing	Tensile	100	100	61	50.107	99.405	63	78.959	121.561
Homogeneous Mixing	Compression	100	100	61	44.039	105.84	63	60.002	115.294
Homogeneous Mixing	Tensile	100	200	61	53.144	96.428	63	106.72	160.25
Homogeneous Mixing	Compression	100	200	61	43.975	56.849	63	21.021	92.238

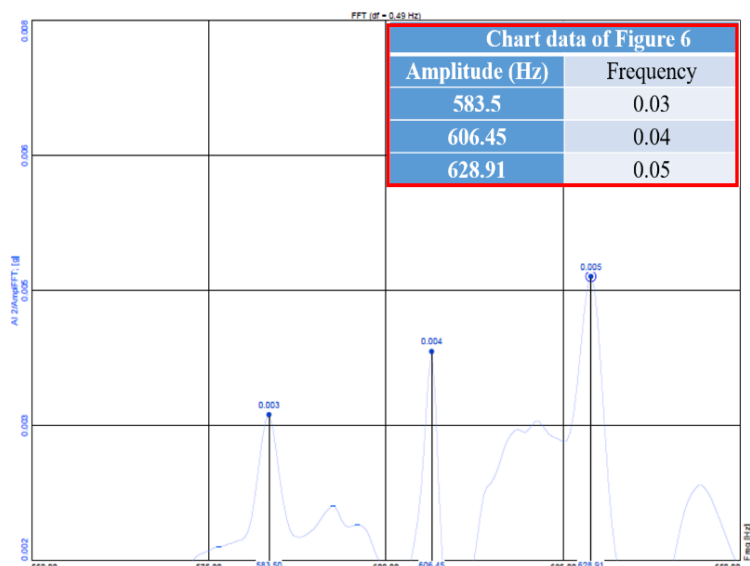| Chart data of Figure 6	
Amplitude (Hz)	Frequency
583.5	0.03
606.45	0.04
628.91	0.05

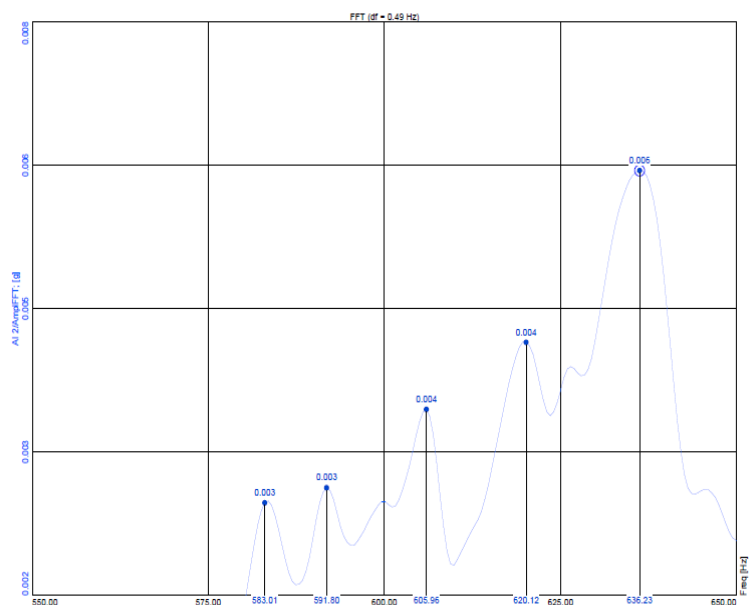**Fig. 7.** Natural frequency of the system (without rubber)

Fig. 8. Natural frequency graphs of MWCNTs reinforced NR rubber produced with homogeneous method

Table 4. Chart data of natural frequency graphs of MWCNTs reinforced NR rubber produced by three methods

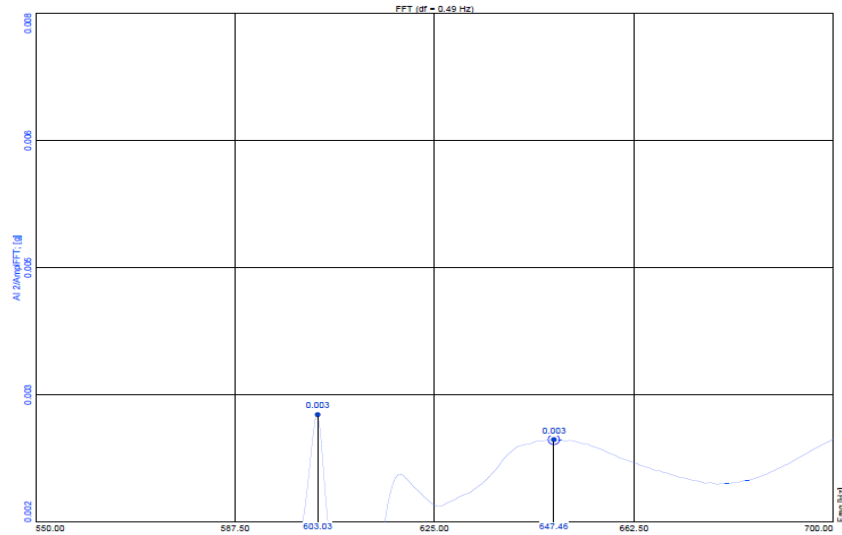| MWCNTs -reinforced NR by homogeneous mixing method		MWCNTs -reinforced NR by hand lay method		MWCNTs -reinforced NR by spraying method	
Amplitude (Hz)	Frequency	Amplitude (Hz)	Frequency	Amplitude (Hz)	Frequency
583.01	0.003	606.45	0.005	586.91	0.004
591.80	0.003	613.77	0.007	606.93	0.008
605.96	0.004	630.86	0.007	621.58	0.006
620.12	0.004			635.25	0.005
636.23	0.006				

Fig. 9. Natural frequency graphs of MWCT reinforced EPDM rubber produced by homogeneous mixing method

Table 5. Chart data of natural frequency graphs of MWCNTs reinforced EPDM rubber produced by three methods

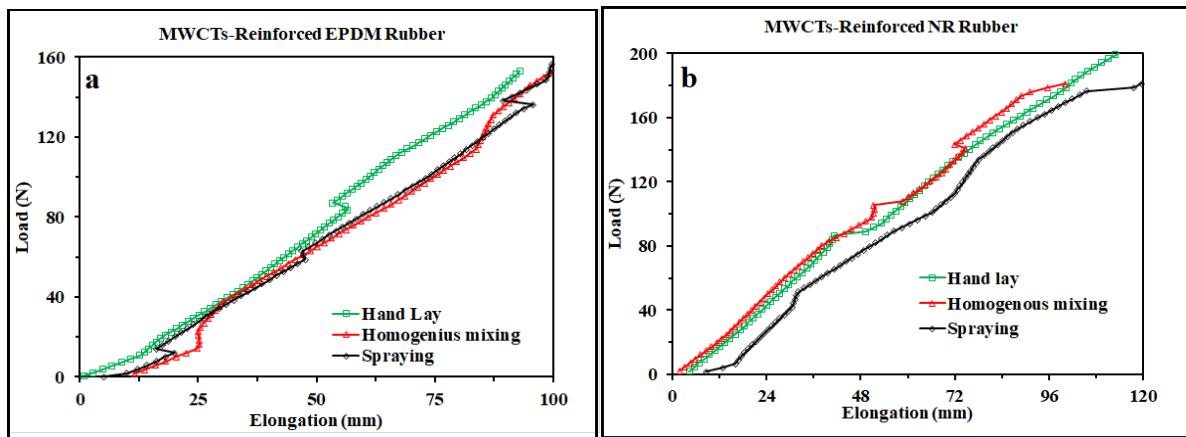| MWCNTs -reinforced EPDM by homogeneous mixing method		MWCNTs -reinforced EPDM by hand lay method		MWCNTs -reinforced EPDM by spraying method	
Amplitude (Hz)	Frequency	Amplitude (Hz)	Frequency	Amplitude (Hz)	Frequency
603.03	0.003	604.98	0.004	616.21	0.005
647.46	0.003				

Fig. 10. Tensile loads – elongation plot of MWCTs reinforced (a) EPDM and (b) NR rubbers

The natural frequency values of the system should be in all test setups and these frequencies should be distinguished. It is seen that the natural frequency of the crankshaft without a crank pulley is the closest to the natural frequency measurement values of the pulleys, with a homogeneously mixed MWCNTs reinforced EPDM rubber pulley. When the crankshaft enters the resonance state, it will get by 1.09% closer to the crank pulley and will attract torsional vibrations. A different natural frequency interpretation could not be made for nano-reinforced NR rubber since it has the same natural frequencies as the system. However, since MWCT reinforced EPDM rubber has different natural frequencies, it has destroyed the natural frequencies of the system. As can be seen in Figure 9, the vibration damping ability of EPDM rubber changes with nano reinforcement.

As the preload stress rate increases, the difference between the tensile and compressive loads of the sample mixtures increases. Due to this situation, three different methods that are subjected to the highest load are given in Figure 10. For MWCNTs -reinforced NR rubber, the highest load was with the spraying method, while the least load was formed in the homogeneous mixing method. In

EPDM rubber, while the highest load is in the homogeneous mixing method, the least load is seen in the hand laying method.

CONCLUSION

The mechanical behavior of the MWCNTs reinforced sample rubbers was carried out in two different ways in tensile and compression directions with the tensometer test, and it was observed that the difference in tensile and compression load was that the rubber had a hysteretic structure and did not lose its elasticity. Although there was a difference in torsional stiffness in EPDM rubber within the three methods, such a difference did not occur in natural rubber.

In the natural frequency test, natural frequencies of the system (without rubber) were observed and variable natural frequencies in the system when EPDM and natural rubber were used. It was observed that vibration damping of EPDM rubber with nano reinforcement is different from that of natural rubber.

REFERENCES

1. V. Vahapoğlu, Experimental Investigation of the Inelastic Properties of Rubber-like Materials, Doctoral Thesis, Karadeniz Technical University, Graduate School of Natural and Applied Science, Trabzon, 2006.
2. V. Vahapoğlu, *The Journal of Graduate School of Natural and Applied Sciences of Mehmet Akif Ersoy University*, **4**(1), 25 (2013).
3. A. Karataş, M.Sc. Thesis, Istanbul Technical University, Graduate School of Natural and Applied Science, İstanbul, 2001.
4. C. Dong, C. Yuan, L. Wang, W. Liu, X. Bai, X. Yan, *Scientific Reports*, **6**(1), 35023 (2016).
5. M. Ramzan, A. Abdurraheman, B. Kumar, *International Journal of Innovative Research in Science, Engineering and Technology*, **6**(1) (2017).
6. M. Ramzan, B Kumar, *Int. Journal of Innovations in Mechanical & Automobile Engineering*, **2**(1), 53 (2011).
7. S. Ziraki, S.M, Zebarjad, M.J. Hadianfard, *Polymer-Plastics Technology and Engineering*, **55**(16), 1693 (2016).
8. C.Y. Huang, J.L. Tsai, *Journal of Composite Materials*, **49**(5), 545 (2015).
9. M. Ramzan, B. Kumar, A. Chaskar, *IOSR Journal of Mechanical an Civil Engineering (IOSR-JMCE)*, **11**(3), 45 (2014).
10. M.J. Azizli, M. Barghamadi, K. Rezaeeparto, M. Mokhtary, S. Parham, *Composites Communications*, **22**,100442 (2020).
11. Y. Ruksakulpiwat, J. Sridee, N. Suppakarn, W. Sutapun, *Composites Part B: Engineering*, 40(7), 619 (2009).
12. A.M. Enew, M.A. Elfattah, S.R. Fouda, S.A. Hawasha, *Polymer Testing*, **103**, 107341 (2021).
13. A.E.H. Love, Treatise on the mathematical theory of elasticity, Fourth edn., Dover Publication, New York, 1944.
14. ASTM D412, Standard Test Method for Vulcanization Rubber and Thermoplastic Rubber and Thermoplastic Elastomer – Tension, ASTM, Philadelphia, 1992.
15. DIN 53504, Testing of rubber - Determination of tensile strength at break, tensile stress at yield, elongation at break and stress values in a tensile test, Germany, 2017.
16. ISO 37:205, Rubber vulcanized or thermoplastic, determination of tensile stress-strain properties, İnternational Organization for Standardization, Geneva, Switzerland, 2005.
17. D. Robinette, M. Grimmer, R. Beikmann, *SAE International*, 01-1663 (2011).
18. S.K. Sweeney, Analysis and discussion of diesel engine powertrain torsional resonance during start-up, SAE technical paper series, Noise & Vibration Conference and Exhibition Traverse City, Michigan, 2003.
19. B,J, Schwarz, M.H. Richardson, Experımental Modal Analysis, CSI Reliability Week, Orlando, FL, **1** (1993).
20. Z. Tang, P. Pillay, A.M. Omekanda, *IEEE Transactions on Industry Applications*, **39**(4), 978 (2003)

The reactivity properties of platinum-containing anticancer drugs

S. Aydogdu, M. Evirgen, A. Hatipoglu*

Faculty of Arts and Sciences, Department of Chemistry, Yildiz Technical University,34220 Istanbul, Turkey

Cisplatin has been an important platinum-containing anticancer drug for years. Toxic effects of cisplatin and the resistance of tumor cells against treatment lead to new studies about finding new Pt- containing anticancer drugs. In this study, the electronic properties and reactivity indices of cisplatin and its clinically accepted derivatives carboplatin, oxaliplatin, nedaplatin, lobaplatin, and heptaplatin were calculated by density functional theory (DFT). These properties of drugs have been calculated in both vacuum and aqueous medium. The reactivity of the molecules is explained with the global reactivity indices. Local reactivity indices were used to examine the reaction of the hydrolyzed nedaplatin complex with the amino acid cysteine. In anticancer drugs containing Pt, the platinum atom is an important reaction site for anticancer mechanisms.

Keywords: anticancer, cisplatin derivatives, DFT, aqueous medium, reactivity indices

INTRODUCTION

In the late 1960s, a new era began in antineoplastic drugs with the discovery of cisplatin [1, 2]. Understanding the anticancer properties of cisplatin made it the pioneer of metal-based anticancer drugs used from the past to the present [3]. However, cisplatin lacks tumor tissue selectivity and makes target cells resistant to cisplatin over time [4]. Therefore, scientists have synthesized new cisplatin analogs such as carboplatin, oxaliplatin, nedaplatin, lobaplatin, and heptaplatin. These platinum-based chemotherapeutic drugs are the most widely used ones in the treatment of different cancer diseases [5]. Also, scientists have made progress in the research of the different metal-based anticancer drugs in recent years [6, 7].

Cisplatin is used in the treatment of many cancers, especially testicular and ovarian, also colon, stomach, breast, prostate, and small cell and non-small cell lung [8]. The mechanism of action depends on the platinization of DNA bases. In this process, hydrolysis of the drug is an important step that makes it easier to reach the drug to DNA. In addition, hydrolysis of the drug is essential to activate the drug [2, 9]. Pt-S and Pt-N bonds were found in the crystal structure of the drug's addicted product. This means that the platinum atom of the drug binds to amino acids of DNA from their S or N atoms [9]. The resultant structural form suppresses the efficient replication of tumor DNA and as a result of this anticancer effect the tumor cell dies [2].

Despite the great benefits of platinum chemotherapeutics, they have also various side effects such as nephrotoxicity and negative effects on the liver [8]. In addition to the toxicities of the drug, long-term use of cisplatin causes cisplatin resistance. The ability of cross-linking feature of cisplatin provides that cisplatin cross-links to the DNA of the target cell and prevents its dividing [10]. Thus, the formation of resistance is the binding of platinum to DNA and the main cytotoxic mechanism that occurs after cisplatin enters tumor cells [11]. To elucidate the mechanism of such disadvantages and side effects, studies have been carried out to examine many properties of cisplatin such as its electronic and molecular structure [4, 12].

In one of the studies, the effects of catalpol (CAT), a bioactive component, on cisplatin-induced nephrotoxicity and antitumor activity were investigated. As a result of the research, it has been observed that CAT can reverse drug resistance without compromising the antitumor properties of cisplatin. This shows that CAT has positive effects against cisplatin-induced kidney damage by reversing drug resistance *via* the mitochondrial-dependent pathway without affecting the anticancer activity of cisplatin [13]. Another study showed that the anticancer effect of cisplatin was strengthened by nano curcumin. So, they achieved a significant reduction in ovarian tumor volume and weight with cisplatin and nano curcumin administration [14]. A study used nanosheets like Al-doped BN and Ga-doped BN towards cisplatin to understand the adsorption behavior of cisplatin [15]. They achieved higher HOMO energies and lower LUMO energies after the adsorption of cisplatin on the AIBN and GaBN nanosheets.

* To whom all correspondence should be sent:
E-mail: hatiparzu@yahoo.com

The reduction of the energy gap increases the conduction electron population which is important for the drug delivery system. As a result, nanosheets showed high adsorption behavior with small adsorption distances and large variations of the energy gap, especially AIBN. So, AIBN and GaBN nanosheets are promising candidates as drug delivery vehicles for cisplatin [15]. The experimental techniques are expensive to conduct and bring some problems to clinical trials such as losing the activity of a drug candidate before *in vivo* test. So, computational modeling studies are important to get information about molecules and to gain insight into their properties before expensive experimental periods [1].

Density functional theory (DFT) which is the most preferred quantum-mechanical method in recent years, provides important information about the physicochemical properties of compounds. Also, it is known that physicochemical properties are related to the biological activity of compounds [16]. DFT aims to understand the electronic structure and molecular dynamics of the molecules.

In this study, the electronic and physicochemical properties of cisplatin and its derivatives such as carboplatin, oxaliplatin, nedaplatin, lobaplatin, and heptaplatin were investigated. The calculations of the relevant molecules were carried out with the DFT method. The HOMO-LUMO energies, global and local reactivity indices, and thermochemical parameters were calculated in both vacuum and aqueous medium. In addition, the reaction of hydrolyzed nedaplatin complex with cysteine amino acid of DNA was explained by local reactivity indices.

COMPUTATIONAL METHODS

All geometric and electronic calculations were performed with the DFT method within Gaussian 09W software [17]. DFT calculations were carried out by using the three-parameter Becke-Lee-Yang-Parr (B3LYP) exchange-correlation functional with LanL2DZ basis set. Frequency analysis of the molecular structure as a global minimum was performed and all frequency values are positive. Frontier molecular orbitals (FMO), molecular electrostatic potential (MEP) surfaces, and structural visualizations of all molecules were prepared by using Gaussview 5.0 [18].

Global and local reactivity indices were also calculated for the studied molecules. Solvent effects were computed by using conductor-like polarizable continuum model (CPCM) as the solvation model. In this study solvent was water with a dielectric constant value of $\varepsilon=78.355$ [19].

Reactivity indices calculation

Reactivity indices are based on the perturbation of one chemical attacking another chemical species. These perturbations are related to the changing number of electrons or changing of an external potential. Global reactivity indices are related to changing of electrons. The variation of the boundary electron densities is defined by the local indices proposed by Fukui. Local indices give information about the reactivity of a particular region of the molecule [20, 21].

The global reactivity indices are calculated with the following Eq. (1-4). In these equations, E_{HOMO} and E_{LUMO} are the energy of the highest occupied molecular orbital and the lowest unoccupied molecular orbital, respectively. The hardness (η) is calculated by using Koopmans'theorem. [22].

$$\eta = \frac{(E_{LUMO} - E_{HOMO})}{2} \qquad (1)$$

The global softness (S) is defined as inverse of the chemical hardness.

$$S = \frac{1}{2\eta} \qquad (2)$$

Electronegativity (X), which is the negative of chemical potential (μ), is calculated with HOMO and LUMO energies. The electrophilic index depends on the values of chemical potential and hardness values.

$$X = -\mu = (\frac{-E_{HOMO} - E_{LUMO}}{2}) \qquad (3)$$

$$\omega = \frac{\mu^2}{2\eta} = \frac{X^2}{2\eta} \qquad (4)$$

The fukui indices can be calculated by Eqs. (5-7). In these equations, p_{N0}, p_{N+1} and p_{N-1} represent the electronic population on an atom for the neutral, cation and anion systems, respectively. And $f_{(r)}^+$, $f_{(r)}^-$, $f_{(r)}^0$ are fukui indices for the nucleophilic attack, electrophilic attack, and radicalic attack, respectively [21, 23].

$$f_{(r)}^+ = p_{N+1}(r) - p_N(r), \qquad (5)$$
$$f_{(r)}^- = p_N(r) - p_{N-1}(r), \qquad (6)$$
$$f_{(r)}^0 = \frac{p_{N+1}(r) - p_{N-1}(r)}{2} = \frac{f_{(r)}^+ - f_{(r)}^-}{2}, \qquad (7)$$

RESULTS AND DISCUSSION

Ground state geometries and global reactivity indices

The molecular structures and the optimized structures of the studied molecules are given in Fig S1 and Fig. 1. The optimized geometrical parameters

and IR data of cisplatin are based on experimentally obtained results [24, 25]. The geometric parameters for other studied Pt- containing anticancer drugs are given in Table 1. The bond lengths of Pt-O and Pt-N are found to be 2.0 and 2.1 Å, respectively, for carboplatin, oxaliplatin, nedaplatin, lobaplatin, and heptaplatin. The approximate dihedral angle value of the five molecules is 0.51°. As also demonstrated in Fig 1, square planar geometric orientation is obtained for all studied molecules.
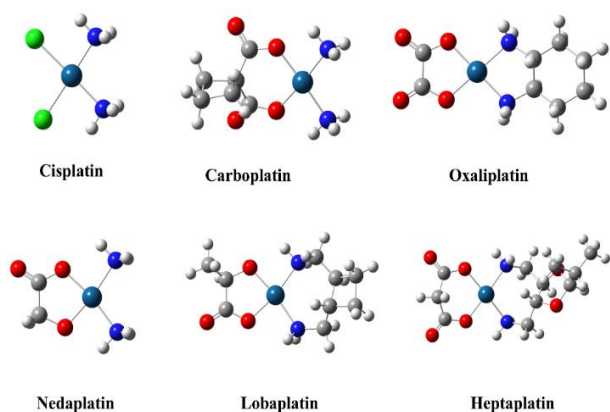

Figure 1. Optimized structures of cisplatin and derivatives.

Anticancer molecules containing Pt have different reactivity and stability due to their structures. In this study, global reactivity indices such as chemical hardness (η), global softness (S), electronegativity (X), and electrophilic index (ω) are calculated for vacuum (vac) and aqueous (aq) medium and they are listed in Table 2. The reactivity and stability of molecules can be interpreted by global reactivity indices. The higher hardness value indicated higher stability and lower reactivity because of the bigger energy gap between frontier orbitals. Softness is the inverse of hardness. As seen in Table 2, carboplatin and heptaplatin have the highest hardness values of 2.55 and 2.54 eV, respectively.

The hardness value of heptaplatin is close to that of carboplatin. These two molecules are more stable and less reactive than others. On the other hand, cisplatin has the highest softness value which is 0.23 eV and this makes cisplatin the most reactive molecule compared to others. This result is also in accordance with Alberto *et al*. study [2, 26].

The reactivity order of the molecules is: cisplatin > oxaliplatin > nedaplatin > lobaplatin > heptaplatin > carpoplatin. The acids must be more electronegative than the bases [27]. The highest electronegativity value has cisplatin with 4.09 eV, so cisplatin is the most acidic molecule.

Table 1. Calculated bond lengths, r and bond angles, a values of molecules

	Carboplatin	Oxaliplatin	Nedaplatin	Lobaplatin	Heptaplatin
r (Å)					
Pt-O	2.0	2.0	2.0	2.0	2.0
Pt-N	2.1	2.1	2.1	2.1	2.1
a (⁰)					
N-Pt-N	105.6	83.3	106.8	107.3	102.1
O-Pt-O	96.6	83.4	86.8	86.1	98.8

Table 2. Electronic properties (eV) of molecules

	Cisplatin		Carboplatin		Oxaliplatin		Nedaplatin		Lobaplatin		Heptaplatin	
	vac	aq	vac	aq	vac	aq	vac	aq	vac	aq	vac	aq
E_{HOMO}	-6.27	-6.49	-6.39	-6.40	-5.83	-6.44	-5.40	-5.62	-5.18	-5.55	-6.39	-6.46
E_{LUMO}	-1.90	-1.85	-1.28	-1.01	-1.06	-1.75	-0.66	-0.63	-0.38	-0.53	-1.30	-1.11
ΔE	4.37	4.65	5.11	5.39	4.77	4.69	4.74	4.99	4.80	5.02	5.08	5.35
X	4.09	4.17	3.84	3.70	3.44	4.09	3.03	3.12	2.78	3.04	3.85	3.79
η	2.18	2.32	2.55	2.70	2.39	2.35	2.37	2.50	2.40	2.51	2.54	2.68
ω	3.82	3.74	2.88	2.54	2.48	3.57	1.93	1.95	1.61	1.84	2.91	2.68
S	0.23	0.22	0.20	0.19	0.21	0.21	0.21	0.20	0.21	0.20	0.20	0.19

Lobaplatin is a basic molecule with the lowest electronegativity value of 2.78 eV. All of the molecules have electrophilic index values greater than 1.5 eV, which means that they are all strong electrophiles [28]. The chemical potential is negative. The electrophilic index contains information about electron transfer and it shows similar trends with chemical potential [29].

Frontier molecular orbitals

Frontier molecular orbitals (FMOs) are the electron distribution representations of HOMO and LUMO. They provide very important information such as electronic properties, kinetic stability, and chemical reactivity of molecules [30]. Frontier molecular orbitals of the studied molecules are given in Fig. 2. As seen in Fig 2 HOMO is located on the Pt atom, and chloride substitutions for cisplatin. In contrast to cisplatin results, HOMO of other drugs is located at the central Pt atom and butane dicarboxylate, glycolate, oxalate, 3-methyl butane-2-one, and pentane-2,4-dione for carboplatin, oxaliplatin, nedaplatin, lobaplatin, and heptaplatin respectively. LUMO of the molecules is distributed through the molecules except for oxaliplatin, lobaplatin, and heptaplatin. Electron distribution of LUMO for these molecules is mainly on the glycolate, 3-methyl butane-2-one, and pentane-2,4-dione parts of the molecules.

It is understood from Table 1 that HOMO energies decreased for all molecules in aqueous medium than in vacuum. On the other hand, LUMO energies did not decrease for all such as oxaliplatin and lobaplatin. However, the energy gap between HOMO and LUMO decreased only for oxaliplatin in aqueous medium than vacuum. Accordingly, unlike the others, oxaliplatin is more photochemically reactive in an aqueous medium than in vacuum.
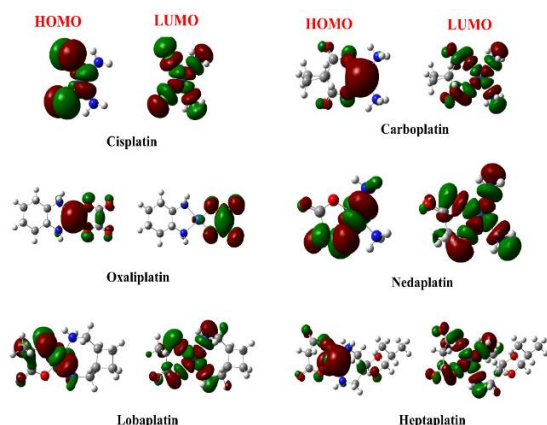

Figure 2. Frontier molecular orbitals of cisplatin derivatives

Molecular electrostatic potential (MEP)

The molecular electrostatic potential (MEP) surface is a three-dimensional visualized representation of the charge distributions of molecules on the electron density surface. MEP surfaces help to predict the shape, size, and reactive sides of molecules. The color identification of electrostatic potential is in the range of red and blue. The red depicts negative regions and they are related to an electrophilic attack whereas blue depicts positive regions and they are related to the nucleophilic attack. Electrostatic potential increases from red to blue [31]. MEP surfaces of studied molecules are illustrated in Fig. 3.

The positively charged regions shown in blue are mainly over the amine groups of all molecules. The negative charge distribution of the molecules is on carbonyl groups and oxygen, except for cisplatin. In cisplatin, it is on the chloride atoms. These blue regions have high electron abundance and an electrophilic attack occurs most likely from this side of the molecules. Pt atoms in these MEP surfaces are at the central place of the boundary between the negatively and positively charged areas for all molecules.
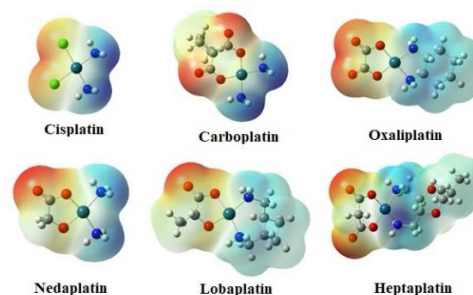

Figure 3. MEP surfaces of cisplatin derivatives

Reaction of nedaplatin with cysteine amino acid

Fukui indices are the most important local properties used in determining the reactivity of different regions of a molecule. In this part of the study, the reaction of cysteine amino acid with anticancer drugs containing Pt was investigated by local fukui indices. For this, nedaplatin was chosen as the model molecule. These types of reactions are necessary to understand the anticancer activities of Pt-containing anticancer drugs with DNA.

It is known from the literature that the Pt atom has a soft character, so it can interact with the S atom in the cysteine amino acid of DNA [32, 33]. Fukui indices results of nedaplatin in aqueous medium are given in Table 3.
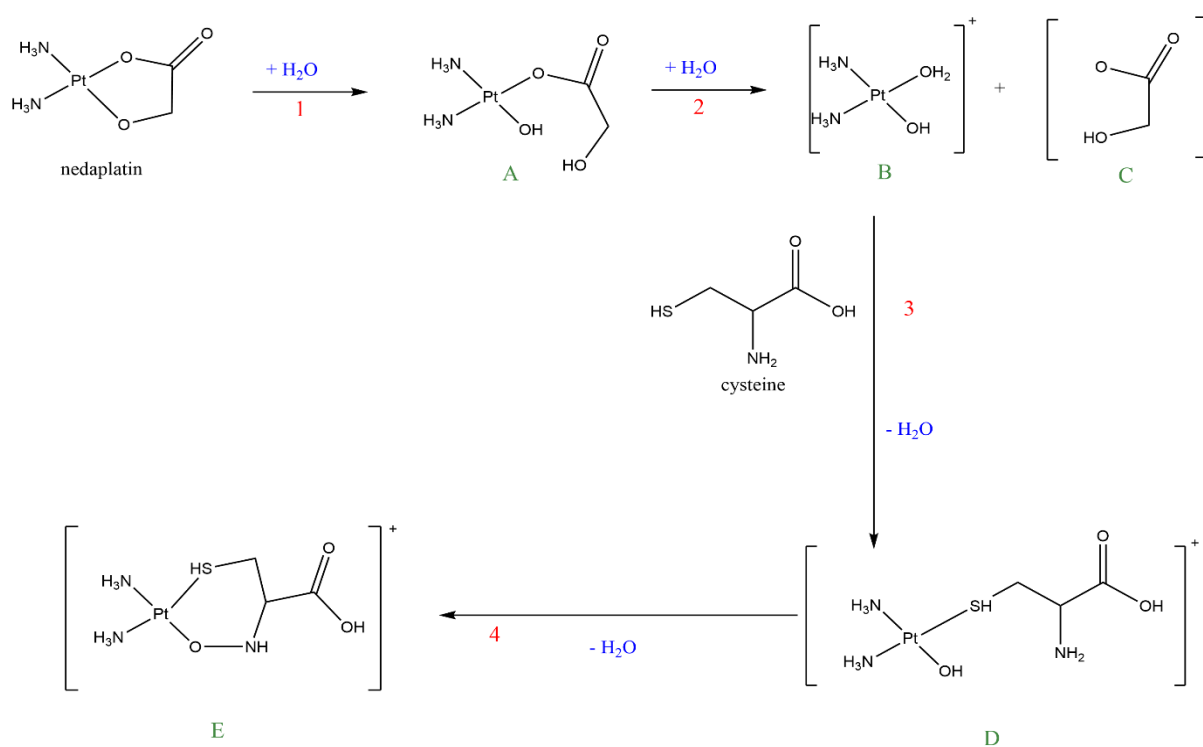
Scheme 1. The predicted reaction mechanism of nedaplatin

Table 3. Fukui indices of nedaplatin and cysteine

		Nedaplatin					Cysteine		
		f+	f-	f0			f+	f-	f0
1	Pt	0.472	0.422	0.447	1	N	0.015	0.188	0.102
2	O	0.037	0.186	0.112	3	C	0.040	-0.028	0.006
3	O	0.015	0.017	0.016	5	C	-0.008	0.004	-0.002
4	C	0.056	0.047	0.052	6	C	0.262	0.040	0.151
5	O	0.044	0.043	0.044	9	S	0.074	0.313	0.194
12	N	0.042	0.012	0.027	10	O	0.209	0.073	0.141
13	N	0.031	0.013	0.022	13	O	0.094	0.029	0.062
14	C	0.033	-0.004	0.015					
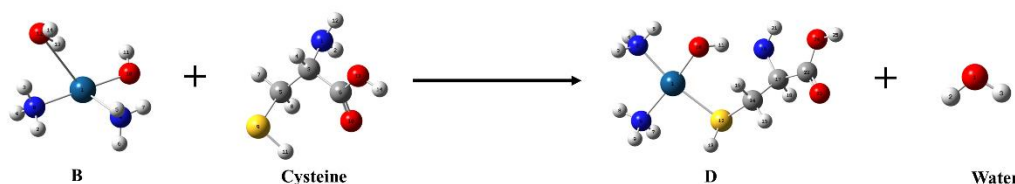
Figure 4. Optimized geometries for the reaction path 3.

The greater the value of the fukui indices of an atom in the molecule, the higher its reactivity. Therefore, these values are listed in the table. It is demonstrated in Table 3 that the Pt atom site is a suitable part for nucleophilic attack of amino acids and this result is compatible with the literature [32, 33]. Fukui indices of other studied molecules are given in the Supplementary material. Similar to Zimmermann *et al*. study Pt atom sites of other drugs are also found as the most suitable part for DNA reactions [33].The reaction mechanism of nedaplatin

with cysteine is given in Scheme 1. As seen from Scheme 1 the reaction mechanism begins with the hydrolyzing of nedaplatin. It is accepted that hydrolysis of nedaplatin is essential to react with DNA [26]. Thus, hydrolysis of nedaplatin occurs first in the mechanism, and then it binds to the amino acid portion of the DNA.

It is understood from Scheme 1 that hydrolysis of nedaplatin is occurred with two executive steps, paths 1 and 2. As nedaplatin is completely hydrolyzed, the diaqua nedaplatin form approaches

DNA [2, 26]. With these steps a charged active drug is generated and then it can further interact with the nucleophilic part of DNA. In reaction path 1, as a result of the addition of one water molecule to the drug, nedaplatin's ring is opened and A is obtained. With the addition of a second water molecule to A in reaction path 2, molecule B and ligand C products are obtained with the SN^2 mechanism.

In reaction paths 3 and 4, cysteine reactions occur with B. As can be seen from the fukui indices values of nedaplatin and cysteine listed in Table 3, S and N atoms of cysteine are suitable sites for the reaction. Therefore, the interactions of cysteine and nedaplatin with the S and N atoms were investigated in paths 3 and 4. It is also stated in the literature that diaquanedaplatin (B) interacts with the S atom of cysteine and the N atoms of amino acids [4]. Thus, our result coincides with the literature. In path 3, the interaction of cysteine and B atom with S atom led to the formation of the monodentate cysteine complex (D). Finally, the bidention D molecule is formed from the N atom of cysteine and the Pt atomic part of nedaplatin. then E molecule is obtained by separating a water molecule. The molecular structures of the reaction intermediate for path 3 are given in Fig. 4. The molecular structures for other paths are given in the Supplementary information.

CONCLUSION

In this study, the electronic properties of cisplatin, carboplatin, oxaliplatin, nedaplatin, lobaplatin, and heptaplatin were investigated by the DFT method. Reactivities of the drugs were calculated by the means of global reactivity indices. Global reactivity indices results demonstrate that cisplatin is the most reactive molecule. The reaction of nedaplatin with cysteine amino acid was also analyzed by using local indices. For the molecules studied, Pt atoms according to the fukui indices values, as with nedaplatin, are suitable sites that can react with the nucleophilic region of the DNA molecule. In general, in platinum-containing drugs, as understood from the fukui indices, the Pt atom is the region that can react with amino acids. This study provides a theoretical basis for predicting the electronic properties of Pt-containing anticancer drugs and their reactivity.

REFERENCES

1. Y. Arbia, S. Abtouche, M. Dahmane, M. Brahimi, *Theor. Chem. Acc.,* **142**(1), (2023).
2. M.E. Alberto, V. Butera, N. Russo, *Inorg. Chem.* **50**(15), 6965 (2011).
3. ACPt 14) M1 rosenberg1969, (n.d.).
4. T. Minervini, B. Cardey, S. Foley, C. Ramseyer, M. Enescu, *Metallomics,* **11**(4), 833 (2019).
5. M. Torres, S. Khan, M. Duplanty, H.C. Lozano, T.J. Morris, T. Nguyen, Y. V. Rostovtsev, N.J. Deyonker, N. Mirsaleh-Kohan, *Journal of Physical Chemistry A,* **122**(34), 6934 (2018).
6. A. de Almeida, R. Bonsignore, *Bioorg. Med. Chem. Lett.,* **30**(13), (2020).
7. A. Pöthig, A. Casini, *Theranostics,* **9**(11), 3150 (2019).
8. C.A. Rabik, M.E. Dolan, *Cancer Treat. Rev.,* **33**(1), 9 (2007).
9. D. Miodragović, A. Merlino, E.P. Swindell, A. Bogachkov, R.W. Ahn, S. Abuhadba, G. Ferraro, T. Marzo, A.P. Mazar, L. Messori, T. V. O'Halloran, *J. Am. Chem. Soc.,* **141**(16), 6453 (2019).
10. L. Qi, Q. Luo, Y. Zhang, F. Jia, Y. Zhao, F. Wang, *Chem. Res. Toxicol.,* **32**(8), 1469 (2019).
11. S.H. Chen, J.Y. Chang, *Int. J. Mol. Sci.,* **20**(17), (2019).
12. E. Shakerzadeh, *Comput. Theor. Chem.,* **1202**, (2021).
13. J. Zhang, T. Zhao, C. Wang, Q. Meng, X. Huo, C. Wang, P. Sun, H. Sun, X. Ma, J. Wu, K. Liu, *Oxid. Med. Cell Longev.,* **2021**, (2021).
14. N.M.D. Sandhiutami, W. Arozal, M. Louisa, D. Rahmat, P.E. Wuyung, *Front. Pharmacol.,* **11**, (2021).
15. A.A. Piya, S.U.D. Shamim, M.N. Uddin, K.N. Munny, A. Alam, M.K. Hossain, F. Ahmed, *Comput. Theor. Chem.,* **1200**, (2021).
16. M. Salihović, M. Pazalja, S. Špirtović Halilović, E. Veljović, I. Mahmutović-Dizdarević, S. Roca, I. Novaković, S. Trifunović, *J. Mol. Struct.,* **1241**, (2021).
17. Gaussian 09, Revision B.04, Gaussian Inc., Pittsburgh, PA, 2009.
18. R. Dennington, T. Keith, J. Millam, GaussView, Version 5, Semichem Inc., Shawnee Mission, KS, 2009.
19. J. B. Foresman, A. Frisch, Exploring Chemistry with Electronic Structure Methods, Gaussian Inc., USA,1996.
20. Y.Y. Gurkan, N. Turkten, A. Hatipoglu, Z. Cinar, *Chemical Engineering Journal* **184**, 113 (2012).
21. W. Yang, R.G. Parr, *Proc. Natl. Acad. Sci. USA*, **82**, 6723, (1985).
22. R.G. Parr, W. Yang, Density Functional Theory of Atoms and Molecules, Oxford Univ. Press, New York, 1989.
23. R.K. Roy, S. Pal, K. Hirao, *Journal of Chemıcal Physıcs*, **110** (17), 8236 (1999).
24. M. Malik, D. Michalska, *Spectrochim Acta A, Mol. Biomol. Spectrosc.,* **125**, 431 (2014).

25. G.H.W. Milburn, M.R. Truter, *Journal of the Chemical Society A: Inorganic, Physical, Theoretical,* 1609 (1966).

26. M.E. Alberto, M.F.A. Lucas, M. Pavelka, N. Russo, *Journal of Physical Chemistry B* **113**(43), 14473 (2009).

27. R.G. Pearson, Chemical Hardness and Density Functional Theory, 2005.

28. L.R. Domingo, P. Pérez*, Org. Biomo.l Chem.,* **9**(20), 7168 (2011).

29. M. Elango, R. Parthasarathi, G. K. Narayanan, A.M. Sabeelullah, U. Sarkar, N.S. Venkatasubramaniyan, V. Subramanian, P.K. Chattaraj, *Journal of Chemical Sciences,* **117,** 61 (2005)

30. S. Aydogdu, A. Hatipoglu, *Acta Chim. Slov.,* **69**(3), 647 (2022).

31. I. Erden, A. Hatipoglu, C. Cebeci, S. Aydogdu, *J. Mol. Struct.,* **1201**, (2020).

32. D. Corinti, R. Paciotti, C. Coletti, N. Re, B. Chiavarino, M.E. Crestoni, S. Fornarini, *J. Inorg. Biochem.,* **237**, (2022).

33. T. Zimmermann, M. Zeizinger, J. V. Burda, *J. Inorg. Biochem.,* **99**(11), 2184 (2005).

Effects of drying methods on the drying kinetics of blanched brown crab meat

Z. Ozden Ozyalcin, A. Seyhun Kipcak[*]

Department of Chemical Engineering, Faculty of Chemical and Metallurgical Engineering, Yildiz Technical University, Davutpasa Campus, Davutpasa Street No. 127, Esenler, 34220 Istanbul, Turkey

The study was conducted to examine the effect of various drying methods on the drying kinetics of brown crab meat pre-treated by blanching in a 5% brine solution. The drying methods used in this study included oven drying, infrared (IR) drying, and microwave (MW) drying. The results obtained were analyzed and evaluated through statistical and color analyses. To conduct the study, oven and IR drying were carried out at varying temperatures between 60°C - 80°C, while MW drying was performed at different power settings between 140 W - 350 W. The data collected from these experiments were analyzed to determine the drying rates, effective moisture diffusivities (D_{eff}), and activation energies (E_a). Mathematical models were used to compare the drying times, and graphical representations were created to present the findings. The outcomes of the study showed that the microwave drying method had the highest D_{eff} value, which ranged between 2.83×10^{-9} and 9.76×10^{-9} m²/s, while the oven drying method had the lowest D_{eff} value, which ranged between 1.90×10^{-10} and 2.62×10^{-10} m²/s. The E_a values for the oven, IR, and MW methods were calculated as 15.74 kJ/mol, 37.55 kJ/mol, and 72.71 kW/kg, respectively. Furthermore, the highest R^2 value was obtained with Aghbashlo *et al*. model for the oven and Alibas model for IR and MW. In addition, the color analysis showed that the MW drying method caused the highest total color change (ΔE), followed by IR and oven drying.

Keywords: Activation energy, brown crab, color change, effective moisture diffusivity

INTRODUCTION

The brown crab, scientifically known as *Cancer pagurus*, is a type of crustacean with a heavy, oval-shaped reddish-brown body characterized by its large, powerful pincers with pie-crusty edges. The brown crab is highly regarded and widely appreciated as a crustacean in European countries [1]. The countries with the highest volume of brown crab catch include the United Kingdom, Ireland, Norway, and France. The main distribution of the brown crab spans from Norway in the North Sea to the coast of Portugal, primarily utilizing the English Channel [1]. In the global market, male crabs with more enormous claws are in higher demand than female crabs, due to their higher meat content [2]. The carapace of a mature *Cancer pagurus* can be up to 30 cm wide and weigh up to 3 kg. Their lifespan can vary between 20 and 50 years [3, 4]. Their growth rate depends on multiple variables such as food availability, water depth, and temperature [4]. Brown crab contains high protein, amino acids, essential elements (e,g, Zn, Se), and fatty acids while keeping fat and cholesterol levels low, making it a healthy and beneficial food choice [1, 5]. Crab meat undergoes rapid microbial degradation after hunting. It is often immediately incorporated into food processing for consumption of this product of high economic value [6].

In order to maintain and improve the quality and lifespan of food products, drying is one of the oldest and most used techniques [7]. The process itself is a combination of heat and mass transfer and needs an energy supply [8]. It requires high amounts of energy and generates phase change for the water molecules inside the food and converts liquid to vapor. The transfer mechanism for heat may vary depending on the method. It can be transferred *via* radiation, conduction with the help of a hot plate, or even microwaves using radio frequency.

There are many studies in the literature on drying seafood with different methods. Some of these studies were carried out on molluscs, crustaceans, and fish such as sea cucumber [9, 10], shrimp [11, 12], mussels [13, 14], octopus [15], calamari [16], and catfish [17]. Despite its high consumption rates, crab meat has received little attention among seafood drying studies. In this study, blanched crab meat was examined using infrared (IR) and microwave (MW) drying methods and evaluated in comparison with the results of a previous oven-drying study [18]. Drying rate, effective moisture diffusion, and activation energies were calculated and drying data were tested for 13 mathematical models to determine the best-fitting model. In addition, color analysis was performed to appoint the visual changes in drying methods.

---

* To whom all correspondence should be sent:
E-mail**:** skipcak@yildiz.edu.tr

EXPERIMENTAL

The crab was bought from a fish market in Istanbul, Turkey in February 2021 and was kept in a refrigerator at a temperature of -18 °C. Before the experiments, the crabs were thawed at +4 °C and brought to room temperature in a desiccator. For blanching, 700 ml of distilled water containing 5% of salt was brought to boiling and the crab was boiled in this water for 10 minutes. The shell of the crab changed color from brown to red after boiling as seen in Figure 1. After the boiling process, the crabs were cooled for 5 minutes, and the meat and shells were separated from each other. The 0.5 cm thick samples weighed 5.0 ± 0.2 g, as shown in Figure 2.

Figure 1. Crab before and after blanching

The average moisture content was determined by using a hot air-drying oven (KH-45; Kenton, Guangzhou, China) at 120°C for 3 hours. The drying temperatures were selected as 60, 70, and 80 °C for oven [18] and infrared (IR), and 140, 210, and 350 W were selected for the microwave (MW). During the drying process, the weight of the sample was noted at intervals of 15 minutes. Drying ended when the moisture content of the sample dropped under 10%.

Figure 2. Blanched crab meat

The weight of the sample was noted at intervals of 15 minutes [18] during the oven and IR processes, and each minute for 140 and 210 W and every 30 seconds for 350 W in MW. Drying ended when the moisture content of the sample dropped under 10%.

Mathematical modeling of drying curves

Moisture content, drying rate, and moisture ratio were calculated to draw the drying curves and test the drying data's compatibility with mathematical models (Equations 1-3). In the formulas, moisture content (*M*) was calculated based on kg water content (m_w) and kg dry matter (m_d). Drying rate (*DR*) was calculated based on the values of moisture content at time t min (M_t) and time t+dt (M_{t+dt}). The moisture ratio (*MR*) was calculated dimensionless depending on the initial (M_0), t-minute (M_t), and equilibrium (M_e) moisture contents [14, 19].

$$M = \frac{m_w}{m_d} \qquad (1)$$

$$DR = \frac{M_{t+dt} - M_t}{dt} \qquad (2)$$

$$MR = \frac{M_t - M_e}{M_0 - M_e} \qquad (3)$$

Mathematical modeling was performed with 13 different models whose formulas are given in Table 1 with Statistica 10.0 (StatSoft Tulsa, USA) program using the Levenberg-Marquardt algorithm for parameter estimation in nonlinear regression. The fit of the models was determined by the regression coefficient (R^2), the lowest root mean square error (*RMSE*), and reduced chi-square (χ^2) values [20]. Here, the calculated ($MR_{exp,i}$) and predicted values ($MR_{pre,i}$) for moisture ratios were calculated as given in equations 4-6, depending on the total number of experiments (*N*) and the model constant number (*z*) [20, 21].

$$R^2 \equiv 1 - \frac{\sum_{i=1}^{N}\left(MR_{exp,i} - MR_{pre,i}\right)^2}{\sum_{i=1}^{N}\left(MR_{exp,i} - \left(\frac{1}{n}\right)MR_{exp,i}\right)^2} \qquad (4)$$

$$RMSE = \left(\frac{1}{N}\sum_{i=1}^{N}\left(MR_{exp,i} - MR_{pre,i}\right)^2\right)^{\frac{1}{2}} \qquad (5)$$

$$\chi^2 = \frac{\sum_{i=1}^{N}\left(MR_{exp,i} - MR_{pre,i}\right)^2}{N - z} \qquad (6)$$

represents the number of the total experiments, MR_{exp} and MR_{pre} represent experimental and predicted values for moisture ratios, respectively, and z is the number of constants in the model used for evaluation.

Table 1. Model names and equations used for the experiments [22]

Name of the model	Model equation
Aghbaslo *et al.*	$MR = \exp\left(-k_1 t / (1 + k_2 t)\right)$
Alibas	$MR = a \times \exp\left((-kt^n) + bt\right) + g$
Henderson *et al.*	$MR = a \times \exp\left(-kt\right)$
Jena *et al.*	$MR = a \times \exp\left(-kt + b\sqrt{t}\right) + c$
Lewis	$MR = \exp\left(-kt\right)$
Logarithmic	$MR = a \times \exp\left(-kt\right) + c$
Midilli & Kucuk	$MR = a \times \exp\left(-kt^n\right) + bt$
Page	$MR = \exp\left(-kt^n\right)$
Parabolic	$MR = a + bt + ct^2$
Two-Term Exponential	$MR = a \times \exp(-k_0 t) + b \times \exp(-k_1 t)$
Verma *et al.*	$MR = a \times \exp\left(-kt\right) + (1 - a) \times \exp\left(-gt\right)$
Wang *et al.*	$MR = \exp\left(-(t/b)^a\right)$
Weibull	$MR = a - b \times \exp\left(-(kt)^n\right)$

Effective moisture diffusivity and activation energy

The drying mechanism in food products is explained with formulas based on Fick's second law of diffusion. The effective moisture diffusion coefficient (D_{eff}) which requires basic assumptions to be made, can be calculated with Equation 7 depending on the sample half-thickness (L) in meters and the positive integer n. Within the calculation, it is assumed that there is no shrinkage or change in the diffusion coefficient and that mass transfer occurs symmetrically with respect to the center by diffusion only. In addition, the n value is accepted as 1 due to the length of the drying time [23].

$$MR = \frac{8}{\pi^2}\sum_{n=1}^{\infty}\frac{1}{(2n+1)^2}\exp\left(-\frac{(2n+1)^2\pi^2 D_{eff} \times t}{4L^2}\right) \qquad (7)$$

Activation energy (E_a) also plays an important role in the separation of water molecules from the

product to be dried. Accordingly, the lower the activation energy of the water molecules, the faster the drying occurs. When this calculation is made as the energy provided by the drying devices to the product to be dried, the higher the activation energy, the faster the drying will be. The calculation of the activation energy is derived from the slope of the graph plotted against $1/T$ (T in Kelvin) of the natural logarithm of the D_{eff} value for the temperature-based furnace and IR (Equation 8). Since the MW process is based on power, the graph is drawn for $\ln(D_{eff})$ against the ratio of kg sample weight (m) to microwave power (P) as in Equation 9. The slope of this graph gives the value E_a for MW. In this calculation based on the Arrhenius equation, D_0 is the exponential factor in m^2/s and R is the universal gas constant in kJ/mol×K [20].

$$D_{eff} = D_o \exp\left(-\frac{E_a}{RT}\right) \qquad (8)$$

$$D_{eff} = D_0 \exp\left(\frac{E_a \times m}{P}\right) \qquad (9)$$

Color analysis

Color value is one of the visual elements that change during the drying of foods. The color change (ΔE) of the product to be dried before and after processing can be obtained by calculating the change in lightness-darkness value (L^*), redness-greenness value (a^*), and yellowness-blueness value (b^*) with equation 10 [22].

$$\Delta E = \sqrt{(L_0 - L)^2 + (a_0 - a)^2 + (b_0 - b)^2} \qquad (10)$$

In this equation, L_0, a_0, and b_0 values represent the color values of the samples before drying. Detection of color changes in the drying process of Blanched crabmeat was performed using a model PCE-CSM 1 colorimeter available from PCE Instruments UK Ltd., with the average of values taken from samples from 5 different areas [20].

RESULTS AND DISCUSSION

In determining the moisture content of the samples to be dried, the initial moisture content was found to be 76.05% on a wet basis, corresponding to 3.175 kg water/kg dry meat on a dry basis. The dried samples are shown in Figure 3.
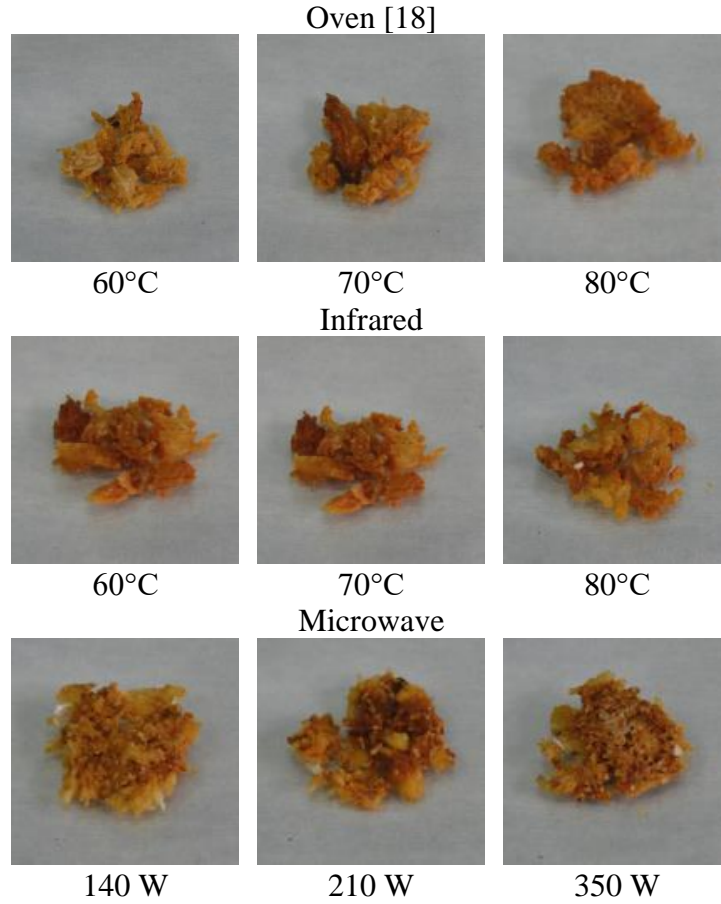
Oven [18]

60°C   70°C   80°C

Infrared

60°C   70°C   80°C

Microwave

140 W   210 W   350 W

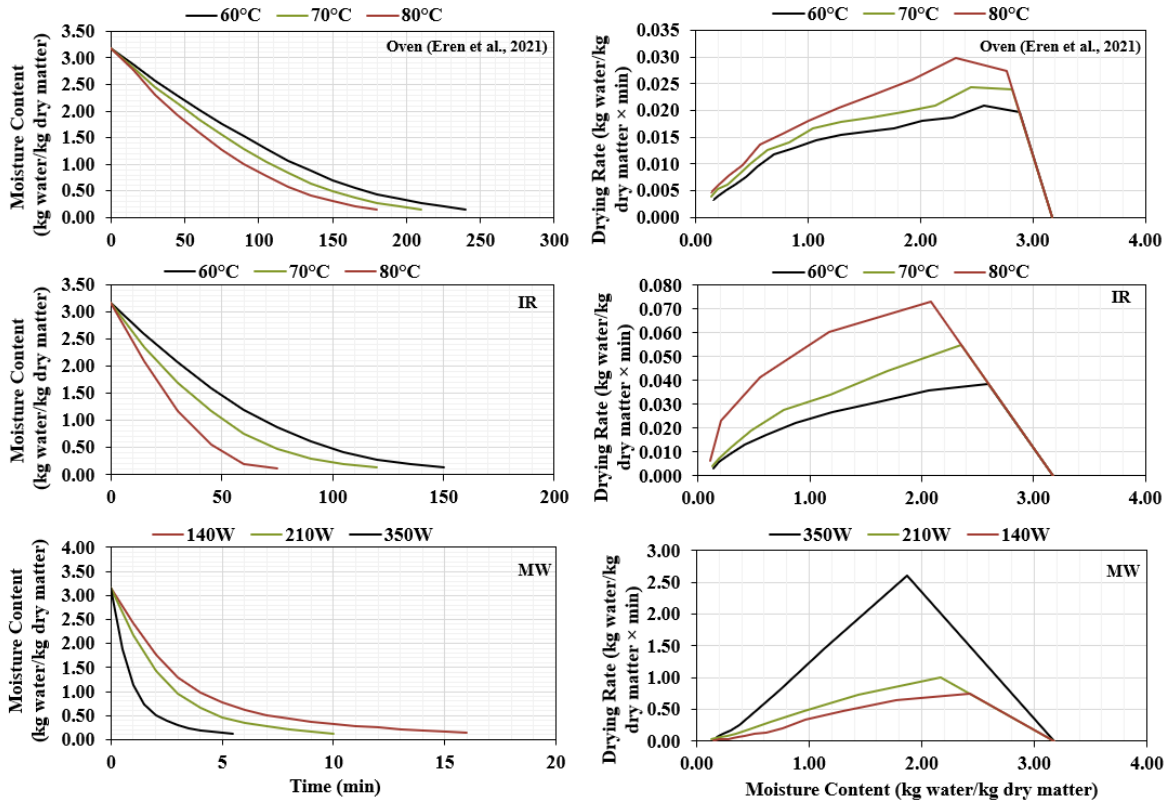**Figure 3.** Dried blanched crab meat

Figure 4. Moisture content *vs.* time and drying rate *vs.* moisture content plots of oven [18], IR, and MW

237

Mathematical modeling of drying curves

In the oven drying of the samples whose moisture content was determined, 240, 210, and 180 minutes at 60, 70, and 80 C, respectively, the final moisture contents were obtained as 0.1591, 0.1427, and 0.1389 kg water/kg dry matter [18]. For IR, drying times were 150, 120, and 75 minutes at 60, 70, and 80 °C, respectively, and final moisture contents were 0.1391, 0.1322, and 0.1113 kg water/kg dry matter. For MW drying times were 17, 10, and 6 minutes at 140, 210, and 350W, respectively, and final moisture contents were 0.1363, 0.1269, and 0.1124 kg water/kg dry matter. The drying curves given in Figure 4 were drawn by using the moisture change *versus* time data in the drying processes. When the moisture content *versus* time plots is examined, it is seen that MW is the fastest drying method and the oven is the slowest drying method in drying processes. Additionally, it may be concluded that higher temperatures and power levels at the end of drying lead to lower final moisture content. When the graphs of moisture content *versus* drying rate were looked at, it was found that for all techniques practically all of the drying occurred in the falling rate period.

Model constants and parameters were obtained by fitting the drying data into mathematical model equations. The model outputs for the three models with the highest R^2 and the lowest χ^2 and RMSE values for each method among the 13 models applied are given in Table 2.

According to the evaluated parameters, the model with the highest compatibility with the drying data was found to be Aghbashlo *et al.* for the oven [18] with R^2 values of 0.99963, 0.99981, and χ^2 values of 0.99981, 0.00004, 0.00001, and 0.00002 and RMSE of 0.00582, 0.00354, and 0.00382, for 60, 70, and 80°C, respectively.

The most compatible methods for IR and MW were determined as Alibas. R^2 values for 60, 70, and 80°C for IR, respectively, were 0.99999, 0.99995, and 0.99999, $^2\chi$ values were 0.00001, 0.00001, and 0.00001 and RMSE were 0.00107, 0.00220, and 0.00081. R^2 values for 140, 210, and 350 W for MW, respectively, were 0.99991, 0.99999, and 0.99997, $^2\chi$ values were 0.000009, 0.000002, and 0.000003 and RMSE were 00.002506, 0.000962, and 0.001412.

Effective moisture diffusivity & activation energy results

The D_{eff} values were calculated from the slope of the graphs plotted against the drying time of In (MR) which are given in Figure 5. D_{eff} values for oven were obtained as 1.9×10^{-10}, 2.23×10^{-10}, and 2.62×10^{-10} m^2/s for 60, 70 and 80 °C, respectively. D_{eff} values for IR were obtained as 3.27×10^{-10}, 4.16×10^{-10}, and 7.08×10^{-10} m^2/s for 60, 70 and 80 °C, respectively. D_{eff} values for MW were obtained as 2.83×10^{-9}, 4.83×10^{-9}, and 9.76×10^{-9} m^2/s for 140, 210 and 350 W, respectively. It is seen that the increase in temperature and power values increases the D_{eff} values for all methods. It was observed that the calculated D_{eff} values are in the range of 10^{-8} and 10^{-12} m^2/s, which is the literature range for biological materials [24]. The obtained D_{eff} values were used to calculate the activation energy as the energy transferred to the sample by the dryers during drying. E_a values were obtained from the relationship of the slope of the graph of $\ln(D_{eff})$ *vs.* 1/T for oven and IR with the gas constant R, and from the slope of the graph of $\ln(D_{eff})$ against m/P for MW.

Accordingly, E_a values for oven, IR, and MW were obtained as 15.74 kJ/mol, 37.55 kJ/mol, and 72.719 kW/kg, respectively. Obtaining lower E_a with oven than with IR indicates that a lower level of energy is transferred to the samples for drying. This is also consistent with oven drying taking longer than IR.

Color analysis

The results of color analyses are shown in Figure 6 with parameters L*, a*, b*, and ΔE values which are mean values of five repeated measurements of each method in every different medium of temperature or power. L*, a*, and b* values of fresh samples were measured as 32.14, -5.453, and -2.276, respectively. MW drying was determined to have higher L* and the oven had lower values. The reason behind this result is that the drying time in MW was the shortest and in the oven was the longest. For the redness-greenness value a*, it was observed that lower temperature and power settings lead to more reddish color on the dried sample, which means it is inversely proportional to the lightness values and hence, inversely proportional to drying time. It is concluded that more reddish colors occurred in MW, IR, and oven in decreasing order due to their drying times. The yellowness-blueness value b* was seen to be directly proportional to L* but inversely proportional to a*. Also, it was observed that all three methods gave relatively close b* values in the final product.

Table 2. Mathematical model coefficients and statistical data

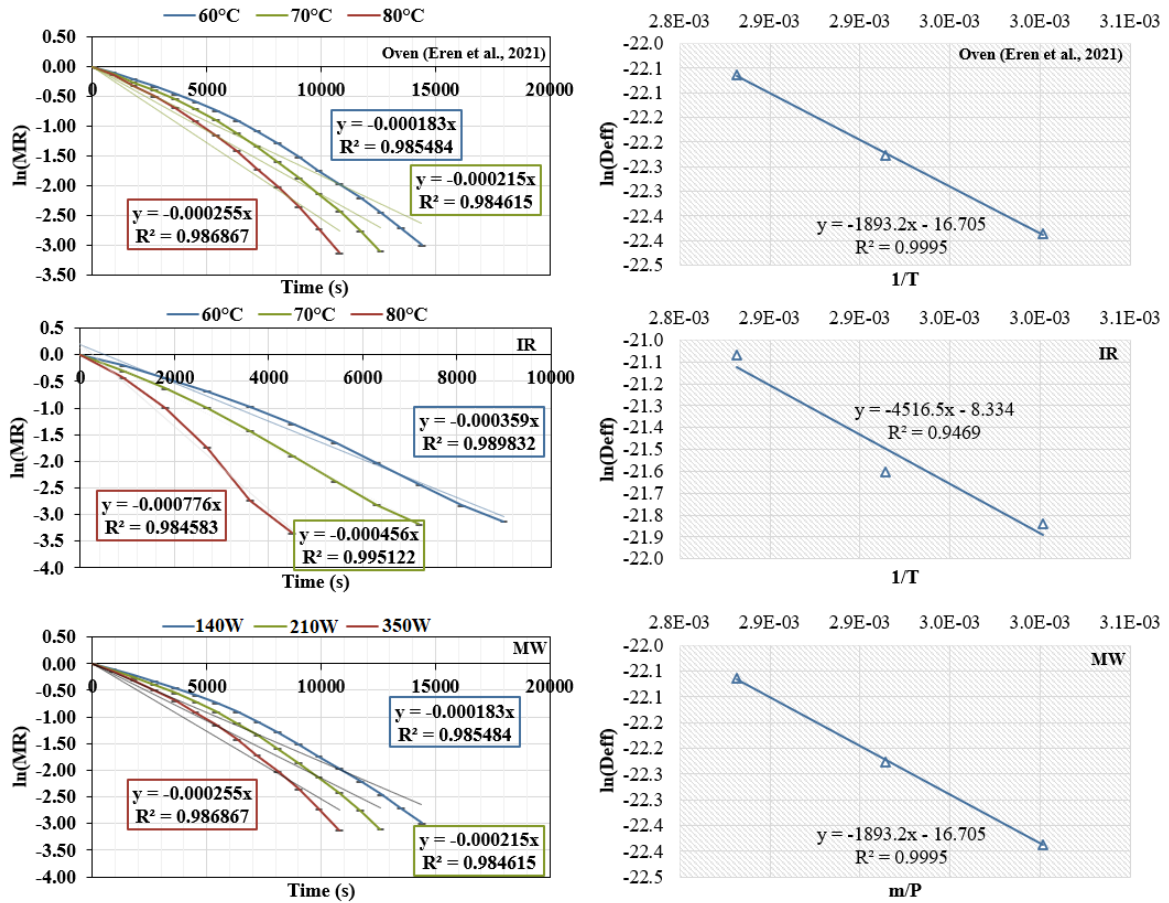|	Oven [18]								
Model	Aghbashlo *et al.*			Parabolic			Wang *et al.*		
Coeff.	60°C	70°C	80°C	60°C	70°C	80°C	60°C	70°C	80°C
a				1.01120	1.00617	1.00487	-0.00700	-0.00816	-0.00985
b				-0.00718	-0.00827	-0.00996	0.00001	0.00002	0.00003
c				0.00001	0.00002	0.00003			
k_1	0.00671	0.00792	0.00982						
k_2	-0.00210	-0.00234	-0.00253						
R^2	0.99963	0.99981	0.99981	0.99958	0.99980	0.99987	0.99939	0.99974	0.99983
χ^2	0.00004	0.00001	0.00002	0.00005	0.00002	0.00001	0.00006	0.00003	0.00002
RMSE	0.00582	0.00354	0.00382	0.00618	0.00431	0.00326	0.00746	0.00484	0.00383
	IR								
Model	Alibas			Parabolic			Wang *et al.*		
Coeff.	60°C	70°C	80°C	60°C	70°C	80°C	60°C	70°C	80°C
a	2.94015	2.79395	3.71385	0.99908	0.98608	1.00406	-0.01295	-0.01745	-0.02629
b	0.00701	0.00825	0.01974	-0.01293	-0.01702	-0.02648	0.00004	0.00008	0.00018
c				0.00004	0.00008	0.00018			
g	-1.94060	-1.79420	-2.71404						
k	0.00592	0.00965	0.01013						
n	1.05122	1.00628	1.08018						
R^2	0.99999	0.99995	0.99999	0.99987	0.99895	0.99986	0.99987	0.99862	0.99983
χ^2	0.00001	0.00001	0.00001	0.00002	0.00016	0.00003	0.00002	0.00018	0.00003
RMSE	0.00107	0.00220	0.00081	0.00358	0.01029	0.00409	0.00360	0.01177	0.00448
	MW								
Model	Alibas			Two Term-Exponential			Verma *et al.*		
Coeff.	140W	210W	350W	140W	210W	350W	140W	210W	350W
a	0.82899	0.86441	0.89716	0.12511	-11.8548	1.59939	0.89115	0.01815	0.84633
b	-0.00787	-0.00980	-0.01168	-0.05973	-0.38050	-0.91048			
c				0.88630	12.84920	-0.62597			
d				-0.34729	-0.38050	-0.91036			
g	0.17196	0.13544	0.10301				0.05160	0.40865	0.24733
k	0.32663	0.43575	1.20344				0.33627	-0.04496	1.25855
n	1.13913	1.11625	0.99652						
R^2	0.99991	0.99999	0.99997	0.99918	0.99784	0.98806	0.99906	0.99964	0.99998
χ^2	0.000009	0.000002	0.000003	0.000074	0.000295	0.001278	0.000079	0.004536	0.000002
RMSE	0.002506	0.000962	0.001412	0.00758	0.013703	0.029748	0.008132	0.057433	0.001179

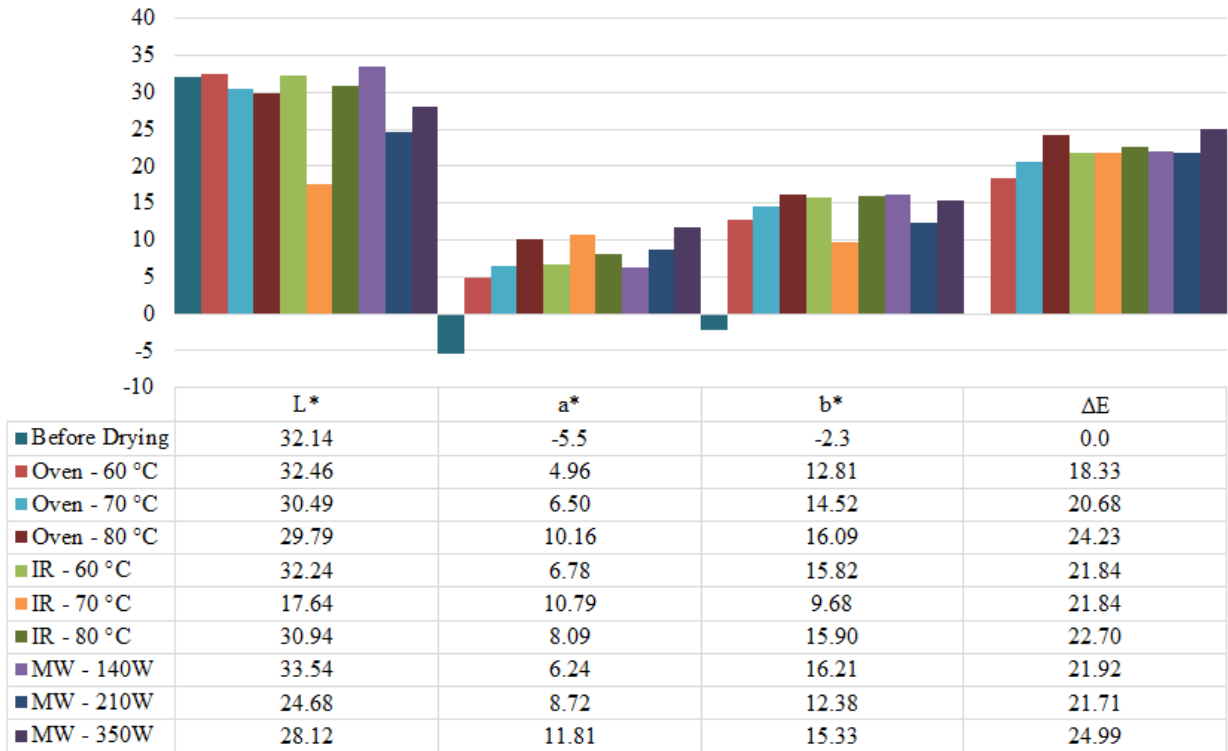**Figure 5.** D_{eff} and activation energy curves for oven [18], IR, and MW

Figure 6. Color values of oven [18], IR, and MW dried blanched crab meat

	L*	a*	b*	ΔE
■ Before Drying	32.14	-5.5	-2.3	0.0
■ Oven - 60 °C	32.46	4.96	12.81	18.33
■ Oven - 70 °C	30.49	6.50	14.52	20.68
■ Oven - 80 °C	29.79	10.16	16.09	24.23
■ IR - 60 °C	32.24	6.78	15.82	21.84
■ IR - 70 °C	17.64	10.79	9.68	21.84
■ IR - 80 °C	30.94	8.09	15.90	22.70
■ MW - 140W	33.54	6.24	16.21	21.92
■ MW - 210W	24.68	8.72	12.38	21.71
■ MW - 350W	28.12	11.81	15.33	24.99

When *ΔE* values were compared, it was seen that the least change occurred in the furnace, and the highest change was in MW. It appears that the increase in temperature and power levels causes an increase in *ΔE*.

CONCLUSION

The drying kinetics and statistical analyses of blanch pre-treated brown crab (*Cancer pagurus*) with IR and MW were studied and evaluated together with the previous oven study [18]. Drying times were obtained as an average of 210 minutes in an oven, 110 minutes in IR, and 11 minutes in MW. Based on the highest R^2 and lowest χ^2 and RMSE values among the 13 models tested in mathematical models, it was determined that the Aghbashlo model for the oven and the Alibas model for IR and MW had the highest compatibility. Effective moisture diffusion coefficients are between 1.9×10^{-10} - 2.62×10^{-10} m^2/s in the oven, 3.27×10^{-10} - 7.08×10^{-10} m^2/s in the IR, and 2.83×10^{-9} - 9.76×10^{-9} m^2/s in the MW. It was determined that the effective diffusion coefficient increased with the increase in temperature and power. In the calculation of the activation energy transferred from the drying device to the crab meat, 15.74 kJ/mol for the oven, 37.55 kJ/mol for IR, and 72.719 kW/kg for MW were obtained. Accordingly, it was determined that the method with a higher activation energy value resulted in shorter drying times. In color analysis studies, it was found that the total color change was at the highest for MW and lowest for the oven. Accordingly, in a color-based evaluation, it can be said that the oven is closer to the blanched crab meat. When all outputs are evaluated, it can be said that drying with MW provides much better performance compared to other methods in terms of drying time, energy consumption, and effective diffusion.

REFERENCES

1. H. Ervik, S. Lierhagen, A. G. Asimakopoulos, *Science of The Total Environment*, **716**, 135175 (2020), https://doi.org/10.1016/j.scitotenv.2019.135175.
2. A. L. Maulvault, P. Anacleto, H. M. Lourenço, M. L. Carvalho, M. L. Nunes, A. Marques, *Food Chemistry*, **133**(2), 277 (2012). https://doi.org/10.1016/j.foodchem.2012.01.023
3. FAO (n.d.) http://www.fao.org/fishery/species/2627/en
4. IFCA (n.d.). Brown edible crab. https://www.nw-ifca.gov.uk/managing-sustainable-fisheries/brown-edible-crab/
5. S. Condón-Abanto, C. Arroyo, I. Álvarez, N. Brunton, P. Whyte, J. Lyng, *Ultrasonics Sonochemistry*, **40**, 497 (2018). https://doi.org/10.1016/j.ultsonch.2017.07.044
6. J. B. Jethrow, E. E. Wisdom, *Saudi J. Eng. Technol.*, **7**(3), 165 (2022).
7. M. Radojčin, I. Pavkov, D. Bursać Kovačević, P. Putnik, A. Wiktor, Z. Stamenković, ... A. Gere, *Processes*, **9**(1), 132 (2021).
8. A. C. Cruz, R. P. F. Guiné, J. C. Gonçalves, *International Journal of Fruit Science*, **15**(1), 54 (2014). https://doi.org/10.1080/15538362.2014.931166
9. X. He, R. Lin, S. Cheng, S. Wang, L. Yuan, H. Wang, ... M. Tan, *Journal of Food Science*, **86**(6), 2499 (2021).
10. P. Jiang, W. Jin, Y. Liu, N. Sun, K. Zhu, Z. Bao, X. Dong, *Journal of Food Quality*, (2022).
11. S. Murali, D. A. Delfiya, K. S. Kumar, L. R. Kumar, S. E. Nilavan, P. R. Amulya, ... M. P. Samuel, *Journal of Aquatic Food Product Technology*, **30**(5), 561 (2021).
12. M. P. Nguyen, T. T. Ngo, T. D. Le, *Case Studies in Thermal Engineering*, **14**, 100465 (2019).
13. M. Kouhila, H. Moussaoui, H. Lamsyehe, Z. Tagnamas, Y. Bahammou, A. Idlimam, A. Lamharrar, *Renewable Energy*, **147**, 833 (2020).
14. A. S. Kipcak, İ. Doymaz, E. Moroydor-Derun, *Chemical Industry and Chemical Engineering Quarterly*, **25**(1), 1 (2019).
15. M. Lekrati, Z. H. Vezaz, *Biosciences, Biotechnology Research Asia*, **18**(3), 619 (2021).
16. Z. O. Ozyalcin, A. S. Kipcak, *Turkish Journal of Fisheries and Aquatic Sciences*, **21**(3), 135 (2021).
17. C. Ogbonnaya, M. I. Shaba, Effects of drying methods on proximate compositions of catfish (*Clarias gariepinus*), 2019.
18. M. Eren, O. Akkoc, Z. O. Ozyalcin, A. S. Kipcak, 6th International Conference on Advances in Mechanical Engineering, 20 - 22 October, Istanbul, Turkey, 2021, p. 1185.
19. S. Sevim, E. M. Derun, N. Tugrul, I. Doymaz, A. S. Kipcak, *J. Indian Chem. Soc.*, **96**, 1233 (2019)
20. C. Tunckal, İ. Doymaz, *Renewable Energy*, **150**, 918 (2020).
21. A. S. Kipcak, *Res. Chem. Intermed.*, **43**(3), 1429 (2017).
22. Z. O. Ozyalcin, A. S. Kipcak, *J. Aquat. Food Prod. Technol.*, **31**(2), 187 (2022). doi:10.1080/10498850.2021.2024634.
23. A. S. Kipcak, I. Doymaz, *International Journal of Fruit Science*, **20** (sup 3), S1222 (2020).
24. M. Ayriksa, A. Bahadir, A. Dağdeviren, K. Roshanaei, T. Coşkun, G. K. Ongun, M. Özkaymak, *Politeknik Dergisi*, **25** (3), 1217 (2022).

Calculating analysis of seasonal changes and degradation reactions of pesticides in surface waters feeding Süleymanpasa district, Tekirdag

C. Sayıklı Sımsek, Y. Yalcın Gurkan[*]

Tekirdag Namık Kemal University, Department of Chemistry, Tekirdag, Turkey

In this study, the possible reaction paths of 2,3,4,5,6-pentachlorotoluene, benzylbenzoate and demeton molecules with OH radicals were determined. Optimized geometries were drawn with Gauss View 5. Later, with the Gaussian 09 program, geometric optimization was made and the lowest energy states were found. Geometric structure analysis was done and bond lengths and bond angles were calculated. The purpose of this study is to determine the most likely way of interaction of 2,3,4,5,6-pentachlorotoluene, benzylbenzoate and demeton molecules with OH in gas phase and in aqueous medium. The effect of solvent water was studied, COSMO was used as the dissolution model which had a stabilizing effect in reducing the energy in the reactions. The molecule with the lowest energy has the most stable structure. Apart from these studies, the seasonal changes of the 3 pesticides mentioned in the water samples taken in 4 different seasons from the Naip Dam, which feeds the central neighborhoods of Süleymanpaşa district of Tekirdağ Province, were examined. These results will guide experimental studies and determine the fragmentation mechanism.

INTRODUCTION

Water is the basic building block for all living things in nature. The fact that three-quarters of the world is covered with water and that 75% of living things are made up of water clearly reveals the importance of water for life. While water consumption and need are constantly increasing, the importance of efficient use of water resources has become more evident due to the pollution of resources by external factors and droughts due to global warming. It has been reported that water consumption worldwide has doubled in recent years [1].

With the increase in population in recent years, the amount of need for nutrients has increased. Since the yield of food products has decreased due to reasons such as weeds and pests, there has been a need to take serious measures in the fight against this issue. Researches show that the loss of productivity in this way is equivalent to the 1-year food requirement of 150 million people [2]. For this reason, various methods are used to increase the durability of foodstuffs and productivity in agriculture, and chemical control in this regard is carried out with pesticides.

Especially in populated areas, water resources are polluted due to factors such as agricultural activities and industrialization [3]. Pesticides used in the fight against pests in agricultural areas are mixed with surface waters by wind, rain and drift. From past to present, premature deaths have occurred due to water pollution [4]. Pesticides, which are quite resistant to degradation by natural means, accumulate in nature and cause soil and water pollution. In this case, with the pollution of water resources, it causes a decrease in the number of water resources that can be used and negatively affects aquatic organisms [5, 6]. When used as a chemical weapon, it is very effective on the target creature. However, due to its accumulation, effects are also seen on non-target organisms [7, 8].

In recent years, pesticide accumulations in the USA and European Union countries have been closely monitored in agricultural activities and food products, and accumulation over a certain limit is not accepted. The self-cleaning period of the surface water source, whose authenticity is deteriorated by such deposits, is long enough to adversely affect living things.

In this study, computational analysis was used to assess seasonal changes of 3 pesticides determined as possible pollutants in surface waters. The priority environmental pesticides investigated were: 2,3,4,5,6-pentachlorotoluene, benzylbenzoate, benzo(a)fluorene. Possible reaction pathways of these pesticides with OH radicals were determined.

METHODOLOGY

The mathematical expression of energy derived from dihedral angles (atomic positions) of molecular atoms, cartesian coordinates, bond lengths and angles, atomic types and and interatomic bond arrangements depending on atomic radii and positions is called molecular modeling.

* To whom all correspondence should be sent:
E-mail: yyalcin@nku.edu.tr

All computational manipulations used to mimic or model the behavior of molecules fall within molecular modeling. Many computer programs are available for these models. As a result of solving the Schrödinger equation with different methods, different programs have emerged. Especially in the field of chemistry and in the pharmaceutical sector, computer software is widely used in areas such as new drug development.

In this study, the Gaussian 09W package program, which is a product of the Gaussian series of Gauss 09 programs, was used. Gaussian 09W is a very comprehensive program that includes semi-experimental molecular mechanics and *ab initio* methods. With the Gaussian 09W program, the energies of atoms and molecules can be calculated, geometric optimizations can be made and energy-dependent force constants, vibration frequencies and dipole moments can be calculated. The conformation analysis of the molecules of 2,3,4,5,6-pentachlorotoluene, benzylbenzoate and demeton, which should be monitored in the surface waters examined in this study, was performed with the previously explained molecular mechanical modeling method and the most durable conformer was determined. Gaussian 09W package program was used for molecular modeling and molecular mechanics calculations. Molecular orbital calculations of the most stable conformer found as a result of the molecular mechanics method were made by DFT/B3YLP/6-31G* methods. Gaussian 09W package program was used in all molecular orbital calculations.

RESULTS AND DISCUSSION

2,3,4,5,6-Pentachlorotoluene

The lowest energy and most durable structure of 2,3,4,5,6 pentachlorotoluene molecule is shown in Figure 1 according to the conformer analysis performed by the molecular mechanical method. Possible reaction pathways of 2,3,4,5,6 pentachlorotoluene were identified as C-Cl bond breaking and benzene ring breaking. The reaction sites were determined according to the Mulliken charge distribution of the molecule.
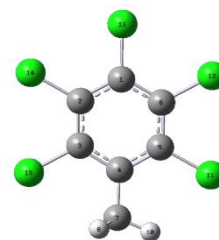
Figure 1. Optimized geometric structure of 2,3,4,5,6 pentachlorotoluene *via* DFT method. (grey: C; white: H; green: Cl).

As a result of DFT calculations, 2,3,4,5,6 pentachlorotoluene's total energy in the gas phase is -1612336.958 kcal/mol, enthalpy -1612336.365 kcal/mol, gibbs free energy -1612369.534 kcal/mol. In addition, the total energy in the water phase, enthalpy and Gibbs free energy, respectively: -1612338.889 kcal/mol, -1612338.296 kcal/mol, -1612371.556kcal/mol.

Table 1 Optimum geometric parameters of the 2,3,4,5,6-pentachlorotoluene

DFT Bond Lengths (Å)		DFT Bond Angles (°)	
12Cl-6C	1.76000	12Cl-6C-1C	120.00800
13Cl-1C	1.76000	13 Cl-1C-2C	119.99722
14 Cl-2C	1.76000	14Cl-2C-3C	120.01055
15 Cl-3C	1.76000	15Cl-3C-4C	119.99304

Table 2. Mulliken loads of 2.3.4.5.6-pentachlorotoluene

1	C	0.599646	10	C	-0.116954	19	C	-0.167128
2	O	-0.495734	11	H	0.136152	20	C	-0.167117
3	C	0.048045	12	H	0.137244	21	C	-0.129929
4	C	-0.159733	13	H	0.136130	22	H	0.133597
5	C	-0.151231	14	O	-0.476466	23	C	-0.129930
6	C	-0.137532	15	C	-0.126853	24	H	0.133599
7	H	0.160805	16	H	0.165318	25	C	-0.125980
8	C	-0.138939	17	H	0.165316	26	H	0.133822
9	H	0.162449	18	C	0.144383	27	H	0.133822

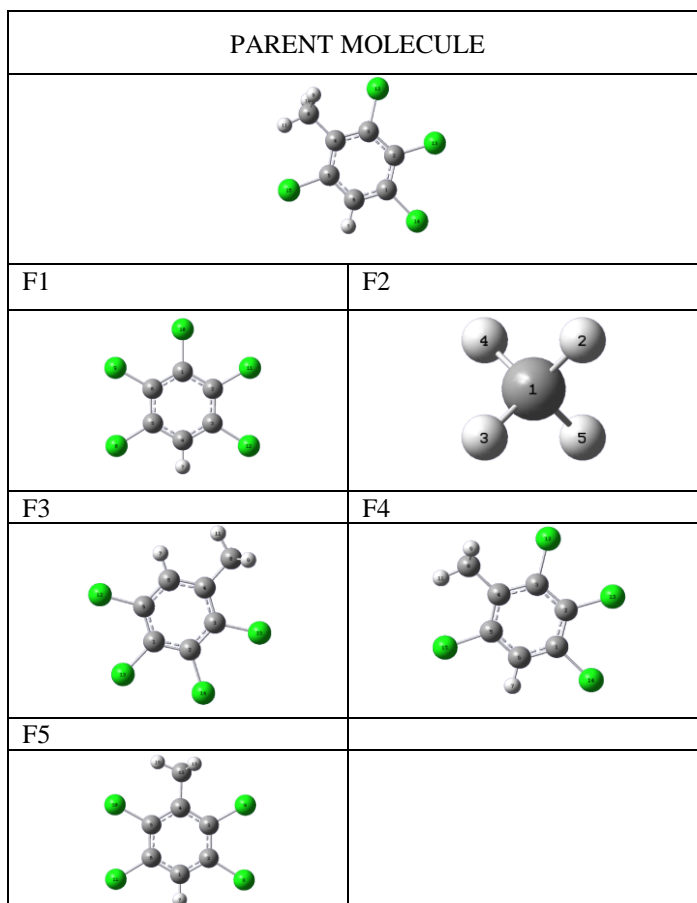| PARENT MOLECULE	
F1	F2
F3	F4
F5	

Figure 2. Possible reaction pathways of 2.3.4.5.6-pentachlorotoluene

Optimum parameters of 2,3,4,5,6-pentachlorotoluene, whose optimum shape is shown in Figure 1, are shown in Table 1. Parameters of pentachlorotoluene obtained by the DFT/B3LYP/6-31G(d) method which was found as the most appropriate method. are shown in Table 2.

Looking at the data in Table 3, fragment 1 (F1) of the possible decomposition pathways of 2.3.4.5.6-pentachlorotoluene has the lowest energy, in other words, it has the most stable structure. This fragment is formed by the detachment of the methyl molecule from the benzene ring to which the electronegative Cl atoms are attached.

In this study, possible reaction pathways were determined in the reaction between 2.3.4.5.6-pentachlorotoluene and the OH radical. The decomposition reaction requires energy. OH radicals are used to degrade pesticides in water.

As seen in the obtained fragments, 2.3.4.5.6-pentachlorotoluene was reduced to F5 and became harmless to the environment. Our aim was to break down the pesticides that enter the waters down to the smallest harmless substances and to remove their toxic effects from the waters. As can be seen from the results. this fragmentation occurred theoretically.

Benzylbenzoate

The durable geometric structure of benzylbenzoate obtained as a result of molecular modeling calculations and optimized by DFT/B3LYP/6-31G(d) methods is shown in Figure 3. As a result of DFT calculations, benzylbenzoate's total energy in the gas phase is -433573.210 kcal/mol, enthalpy -433572.617 kcal/mol, Gibbs free energy -433606.845 kcal/mol. In addition, the total energy in the water phase, enthalpy and Gibbs free energy are, respectively, -433577.433 kcal/mol, -433576.840 kcal/mol and -433612.461kcal/mol.
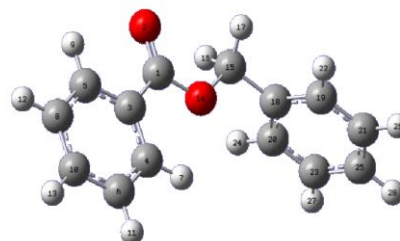
Figure 3. Optimized geometric structure of 2.3.4.5.6-pentachlorotoluene *via* DFT method (grey: C; white: H; red: O).

Table 3. Energy, enthalpy, Gibbs free energy of compounds

Compounds		Phase	ΔE Energy (kcal/mol)	ΔH Enthalpy (kcal/mol)	ΔG Gibbs Free Energy(kcal/mol)
2.3.4.5.6-pentachloro toluene		Gas	-1612336.958	-1612336.365	-1612369.534
		Water	-1612338.889	-1612338.296	-1612371.556
F1		Gas	-1587684.513	-1587683.921	-1587714.764
		Water	-1587686.412	-1587685.820	-1587716.718
F2		Gas	-25395.484	-5394.892	-25408.153
		Water	-25395.708	-25395.115	-25408.377
F3		Gas	-1323938.213	-1323937.620	-1323968.591
		Water	-1323940.550	-1323939.957	-1323970.956
F4		Gas	-1323939.252	-1323938.660	-1323969.831
	*	Water	-1321041.305	-1321040.713	-1321071.048
F5		Gas	-1323939.213	-1323938.620	-1323969.906
		Water	-1323941.132	-1323940.539	-1323971.874

PARENT MOLECULE

F1	F2

F3	F4

F5	
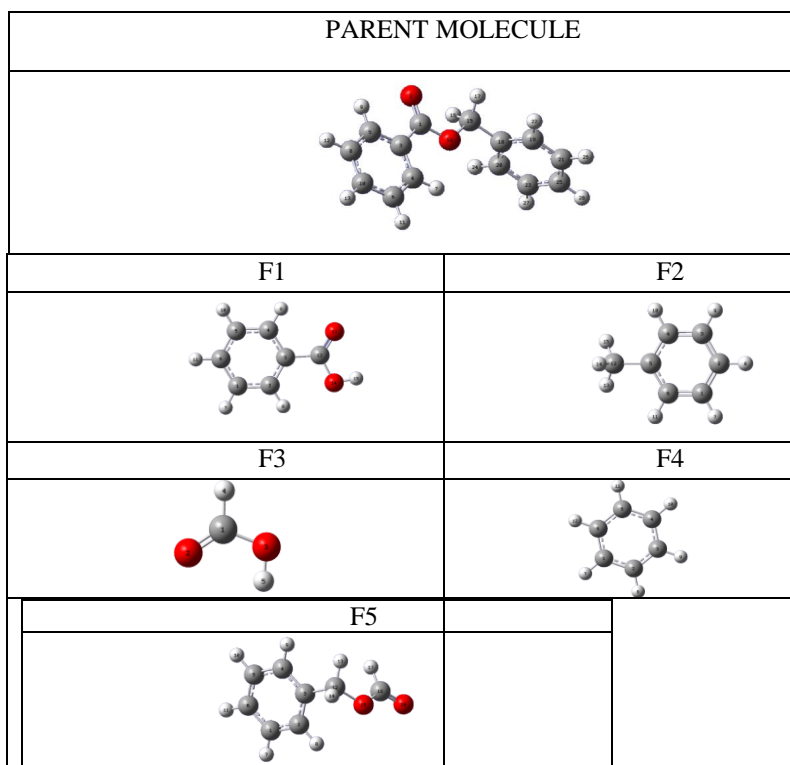
Figure 4. Possible reaction pathways of benzylbenzoate

Possible reaction pathways of benzylbenzoate were identified as breaking of C-C. C-O and aromatic ring bonds. The reaction sites were determined according to the Mulliken charge distribution of the molecule. According to the data in Table 3, the decomposition reaction occurred due to the electronegativity of O.

Table 4. Mulliken loads of benzylbenzoate

1	C	0.599646	10	C	-0.116954	19	C	-0.167128
2	O	-0.495734	11	H	0.136152	20	C	-0.167117
3	C	0.048045	12	H	0.137244	21	C	-0.129929
4	C	-0.159733	13	H	0.136130	22	H	0.133597
5	C	-0.151231	14	O	-0.476466	23	C	-0.129930
6	C	-0.137532	15	C	-0.126853	24	H	0.133599
7	H	0.160805	16	H	0.165318	25	C	-0.125980
8	C	-0.138939	17	H	0.165316	26	H	0.133822
9	H	0.162449	18	C	0.144383	27	H	0.133822

Looking at the data in Table 5, fragment 1 (F1) of the possible degradation ways of the benzylbenzoate molecule has the lowest energy, in other words, it has the most stable structure. This fragment is formed by the bond breaking of the C to which the electronegative O atom is attached.

In this study. possible reaction pathways were determined in the reaction between benzylbenzoate and OH radical. The decomposition reaction requires energy. OH radicals are used to degrade pesticides in water. As seen in the resulting fragments, benzylbenzoate was reduced to F5 and became environmentally safe. Our aim was to break down the pesticides that enter the waters down to the smallest harmless substances and to remove their toxic effects from the waters. As can be seen from the results, this fragmentation occurred theoretically.

Demeton

According to the conformer analysis made by the molecular mechanics method, the lowest energy and most durable structure of the demeton molecule is shown in Figure 5. The most durable geometric structure of demeton, obtained as a result of MM calculations, was optimized with DFT/B3LYP/6-31G(d) methods.

As a result of DFT calculations the total energy of demeton in the gas phase is -1053887.648 kcal/mol, its enthalpy is -1053887.056 kcal/mol and its Gibbs free energy is -1053933.845 kcal/mol. In addition. the total energy, enthalpy and Gibbs free energy in the water phase are, respectively, -1053897.525 kcal/mol, -1053896.932 kcal/mol and -1053943.972 kcal/mol. The geometric structure of demeton, which was optimized by DFT/B3LYP/6-

246

31G(d) methods, is shown in Figure 6 and its geometric parameters are shown in Table 6.
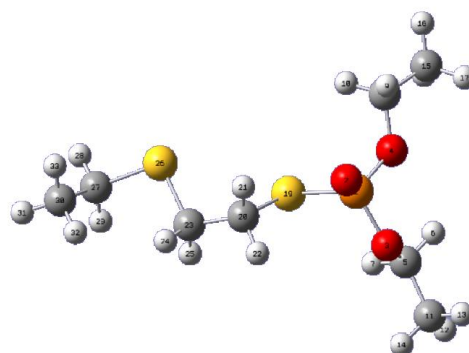
Figure 5. Optimized geometric structure of demeton *via* DFT method. (grey: C; white: H; red: O; yellow: S; orange: P).

Looking at the data in Table 7, fragment 4 (F4) among the possible fragmentation paths of demeton has the lowest energy, in other words, it has the most stable structure. This fragment is formed by bond breaking from the S atom.

In this study, possible reaction pathways were determined in the reaction between demeton and OH radical. The decomposition reaction requires energy. OH radicals are used to degrade pesticides in water. As seen in the resulting fragments, demeton has been downgraded to F5 and has become harmless to the environment. Our aim was to break down the pesticides that enter the waters down to the smallest harmless substances and to remove their toxic effects from the waters. As can be seen from the results, this fragmentation occurred theoretically.

CONCLUSIONS

In this study. the possible reaction paths between 2.3.4.5.6-pentachlorotoluene, benzylbenzoate and demeton molecules and the OH radicals were determined. Optimized geometries were drawn with Gauss View 5. Then, the lowest energy states were found by geometric optimization with the Gaussian 09 program. These results will guide experimental studies and determine the fragmentation mechanism.

These pesticides have been identified as primary endocrine disruptors in surface waters to be used as drinking water. Considering that classical biological enhancement methods are insufficient for the removal of these endocrine disrupting molecules, computational analysis of the degradation reactions of priority pesticides in surface waters, which will guide the application of alternative treatment methods to increase treatment efficiency was carried out.

In this work, besides theoretical studies, seasonal concentration differences of the aforementioned 4 pesticides in Naip dam were tried to be determined.

These experimental studies were carried out in the Çınar Çevre Laboratory and it was found that all 4 pesticides did not show seasonal changes (Figs. 7-9).

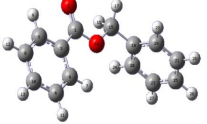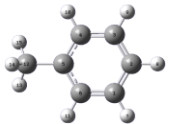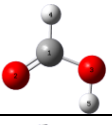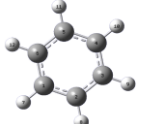**Table 5.** Energy, enthalpy, Gibbs free energy of compounds
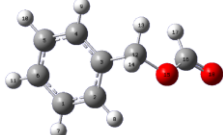
Compounds		Phase	ΔE Energy (kcal/mol)	ΔH Enthalpy (kcal/mol)	ΔG Gibbs Free Ennergy (kcal/mol)
Benzyl benzoate		Gas	-433573.210	-433572.617	-433606.845
		Water	-433577.433	-433576.840	-433612.461
F1		Gas	-263992.485	-263991.892	-264017.011
		Water	-263997.061	-263996.468	-264021.664
F2		Gas	-169174.769	-169174.176	-1691983.905
		Water	-170327.810	-170327.218	-170350.841
F3		Gas	-119049.983	-119049.391	-119067.075
		Water	-119054.193	-119053.601	-119071.294
F4		Gas	-145672.132	-145671.540	-145692.120
		Water	-145673.820	-145673.227	-145693.803
F5		Gas	-288626.528	-288625.935	-288654.281
		Water	-288632.525	-288631.932	-288660.627

Table 6. Optimum geometric parameters of demeton

DFT Bond Length (Å)		DFT Bond Angle (°)	
26S-23C	1.83980	27C-26S-23C	99.99185
19S-20C	1.85785	20C-19S-1P	98.08497
19S-1P	2.11478	2O-1P-4O	117.86752
1P-2O	1.48060	3O-1P-4O	101.00592
1P-4O	1.61568	2O-1P-3O	112.72439
1P-3O	1.60744	1P-3O-5C	122.86610
3O-5C	1.44850	1P-4O-8C	119.41604
8C-4O	1.45384	19S-1P-4O	101.99261

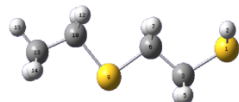| PARENT MOLECULE	
F1	F2
F3	F4
F5	
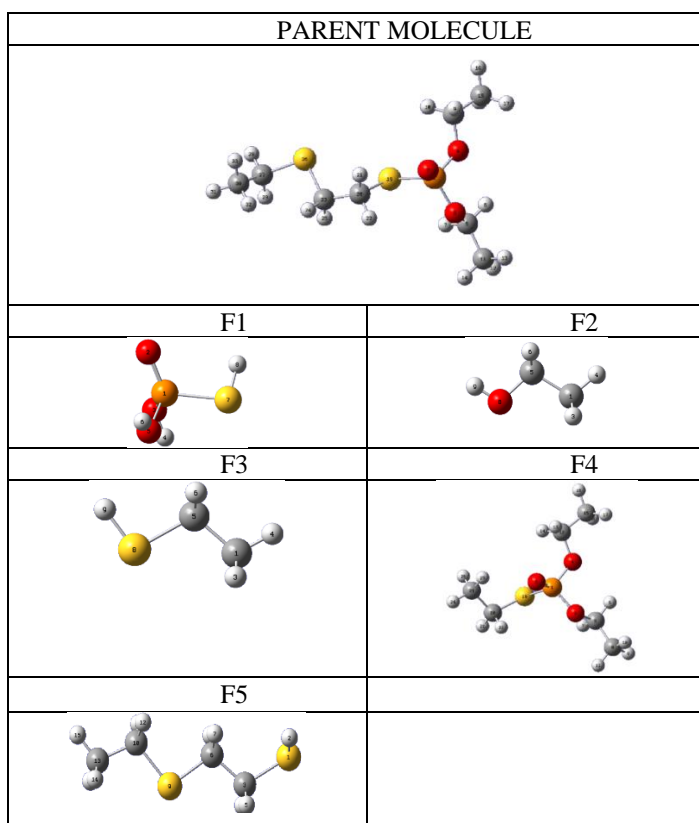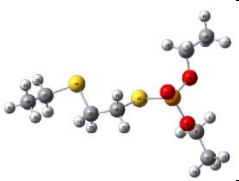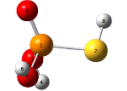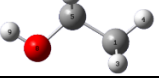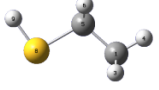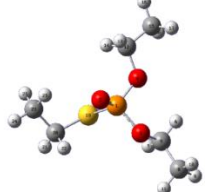
Figure 6. Possible reaction pathways of demeton

Table 7. Energy, enthalpy, Gibbs free energy of compounds

Compounds		Phase	ΔE Energy (kcal/mol)	ΔH Enthalpy (kcal/mol)	ΔG Gibbs Free Energy (kcal/mol)
Demeton		Gas	-1053887.648	-1053887.056	-1053933.845
		Water	-1053897.525	-1053896.932	-1053943.972
F1		Gas	-606820.745	-606820.153	-606844.561
		Water	-606830.41	-606829.817	-606853.893
F2		Gas	-97232.029	-97231.437	-97250.612
		Water	-97235.139	-97234.546	-972537.576
F3		Gas	-299907.151	-299906.558	-299926.956
		Water	-299909.648	-299909.056	-299929.512
F4		Gas	-754725.733	-754725.141	-754763.088
		Water	-754725.111	-754724.519	-754762.634
F5		Gas	-599071.678	-599071.085	-599099.515
		Water	-599075.779	-599075.187	-599103.911
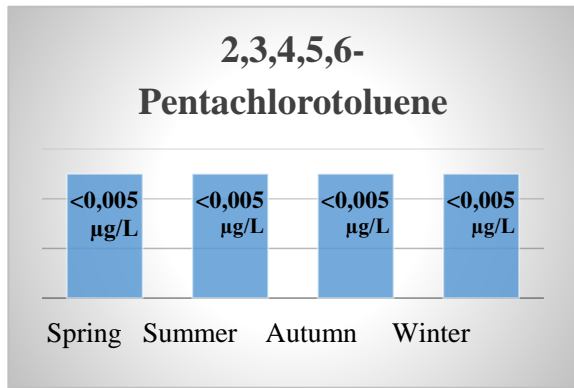
Figure 7 Concentration of 2.3.4.5.6-pentachlorotoluene in Naip Dam in four different seasons
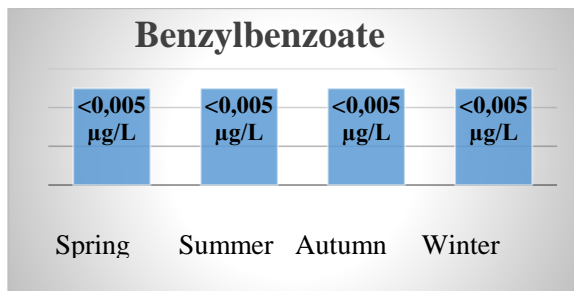
Figure 8 Concentration of benzylbenzoate in Naip dam in four different seasons
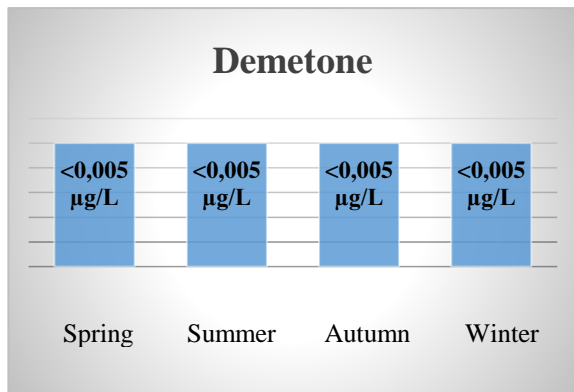
Figure 9. Concentration of demetone in Naip Dam in four different seasons

REFERENCES

1. Y. Zeyrek, *Industrialization and Environment in Thrace, Symposium Proceedings,* Çorlu, M.M.O. **183,** 548 (1996).
2. A. Akdoğan, Ü. Divrikli, L. Elç, *Academic Food,* **10**(1), 125 (2012).
3. A. Filibelij, *Journal of Water Poppulation Control,* **9**, 5 (1999).
4. H. H. Tok, T. Ü. Tekirdağ Ziraat Fakültesi, Tekirdağ, 1997.
5. S. Gedikli, Determination of Organochlorine Pesticide Residues in Drinking Waters of Kayseri Province, Master Thesis, Erciyes University Institute of Science, Kayseri, 2001.
6. Z. Korsak, J.A. Sikal, T. Wasiela, R. Swiercz, *Pol. J. Occup. Med*., **3**, 221 (1990).
7. M. T. Ahmed. M. M. Saad. S. S. Mabrouk. *Environment International. Apr.,* **24**, 665 (1998).
8. Z. Demircan, A Preliminary Study on Organochlorine Pesticide Residues in Marmara Sea Butt and Haddock, Master Thesis, İstanbul University Institute of Marine Sciences and Management, Istanbul, 1998.

Pervaporative desalination by phosphomolybdic acid/PVA hybrid membrane

D. Unlu

Bursa Technical University, Faculty of Engineering and Natural Sciences, Chemical Engineering Department, 16310, Bursa, Turkey

Water is indeed a precious natural resource and essential for all living organisms. Despite the Earth's abundant water resources, only a small portion is freshwater suitable for drinking and utilization. This accounts for approximately 0.3% of the Earth's total water capacity, equivalent to about 105 thousand km³. As a result, desalination has emerged as a viable solution to produce clean water by converting seawater, which is an almost limitless supply. Among the various desalination processes, pervaporation (PV) has attracted significant attention due to its numerous advantages, including low energy consumption, simplicity in operation, low cost, and high separation performance within a short period. The current study proposes the application of pervaporation for desalination purposes. Specifically, a hydrophilic polymer, polyvinyl alcohol (PVA), is chosen for membrane synthesis in the desalination process. Polymeric membranes are comparatively easier to produce and more cost-effective than other types of membranes. However, polymeric membranes tend to exhibit a swelling behavior, resulting in high flux and low selectivity. To address this challenge, recent advancements have led to the development of hybrid membranes, known as organic-inorganic composite membranes. In this study, phosphomolybdic acid (PMA) is chosen as an additive material. The effects of the amount of phosphomolybdic acid, salt concentration, and operation temperature on desalination performance are examined. Optimal operating conditions are determined, resulting in a salt rejection rate of 99.99% and a flux value of 2.45 kg/m² h. These findings demonstrate the potential of the proposed membrane system for efficient desalination applications.

Keywords: Desalination, membrane, pervaporation, phosphomolybdic acid, water

INTRODUCTION

The scarcity of freshwater resources and the increasing population, along with water contamination, pose significant threats to human livings sustainability. As a result, researchers have been actively searching for alternative sources of freshwater. In recent years, there has been a growing focus on obtaining freshwater from saline sources such as brackish water and seawater through a process known as desalination. Among the various technologies used in desalination, membrane technology has gained considerable attention due to its high separation efficiency, energy savings, environmental friendliness, ease of installation, and scalability [1].

Pervaporation, in particular, has emerged as a promising membrane technology for desalination. It offers cost efficiency and energy efficiency compared to traditional separation methods. Pervaporation can be operated under moderate process conditions, making it a viable option. It is also an environmentally friendly process and can be easily scaled up [2-4]. These advantages make pervaporation an attractive option in the field of desalination, providing a potential solution to the global water scarcity challenge.

The transport mechanism in the pervaporation process is defined with a solution–diffusion model. According to this model, the membrane surface is contacted with the feed solution, the components in the feed solution are sorbed by the membrane selectively, this selective component is transported through the membrane and the sample is obtained in vapor phase by executing vacuum on the downside of the membrane. The pervaporation process is conducted by a chemical potential gradient [5-7].

The selection of a membrane plays a crucial role in the pervaporation process, and in recent years, hybrid membranes have been increasingly utilized to improve membrane properties [8, 9]. Hybrid membranes offer a smart approach to modify the membrane structure by incorporating both organic and inorganic phases. Typically, inorganic particles are dispersed within a polymeric matrix to create hybrid membranes. Commonly used inorganic fillers in hybrid membrane preparation include zeolites, silicas, metal oxides, heteropolyacids, carbon nanotubes, and graphene oxides. In the specific context of this study, phosphomolybdic acid is chosen as the inorganic filler material. Phosphomolybdic acid is classified as a heteropolyacid consisting of a heteroatom

---

* To whom all correspondence should be sent:
E-mail: derya.unlu@btu.edu.tr

surrounded by four oxygen atoms in a tetrahedral structure. The bridging and terminal oxygen atoms on the periphery of the structure can associate with water molecules to form hydrates, thereby potentially enhancing selectivity to water. This property makes phosphomolybdic acid an attractive choice for improving the performance of the hybrid membrane in terms of water separation and selectivity. By incorporating phosphomolybdic acid as an inorganic filler material in the hybrid membrane, the researchers aim to foster its unique chemical characteristics to enhance the desalination performance of the pervaporation process [10, 11].

The present study focuses on the synthesis and application of phosphomolybdic acid (PMA)-loaded polyvinyl alcohol (PVA) membrane for desalination using the pervaporation (PV) process. PVA has been widely used in pervaporation desalination due to its favorable properties. It is relatively easy to obtain PVA films, and they exhibit good hydrophilic properties, as well as chemical and mechanical resistance [12, 13]. The novelty of this study proceeds from the preparation and usage of PMA-incorporated PVA membranes specifically for pervaporative desalination. The membranes were characterized using techniques such as FTIR, TGA, and SEM. The effects of feed salt concentration, temperature, and PMA loading ratio on salt rejection and flux were investigated. This study contributes valuable insights for the development of high-performance PMA/PVA hybrid membranes in pervaporation-based desalination. By exploring the influence of various parameters on the membrane's desalination efficiency, it paves the way for further improvements in membrane design and performance in the field of desalination.

EXPERIMENTAL

Materials

In this study, the materials used for the membrane synthesis and experimental procedures were purchased from specific suppliers. Polyvinyl alcohol, phosphomolybdic acid, and glutaraldehyde were acquired from Sigma-Aldrich. Sodium chloride and acetone were obtained from Merck Chemicals.

Membrane preparation

5 wt.% of PVA was dissolved in deionized water to create a homogeneous polymeric membrane solution. A certain amount of PMA particles (ranging from 5 wt.% to 20 wt.%), based on the mass of the polymer, were added to the PVA solution. The PMA particles were mixed thoroughly with the PVA solution to ensure homogeneity and dispersion of the additive within the membrane material. The solution casting method, also known as the solvent evaporation method, was utilized for membrane fabrication. The PVA-PMA mixture was cast as a thin film onto a suitable surface. The cast membrane was then subjected to a drying process to remove the solvent (water in this case) and obtain a solid membrane structure. After drying, the membrane was crosslinked to improve its stability and mechanical properties. A 1 wt.% solution of glutaraldehyde was prepared in a 50% v/v aqueous acetone solution. The dried membrane was immersed in the glutaraldehyde solution for crosslinking.

Membrane characterization

In this study, the synthesized membranes were subjected to characterization using three techniques: FTIR, TGA, and SEM. These characterization methods provide valuable insights into the chemical structure, thermal stability, and structural morphology of the membranes.

FTIR analysis was performed to examine changes in the chemical structure of the PVA membrane as a result of the addition of PMA. FTIR allows for the identification of functional groups and chemical bonds, thus providing information on the molecular changes occurring in the membrane due to the presence of PMA.

TGA was employed to evaluate the thermal stability of the membranes. TGA measures the weight loss of membranes as a function of temperature. The thermal behavior of the membranes is analyzed, including factors such as decomposition temperature, degradation profile, and thermal stability, which are crucial for their application in desalination.

SEM was utilized to examine the structural morphology of the membranes at a microscopic level. SEM imaging helps visualize the dispersion of PMA particles within the PVA matrix and assess the interfacial interactions between the components, contributing to a better understanding of the membrane structure.

Pervaporative desalination experiments

Water desalination tests were performed in the pervaporation system which is represented in Fig. 1.

In the desalination setup, the hybrid membrane with an active surface area of 9.62 cm^2 was placed inside the membrane chamber. The volume of the membrane chamber was filled with NaCl-water solution.
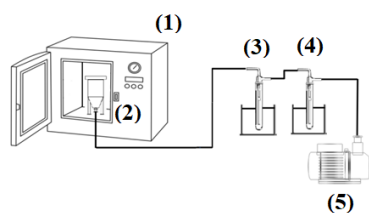
Fig. 1. Pervaporation system: (1) oven, (2) membrane chamber, (3-4) cold trap, (5) vacuum pump

The feed mixture in the membrane chamber was kept at atmospheric pressure and the downstream side of the membrane chamber was kept at 5 mbar. The permeate fresh water, which is the desalinated water passing through the membrane, was condensed using cold traps. The permeate samples were collected on an hourly basis. The collected samples were then subjected to analysis using the conductivity method. To evaluate the performance of the water desalination tests using the hybrid membrane, two metrics were used: flux (Eq. 1) and salt rejection (Eq. 2).

$$J = \frac{m}{A.t} \qquad (1)$$

$$R = \frac{C_f - C_p}{C_f} \times 100 \qquad (2)$$

J represents the flux, which is the rate of water permeation through the membrane. V is the volume of permeate water collected (in liters). A is the active surface area of the membrane (in square meters). t is the time taken to collect the permeate (in hours). R represents the salt rejection, which indicates the percentage of salt removed from the feed mixture. C_p is the concentration of salt in the permeate (in mg/L or ppm). C_f is the concentration of salt in the feed mixture (in mg/L or ppm).

RESULTS AND DISCUSSION

Characterization results

FTIR analysis. By using FTIR, it was possible to compare the chemical bonds in the membranes. The FTIR spectra of the membranes are displayed in Figure 2.

For the pristine PVA membrane, the OH group is observed at a characteristic band around 3278 cm^{-1}. The C-H (carbon-hydrogen) bonds are identified by the band at approximately 2924 cm^{-1}. The C=O (carbonyl) group is indicated by the band at around 1710 cm^{-1}. The presence of phosphomolybdic acid is revealed by the characteristic bands at 807, 957, 1079, 1420, 1653, 1740, 2926, and 2975 cm^{-1} in the FTIR spectra. The intensity of the -OH band around 3288 cm^{-1}, representing the hydroxyl bonds in the

PVA membrane, shows a reduced intensity compared to the pristine PVA film.
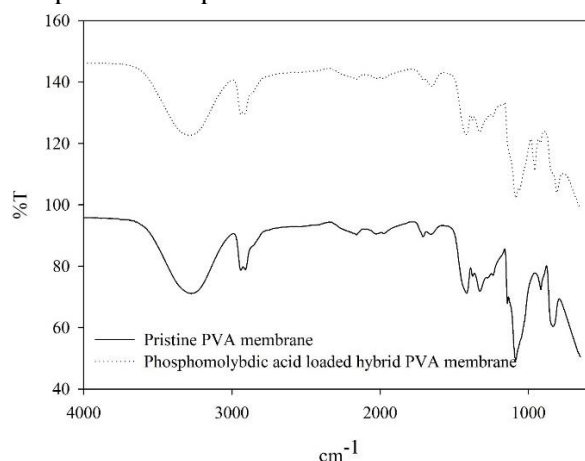

Fig. 2. FTIR spectra of the membranes: (a) pristine PVA membrane, (b) phosphomolybdic acid-loaded hybrid PVA membrane

The reduced intensity suggests an interaction between the phosphomolybdic acid and the hydroxyl bonds in the PVA membrane through various possible interactions, such as (Mo-Ot), (Mo-Oc-Mo), and (Mo-Oe-Mo) [14-16]. These observations indicate that the hybrid membrane with phosphomolybdic acid exhibits modifications and new chemical bonds compared to the pristine PVA film. The presence of phosphomolybdic acid in the hybrid membrane introduces additional functional groups and potentially influences the membrane's properties and performance in the desalination process.

TGA analysis. The thermal stability of the film was tested by TGA. Figure 3 shows the TGA curves of the membrane. The TGA of the hybrid membrane loaded with phosphomolybdic acid showed mass loss between 180 and 200°C. The mass loss occurring in this temperature range is attributed to the evaporation of water molecules. From 250 to 420∘C, the mass loss in this temperature range is likely due to the decomposition or oxidation of side chains and main chains present in the hybrid membrane. This indicates that the membrane undergoes chemical changes or degradation under the influence of heat, resulting in the release of volatile components. The mass loss in the temperature range from 420 °C to 500 °C is associated with a chemical reaction involving phosphomolybdic acid. The reaction is described as $H_3PMo_{12}O_{40} \rightarrow (1/2) P_2O_5 + 12MoO_3 + (3/2)H_2O$ (Mo=W). This reaction indicates the decomposition of phosphomolybdic acid into various products such as phosphorus pentoxide (P_2O_5), molybdenum trioxide (MoO_3), and water (H_2O) [14, 15].
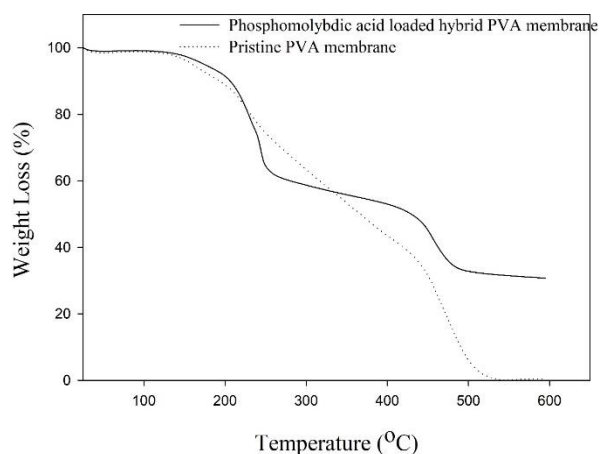
Fig. 3. TGA curve of membranes: (a) pristine PVA membrane (b) phosphomolybdic acid-loaded hybrid membrane

SEM analysis. The surface images of pristine and hybrid membranes are shown in Figure 4. While Fig. 4(a) shows the surface image of the pristine membrane, Fig. 4 (b) shows the surface image and SEM-EDX analysis of the hybrid membranes.

The surface image of the pristine PVA membrane (Fig. 4(a)) shows a dense structure. This suggests a compact and smooth surface without significant visible features or particles. The surface image of the hybrid membrane (Fig. 4(b)) reveals the presence of small white particles on the surface of the membrane. These particles are identified as phosphomolybdic acid, as mentioned. The particles appear to be evenly distributed throughout the membrane.
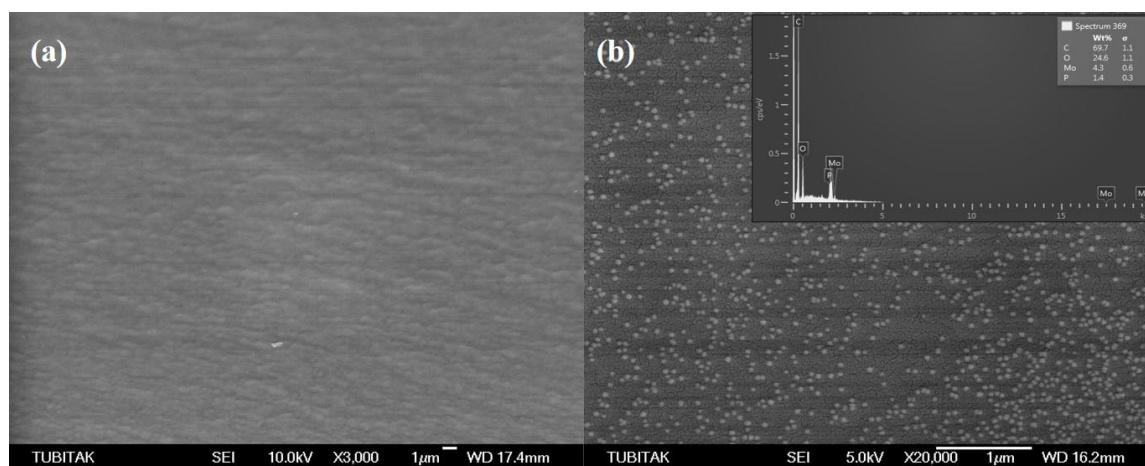
Fig. 4. SEM surface images of the membranes: (a) pristine PVA membrane (b) PMA/PVA hybrid membrane and SEM-EDX analysis

The SEM-EDX analysis conducted on the hybrid membrane (Fig. 4(b)) confirms the presence of phosphomolybdic acid. The elements phosphorus (P), molybdenum (Mo), and oxygen (O) are clearly visible in the EDX spectrum, indicating their presence in the membrane. This further confirms the successful incorporation of phosphomolybdic acid particles into the hybrid membrane.

Overall, the comparison of the surface images and SEM-EDX analysis between the pristine PVA membrane and hybrid membrane provides evidence of the modification and incorporation of phosphomolybdic acid particles onto the surface of the membrane. These observations indicate the successful synthesis and loading of phosphomolybdic acid in the hybrid membrane, which can potentially impact its properties and performance in various applications.

DESALINATION RESULTS

Effect of feed salt concentration

Figure 5 shows the effect of feed salt concentration on water flux and salt rejection values of hybrid films loaded with 5% PMA by weight.

As the NaCl concentration in the feed stream increases from 250 ppm to 1000 ppm, the water flux decreases from 5.98 to 2.87 kg/m^2 h. This suggests that the presence of higher salt concentration has a negative impact on the water permeability of the membrane. With an increase in the feed concentration of NaCl, the mole fraction of water decreases. This indicates that the proportion of water molecules in the feed stream decreases as the NaCl concentration increases.
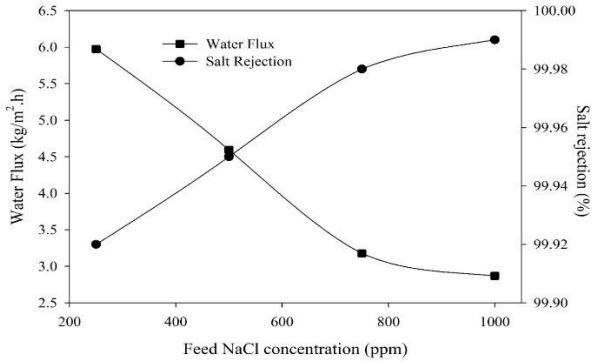
Fig. 5. Effect of feed salt concentration on salt rejection and flux

Despite the decrease in water flux, the salt rejection remains consistently high, around 99.99% and 99.92%. This demonstrates that the hybrid membrane loaded with 5 wt% of PMA effectively removes the salt ions from the feed stream, regardless of the increasing NaCl concentration. With a higher concentration of salt in the feed stream, water molecules form stronger interactions with salt ions, reducing the amount of free water molecules available for transport through the membrane. According to Fick's law, the decrease in the thermodynamic activity of water due to increased salt concentration reduces the solubility of water in the membrane. This reduction in solubility is a primary factor contributing to the decrease in water flux observed [17].

Effect of temperature

Fig. 6 presents the variations in flux and salt rejection *versus* operating temperature by the membrane loaded with 5 wt.% of phosphomolybdic acid and with constant NaCl concentration (250 ppm).
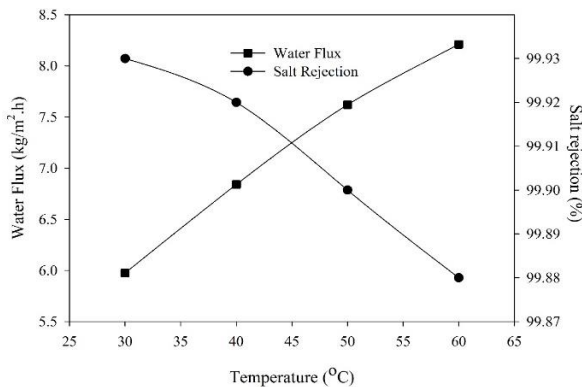

Fig. 6. Effect of temperature on salt rejection and flux

Increasing the temperature leads to an increase in water flux. This is because the vapor pressure of the feed mixture rises with temperature, creating a higher driving force for diffusion of components across the membrane. The constant vapor pressure

on the permeate side maintains a concentration gradient that further enhances the driving force and increases the water flux. The mobility of the PVA chains within the membrane increases as the process temperature rises. This increased mobility results in the creation of additional free volume in the membrane. The increase in membrane mobility and the associated increase in free volume have an impact on salt rejection. As the width of the polymer diffusion channel widens due to increased mobility, the dimensional separation effect becomes less pronounced. This means that dissolved ions with larger kinetic diameters can more easily pass through the membrane. Consequently, the salt rejection of the membrane decreases. Due to the reduced dimensional separation effect and increased mobility of the PVA chains, the flux increases while salt retention decreases. This allows for the transportation of dissolved ions through the membrane, resulting in increased water flux and lower salt rejection. In summary, the increase in water flux with temperature is attributed to the increased vapor pressure of the feed mixture. The mobility of PVA chains also increases with temperature, leading to additional free volume in the membrane. However, this increase in mobility negatively affects the dimensional separation effect, resulting in decreased salt rejection and increased water flux [18].

Effect of PMA loading ratio

Effect of PMA loading ratio on separation performance of membrane was analyzed by the water-NaCl mixture containing 250 ppm NaCl at 30°C. Fig. 7 shows the change in flux and salt rejection values by PMA ratio.
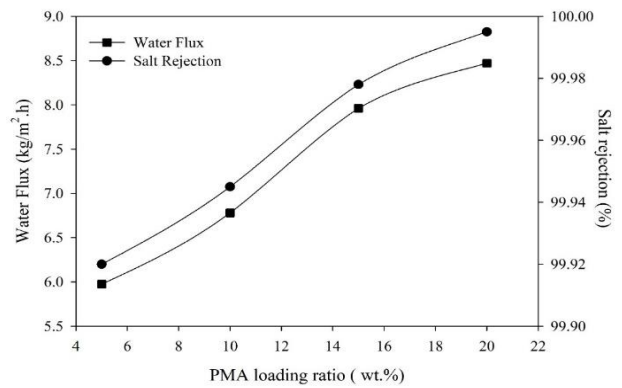

Fig. 7. Effect of PMA loading ratio on salt rejection and flux

According to Fig. 7, the addition of PMA to the membrane increases salt rejection. This indicates that PMA contributes to the membrane's ability to effectively remove salt ions from the feed solution.

254

PMA is described as a heteropolyacid with a specific molecular structure. It contains a central heteroatom surrounded by four oxygen atoms, forming a tetrahedral arrangement. Additionally, there are 12 octahedral moieties (MO_6 units) linked to each other by neighboring oxygen atoms, resulting in the presence of 24 bridging oxygen atoms. The peripheral oxygen atoms, both terminal and bridging, in the PMA structure are available to bind with water molecules, forming hydrates. These hydrates are believed to improve the selectivity of water transport through the membrane. The interaction between PMA and water molecules potentially contributes to enhanced water selectivity and salt rejection. A high loading ratio of PMA in the hybrid membrane results in a higher absorption of water molecules by the membrane. This increased hydration can lead to improved selectivity and enhanced flux values compared to a pristine PVA membrane [19]. Overall, the addition of PMA to the hybrid membrane is shown to increase salt rejection and water flux. The unique molecular structure of PMA allows for interactions with water molecules, forming hydrates, which potentially improve the selectivity of water transport. Moreover, higher loading ratios of PMA can result in greater water absorption and improved membrane performance compared to a pristine PVA membrane.

CONCLUSION

This study focuses on the development of a novel hybrid membrane for water desalination through pervaporation. The hybrid membrane is composed of PMA particles and PVA, and its performance was characterized and evaluated. The hydrophilic structure of PMA plays a significant role in enhancing water purification. This implies that the presence of PMA in the hybrid membrane improves its ability to remove salt and impurities from water during the desalination process. The membranes were characterized using FTIR, TGA, and SEM. These techniques are commonly used to analyze the chemical composition, thermal stability, and surface morphology of membranes. The study investigated the effects of feed salt concentration, PMA loading ratio, and process temperature on the performance of the hybrid membrane for desalination. A higher PMA loading ratio in the hybrid membrane resulted in increased salt rejection percentage and flux value. This indicates that a greater amount of PMA in the membrane improves its desalination performance. The optimum process temperature for the hybrid membrane was found to be 30°C. At temperatures higher than 30°C, the salt rejection value decreased,

suggesting that the membrane's performance in salt removal was less effective at elevated temperatures. The hybrid membrane, comprised of PMA particles and PVA, demonstrated excellent separation performance for water desalination. The highest salt rejection achieved was around 99.99%, while the permeate flux reached 8.47 kg/(m² h) under the conditions of 30°C process temperature and 20 wt.% PMA loading ratio. A hybrid phosphomolybdic acid/PVA membrane has shown a great separation performance for use in water desalination.

REFERENCES

1. A. Selim, A. T. Jozsef, E. Haaz, D. Fozer. A. Szanyi, N. Hegyesi, P. Mizsey, *Sep. Purif. Technol.*, **221**, 201 (2019).
2. B.G. Park, T. T. Tsotsis, *Chem. Eng. Process.*, **43**, 1171 (2004).
3. D. Unlu, N. D. Hilmioglu, *J. Chem. Technol. Biotechnol.*, **91**, 122 (2014).
4. S. Assabumrungrat, J. Phongpatthanapanich, P. Praserthdam, T. Tagawa, S. Goto, *Chem. Eng. J.,* **95**, 57 (2003).
5. B. Smitha, D. Suhanya, S. Sridhar, M. Ramakrishna, *J. Membr. Sci.*, **241**, 1 (2004).
6. J. G. Wijmans, R. W. Baker, *J. Membr. Sci.*, **107**, 1 (1995).
7. R. Y. M. Huang, Pervaporation Membrane Separation Processes, 1st edn., Elsevier Science Publishers BV, Amsterdam, 1991.
8. H. X. Liu, N. Wang, C. Zhao, S. Ji, J. R. Li, *Chin. J. Chem. Eng.,* **6**, 1 (2018).
9. P. Peng, B. Shi, Y. A. Lan, *Sep. Sci. Technol.,* **46**, 234 (2011).
10. A. H. Bhat, I. U. H. Bhat, H. P. S. A. Khalil, R. K. Mishra, M. Datt, A.K. Banthia, *J. Compos. Mater.,* **45**, 39 (2011).
11. V. T. Magalad, G.S. Gokavi, K. V. S. N. Raju, T. M. Aminabhavi, *J. Membr. Sci.,* **354**, 150 (2010).
12. M. Dmitrenko, A. Penkova, A. Kuzminova, A. Missyul, S. Ermakov, D. Roizard, *Polymers,* **10**, 571 (2018).
13. A. M. Sajjan, B. K. J. Kumar, A. A. Kittur, M. Y. Kariduraganavar, *J. Ind. Eng. Chem.*, **19**, 427 (2013).
14. G. Lakshminarayana, M. Nogami, *Electrochim. Acta.,* **54**, 4731 (2009).
15. K. S. Reddy, M. N. Prabhakar, K. M. Rao, D. M. Suhasini, V. N. M. Reddy, P. K. Babu, K. Sudhakar, A. C. Babu, M. C. S. Subha, K. C. Rao, *Indian J. Adv. Chem. Sci.,* **2**, 38 (2013).
16. E. N. Zilberman, F. Lerner, H. M. Joseph, M. Alon, *J. Appl. Polym. Sci.,* **48**, 435 (1993).
17. D. Unlu, *Water Air Soil Pollut.*, **234**, 96 (2023).
18. D. A. R. O. Da Silva, L. C. B. Zuge, A. de Paula Scheer, *Sep. Purif. Technol.*, **247**, 116852 (2020).
19. V. T. Magalad, G. S. Gokavi, K. V. S. N. Raju, T. M. Aminabhavi, *J. Membr. Sci.,* **354**, 150 (2010).

The effect of ultrasound pretreatment on oven and vacuum oven drying kinetics of blueberries

Z. Emin Taşçı, Ekin Kıpçak[*]

Department of Chemical Engineering, Faculty of Chemical and Metallurgical Engineering, Yildiz Technical University, Davutpasa Campus, Davutpasa Street No. 127, 34220, Esenler, Istanbul, Turkey

Blueberries (*Vaccanium corymbosum*) are small, round fruits having vital nutritional and functional properties. However, they are seasonal fruits with short shelf lives, a feature which hinders their desired commercialization. This condition necessitates the investigation of efficient drying methods for their extensive preservation. In literature, although there are numerous articles focusing on the antioxidant capacities and nutritional contents of blueberries, studies investigating their drying kinetics and the effects of various pretreatments on the process are still scarce. Therefore, in this study, the effect of ultrasound pretreatment on the oven drying and vacuum oven drying of blueberries is investigated. During the experiments, drying temperatures were selected as 60, 70 and 80°C. For both methods, experiments were conducted with 30 s and 60 s ultrasound pretreatment and the results were compared with the untreated sample data. The kinetic parameters of effective moisture diffusivities (D_{eff}) and activation energies (E_a) were calculated. Moreover, the drying curves were modeled with 14 mathematical modeling equations given in the literature. The drying times were seen to decrease by increasing the drying temperature and with the effect of vacuum. The lowest drying time (150 min), highest D_{eff} (8.41×10^{-10} m^2/s) and highest E_a (48.23 kJ/mol) were obtained at the vacuum oven drying experiment conducted without any pretreatments. Ultrasound pretreatment was seen to have an adverse effect on the drying of blueberries. The highest drying time (960 min), lowest D_{eff} (1.57×10^{-10} m^2/s) and lowest E_a (29.47 kJ/mol) were obtained at the oven drying experiment performed after 60 s of ultrasound pretreatment.

Keywords: Blueberries, oven drying, vacuum oven drying, ultrasonic pretreatment, effective moisture diffusivity, activation energy.

INTRODUCTION

In the recent years, the significance of berries has substantially increased due to their taste, phytonutrients and health benefits. Among the most salient ones are blueberries, which are known as the second most consumed kind of berry after strawberries. Blueberries (*Vaccinium corymbosum*) are small, round fruits with dark purple color and a sweet-sour taste [1]. They are mostly cultivated in America, with the United States being the largest producer, and in Europe [2].

Blueberries are excellent sources of vitamins, minerals, phenolic acids, anthocyanins, proanthocyanidins, flavonoids and dietary fibers. They are considered as one of the richest fruits in vitamin C and antioxidants. Consequently, they have protective properties against many diseases like Alzheimer's disease, muscular degeneration, cardiovascular and urinary diseases, vision problems, diabetes, cancer, as well as aging [1-3]. However, blueberries have a limited seasonal availability. They are prone to mechanical damage due to their tender structure, and they are easily perishable [1, 3, 4]. Therefore, various food processing technologies are employed to enhance their preservation and consequently, their shelf lives.

Drying is extensively used to preserve food products, especially fruits. Drying is the reduction of the water content present in food products with the purpose to prevent harmful microbial and physicochemical reactions, while inhibiting enzymatic activities. It is of great importance in the field of food science, as it offers numerous advantages. For instance, drying provides longer shelf lives, while decreasing the costs of packaging, storage and transportation due to reduced weight and volume. Furthermore, dried fruits are excellent options for new alternative product patterns with maintained, or even enhanced nutritional values, and can be used as additives in various other food products [5-7].

Among the traditional methods employed for drying, oven drying offers the most simple and easy application. Oven drying provides a faster, more hygienic and homogeneous drying than sun or solar drying, methods of which can also be stated among the traditional drying procedures. It provides a more flexible process with a high throughput. Moreover, installation, maintenance and repair costs are lower for oven drying [8, 9]. Sometimes, oven drying is assisted with vacuum. Vacuum drying is a process suitable for the drying of food products which are

---

* To whom all correspondence should be sent:
E-mail: eyildir@yildiz.edu.tr

sensitive to oxygen and heat [1]. The use of vacuum in drying protects the food products against oxidation and preserves their nutritional values, tastes, textures and colors. Moreover, it provides a shorted drying time and higher energy efficiency [1, 7, 10]. However, drying is a time and energy consuming process. Therefore, additional measures are investigated to optimize its use. The application of pretreatment processes can be stated among these measures. Pretreatments shorten the drying time, reduce the energy consumption and preserve the quality of food products [6, 11]. One of these trending pretreatment methods is the ultrasound pretreatment, which is reported to have a great potential in decreasing the processing time and increasing the quality of the dried fruits. In fact, ultrasonic energy applications have been a topic of interest for the last four decades. Ultrasound is defined as a sound frequency in the range above 16 KHz, which is greater than the range above the threshold of the human ear [5]. When ultrasound is applied in a liquid, the ultrasound waves cause alternating expansions and compressions. In the literature, this is usually explained by the repeated squeeze and release of a sponge (so called sponge effect) [5, 11-14]. During these rapid expansions and compressions, bubbles are formed and collapsed with varying intensities, which is considered as the main trigger for cellular disruption. Because of the resulting air pressure disturbances, cavitation is also responsible for the formation of some microscopic channels in the fruits that enhances moisture removal by reducing the diffusion boundary layer and increasing the convective mass transfer in the fruit [5-7, 13]. In short, the ultrasonic waves improve mass transfer through the cavitation effect, which provides easier moisture transport.

Ultrasonic pretreatment is considered as a safe and environmentally benign operation. Other advantages of ultrasound pretreatment are not having the necessity of using mechanical agitation and high temperatures, as the process can easily be carried out at ambient conditions [5, 7]. Studies in literature, in which ultrasound pretreatment is employed in agro-products have been extensively reviewed in some articles [6, 15]. Nevertheless, Mothibe *et al*. [5] stated that ultrasound pretreatment shows varying effects on different fruit materials. The authors explained that while some fruits gain water during their exposure to ultrasound, others show loss of water. This is also mentioned in the work of Fernandes *et al.* [16]. As stated by the foresaid authors, the application of the ultrasound technology is still troublesome, especially in dense and less porous fruit and vegetables. Therefore, with

the aim of contributing to the obscurities in this field of investigation, in this study the effect of ultrasound pretreatment on the oven drying and vacuum oven drying of blueberries is investigated. During the experiments, the drying temperatures were selected as 60, 70 and 80°C. For both oven drying and vacuum oven drying, the experiments were conducted with 30 s and 60 s prior ultrasound pretreatment and the results were compared with the untreated dried sample data. The kinetic parameters of effective moisture diffusivities (D_{eff}) and activation energy (E_a) values were calculated. Moreover, the drying curves were modeled with the 14 most known mathematical modeling equations given in the literature.

EXPERIMENTAL

Sample preparation

The blueberries used in the experiments were imported from Peru and were retrieved from a local market in Istanbul, Turkey. Similar-sized blueberries, with approximately 1 cm radius were selected and horizontally cut into two parts in order to investigate the thin-layer diffusion. 5 g of blueberries were dried in each experiment. Prior to drying, the initial moisture contents (M_0) of the blueberries were determined through AOAC method [17], by drying the blueberries at a conventional hot air-drying oven (KH-45, Kenton, Guangzhou, China) at 105°C for 3 hours. Accordingly, the initial moisture content of the blueberries without any pretreatment was determined as 6.0388 kg water/kg dry matter and 85.79% on wet basis. On the other hand, for the blueberry samples that were subjected to 30 s and 60 s ultrasonic pretreatment, the initial moisture contents were determined as 6.1208 kg water/kg dry matter (85.96% on wet basis) and 6.1020 kg water/kg dry matter (85.92% on wet basis), respectively.

Experimental methods

The oven drying experiments were carried out at a Nüve EV-018 model oven (Nüve, Ankara, Turkey). The vacuum oven drying experiments were made on the same oven of Nüve EV-018, while vacuum assistance was supplied through a KNF N022AN.18 model vacuum pump (KNF, Freiburg, Germany). The pressure inside the oven was measured as 0.3 atm during the experiments. The ultrasonic pretreatments prior to drying experiments were performed by using an ultrasonic bath which had an accuracy of 1°C and 120 W ultrasonic power (Isolab, Escau, Germany).

In order to calculate the kinetic parameters, the drying experiments were performed at 60, 70 and

80°C. Blueberry samples were weighed to determine their moisture contents in every 15 minutes. Sample weights were measured by using a digital balance (AS 220.R2, Radwag, Radom, Poland), which had a weighing accuracy of 0.001 g. Two parallel experiments were conducted in each drying method and the drying process was stopped when the weights of the blueberry samples were reduced approximately to 5% of their initial moisture contents.

Drying curves

In order to obtain the drying curves, the moisture contents (M), drying rates (DR) and moisture ratios (MR) of the blueberries must be determined. These parameters were calculated by using Equations 1, 2 and 3 given below [18-20]:

$$M = \frac{m_w}{m_d} \qquad (1)$$

In Equation 1, M is the moisture content (kg water/kg dry matter), m_w is the water content of the blueberries (kg), and m_d is the dry matter content of the blueberries (kg).

$$DR = \frac{M_{t+dt} - M_t}{dt} \qquad (2)$$

In the abovementioned Equation 2, DR represents the drying rate (kg water/kg dry matter × min), t represents the drying time (min), M_t is the moisture content at any time t (kg water/kg dry matter) and M_{t+dt} is the moisture content at the time t+dt (kg water/kg dry matter).

$$MR = \frac{M_t - M_e}{M_0 - M_e} \qquad (3)$$

In Equation 3, MR is the moisture ratio (dimensionless), M_0, M_t and M_e are the moisture contents initially, at any time and at balance, respectively (kg water/kg dry matter). Since the moisture content at balance is very low when compared to the initial and instantaneous moisture contents, M_e is neglected in the calculations [18, 19].

Effective moisture diffusivity and activation energy calculations

In order to describe the moisture diffusion in the drying of food products, Fick's second law of diffusion is used. In this study, several assumptions were made while solving this equation. Firstly, the shrinkage of the blueberries was neglected. Moreover, it was assumed that the mass transfer occurred symmetrically with respect to the center only by diffusion, and the diffusivity was accepted as constant. In regard to the aforementioned assumptions, Fick's second law for a thin layer with a thickness of 2L is transformed to Equation 4 [19, 21]:

$$MR = \frac{8}{\pi^2} \sum_{n=1}^{\infty} \frac{1}{(2n+1)^2} \exp\left(-\frac{(2n+1)^2 \pi^2 D_{eff} \times t}{4L^2}\right) \qquad (4)$$

In Equation 4, *n* is a positive integer, t is the time (s), D_{eff} is the effective moisture diffusivity (m²/s) and L is half of the thickness of the sample (m). For elongated drying times, n is assumed as 1 [19, 21]. Hence, Equation 4 can be simplified into Equation 5:

$$\ln(MR) = \ln\left(\frac{8}{\pi^2}\right) - \left(\pi^2 \frac{D_{eff} \times t}{4L^2}\right) \qquad (5)$$

By using Equation 5, D_{eff} can be calculated from the slope of the ln(MR) *versus* t plot. Once D_{eff} is calculated, its relation with temperature can be given through Arrhenius equation given below as Equation 6 [19, 22]:

$$D_{eff} = D_o \exp\left(-\frac{E_a}{R \times (T+273.15)}\right) \qquad (6)$$

Here, D_0 is is the pre-exponential factor (m²/s), E_a is the activation energy (kJ/mol), R is the universal gas constant (kJ/mol × K) and T is the drying temperature (°C). Thus, E_a can be calculated from the slope of the plot of ln(D_{eff}) *versus* 1/T graph. Activation energy is an important parameter in drying kinetics, as in regard to the energy provided by the drying devices to the product to be dried, higher activation energy will result in faster drying.

Mathematical modeling

For the mathematical modeling of the drying of blueberries, 14 abundantly used mathematical drying models present in the literature were considered. The models applied to the experimental data were Aghbaslo *et al.,* Alibas, Henderson & Pabis, Jena *et al.*, Lewis, Logarithmic, Midilli & Kucuk, Page, Parabolic, Peleg, Two-Term Exponential, Verma *et al.,* Wang & Singh and Weibull models, which are presented in Table 1.

For the models presented in Table 1, a, b, c and g are coefficients; n is the drying exponent specific to each equation; k, k_1 and k_2 are drying coefficients and t is the time in minutes. In the modeling process, Statistica software (Statsoft Inc., Tulsa, OK) was used for the nonlinear Levenberg-Marquardt procedure regressions. The suitability of the models to the drying data was determined with respect to the coefficient of determination (R^2), reduced chi-square (χ^2) and root mean square error (RMSE) values, which were obtained from Equations 7 to 9, given below [22, 23]. In these equations, N is the total number of experiments, z is the number of constants used in the model equations, MR_{exp} and MR_{pre} represent the experimental and predicted moisture ratios, respectively. The model that yielded the highest R^2, the lowest χ^2 and the lowest RMSE was selected as the most convenient model.

Table 1. Mathematical drying models applied to the experimental data [18, 19].

Model Name	Model Equation
Aghbaslo *et al.*	$MR = \exp(-k_1 t / (1 + k_2 t))$
Alibas	$MR = a \times \exp((-kt^n) + bt) + g$
Henderson & Pabis	$MR = a \times \exp(-kt)$
Jena *et al.*	$MR = a \times \exp(-kt + b\sqrt{t}) + c$
Lewis	$MR = \exp(-kt)$
Logarithmic	$MR = a \times \exp(-kt) + c$
Midilli & Kucuk	$MR = a \times \exp(-kt^n) + bt$
Page	$MR = \exp(-kt^n)$
Parabolic	$MR = a + bt + ct^2$
Peleg	$MR = a + t/(k_1 + k_2 t)$
Two-Term Exponential	$MR = a \times \exp(-kt) + (1-a) \times \exp(-kat)$
Verma *et al.*	$MR = a \times \exp(-kt) + (1 - a) \times \exp(-gt)$
Wang & Singh	$MR = 1 + at + bt^2$
Weibull	$MR = a - b \times \exp(-(kt)^n)$

$$R^2 = 1 - \frac{\sum_{i=1}^{N}(MR_{exp,i} - MR_{pre,i})^2}{\sum_{i=1}^{N}\left(MR_{exp,i} - \left(\frac{1}{n}\right)MR_{exp,i}\right)^2} \tag{7}$$

$$\chi^2 = \frac{\sum_{i=1}^{N}(MR_{exp,i} - MR_{pre,i})^2}{N - z} \tag{8}$$

$$RMSE = \left(\frac{1}{N}\sum_{i=1}^{N}\left(MR_{exp,i} - MR_{pre,i}\right)^2\right)^{\frac{1}{2}} \tag{9}$$

RESULTS AND DISCUSSION

Drying curve results

Figure 1 presents the drying curves and the drying rate curves of blueberries for oven drying, without any pretreatment (Figure 1a), with 30 s ultrasound (US) pretreatment (Figure 1b) and 60 s US pretreatment (Figure 1c). Considering the moisture contents, for oven drying without any pretreatments, the initial moisture content of 6.0388 kg water/kg dry matter decreased to 0.4480, 0.3939 and 0.3858 kg water/kg dry matter for drying temperatures of 60°C, 70°C and 80°C, respectively. The drying times were obtained as 390, 270 and 195 min for the aforementioned temperatures. For oven drying with prior 30 s US pretreatment, the initial moisture content of 6.1208 kg water/kg dry matter decreased to 0.4522, 0.3640 and 0.3350 kg water/kg dry matter for drying temperatures of 60°C, 70°C and 80°C, respectively. For this set of experiments, a remarkable increase in the drying times was observed. The drying times increased from 390 min to 630 min at 60°C, from 270 min to 300 min at 70°C, and from 195 min to 255 min at 80°C, when 30 s US pretreatment was employed. When the duration of the US pretreatment was further increased to 60 s, even more prolonged drying times

were encountered. The drying times were obtained as 960, 480 and 300 min for drying temperatures of 60°C, 70°C and 80°C, respectively.

Ultrasonic pretreatment on vacuum oven drying of blueberry samples gave similar results. Figure 2 presents the drying curves and the drying rate curves of blueberries for oven drying, without any pretreatment (Figure 2a), with 30 s US pretreatment (Figure 2b) and 60 s US pretreatment (Figure 2c). Nevertheless, the prominent impact of vacuum assistance on the drying durations is incontrovertible. During vacuum oven drying without any pretreatments, the drying times were 345 min, 210 min and 150 min at 60°C, 70°C and 80°C, respectively. Likewise, in the oven drying experiments, ultrasonic pretreatments resulted in an increase in drying times, though their effects were less distinct. The drying times increased from 345 min to 375 min at 60°C, from 210 min to 255 min at 70°C, and from 150 min to 180 min at 80°C, when 30 s US pretreatment was employed. For 60 s US pretreatment on the other hand, the drying times were obtained as 390, 270 and 180 min for drying temperatures of 60°C, 70°C and 80°C, respectively.

Drying kinetics results

As it was elaborately given in the Experimental section, D_{eff} values were calculated by using Equation 5 from the slope of ln(MR) *versus* drying time plots. The obtained equations from these plots are given in Equations 10 to 27 below. In these equations, oven drying is designated with the initials OD and vacuum oven drying is designated with the initials VOD, respectively.
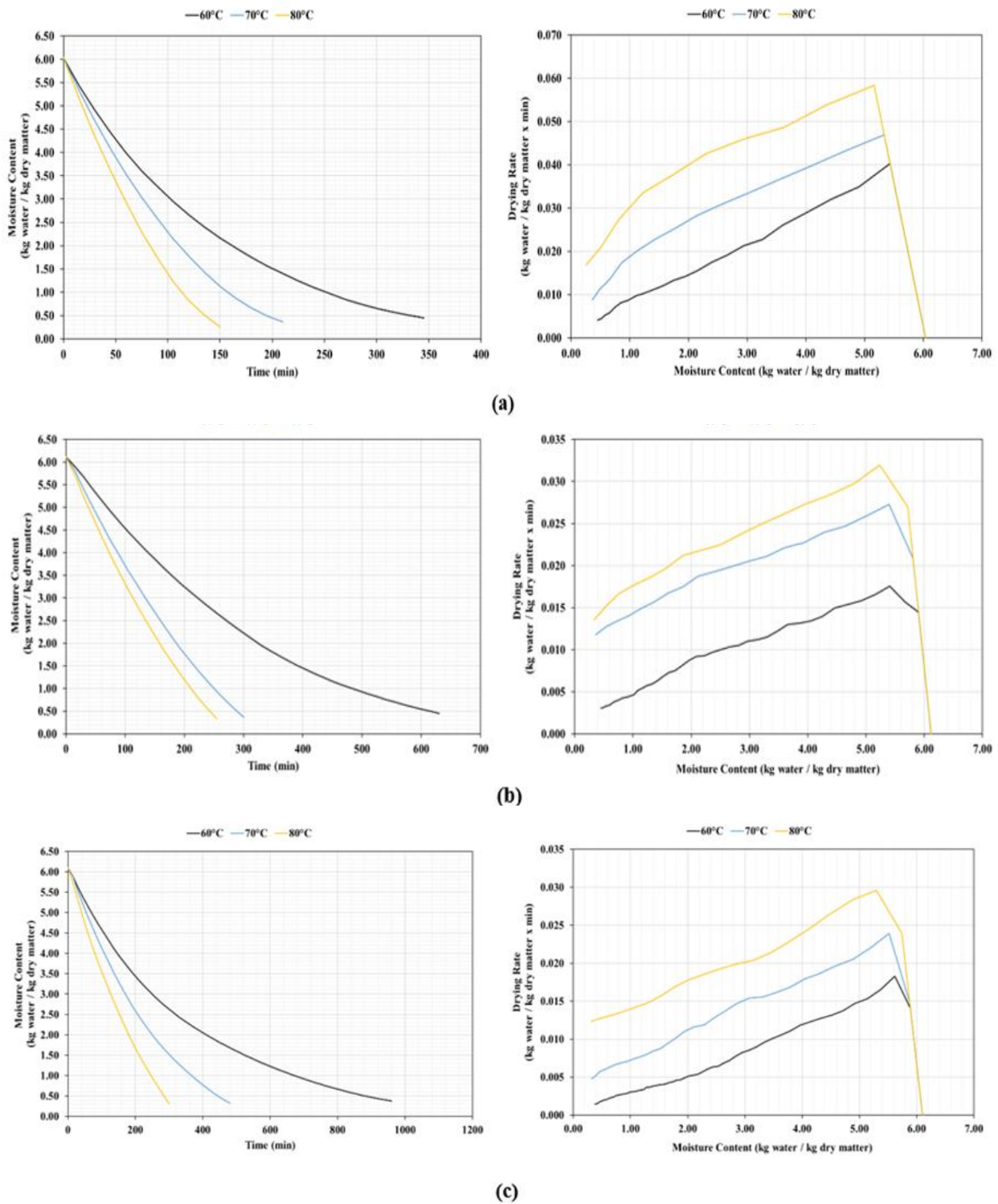
Figure 1. Drying curves (on the left) and drying rate curves (on the right) of blueberries for oven drying (a): without any pretreatment, (b): 30 s US pretreatment, (c): 60 s US pretreatment.
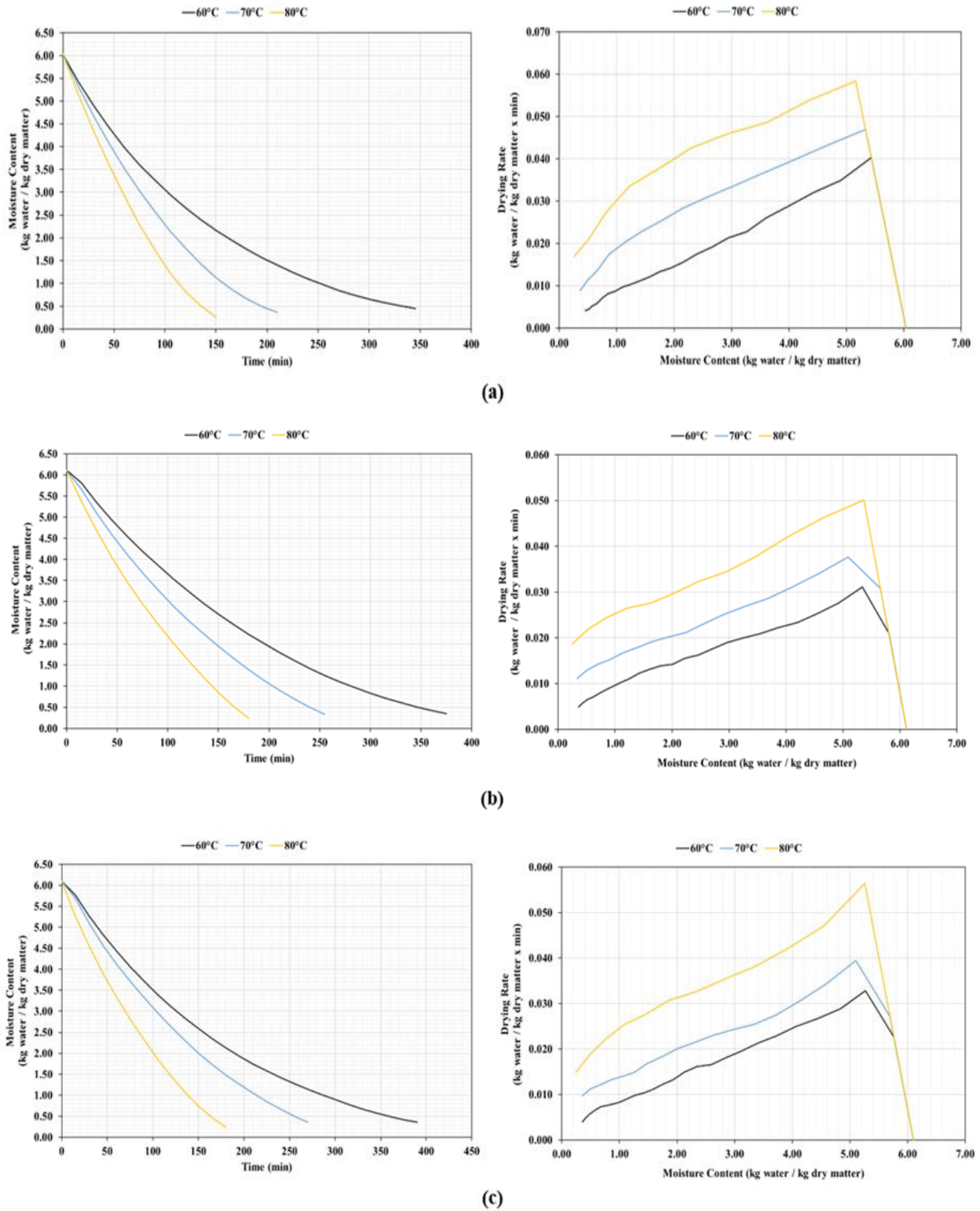
Figure 2. The drying curves (on the left) and the drying rate curves (on the right) of blueberries for vacuum oven drying (a): without any pretreatment, (b): 30 s US pretreatment, (c): 60 s US pretreatment

$$\text{OD, no US (60°C)} \quad \rightarrow \quad \ln(MR) = -0.000108t + 0.127915 \quad (R^2 = 0.989875) \tag{10}$$

$$\text{OD, no US (70°C)} \quad \rightarrow \quad \ln(MR) = -0.000162t + 0.208640 \quad (R^2 = 0.973694) \tag{11}$$

$$\text{OD, no US (80°C)} \quad \rightarrow \quad \ln(MR) = -0.000214t + 0.255830 \quad (R^2 = 0.936406) \tag{12}$$

$$\text{OD, 30 s US (60°C)} \quad \rightarrow \quad \ln(MR) = -0.000068t + 0.138591 \quad (R^2 = 0.992120) \tag{13}$$

$$\text{OD, 30 s US (70°C)} \quad \rightarrow \quad \ln(MR) = -0.000142t + 0.269506 \quad (R^2 = 0.941314) \tag{14}$$

$$\text{OD, 30 s US (80°C)} \quad \rightarrow \quad \ln(MR) = -0.000171t + 0.280785 \quad (R^2 = 0.934234) \tag{15}$$

$$\text{OD, 60 s US (60°C)} \quad \rightarrow \quad \ln(MR) = -0.000046t + 0.012590 \quad (R^2 = 0.997188) \tag{16}$$

$$\text{OD, 60 s US (70°C)} \quad \rightarrow \quad \ln(MR) = -0.000096t + 0.201783 \quad (R^2 = 0.975189) \tag{17}$$

$$\text{OD, 60 s US (80°C)} \quad \rightarrow \quad \ln(MR) = -0.000146t + 0.261697 \quad (R^2 = 0.937894) \tag{18}$$

$$\text{VOD, no US (60°C)} \quad \rightarrow \quad \ln(MR) = -0.000124t + 0.053750 \quad (R^2 = 0.997411) \tag{19}$$

$$\text{VOD, no US (70°C)} \quad \rightarrow \quad \ln(MR) = -0.000219t + 0.202322 \quad (R^2 = 0.977932) \tag{20}$$

$$\text{VOD, no US (80°C)} \quad \rightarrow \quad \ln(MR) = -0.000322t + 0.295706 \quad (R^2 = 0.946609) \tag{21}$$

$$\text{VOD, 30 s US (60°C)} \quad \rightarrow \quad \ln(MR) = -0.000123t + 0.197021 \quad (R^2 = 0.980831) \tag{22}$$

$$\text{VOD, 30 s US (70°C)} \quad \rightarrow \quad \ln(MR) = -0.000175t + 0.238284 \quad (R^2 = 0.955666) \tag{23}$$

$$\text{VOD, 30 s US (80°C)} \quad \rightarrow \quad \ln(MR) = -0.000265t + 0.295492 \quad (R^2 = 0.920488) \tag{24}$$

$$\text{VOD, 60 s US (60°C)} \quad \rightarrow \quad \ln(MR) = -0.000118t + 0.146794 \quad (R^2 = 0.988373) \tag{25}$$

$$\text{VOD, 60 s US (70°C)} \quad \rightarrow \quad \ln(MR) = -0.000165t + 0.215812 \quad (R^2 = 0.967004) \tag{26}$$

$$\text{VOD, 60 s US (80°C)} \quad \rightarrow \quad \ln(MR) = -0.000273t + 0.281198 \quad (R^2 = 0.939041) \tag{27}$$

Table 2. Calculated D_{eff} and E_a values for the drying of blueberries

Method	D_{eff} (m²/s)	E_a (kJ/mol)
Oven Drying No US, 60°C	2.74×10^{-10}	
Oven Drying No US, 70°C	4.10×10^{-10}	33.50
Oven Drying No US, 80°C	5.42×10^{-10}	
Oven Drying 30 s US, 60°C	2.01×10^{-10}	
Oven Drying 30 s US, 70°C	2.91×10^{-10}	31.56
Oven Drying 30 s US, 80°C	3.83×10^{-10}	
Oven Drying 60 s US, 60°C	1.57×10^{-10}	
Oven Drying 60 s US, 70°C	2.15×10^{-10}	29.47
Oven Drying 60 s US, 80°C	2.86×10^{-10}	
Vacuum Oven Drying No US, 60°C	3.14×10^{-10}	
Vacuum Oven Drying No US, 70°C	5.55×10^{-10}	48.23
Vacuum Oven Drying No US, 80°C	8.41×10^{-10}	
Vacuum Oven Drying 30 s US, 60°C	3.12×10^{-10}	
Vacuum Oven Drying 30 s US, 70°C	4.43×10^{-10}	37.50
Vacuum Oven Drying 30 s US, 80°C	6.71×10^{-10}	
Vacuum Oven Drying 60 s US, 60°C	2.99×10^{-10}	
Vacuum Oven Drying 60 s US, 70°C	4.18×10^{-10}	36.98
Vacuum Oven Drying 60 s US, 80°C	6.37×10^{-10}	

With respect to the equations given above, the calculated D_{eff} and E_a values are presented in Table 2. As it can be seen from Table 2, the effective moisture diffusivity values increase with drying temperature and vacuum assistance. The application of ultrasonic pretreatment resulted in a decrease in both D_{eff} and E_a values. The longer ultrasonic pretreatment was employed, the greater decrease in the kinetic parameters was observed. In the literature, ultrasonic pretreatments on the drying of agro-products do not show a distinct influence in a certain way. As stated by Mothibe *et al.*, ultrasound

pretreatment shows varying effects on different fruit materials [5]. Though ultrasonic pretreatment shows a positive impact on the drying behavior of some food products, it has an adverse effect on others, similar to the results obtained from this study. For instance, in a study on the drying of melon tissues [11], it was reported that the fruit gained water as a result of ultrasonic pretreatment. Nowacka and Wedzik [13] analyzed the effect of ultrasound pretreatment on fresh and dried carrot slices in a convective dryer operated at 70°C. The authors stated that there was no reduction in the drying time

in the ultrasound-pretreated samples. Instead of expected shortening of the drying time, a small prolongation was observed for the time needed for achieving the desired moisture content. As for the effective moisture diffusivity, D_{eff}, the highest value was found for the untreated sample, just like the case in the present study. There was an 8-12% reduction observed for D_{eff} values calculated for ultrasound-pretreated samples. The authors observed structural changes and formation of microchannels during the pretreatment, which were reported not to cause an acceleration in the drying process.

Ozyalcin and Kipcak investigated the effect of ultrasonic pretreatment on the thin layer infrared drying characteristics of squid [14]. The authors found out that, without any pretreatment, the drying times were 277 min, 240 min and 150 min for drying temperatures of 60°C, 70°C and 80°C, respectively. When ultrasonic pretreatment was used, the aforementioned drying times were seen to increase to 315 min, 300 min and 190 min, respectively. Moreover, similar to the presented findings here, a reduction in the effective moisture diffusivities and activation energies were also observed when ultrasound pretreatment was employed. This was attributed to the swelling with water during the pretreatment. In another article, in which the oven and vacuum oven drying characteristics of *Loligo vulgaris* (European squid) was investigated, conformable findings were reached [10]. The drying times for oven drying without any pretreatment were found as 300, 210, and 180 minutes for the drying temperatures of 60°C, 70°C and 80°C, respectively. When ultrasound pretreatment was employed, these durations at the same drying temperatures increased to 315, 240, and 210 minutes, respectively. Also, when ultrasonic pretreatment was employed in oven drying, a decrease in the effective moisture diffusivities was also recorded. When vacuum was assisting the oven drying process, a significant decrease in drying times were observed. The authors stated that the vacuum effect on the drying process reduced the moisture content. After applying ultrasound pretreatment, the same drying times were recorded. There was a 26.4% increase in activation energy when vacuum oven drying process was employed, and a reduction in activation energies when there was a prior ultrasonic pretreatment [10].

Fernandes *et al.* observed a decrease in water diffusivity during the drying of mangoes, when ultrasonic pretreatment was used [16]. The decrease in the water diffusivity ranged from 9.3 to 29.4%. Moreover, mangoes without pretreatment required 168 min to dry, removing 90% of its initial moisture while 5 minutes of ultrasound pretreatment increased this duration to 221 min. The authors attributed this result to the fact that mangoes are dense and have more fibers than most fruits. This kind of tissue structure differs from that of other fruits and is less susceptible to the effects induced by ultrasound application.

Mathematical modeling results

The mathematical modeling results obtained for oven drying of blueberries, with and without pretreatments are presented in Table 3 and those for vacuum oven drying are presented in Table 4. The tables show the results for the three models having the highest average R^2, the lowest χ^2 and lowest RMSE values among the 14 models that have been considered.

In regard to Table 3, for oven drying, the model having the highest compatibility with the drying data was found to be Midilli & Kucuk model for all sets. Considering the oven drying experiments without any pretreatments, R^2 values of 0.999956, 0.999907 and 0.999974 were obtained for this model at 60, 70 and 80°C, respectively. For oven drying with 30 s ultrasonic pretreatment, R^2 values of 0.999962, 0.999982 and 0.999986 were obtained at the same temperatures. Oven drying with 60 s prior ultrasonic pretreatment yielded R^2 values of 0.999882, 0.999971 and 0.999969 at 60, 70 and 80°C, respectively.

For vacuum oven drying experiments without any pretreatment, as it can be seen from Table 4, the most compatible model was seen to be Aghbashlo *et al.*, with R^2 values of 0.999885, 0.999982 and 0.999953 at the selected drying temperatures. For vacuum oven drying experiments with 30 s and 60 s ultrasonic pretreatment, again Midilli & Kucuk model was the most suitable. This model showed R^2 values of 0.999947, 0.999970 and 0.999987 for 30 s ultrasound; and 0.999954, 0.999929 and 0.999899 for 60 s ultrasound at the drying temperatures of 60, 70 and 80°C, respectively.

Table 3. Statistical data for the best 3 mathematical models obtained for oven drying

	Oven Drying, No Pretreatment								
Model	Midilli & Kucuk			Aghbashlo *et al.*			Parabolic		
Coeff.	60°C	70°C	80°C	60°C	70°C	80°C	60°C	70°C	80°C
a	0.995396	0.993993	0.997970				0.986549	1.000218	0.999966
b	-0.000133	-0.000367	-0.001263				-0.004268	-0.005709	-0.006542
c							0.000005	0.000008	0.000009
k	0.003432	0.003320	0.004203						
n	1.073446	1.128176	1.068818						
k_1				0.004683	0.005588	0.006109			
k_2				-0.000726	-0.001632	-0.002726			
R^2	0.999956	0.999907	0.999974	0.999955	0.999989	0.999774	0.999692	0.999992	0.999994
χ^2	0.000008	0.000020	0.000006	0.000007	0.000002	0.000045	0.000053	0.000002	0.000001
RMSE	0.002584	0.003929	0.002116	0.002618	0.001340	0.006200	0.006852	0.001131	0.001006
	Oven Drying, 30 s US Pretreatment								
Model	Midilli & Kucuk			Parabolic			Wang & Singh		
Coeff.	60°C	70°C	80°C	60°C	70°C	80°C	60°C	70°C	80°C
a	0.997453	1.001313		0.996298	1.008536	1.005261	-0.002733	-0.004325	-0.005127
b	-0.000060	-0.000683		-0.002709	-0.004436	-0.005207	0.000002	0.000004	0.000006
c				0.000002	0.000004	0.000006			
k	0.001685	0.002335	1.000725						
n	1.113352	1.113716	-0.000871						
R^2	0.999962	0.999982	0.999986	0.999842	0.999964	0.999978	0.999831	0.999905	0.999956
χ^2	0.000076	0.000004	0.000003	0.000001	0.000007	0.000004	0.000001	0.000018	0.000008
RMSE	0.008378	0.001714	0.001572	0.001134	0.002469	0.001932	0.001007	0.003979	0.002747
	Oven Drying, 60 s US Pretreatment								
Model	Midilli & Kucuk			Logarithmic			Aghbashlo *et al.*		
Coeff.	60°C	70°C	80°C	60°C	70°C	80°C	60°C	70°C	80°C
a	1.015031	1.005315	1.003840	0.989660	1.209125	1.552454			
b	-0.000034	-0.000166	-0.000711						
c				-0.000033	-0.192161	-0.546640			
k_1							0.002827	0.003570	0.004431
k_2							0.000052	-0.000789	-0.001643
k	0.004685	0.002581	0.003686	0.002727	0.003343	0.003175			
n	0.905849	1.078765	1.032469						
R^2	0.999882	0.999971	0.999969	0.999621	0.999900	0.999961	0.999624	0.999837	0.999588
χ^2	0.000005	0.000005	0.000006	0.000004	0.000018	0.000008	0.001027	0.000028	0.000075
RMSE	0.002151	0.002165	0.002267	0.002310	0.003997	0.002543	0.030217	0.005115	0.008251

Table 4. Statistical data for the best 3 mathematical models obtained for vacuum oven drying

	Vacuum Oven Drying, No Pretreatment								
Model	Aghbashlo *et al.*			Midilli & Kucuk			Logarithmic		
Coeff.	60°C	70°C	80°C	60°C	70°C	80°C	60°C	70°C	80°C
a				0.999504	0.995406	0.995971	1.036386	1.251195	1.444275
b				-0.000106	-0.000395	-0.000876			
c							-0.041313	-0.242949	-0.435884
k				0.007207	0.005143	0.005727	0.006390	0.006984	0.007581
n				0.981632	1.115297	1.146942			
k_1	0.006618	0.007817	0.009502						
k_2	-0.000296	-0.001994	-0.003566						
R^2	0.999885	0.999982	0.999953	0.999980	0.999879	0.999835	0.999964	0.999740	0.999640
χ^2	0.000018	0.000003	0.000011	0.000004	0.000021	0.000050	0.000006	0.000037	0.000095
RMSE	0.004100	0.001761	0.003014	0.001733	0.004589	0.005622	0.002281	0.006721	0.008299

	Vacuum Oven Drying, 30 s US Pretreatment								
Model	Midilli & Kucuk			Logarithmic			Parabolic		
Coeff.	60°C	70°C	80°C	60°C	70°C	80°C	60°C	70°C	80°C
a	1.002306	1.002973	1.000091	1.208746	1.378660	1.527093	0.998850	0.999427	0.991238
b	-0.000196	-0.000585	-0.001314				-0.004495	-0.005852	-0.007828
c				-0.192686	-0.370053	-0.529397	0.000005	0.000009	0.000014
k	0.003135	0.004492	0.007462	0.004306	0.004647	0.005491			
n	1.095731	1.060502	0.993375						
R^2	0.999947	0.999970	0.999987	0.999845	0.999941	0.999978	0.999830	0.999873	0.999867
χ^2	0.000049	0.000006	0.000003	0.000143	0.000012	0.000005	0.000012	0.000026	0.000031
RMSE	0.006573	0.002246	0.001540	0.010984	0.003155	0.001971	0.003155	0.004624	0.004868

	Vacuum Oven Drying, 60 s US Pretreatment								
Model	Midilli & Kucuk			Logarithmic			Aghbashlo *et al.*		
Coeff.	60°C	70°C	80°C	60°C	70°C	80°C	60°C	70°C	80°C
a	1.006484	1.004591	0.997235	1.119371	1.296584	1.395313			
b	-0.000124	-0.000420	-0.001062						
c				-0.104556	-0.283812	-0.399041			
k_1							0.005068	0.005722	0.008379
k_2							-0.000726	-0.001564	-0.002648
k	0.004167	0.004323	0.007954	0.004992	0.004976	0.006507			
n	1.054670	1.074623	1.008721						
R^2	0.999954	0.999929	0.999899	0.999906	0.999872	0.999920	0.999845	0.999779	0.999451
χ^2	0.000009	0.000015	0.000026	0.000017	0.000025	0.000019	0.000026	0.000041	0.000116
RMSE	0.002712	0.003439	0.004250	0.003870	0.004631	0.003783	0.004950	0.006084	0.009902

CONCLUSION

In this study, the effect of ultrasound pretreatment on the oven drying and vacuum oven drying of blueberries was investigated. It was observed that an increase in drying temperature and assistance of vacuum caused shorter drying times.

On the other hand, ultrasonic pretreatment was seen to have an adverse effect on the drying durations. The drying duration was between 195-390 min for oven drying without pretreatments. This duration increased to 255-630 min for 30 s ultrasound pretreatment, and to 300-960 min for 60 s ultrasound pretreatment, respectively. Even though the drying

times were shorter, vacuum oven drying experiments showed similar results. The drying duration of 150-345 min increased to 180-375 min for 30 s ultrasound pretreatment, and to 180-390 min for 60 s ultrasound pretreatment, respectively. By the application of ultrasonic pretreatment, a decrease in effective moisture diffusivities and activation energies was also observed. D_{eff} values were found between 2.74×10^{-10} - 5.42×10^{-10} m^2/s for oven drying without pretreatments; 2.01×10^{-10} - 3.83×10^{-10} m^2/s for oven drying with 30 s ultrasound pretreatment; and 1.57×10^{-10} - 2.86×10^{-10} m^2/s for oven drying with 60 s ultrasound pretreatment. When vacuum assistance was employed, D_{eff} values increased to 3.14×10^{-10} - 8.41×10^{-10} m^2/s for vacuum oven drying without pretreatments; 3.12×10^{-10} - 6.71×10^{-10} m^2/s for vacuum oven drying with 30 s ultrasound pretreatment; and 2.99×10^{-10} - 6.37×10^{-10} m^2/s for vacuum oven drying with 60 s ultrasound pretreatment. For activation energies, on the other hand, E_a of 33.50 kJ/mol decreased to 31.56 kJ/mol and 29.47 kJ/mol when 30 and 60 s of ultrasonic pretreatments were applied in oven drying, respectively. A similar tendency was observed in vacuum oven drying experiments. E_a of 48.23 kJ/mol decreased to 37.50 kJ/mol and 36.98 kJ/mol for 30 and 60 s of ultrasonic pretreatment, respectively. When the experimental data was statistically analyzed, Midilli & Kucuk model was seen to be the most compatible one in oven drying of blueberries. For vacuum oven drying without any pretreatments, Aghbashlo et al. model was seen to yield the best fit with the experimental data. For ultrasonic pretreatment sets, again Midilli & Kucuk model yielded the highest R^2 values in vacuum oven drying. In consequence, it can be concluded that the application of ultrasound pretreatment on the oven drying of blueberries, with and without the assistance of vacuum, did not show a positive effect on the drying duration, effective moisture diffusivity and activation energy values.

REFERENCES

1. K. S. Ravichandran, K. Krishnaswamy, *Crit. Rev. Food. Sci. Nutr.*, DOI: 10.1080/10408398.2021.1999901, (2021).
2. M. Zielinska, A. Michalska, *Food Chem.*, **212**, 671 (2016).
3. M. Zielinska, P. Sadowski, W. Blaszczak, *LWT Food Sci. Technol.*, **62**, 555 (2015).
4. F. U. Akharume, K. Singh, L. Sivanandan, *LWT Food Sci. Technol.*, **73**, 448 (2016).
5. K. J. Mothibe, M. Zhang, J. Nsor-atindana, Y. Wang, *Drying Technol.*, **29** (14), 1611 (2011).
6. L. Deng, A. S. Mujumdar, Q. Zhang, X. Yang, J. Wang, Z. Zheng, Z. Gao, H. Xiao, *Crit. Rev. Food Sci. Nutr.*, DOI: 10.1080/10408398.2017.1409192, (2017).
7. M. Pateiro, M. Vargas-Ramella, D. Franco, A. Gomes da Cruz, G. Zengin, M. Kumar, K. Dhama, J. M. Lorenzo, *Food Chemistry, X* (16), 100465 (2022).
8. R. P. Guiné, *Int. J. Food Eng.*, **4**(2), 93 (2018).
9. B. Nemzer, L. Vargas, X. Xia, M. Sintara, H. Feng, *Food Chem.*, **262**, 242 (2018).
10. Z. O. Ozyalcin, A. S. Kipcak, *J. Aquat. Food Prod. Technol.*, **31** (2), 187 (2022).
11. F. A. N. Fernandes, M. I. Gallaub, S. Rodrigues, *LWT*, **41**, 604 (2008).
12. S. Shamaei, Z. Emam-djomeh, S. Moini, *J. Agr. Sci. Tech.*, **14**, 1523 (2012).
13. M. Nowacka, M. Wedzik, *Appl Acoust.*, **103**, 163 (2016).
14. Z. O. Ozyalcin, A. S. Kipcak, *Turk. J. Fish & Aquat. Sci.*, **21**(3), 135 (2020).
15. A. Özkan Karabacak, C. E. Tamer, Ö. U. Çopur, M. Yagcilari, *Bursa Uludag Üniv Ziraat Fak Derg*, **33**(2), 375 (2019).
16. F. A. N. Fernandes, T. R. Braga, E. O. Silva, S. Rodrigues, *J. Food Sci, Technol.*, **56**(4), 1793 (2019).
17. AOAC, Association of Official Analytical Chemists, Official Methods of Analysis of AOAC International, 16th edn., AOAC International, Rockville, MD, 1995.
18. A. S. Kipcak, E. M. Derun, N. Tugrul, I. Doymaz, *Chem. Ind. Chem. Eng. Q*, **27**(3), 279 (2021).
19. E. Kıpçak, *Journal of the Turkish Chemical Society, Section B: Chemical Engineering*, **6**(1), 1 (2023).
20. O. Ismail, O. G. Kocabay, *Turk. J. Fish & Aquat. Sci.*, **18**, 259 (2018).
21. İ. Doymaz, A. S. Kipcak, S. Piskin, *Czech J. Food Sci.*, **33**(4), 367 (2015).
22. C. Tunckal, I. Doymaz, *Renewable Energy*, **150**, 918 (2020).
23. M. Ayriksa, A. Bahadir, A. Dağdeviren, K. Roshanaei, T. Coşkun, G. K. Ongun, M. Özkaymak, *Politeknik Dergisi*, **25**(3), 1217 (2022).

Effect of anionic/nonionic surfactant systems on the properties of water-based styrene/acrylic copolymer latexes

B. C. Ayhan[1], D. Şakar[1]*, E. C. Tarakçı[2]

[1]Yildiz Technical University, Chemistry Department, 34220 Esenler, Istanbul, Turkey
[2]Hürkimsa Kimya Sanayi, Çayırova, Kocaeli, Turkey

The effect of anionic, nonionic and anionic/nonionic surfactants on the reaction during the emulsion copolymerization of styrene and acrylic monomers was investigated. For this purpose, the effect of anionic, nonionic and anionic/nonionic surfactant systems at different ratios on the emulsion copolymerization of styrene with butyl acrylate, acryl amide and acrylic acid in the presence of ammonium persulfate initiator to obtain water-based styrene copolymer-based paint binders was examined and characterized *via* solid substance analysis, FTIR/ATR, DSC and viscosity. Then, after comparing the obtained results, the optimum anionic/nonionic surfactant system was created and water-based emulsion paint binders contributed to the properties such as better bonding of the paint to the surface to be applied and better distribution of the pigment in the system.

Keywords: Paint binder; water-based styrene/acrylic copolymer; surfactant

INTRODUCTION

Emulsion polymerization is an important process that has been used for many years for the industrial production of synthetic polymers and copolymers. Selection of process type (batch, semi-batch, continuous) is important in emulsion polymerization, especially in a copolymerization system with monomers with different reactivity rates and quite different solubility values in water. It determines the homogeneity of the copolymer composition, the molecular, surface and colloidal properties of the copolymer and, accordingly, its physical and mechanical behavior. In the synthesis of St/A latexes, the semi-batch method is commonly used to increase the homogeneity of the copolymer [1-3] When monomers with different water solubility and different reactivity degrees are used in semi-batch emulsion processes, it is assumed that particle nucleation occurs predominantly in the aqueous phase. The fact that the polymerization is devoid of monomer makes the copolymer composition in the particle homogeneous. It has been observed that the latex properties change depending on the difference in the polymerization mechanism. In dispersed media, an important component of the formulation of emulsion polymerization is the surfactant. Anionic surfactants act as strong particle generators and stabilize the latex particles *via* electrostatic repulsion while nonionic surfactants provide entropic repulsion and steric stabilization. To overcome the limited stabilizing effect at high solid content and high water sensitivity of latexes, stabilization with anionic surfactants or with a mixture of anionic/nonionic surfactant is used in latexes [4-6].

In this study, styrene-acrylate latexes were synthesized *via* semi-batch emulsion polymerization method in the presence of anionic, nonionic and anionic/nonionic surfactant mixture and ammonium persulfate initiator. The characterization of the synthesized latexes was done by FTIR/ATR, DSC, determining solid content percentage, viscosity and minimum film forming temperature.

EXPERIMENTAL

Chemicals and instrumentation

Styrene, butyl acrylate, acrylic acid and acrylamide (monomers), ammonium persulfate (thermal initiator) were purchased from Merck. An anionic emulsifier (AE, ANIODAC 13P 20-27) based on polyethoxy sulfate and a nonionic emulsifier (NE, NONIDAC 11P 30-70), a fatty alcohol polyethylene glycol ether based on ethylene oxide, were taken from SASOL. The active substance ratio of the anionic emulsifier is 30% and the active substance ratio of the nonionic emulsifier is 70%. Ammonia (NH_3) was used as a pH regulator and defoamer, biocide and plasticizer were added in reaction media.

Bruker Instruments ALPHA II FTIR/ATR was used for structural characterization of St/A latexes. Viscosity of latexes was determined on a Brookfield viscosimeter at 25 °C using spindle 3.

* To whom all correspondence should be sent:
E-mail: dsakar@yildiz.edu.tr

DSC Q20 TGA was used to determine glass transition temperature of St/A latex films under N_2 atmosphere (10 ºC/min heating rate). Mettler Toledo pH meter was used to determine pH of St/A latexes. Rhopoint minimum film forming temperature (MFFT) 90 equipment was used to determine MFF temperature of St/A latex films and measurements were done between -10°C and 90°C.

Determination of the solid content of the latexes

To measure the solids of the synthesized St/A copolymers, a certain amount of polymer was weighed into the tared aluminum foil container. The weighed copolymers were heated up to 120°C in the device used for solids determination. Thus, all the water in the polymer was evaporated and the solid material of the polymer was read from the device.

This process was performed 3 times for each synthesized polymer, and the solid matter content of the polymer was determined according to the following equation by taking the average of the results.

% Solid content = $100[(w_3-w_1)/(w_2-w_1)]$ (1)

where w_1 is the weight of the empty container (g); w_2 is the mass of latex weighed initially (g); w_3 is the mass of solid polymer weighed after drying in an oven at 120°C for 30 minutes (g).

Synthesis of water-based styrene/acrylic copolymer paint binders

St/BA/ AAm /AA latexes were synthesized *via* semi-batch emulsion polymerization method. Firstly, the emulsifier was dissolved in water and defoamer was added to the glass reactor (5L) and the temperature was brought to 80-85 °C at a mixing rate of 200-250 rpm. Monomers, namely styrene, butyl acrylate, acrylamide and acrylic acid were mixed in a 2L balloon. Meanwhile, the APS solution was prepared and poured into a dropping funnel. Monomer mixture and APS solution were fed to the reaction phase with the help of an electric pump in 3 hours (Table 1). When all of the initiator and emulsion phase was added, the reaction mixture was stirred for 1 hour. *Tert*-butyl hydroperoxide (70%)

and sodium formaldehyde sulfoxylate (100%) were added to the polymer when the temperature of the reaction mixture reaction fell below 75 °C. Plasticizer was added to the reaction mixture cooled below 50°C, and ammonia was added below 40°C. Finally, when the reaction temperature reached below 25 °C, the reaction was terminated and the latex was separated by filtration.

Looking at the four syntheses, polymerization occurred when anionic emulsifiers were used alone in the system, as seen in St/A copolymer I. However, when nonionic emulsifier with the same active substance was used in St/A copolymer II, it was seen that no polymerization occurred. While the negatively charged part in anionic emulsifiers affects the stabilization of the formed polymer, namely the latex, the hydrophobic chain part provides the critical micellar concentration (CMC) and lowers the surface tension between monomer/water [7]. However, nonionic emulsifiers are mostly used for freezing of latex, etc. Polymerization took place because the critical micellar concentration was achieved and the surface tension between monomer/water decreased even when only anionic emulsifier was used. However, since micelles did not form at the desired level in nonionic emulsifiers, polymerization did not occur in Synthesis 2. Starting from Synthesis 2, the amount of nonionic emulsifier was increased in Synthesis 3 with a view to bring it to the required level for CMC. It was observed that a lot of pollution was formed during the experiment. It has been observed that when nonionic emulsifiers were used alone, problems occurred in polymerization and pollution increased. In Synthesis 4, an anionic/nonionic emulsifier system was created. While preparing the emulsion phase, both anionic and nonionic emulsifiers were added according to the ratios given in Table 1 and polymerization was realized. No problems were observed during the polymerization, and no pollution was encountered in the reactor. St/A I, III and IV latexes were successfully synthesized (Scheme 1). The pictures of St/A I, III and IV latexes and films are given in Scheme 2.

Table 1. Formulations of St/BA/ AAm /AA latexes

St/A	St (%)	BA (%)	AA (%)	AAm (%)	AE (%)	NE (%)	APS (%)	Others (%)
I	23.60	23.50	0.78	0.82	3.10	-	0.3	47.9
II	23.60	23.50	0.78	0.82	-	1.5	0.3	49.5
III	23.60	23.50	0.78	0.82	-	2.2	0.3	48.8
IV	23.60	23.50	0.78	0.82	1.3	0.8	0.3	48.9
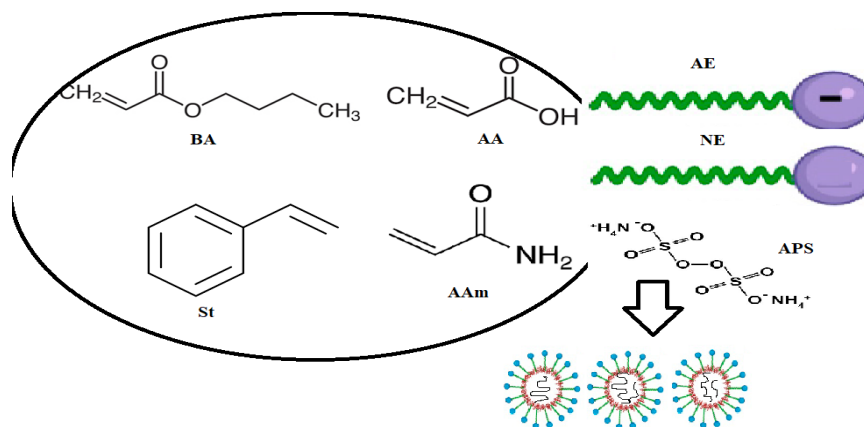
Scheme 1. Synthesis of St/A latexes
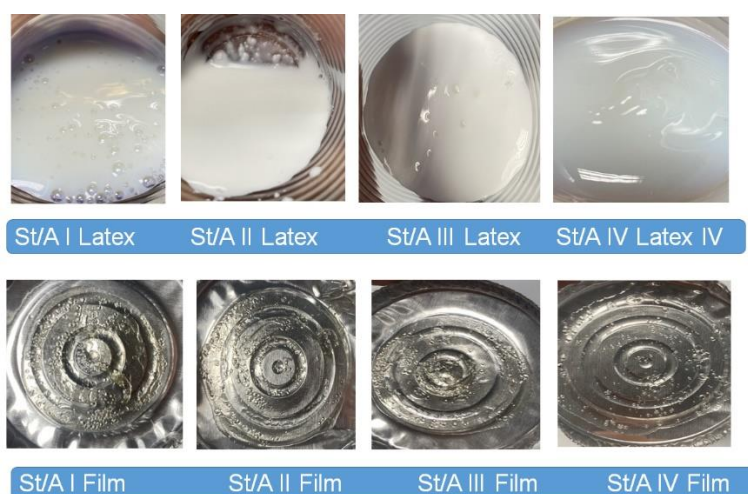
Scheme 2 St/A I, III and IV latexes and films

RESULTS AND DISCUSSION

To examine the effect of anionic/nonionic emulsifier systems on various properties of water-based styrene/acrylic copolymer paint binders, St/BA/AAm/AA latexes were synthesized and structural characterization of St/A copolymers was done by FTIR/ATR. The spectra are given in Figures 1, 2 and 3. The FTIR/ATR spectra of St/BA/AAm/AA latex films showed that monomers participated in the copolymerization reaction. In the FTIR/ATR spectra, the -OH vibration band belonging to the -COOH group was not observed in the 3200-3500 cm^{-1} region. The absence of -OH vibration band indicated the presence of a -COO- group in the environment. Aromatic C-H stretch of polystyrene was 3000 cm^{-1}, aliphatic C-H stretches were 2925, 2928, 2924 cm^{-1}, aromatic C=C stretches of 1451, 1452, 1453 cm^{-1} peaks were observed. Stretching vibrations of AAc (1705 cm^{-1}) and BA (~1730 cm^{-1}) -COO- carbonyl groups coincided and were observed as a sharp band at 1727, 1726 cm^{-1}. Polyacrylamide was observed at C=O ~1650 cm^{-1} and CN ~1400 cm^{-1}. The DSC curves of the St/A latex films depending on the AE and NE are given in Figures 4, 5 and 6.

T_g values of PS, PBA, PAA and PAAm homopolymers are 105, -54, 106 and 165 $^\circ$C, respectively. The latex particles showed only a single Tg, indicating that a copolymer was formed as a result of polymerization [7]. When a low amount of emulsifier was used, insufficient micelles were formed where monomers could emulsify. As the amount of emulsifier increased, the particle size of the micelles decreased. Therefore, while styrene monomers had difficulty penetrating the micelles, butyl acrylate monomers bound more easily with the reactive sites. Thus, an increase in the amount of soft monomer in the polymer and a decrease in Tg value was observed (Table 2)

Analysis results such as solid matter, pH, viscosity, glass transition temperature and minimum film forming temperature (MFFT) of the synthesized St/A latexes are given in Table 2.
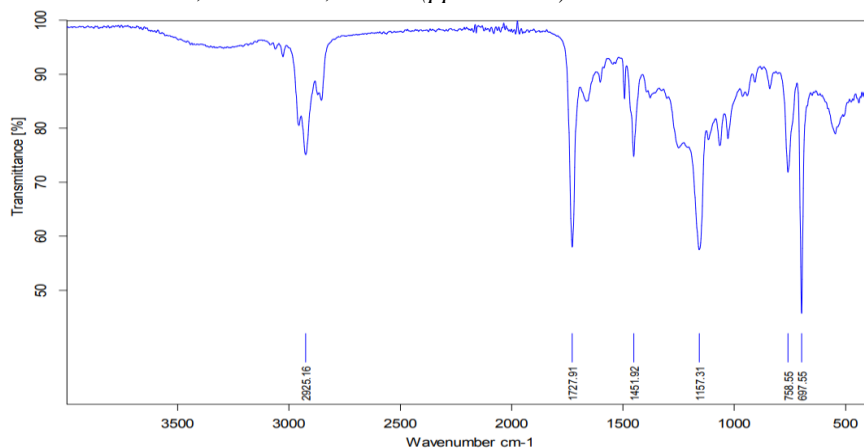
Figure 1. FTIR/ATR spectrum of St /A I latex film
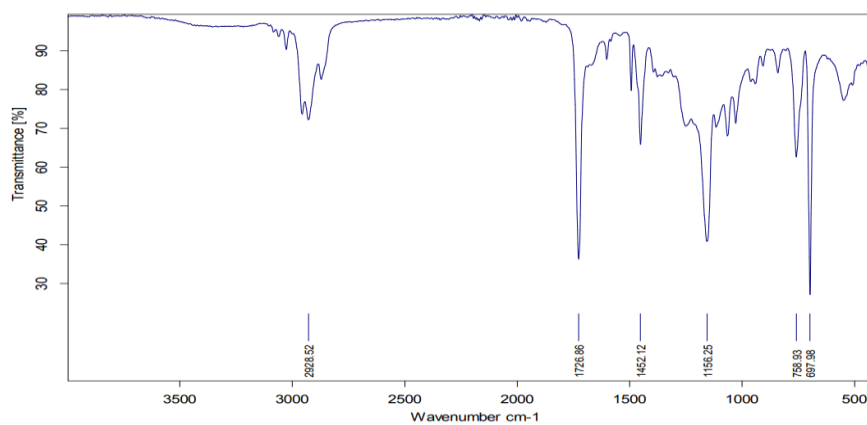
Figure 2. FTIR/ATR spectrum of St /A III latex film
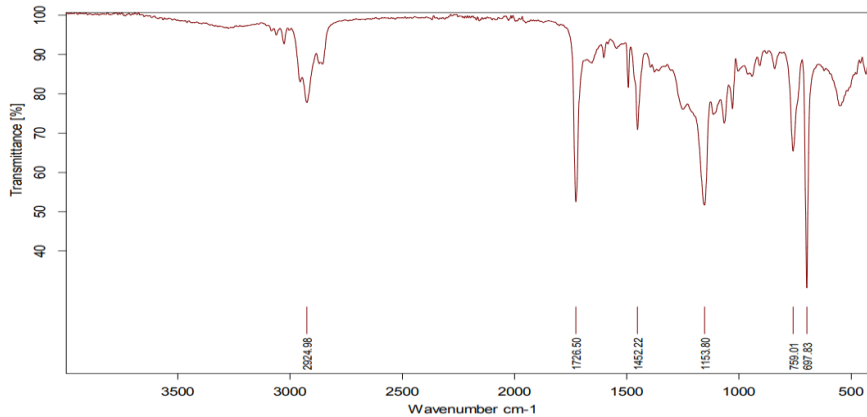
Figure 3. FTIR/ATR Spectrum of St /A IV latex film
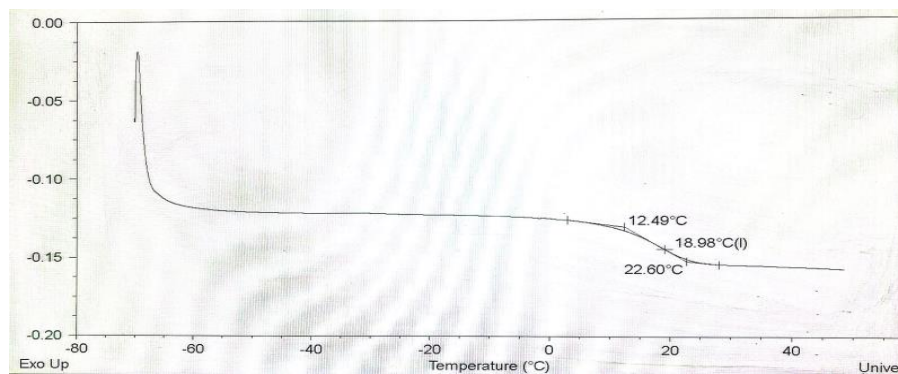
Figure 4. DSC thermogram of St/A I latex

270
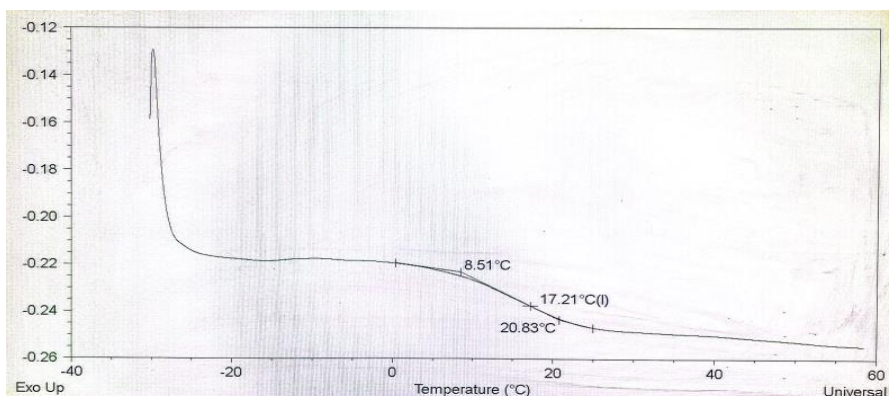
Figure 5. DSC thermogram of St/A III latex
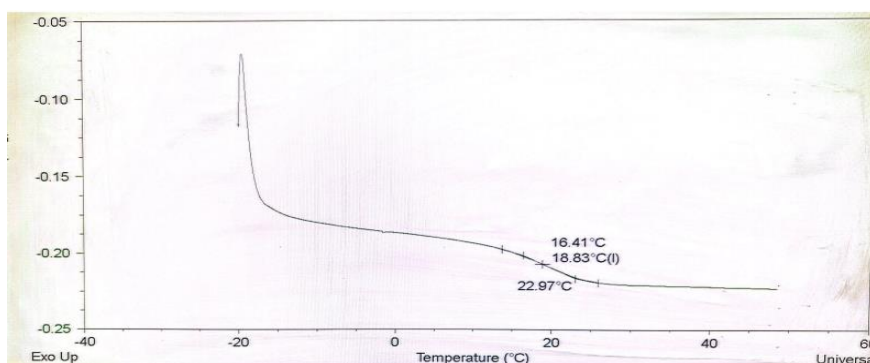
Figure 6. DSC thermogram of St/A IV latex

Table 2. Solid matter percentage, pH, viscosity, glass transition temperature and minimum film forming temperature (MFFT) of the synthesized St/A latexes

St/A	Solid matter (%)	pH	Viscosity (cP)	T_g (°C)	MFFT (°C)
I	49.91	9.13	1675	18.98	19.4
III	46.30	6.77	40	17.21	18.7
IV	49.86	8.34	9235	18.83	16.2

As the total concentration of anionic and nonionic emulsifiers increased in the latexes, the viscosity of the latex increased from 1675 to 9235. As the number of micelles acting on the CMC increased with the increasing emulsifier ratio, the size of the micelles decreased and the viscosity increased. The stability of emulsions with high viscosity also increased.

The minimum film forming temperature (MFFT) indicates the lowest temperature at which a paint or coating can form a film on the surface. Since both the MFFT value and the Tg value of a polymer are affected by the same morphological properties of the polymer, they usually have close values. When the emulsifier used in the emulsion is selected in accordance with the polymer, it shows plasticizer properties and plasticizers can soften the polymer and decrease the Tg and MFFT values [8].

Therefore, since the anionic/nonionic emulsifier system used in St/A IV latex was in the most suitable structure with the synthesized polymer and optimized the particle size, it acted as a plasticizer to the polymer and reduced the MFFT value (Table 2).

CONCLUSION

In the present study styrene/acrylic copolymers were synthesized in 4 different formulations by semi-batch emulsion polymerization using different emulsifier systems. Styrene and butyl acrylate were used as the main monomers in the synthesis, and acryl amide and acrylic acid were used as functional monomers. The observed single T_g values for St/A latexes showed that the latexes were successfully prepared. The ideal result for synthesis was obtained for St/A IV latex, where anionic and nonionic emulsifiers were used together, with a glass

transition temperature of approximately 20°C and a solids ratio of approximately 50% (w/w). At the end of all the studies, the ideal polymerization process was realized when the anionic/nonionic emulsifier system was used in the emulsion polymerization. In addition, the analyses showed that considering the St/A IV latex synthesized with an anionic/nonionic emulsifier system, the most stable and pollution-free dye binder latexes will be obtained.

REFERENCES

1. G. Marinangelo, W. H. Hirota, R. Giudici, *Chemical Engineering Science*, **66** (23), 5875 (2011). https://doi.org/10.1016/j.ces.2011.08.006.
2. V. I. Eliseeva, S. S. Ivanchev, S. I. Kuchanov, A. V. Lebedev, Emulsion polymerization and ıts applications in ındustry, Plenum Publishing Corporation, New York, 1981.
3. A. V. Herk, Chemistry and technology of emulsion polymerization, 1st edn., Blackwell Publishing Ltd., Oxford, 2005.
4. J. F. Richard, Chemistry and technology of surfactants, 1st edn., Blackwell Publishing, Oxford, 2006.
5. S. C. Berasategui, Emulsion and miniemulsion polymerization stabilized with oligomeric surfactants (ASRs), Polymat, 2015.
6. J. I. Amalvy, *Pigment & Resin Technology*, **27**, 20 (1998).
7. B. Eren, Y. Solmaz, *Sakarya University Journal of Science*, **24**(5), 1074 (2020).
8. P. A. Steward, J. Hearna, M. C. Wilkinson, An Overview of polymer latex film formation and properties, Elsevier Journal, 2000, p. 200.

Study of the toxicity of benzanthrone luminescent dyes

A. Kırılova, M. Savıcka, T. Grıgorjeva, E. Kırılova*

Institute of Life Sciences and Technology, Daugavpils University, Daugavpils, Latvia

Many dyes, including luminescent ones, are widely used in our everyday consumption, therefore they are potentially dangerous for the environment, as they can get into sewage and groundwater. In this regard, a sensitive, fast, reliable and inexpensive toxicity assay is needed to assess toxicity to eukaryotic cells. To identify the toxicity of compounds, it is necessary to use various bioassay methods that complement each other in the spectrum of analytes. For this purpose, the toxicological effect of new benzanthrone aminophosphonates was previously evaluated using wheat germ (*Triticum aestivum*) as a test organism and it was found that the studied compounds exhibit a toxic effect on the growth of wheat seedlings to varying degrees, depending on the concentration and substituent on α-carbon atom. The study of the biotoxicity of these substances was then extended to a new test object. As the test organism, yeast *Saccharomyces cerevisiae* was used. The biological toxicity test used the *S. cerevisiae* lethality test based on the detection of changes in yeast viability. The studied dyes in various concentrations were exposed to yeast cells for various durations. After the selected exposure time, the number of live and dead cells was counted and analyzed to assess the toxicity of the studied luminescent dyes.

Keywords: Luminescent dyes; Benzanthrone derivatives; Toxicity; Yeast *Saccharomyces cerevisiae*; Viability

INTRODUCTION

Today, luminescent dyes are an important research tool in many fields of science. Every year they are increasingly used in natural science and biotechnology: to study biological objects, visualize specific organs and tissues of the body, identify biomolecules - proteins, peptides, nucleic acids and other biologically important compounds [1]. Therefore, scientists are developing new luminescent dyes for various purposes, which makes it necessary to study the properties of newly synthesized substances. Some luminescent dyes are widely used in our daily consumption, therefore they are potentially dangerous for the environment, as they can get into sewage and ground water. Therefore, in order to assess toxicity to eukaryotic cells, it is necessary to carry out toxicity analysis for the substances used. Current microbial and biochemical assays to assess the chemical toxicity of various substances include insects [2], fish [3], freshwater microalgae [4], aquatic crustaceans [5, 6], and tumor cell lines [7] to assess molecular toxicity to eukaryotic cells and tissues. To identify the toxicity of compounds, it is necessary to use various bioassay methods that complement each other in the spectrum of analytes.

EXPERIMENTAL

The studied dyes were synthesized according to Kabachnik-Fields reaction from 3-amino-benzanthrone and appropriate aldehydes and dimethylphosphite, The structures of these compounds are presented in Scheme 1. Synthesis details, as well as spectral data were given earlier [8].
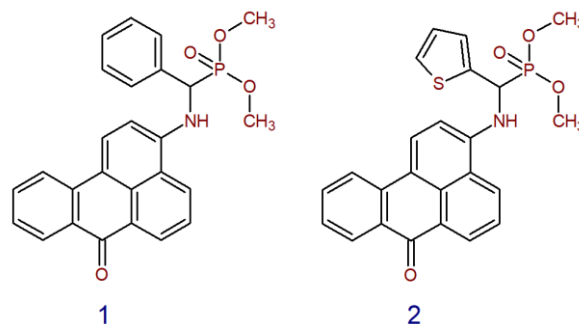
Scheme 1. Chemical structure of the studied compounds.

Instant dehydrated baker's yeast, Saf-Instant, produced in Poland (*S. cerevisiae*) was used.

The scanning of visual field by vision camera and the use of image analysis to evaluate results enabled a significant speed-up and simplification of the work. Axiolab 5 microscope (× 1000) with Axiocam

---

* To whom all correspondence should be sent:
E-mail: jelena.kirilova@du.lv

208 color camera (Zeiss) was used in these experiments (programme Zeiss Labscope).

The microscopic images of colored yeast cells were obtained using a buffered methylene blue solution [9]. For microscopic studies approximately 0.1 g of yeast was suspended in 10 ml of studied substance solution. A water-yeast suspension without any other substance was prepared as a control sample. The quantity of yeast used corresponds to the requirement of 50–150 cells in the visual field of the microscope. A suspension with a larger number of cells in the visual field is difficult to count, a smaller number of cells leads to inaccurate results. After the selected exposure time, one drop of the suspension and one drop of methylene blue were mixed on a slide and examined microscopically. The number of live (colourless) and dead (coloured) cells was immediately calculated in at least 5 visual fields. The same procedure was performed with the control suspension.

The conductivity was determined using a conductivity meter with conductivity cell 980-K19/120 (Mettler Toledo). 20 ml of the examined water were pipetted in five test tubes and 2.0 g of sugar were added in each tube. Other five test tubes with sugar solution without any toxic substances were prepared as control samples. After dissolution, the specific conductivity of the sugar solution was measured in all test tubes.

1.0 g of yeast was added into each of the test tubes and stirred well. After 30 and 60 min of exposure the specific conductivity was measured again in each test tube. It was indispensably necessary to keep the same temperature in all test tubes during the test.

RESULTS AND DISCUSSION

α-Aminophosphonates have received considerable attention in recent years, mainly due to their interesting biological properties, some of which have already been commercialized [10, 11]. Aryl aminophosphonates are used as starting materials for the synthesis of biologically active compounds [12-14]. Some of them have pronounced fluorescent properties, in connection with which it is proposed to use them as luminescent dyes [15-18].

Since these compounds have been found to be effective protease and phosphatase inhibitors, genotoxicity and cytotoxicity studies have been conducted for some of them. Anthracene-derived aminophosphonates show moderate genotoxic and antiproliferative activity *in vivo* and low toxicity to mouse embryo cells, some of derivatives were potent cytotoxic agents towards colon carcinoma cell line [19]. Pyrene-derived aminophosphonates were found to be cytotoxic for colon cancer cell lines, while exhibiting virtually no toxicity to lymphocytes [20].

Previously, the effect of some alkyl aminophosphonates on the membrane potential and electrical conductivity of the internodal cells of *Nitellopsis obtusa* cells and hemolysis of erythrocytes was studied [21]. It has been established that these organophosphorus compounds at concentrations of 10^{-4} - 10^{-5} M cause depolarization and increase in the electrical conductivity of algae membranes. When used at higher concentrations, aminophosphonates caused hemolysis of erythrocytes. The observed changes are the result of direct interaction of aminophosphonates with the lipids of the plasma membrane. Thus, as was established earlier [22], the biological activity of organophosphorus compounds is associated with their interaction with the lipid phase of biological membranes.

It was of interest to evaluate the toxicity of newly synthesized benzanthrone aminophosphonates [8], which showed pronounced luminescent properties, like many other N-containing benzanthrone derivatives [23-25]. Convenient objects of toxicity research are various plants, especially their sprouts growing in seedlings. For plants under any stressful conditions, the dominant goal is to reduce the effects of stressors in order to survive and continue to grow. The literature describes studies of the stress effect of various chemical substances on plant development, using different concentrations of substances and exposure times. Athinarayanan *et al*. studied the effect of natural dyes on the germination of *Phaseolus aureus* seeds, showing as a result that these natural dyes do not have a toxic effect on the growth of aquatic plants within the investigated concentrations 50-100 ppm [26]. Studies of the physiological effect of dimethyl sulfoxide (DMSO) on rice seeds (*Oryza sativa L.*) have been carried out [27]. As a result, it was found that a linear decrease in the relative growth rate of rice seedlings was observed as the concentration of DMSO increased from 0.56 to 13.54 mM.

The evaluation of toxicity of compounds **1** and **2** on the wheat seedlings was performed using dye concentrations from 10^{-7} M to 6×10^{-5} M [8]. Both dyes were found to cause significant oxidative damage to wheat seedlings, as evidenced by elevated levels of malondialdehyde (as the indicator of oxidative stress [28]) content and electrolyte leakage compared to control wheat sprouts. Compound **2** showed a very pronounced toxic effect on wheat growth (see Figure 1). As a result of the study, it was concluded that dye **1** and **2** solutions cause

significant oxidative damage to wheat seedlings. It was also established that the toxic properties of the studied substances differed: a substance with a thiophene group is more toxic to plants than a substance containing a phenyl group. It can be concluded that wheat germ is a good object for assessing the toxicity of the studied substances. However, this method requires 6-7 days for one experiment and three weeks for three independent experiments.

Fig. 1. Wheat sprouts cultivated in the presence of dye **2** with concentrations: a (0 M), b (6 $\times 10^{-5}$ M), c (3 $\times 10^{-6}$ M).

The search for other faster methods has led to yeast. Previously, several bioassays using yeast have been proposed [29-31]. The yeast *S. cerevisiae* is a simple eukaryotic model organism for evaluating toxic effects, since its cellular structure and functional organization share many similarities with animal and plant cells [29, 32]. Thus, it is a convenient model organism for assessing toxic effects in human cells and tissues. The study of cell death in *S. cerevisiae* can potentially be productive for understanding cell death. Therefore, we continued our study of toxicity using a new test object - yeast *Saccharomyces cerevisiae*.

The used biological toxicity test – *S. cerevisiae* lethal test is based on detection of yeast viability changes. Viability is a term used to describe whether a cell is alive or dead and refers to the percentage of living cells.

The most common approaches to detect yeast cell viability and concentration is to identify and manually count live yeast cells in a sample stained with methylene blue. To distinguish living cells from dead cells, they were examined under a microscope using methylene blue: dead cells stained blue, while living cells did not stain. Cells constantly die during normal physiological processes such as development and differentiation-based cell turnover. Cells can also die in response to various external (pathogens, toxins, environmental changes) or internal (mutations or epigenetic malfunctions) factors.

The studied dyes at various concentrations were exposed to yeast cells for various durations. After the selected exposure time the number of live (colorless) and dead (colored) cells were calculated and analyzed for evaluation of toxicity of the investigated luminescent dyes.

For the yeast viability test, dye concentrations of 6×10^{-5} M and 10^{-4} M were used. The results are presented in Table 1. No statistically significant increase in the yeast cell mortality after 15 min treatment with different studied dyes in a concentration of 6×10^{-5} M could be detected. The number of living cells of *S. cerevisiae* decreased by about 3% in the presence of dye **1** and **2** and it reached 6% at the end of the investigated period compared with the control. An increase in the concentration of the studied dyes (10^{-4} M) slightly reduced the number of living yeast cells: by about 7% compared with a lower concentration. However, there were no changes in the number of living cells of yeast after 24-h exposure compared to control. Recent studies showed that dead yeast cells can provide surviving cells with nutrients or induce their stress response by transmitting an alarm signal [33, 34]. Dead yeast cells absorbed more chemicals than control cells to protect living cells from stressors. Perhaps our results are another proof of the "altruistic" death hypothesis [35], and the death of a part of yeast cells can contribute to the survival of other cells. Similar results were obtained on other microorganisms, e.g., *E. coli* [36], algal cells [37], etc.

Table 1. Viability of yeast in the presence of dyes **1** and **2**.

	Concentration 6 $\times 10^{-5}$ M			Concentration 10^{-4} M		
	After 15 min	After 30 min	After 60 min	After 15 min	After 30 min	After 60 min
Standard	100	100	100	100	100	100
Dye **1**	96.5	94.4	94.4	94.7	92.7	93.3
Dye **2**	97.2	94.5	94.4	93.7	94.9	92.6

Further in the work, a conductometric test for water toxicity was carried out, based on the observation of a change in the specific electrical conductivity of a suspension of the yeast *S. cerevisiae* as a result of inhibition of the yeast fermentation activity under toxic conditions [30]. As can be seen from the results (see Table 2), there is no significant change in the electrical conductivity of the yeast suspension, which would indicate cell destruction and electrolyte leakage as a result of this. These data also support the "altruistic" death hypothesis, according to which the death of some yeast cells may contribute to the survival of other cells.

Table 2. Viability of yeast in the presence of dyes **1** and **2** (concentration 10^{-4} M).

	Conductivity, μS/cm	
	After 30 min	After 60 min
Standard	155.7	182.8
Dye **1**	153.8	184.1
Dye **2**	155.8	189.7

CONCLUSION

It was shown that yeast cells, unlike wheat germs, are weakly sensitive to the action of new benzanthrone aminophosphonates, the number of dead cells slightly increases with increasing dose and duration of exposure. Thus, despite the simplicity and speed of obtaining results, yeast is poorly suited for assessing the toxicity of the studied compounds.

REFERENCES

1. X. Fei, Y. Gu, *Prog. Nat. Sci.: Mater.,* **19**, 1 (2009).
2. M. A. Nascarella, J. G. Stoffolano Jr., E. J. Stanek, P. T. Kostecki, E. J., Calabrese, *Environ. Pollut.,* **124,** 257 (2003).
3. S. Pichardo, A. Jos, J. L. Zurita, M. Salguero, A. M. Camean, G. Repetto, *Toxicol. in Vitro,* **21,** 1460 (2007).
4. A. Krishna Moorthy, B. Govindarajan Rathi, S. P. Shukla, K. Kumar, V. Shree Bharti, *Environ. Toxicol. Pharmacol.* **82**, 103552 (2021)
5. J. L. Zurita, A. Jos, A. del Peso, M. Salguero, A. M. Camean, Lopez-Artiguez, G. Repetto, *Sci. Total Environ.,* **387,** 155 (2007).
6. S. W. Reddy, J. W. Osborne, *Biocatal. Agric. Biotechnol.*, **25**, 101574 (2020).
7. N. Yang, J. Pang, Z. Huang, Q. Zhang, Z. Wang, D. Sun, *Food Chem. Toxicol.,* **173**, 113612 (2023).
8. A. Maleckis, E. Griskjans, M. Cvetinska, M. Savicka, S. Belyakov, E. Kirilova, *J. Molec. Struct.*, **1277**, 134838 (2023).
9. K. Painting, B. Kirsop, *World J. Microbiol. Biotechnol.*, **6**, 346 (1990).
10. A. Mucha, P. Kafarski, Ł. Berlicki, *J. Med. Chem.,* **54**, 5955 (2011).
11. A. Amira, Z. Aouf, H. K'tir, Y. Chemam, R. Ghodbane, R. Zerrouki, N.-E. Aouf, *ChemistrySelect*, **6**, 6137 (2021).
12. R. Karpowicz, J. Lewkowski, M. Stasiak, A. Czopor, P. Tokarz, A. Król, D. Rogacz, P. Rychter, *Phosphorus Sulfur Silicon Relat. Elem.*, **193**, 423 (2018).
13. B. Zhang, X. T. Hu, K. M. Zhou, Y. S. Yang, H. L. Zhu, *Bioorg. Chem.*, **102**, 104096 (2020).
14. X. C. Yang, C. M. Zeng, S. R. Avula, X. M. Peng, R. X. Geng, C. H. Zhou, *Eur. J. Med. Chem.*, **245**, 114891 (2023).
15. A. Maleckis, M. Cvetinska, E. Griskjans, L. Mezaraupe, M. Kirjusina, V. Pavlova, E. Kirilova, *J. Photochem. Photobiol*. A., **444**, 114918 (2023).
16. A. Kusnierz, E. Chmielewska, *Phosphorus Sulfur Silicon Relat. Elem.*, **192**, 700 (2017).
17. M. G. Gorniak, P. Kafarski, *Phosphorus Sulfur Silicon Relat. Elem.*, **191**, 511 (2016).
18. M. G. Gorniak, A. Czernicka, P. Młynarz, W. Balcerzak, P. Kafarski, *Beilstein J. Org. Chem.*, 10, 741 (2014).
19. I. Kraicheva, I. Tsacheva, E. Vodenicharova, E. Tashev, T. Tosheva, A. Kril, M. Topashka-Ancheva, I. Iliev, T. Gerasimova, K. Troev, *Bioorg. Med. Chem.,* **20**, 117 (2012).
20. J. Lewkowski, M. Rodriguez Moya, A. Wrona-Piotrowicz, J. Zakrzewski, R. Kontek, G. Gajek, *Beilstein J. Org. Chem.*, **12**, 1229, (2016).
21. Z. Trela, H. Kleszczynska, J. Sarapuk, *Z. Naturforsch. C J. Biosci*., **56**, 838 (2001).
22. R. H. Shimabukuro, *Pestic. Biochem. Physiol.*, **48,** 85 (1994).
23. M. Olipova, A. Maleckis, A. Puckins, A. Kirilova, E. Romanovska, E. Kirilova, *Bulg. Chem. Commun.*, **54**, 253 (2022).
24. U. Tarabara, E. Kirilova, G. Kirilov, K. Vus, O. Zhytniakivska, V. Trusova, G. Gorbenko, *J. Mol. Liq.*, **324**, 115102 (2021).
25. N. Orlova, I. Nikolajeva, A. Puckins, S. Belyakov, E. Kirilova, *Molecules*, **26**, 2570 (2021).
26. G. Athinarayanan, R. Mariselvam, A. J. A. Ranjitsingh, A. U. R. Nanthini, *Int. J. Sci. Res.*, **4**, 2061 (2015).
27. X.-H. Zhang, X.-Z. Yu, D-M. Yue, *Int. J. Environ. Sci. Technol.*, **13**, 607 (2016).
28. M. Khoubnasabjafari, K. Ansarin, A. Jouyban, *Curr. Pharm. Anal.,* **12**, 4 (2016)
29. L. Rumlova, J. Dolezalova, *Environ. Toxicol. Pharmacol.,* **33**, 459 (2012).
30. J. Dolezalova, L. Rumlova. *Environ. Toxicol. Pharmacol.,* **38**, 977 (2014).
31. A. L. Valimaa, A. Kivisto, M. Virta, M. Karp, *Sensors (Basel)*, **8**, 6433 (2008).
32. E. V. Grosfeld, V. A. Bidiuk, O. V. Mitkevich, E. S. M. O. Ghazy, V. V. Kushnirov, A. I. Alexandrov, *J. Fungi*, **7**, 886, (2021).

33. J. M. Hardwick, *mBio*, **9**, 4 (2018).
34. D. Carmona-Gutierrez, T. Eisenberg, S. Buttner, C. Meisinger, G. Kroemer, F. Madeo. *Cell Death Differ*., **17**, 763 (2010).
35. N. A. Kireeva, S. S. Sokolov, E. A. Smirnova, K. V. Galkina, F. F. Severin, D. A. Knorre, *ASM Journals mSphere*, **6**, 6 (2021).
36. M. Snoussi, J. P. Talledo, N-A. Del Rosario, S. Mohammadi, B-Y. Ha, A. Kosmrlj, S. Taheri-Araghi, *Elife,* **7** (2018).
37. N. F. Y. Tam, A. M. Y. Chong, Y. S. Wong, *Mar. Pollut. Bull.,* **45**, 362 (2002).

Polyacrylic acid and polyacrylic acid sodium salt as ınhibitors of calcium oxalate crystal formation

A. S. A. E. Al-Dubai, E. Akyol[*]

Department of Chemical Engineering, Yildiz Technical University, Davutpasa, Istanbul, 34210, Turkey

In both industrial machinery and medical field, calcium oxalate (CaOx) crystal formation is a significant issue. This formation must be minimized to avoid problems and ensure optimal equipment performance in industries. To contribute to the development of preventative measures, this research aimed to examine the inhibitory effects of polyacrylic acid (PAA) and polyacrylic acid sodium salt (PAANa) on CaOx crystal formation. A batch crystallization technique was used to investigate the inhibitory effects of PAA and PAANa on CaOx crystal formation at four different concentrations (0.5, 0.75, 1, and 2 ppm) in aqueous solutions at 37°C. The Langmuir adsorption isotherm was utilized to investigate the adsorption mechanism of the inhibitors.The study found that PAA prevented crystal growth by 50–90%, while PAANa was more effective, reducing it by 95–98%. Additionally, the differential heat of adsorption of Q_{diff} for the kink Langmuir adsorption isotherm for PAA and PAANa was 41.56 and 49.28 KJ/mol, respectively. The findings demonstrate the potential use of PAA and PAANa as inhibitors and advance our understanding of the fundamental principles underlying CaOx crystal formation. Therefore, this research contributes to the development of preventative measures to avoid these problems, ensure optimal equipment performance in industries and prevent kidney stone formation in the medical field.

Keywords: Calcium oxalate, Scale formation, Inhibitors, Polyacrylic acid sodium salt.

INTRODUCTION

In many industries, fouling of industrial plant equipment by inorganic and organic foulants is a serious concern [1]. Among these foulants, calcium oxalate fouling is especially problematic, affecting a wide range of industrial operations. Oxalate ion concentrations rise in numerous industrial process streams as larger organic species degrade, particularly in strongly alkaline conditions. CaOx phases can precipitate in the presence of Ca^{2+} due to their low solubility [2]. Scale formation caused by the accumulation of these oxalate compounds is a major issue in many industries, including pulping and papermaking, as well as in cane sugar mill evaporators [3, 4].

Scale formation causes significant processing challenges in cane sugar mills, with calcium oxalate and amorphous silica being the most difficult scale components generated on the calandria tubes. The formation of these deposits necessitates an increase in energy consumption in order to meet the operating requirements. If the energy input becomes uneconomical, the sugar mill must close in order to remove the scale using chemical and/or mechanical procedures. Failing to remove the scale on a regular basis can result in sucrose deterioration due to prolonged residence time and tube damage [5]. These shutdowns can be costly due to missed production and cleaning costs [6].

Scale formation occurs in the pulp and papermaking industry when oxalate ions interact with various alkaline earth metal ions, such as calcium ions and barium ions, under alkaline circumstances, resulting in poorly soluble oxalates. These oxalates rapidly deposit on the surface of pulp pipelines, washing, and screening equipment, and are difficult to remove once formed. The accumulated deposits can cause pipe obstruction and screen blocking, interfering with the normal operation of machinery [4]. As a result, controlling scale development caused by oxalate compounds is a serious challenge for these businesses.

Scale inhibitors are commonly employed to avoid scaling in a variety of industrial processes. The usage of scale inhibitors is critical in many industries, including sugar manufacturing, to preserve the effectiveness and longevity of equipment. Scale inhibitors act by interfering with the crystallization process of scale components at low concentrations, typically a few parts per million. They have the ability to prevent or greatly inhibit precipitation. The type of scaling substance influences the polymer employed as a scale inhibitor, with anionic polymers typically utilized in the sugar sector for calcium salt inhibition [6].

Using distinct inhibitors at different phases of evaporation allows certain scale components to be targeted without interfering with one another.

---

* To whom all correspondence should be sent:
E-mail: eakyol@yildiz.edu.tr

Scale inhibitors can work in three different ways. The first involves nucleation interference, in which the inhibitors loosely bind to scale-forming ions and damage crystal embryos. The polymers' second effect includes their impeding crystal growth by adhering to the active growth sites of a crystal, causing the crystal morphology to be distorted. Inhibitors interact with the crystal surfaces to repel other charged particles, blocking binding, and functioning as dispersants [6]. Overall, scale inhibitors are a significant tool for preserving equipment efficiency and preventing scaling in a variety of industrial processes.

The presence of a carboxyl group on every two carbon atoms of the main chain gives poly(acrylic acid) (PAA) a high negative charge density. Acrylic polymers have a wide molar mass distribution because they are manufactured industrially through radical polymerization of acrylic acid or sodium acrylic acid. PAA, along with poly (sodium acrylate), is a water-soluble anionic polyelectrolyte that is widely utilized in the creation of hydrogels, superabsorbent and ion exchange resins, as well as dispersion and binding agents. Because of their low toxicity, PAA and PAANa are frequently utilized in industrial applications, such as adhesives, coatings, textiles, and water treatment. Their beneficial features, including hydrophilicity, nontoxicity, and binding capacity, make them an appealing material for changing the structure of bentonite components in foundry binders [7]. PAA was found to be an efficient inhibitor of calcium oxalate monohydrate (COM) crystal formation in a study by Akyol and Öner [8]. The research found that PAA was adsorbed onto the surface of the COM crystals, preventing further crystal formation. The authors hypothesized that PAA's high negative charge density contributed to its effectiveness as a COM crystal growth inhibitor.

This study holds great importance for industries aiming to minimize scale formation and maintain optimal equipment performance. Specifically, we conducted a comparison between the inhibitory effects of PAA and PAANa on calcium oxalate (CaOx) crystals. The findings of this research have the potential to revolutionize scale prevention strategies by introducing more efficient and cost-effective inhibitors. Additionally, this study provides valuable insights into the mechanisms of calcium oxalate inhibition and opens up possibilities for the development of novel inhibitors. In summary, this research underscores the significance of comprehending the inhibitory capabilities of PAA and PAANa polymers, along with their prospective industrial applications.

EXPERİMENTAL

A one-liter Pyrex glass jar with a water-jacket was used to carry out the experiment. Supersaturated solutions were made by progressively combining calcium chloride and sodium oxalate solutions in equal proportions, with freshly prepared solutions frequently added to the oxalate component. In order to conduct the growth investigations, a predetermined amount of stock solutions containing 0.7 mM $CaCl_2$ and $Na_2C_2O_4$ were added, with the latter being added only after the equilibrium temperature was reached. Software was used to continuously track the temperature, pH (6.7), and calcium concentration during the crystallization process.

The experments were conducted at 37°C with additive concentrations ranging from 0.5 to 2 mg/L and a starting $[Ca^{2+}]/[C_2O_4^{2-}]$ ratio maintained at 1. To determine the impact of the polymer on the rate of calcium oxalate precipitation, solution conductivity was measured, and the decline in conductivity with time was noted. A detailed explanation of the entire experimental methods has already been published [9].

In order to evaluate the impact of polymers, we compared the rate at which crystals were formed in the absence of polymers (R_0, mol/L^{-min}) to the rate of crystal formation in their presence (R_i, measured in mol/L^{-min}) under identical experimental conditions. The ratio of R_0 to R_i was utilized as a quantitative measure of the additive's influence. The rate of rapid growth was determined by analyzing the slope of the calcium ion concentration over time graphs for each individual experiment. Specifically, we calculated the slope using the tangent line at the point where the curve displayed its initial clear change in direction. The reported rates were obtained by averaging the outcomes from a minimum of three separate experiments.

RESULTS AND DISCUSSION

The purpose of the experiments was to determine how PAA and PAANa polymers affected the rate of calcium oxalate crystallization at 37 °C. The study's findings are presented in Table 1. We examined the growth inhibition of calcium oxalate crystals with and without polymer to ascertain the impact of additives on crystal growth. The R_0/R_i ratios were used to quantify the polymer's capacity to prevent crystal formation; a greater ratio denotes a more potent inhibitor. By contrasting the growth rates of the solutions with and without the additives (R_0 and R_1, respectively), the efficiency of the additives was ascertained (R_i). The following formula was then used to determine the inhibitory activity:

$$\text{Inhibition (\%)} = \frac{R_0 - R_i}{R_0} \times 100$$

The results of this study showed that both PAA and PAANa were effective inhibitors of calcium oxalate crystal formation. PAA inhibited the formation of calcium oxalate crystals by 50%, 56%, 70%, and 90% at concentrations of 0.5, 0.75, 1, and 2 ppm, respectively. PAANa, on the other hand, was a more potent inhibitor and inhibited the formation of calcium oxalate crystals by 95%, 97%, 98%, and 98% at concentrations of 0.5, 0.75, 1, and 2 ppm, respectively. The results suggest that PAANa is a more effective inhibitor of calcium oxalate crystal formation than PAA.

The findings of this study highlight the effectiveness of both PAA and PAANa as inhibitors of calcium oxalate crystal formation. The inhibitory mechanism of these polymers is attributed to their ability to disrupt the nucleation and growth processes of calcium oxalate crystals. Notably, the results reveal that PAANa exhibits a greater inhibitory potency compared to PAA. This heightened efficacy may be attributed to the presence of sodium ions in PAANa, which potentially enhance its interaction with calcium ions and consequently inhibit the formation of calcium oxalate crystals. Moreover, the elevated negative charge density of PAANa contributes to its inhibitory activity by electrostatically repelling calcium ions. However, it is important to note that the inhibitory effect of both polymers primarily arises from their adsorption onto the surfaces of the crystals. PAANa, in particular, exhibits a stronger affinity for the surfaces of calcium oxalate crystals. This assumption will be further supported and explored in the forthcoming section addressing the adsorption mechanism within this research.

Overall, the present study demonstrates the potential of PAA and PAANa as effective inhibitors of calcium oxalate crystal formation, with potential applications in various industries. The ability of these polymers to inhibit the formation of calcium oxalate crystals could lead to improved product quality and reduced maintenance costs in industrial settings.

Table 1. Effect of PAA and PAANa on the growth of calcium oxalate crystals.

Polymer	Concentration (mg/L)	R_0/R_i	Inhibition (%)
Control	-	1	-
PAA	0.5	2	50
	0.75	2.85	56
	1	3.33	70
	2	10	90
PAANa	0.5	20	95
	0.75	28.57	97
	1	50	98
	2	50	98

Table 2. Calculated K and Q_{diff} values for CaOx crystal formation in the presence of PAA and PAANa.

Polymers	Adsorption model	K (mole/mole)$^{-1}$	Q_{diff} (KJ/mole)	R^2 (corr. coeff.)
PAA	Kink	1×10^7	41.56	0.9896
	Terrace	4×10^7	37.98	0.9732
PAANa	Kink	5×10^9	49.28	0.8941
	Terrace	1×10^8	47.49	0.8943

Adsorption mechanism

The crystal surface is impacted by polyelectrolytes that hinder or prohibit further crystallization even at low concentrations. The limited amount of polymer present in the solution suggests that the prevention of growth is likely due to the obstruction of active growth sites on the seed crystals, rather than the binding of calcium ions in the solution. Research on crystal morphology and growth rates has explored the effect of additives, with theoretical models based on the concept of additive adsorption onto different crystal surface sites. Cabrera and Vermilyea (CV) [10], for instance, examined the adsorption of impurities at kinks and

surface terraces. According to this model, the growth of crystals is inhibited by a barrier of adsorbed inhibitor ions on the smooth crystal surface. As Vermilyea notes, an inhibitor stops a step moving across the crystal surface. Even a few percent of inhibitor ions covering the available crystal surface can block the growth of various mineral salts, suggesting that preferential adsorption of the inhibitor at active growth sites on the surface is responsible for the inhibition mechanism.

Vermilyea noted that an inhibitor would halt a step moving across the crystal surface. The blocking of crystal growth by a few percent of inhibitor ions covering the available crystal surface for various mineral salts suggests that the inhibition mechanism may be due to the preferential adsorption of the inhibitor at active growth sites on the surface. Kubota and Mullin have recently developed a new kinetic model for crystal growth in the presence of impurities, which describes the adsorption of impurities along steps [11]. The model introduces an impurity effectiveness factor a and assumes that step velocity linearly decreases with increasing surface coverage by impurities adsorbed on the growing crystal.

The relationship between the fraction coverage, θ_i, of the surface in the presence of an impurity and the relative growth rate R_i/R_0 in a spiral growth mechanism can be expressed as follows:

$$\left(\frac{R_0 - R_i}{R_i}\right)^n = \alpha^n \theta_i \tag{1}$$

In the case of impurity adsorption occurring at kinks in step edges, as in the Kubota-Mullin model, the exponent n equals 1, while an exponent of 2 represents adsorption on surface terraces, as in the CV model. The coverage of adsorption active sites, θ_i, can be described by the Langmuir adsorption isotherms.

$$\theta_i = \frac{KC_i}{1 + KC_i} \tag{2}$$

In Eq. (2), K is the Langmuir constant given by:

$$K = \exp\left(\frac{Q_{diff}}{RT}\right) \tag{3}$$

The differential heat of adsorption, Q_{diff}, corresponds to impurity coverage θ_i of the available adsorption sites. By combining Eq. (1) with the Langmuir isotherm (Eq. (2)), we can obtain an equation that is linear in $1/C_i$ for n equal to 1.

$$(R_i/(R_0 - R_i)) = 1/\alpha\,(1 + 1/(KC_i)) \tag{4}$$

For $n = 2$,

$$(R_i/(R_0 - R_i))^2 = 1/\alpha^2\,(1 + 1/(KC_i)) \tag{5}$$

To verify the validity of the models, we fitted our kinetic data to Eqs. (4) and (5) and plotted the results in Fig. 2. The crystal growth rate, R, dependence on C_i allowed us to calculate K from the experimental data. Figs. 1 and 2 display the plots of $R_i/(R_0 - R_i)$ and $[R_i/(R_0 - R_i)]^2$, respectively, against $1/C_i$ for the models involving impurity adsorption at kinks (n equal to 1) and on surface terraces (n equal to 2).
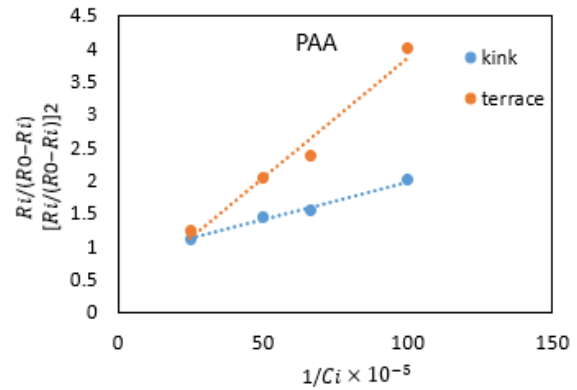
Figure 1. Plots of $R_i/(R_0 - R_i)$ and $[R_i/(R_0 - R_i)]^2$ against $1/C_i$ for PAA.
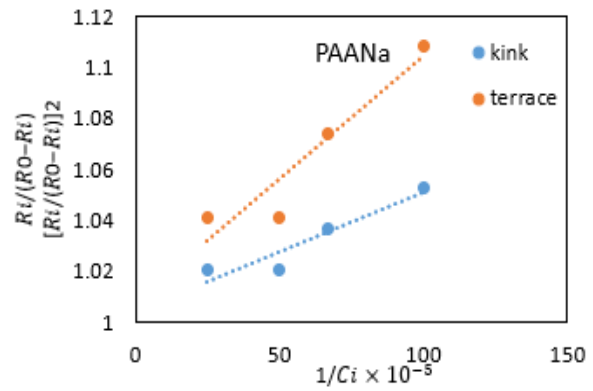
Figure 2. Plots of $R_i/(R_0 - R_i)$ and $[R_i/(R_0 - R_i)]^2$ against $1/C_i$ for PAANa.

We analyzed the experimental data of the COM crystal growth in the presence of polymers using Eqs. (4) and (5). From the slopes of the plots, we determined the values of constant K and estimated the heats of adsorption, Q_{diff}, using Eq. (3). Fig. 5 shows that there is no significant difference between the plots for the exponents 1 and 2. However, it is worth noting that the values of Q_{diff} for kinks or terrace are comparable (as shown in Table 2) and cannot be used to distinguish between adsorption at kinks and on the surface terrace. This suggests that the Langmuir adsorption isotherm does not significantly differ when impurity adsorption occurs

281

at kinks (Kubota-Mullin model) or on the surface terrace (CV model) as it was stated in a prevoius study [8].

CONCLUSION

In conclusion, this study focused on investigating the inhibitory effects of polyacrylic acid and polyacrylic acid sodium salt on calcium oxalate crystal formation. The findings demonstrate that both PAA and PAANa are effective inhibitors of CaOx crystal formation, with PAANa exhibiting higher potency compared to PAA. Through the utilization of a batch crystallization technique and analysis of adsorption mechanisms using the Langmuir adsorption isotherm, it was observed that PAA inhibited crystal growth by 50-90%, while PAANa showcased a higher level of effectiveness by reducing crystal growth by 95-98%. Moreover, the differential heat of adsorption values (Q_{diff}) further supported the superior inhibitory properties of PAANa (49.28 KJ/mol) compared to PAA (41.56 KJ/mol).

These findings have significant implications for various industries facing CaOx-related problems, as well as in the medical field to prevent kidney stone formation. The potential use of PAA and PAANa as inhibitors of CaOx crystal formation is evident, highlighting the importance of understanding the fundamental principles underlying this process. By developing preventative measures based on the inhibitory capabilities of these polymers, industrial equipment performance can be optimized while minimizing issues caused by CaOx crystal formation. Additionally, the insights gained from this study contribute to the broader scientific understanding of CaOx crystal formation, paving the way for future research in this field.

REFERENCES

1. Ch. P. East, Ch M. Fellows, W. O. S. Doherty, *Journal of Food Engineering,* **117** (3), 291 (2013).
2. E. Königsberger, A. Tromans, P. M. May, G. Hefter, *Journal of Chemical & Engineering Data*, **66**(1), 840 (2020).
3. H. Yu, R. Sheikholeslami, W. O. S. Doherty, *Chemical Engineering Science*, **57**(11), 1969 (2002).
4. H. Li, C. Du, S. Ge, M. Liu, *Nordic Pulp & Paper Research Journal,* **35**(1), 18 (2020).
5. H. Yu, R. Sheikholeslami, W. O. S. Doherty, *Developments in Chemical Engineering and Mineral Processing*, **12**(3-4), 309 (2004).
6. C. P. East, C. M. Fellows, W. O. S. Doherty, in: Mineral Scales and Deposits, Elsevier, 2015, p. 619.
7. S. Cukrowicz, M. Sitarz, K. Kornaus, K. Kaczmarska, A. Bobrowski, A. Gubernat, B. Grabowska, *Materials*, **14**(8), 1947 (2021).
8. Akyol, E., M. Öner, *Journal of Crystal Growth*, **307**(1), 137 (2007).
9. E. Akyol, M. Öner, *Journal of Crystal Growth*, **401**, 260 (2014).
10. N. Cabrera, D.A. Vermilyea, Growth and Perfection of Crystals, Wiley, New York, 1958, p. 393.
11. N. Kubota, J. W. Mullin, *Journal of Crystal Growth*, **152**(3), 203 (1995

Photocatalytic activity of TiO$_2$-Cu-metal-organic framework (MOF)

A. Katırcı[1], M. E. Kibar[2], F. Uğur Nigiz[3]*

[1]Çanakkale Onsekiz Mart University, School of Graduate Students, Çanakkale, Türkiye
[2]Kocaeli University, Chemical Engineering Department, Kocaeli, Türkiye
[3]Çanakkale Onsekiz Mart University, Chemical Engineering Department, Çanakkale, Türkiye

The accumulation of greenhouse gases including carbon dioxide (CO$_2$) in the atmosphere has greatly increased with industrialization and creates serious problems on our environment such as global warming, melting of glaciers, sea level rise, and extinction of species. One of the solutions is to reduce the level of CO$_2$. CO$_2$ conversion can be achieved in a sustainable and environmentally safe way by a light-based photocatalytic method.

In this study, a titanium dioxide doped copper metal organic framework (TiO$_2$/Cu-MOF-NH$_2$) based photocatalyst was prepared for the photocatalytic reduction of CO$_2$. MOFs are effective photocatalysts after surface modification, structuring with other semiconductors, and doping with metal nanoparticles. The activity of the photocatalyst (TiO$_2$/Cu-MOF-NH$_2$) was determined by means of synthetic dye reduction reaction. In order to determine the effect of TiO$_2$ on the MOF structure, characterization of TiO$_2$/Cu-MOF-NH$_2$ and Cu-MOF-NH$_2$ was done. The photocatalysts were characterized using Fourier transform infrared spectroscopy, scanning electron microscopy, and X-ray diffraction tests. As a result, 17% of adsorption and 31.7% adsorption-photocatalysis were achieved by TiO$_2$/Cu-MOF-NH$_2$ photocatalysis.

Keywords: CO$_2$ Reduction, Metal-organic framework (MOF), Photocatalyst, Photocatalytic activity

INTRODUCTION

Due to the rapid increase in global population and industrialization, the rate of energy consumption is rapidly increasing. The energy demand has rapidly increased over the years, however, clean and sustainable energy resources are limited. Although the renewable energy sources such as wind energy and solar energy are gaining importance, most the of energy is still provided by fossil fuels such as coal and oil. The use of fossil fuels causes significant accumulation of greenhouse gases such as carbon dioxide (CO$_2$) in the atmosphere. Therefore, this accumulation causes serious problems on the environment such as global warming, melting of glaciers, rising sea level and extinction of species [1]. The increased amount of CO$_2$ should be reduced to an appropriate level. In order to prevent the rising of CO$_2$, different chemical and physical techniques are used [2, 3]. Cryogenic techniques, membrane separation techniques, natural cyclic cycles are some physical techniques that allow carbon dioxide to be removed before or after combustion. However, the removal of carbon dioxide by converting it into more valuable chemicals is the most beneficial approach both environmentally and economically. Catalytic, biocatalytic and photocatalytic conversion of carbon dioxide to chemicals such as methanol, ethanol, formic acid, dimethyl ether has come to the fore in recent years. Among these techniques, photocatalytic carbon dioxide conversion is the most effective one because of its low energy consumption and safe process.

Photocatalysts are semiconductor materials that are activated under light and cause catalytic reactions. Photocatalysts increase product efficiency as they have high surface area for small particle size. They have advantages such as non-toxic nature and possibilities of environmentally friendly process design. They also increase selectivity for a single chemical synthesis [4]. Photocatalyst classification defined by Nikokavoura & Trapalis [5] is as follows:

- Inorganic: single metal oxides, mixed metal oxides, metal oxide composites, layered double hydroxides and salt composites;
- Carbonaceous: graphene (GR), carbon nanotubes (CNTs) and g-C$_3$N$_4$ composites;
- Hybrid organic-inorganic photocatalytic materials.

Low-band gap photocatalysts are preferred as they are easily excitable under visible light. It is common to use additives or incorporate noble metals into the material to create a visible photosensitive catalyst. In addition, physical changes can be made to the catalyst and its support to adjust the photocatalytic performance [6, 7].

* To whom all correspondence should be sent:
E-mail:filiz.ugur@comu.edu.tr

To summarize the ways to develop an effective catalyst, there are two critical points. The first is to increase the visible light absorption by reducing the band gap. The second is to limit the recombination of photoinduced charge carriers [8].

Many photocatalysts have been studied by researchers. It has been reported that semiconductors such as TiO$_2$, ZnO, CdS and Fe$_2$O$_3$ are used as photocatalysts [9]. TiO$_2$ is the most widely used photocatalyst due to its non-toxicity, high activity and stability. ZnO and CdS are less photoactive than TiO$_2$ and have some disadvantages such as releasing Cd^{2+} and Zn^{2+} ions into the solution [10].

There are many studies in the literature on the use of TiO$_2$ as a photocatalyst. The main purpose here is to increase the photocatalytic activity. For this, the surface area of the catalyst must be increased using some supports. In this way, both the photocatalytic surface area and the reaction capacity increase, that is, the conversion efficiency increases. Many materials can be used as supports, such as clays, zeolites, polymers are some of them. In recent years, metal organic cages are preferred as support layers due to their favorable properties.

MOFs are formed by the bonding of metal ions with organic ligand groups. Researches are carried out in many application areas such as gas storage, separation, catalysis, drug release with MOFs. The main features of MOF-based materials are high porosity, high surface area, tunable structure, and multiple active sites. When synthesizing MOFs, they can be designed depending on the way metal ions and organic ligands come together in their structures. Thus, the structures and properties of MOFs can be adjusted during synthesis. Post-synthesis modifications are also possible [11].

Many MOF materials have been used in the literature for carbon dioxide removal. These materials consist of different metal groups [12-15]. In particular, MOF materials containing copper bonded group were found to be successful in chemical reduction. For example, in a study performed by Wang *et al.* [16], CTU/TiO$_2$ composite photocatalysts were successfully prepared. The resulting composites exhibited significantly improved photocatalytic activity for CO$_2$ reduction compared to pure TiO$_2$ or CTU. The outcome of this work has provided new insights into the design of MOF-based hybrid nanomaterials for efficient photoreduction of CO$_2$ [16]. However, the production values are still not at the desired levels. In particular, the success of the structures with NH$_2$ end groups in carbon dioxide adsorption has been observed [17-19].

In this study, a TiO$_2$-supported NH$_2$ end group copper-based MOF material (TiO$_2$/Cu-MOF-NH$_2$) was synthesized for the photocatalytic conversion of carbon dioxide to more valuable chemicals. Basic characterization tests of the synthesized MOF material were carried out. Afterwards, synthetic dye removal studies were carried out to determine its photocatalytic activity.

EXPERIMENTAL

Materials

Aminoterepthalic acid, copper (II) nitrate trihydrate, methylene blue were purchased from Sigma Aldrich. N,N-dimethylformamide (DMF) and methanol solvents were purchased from Merck Chemicals, Turkey.

MOFs preparation

Cu-MOF-NH$_2$ synthesis. 0.724 g of copper (II) nitrate trihydrate and 1.644 g of aminoterephthalic acid were dissolved in a mixed solvent of DMF and methanol (36/4 ml) under magnetic stirring for 30 minutes. The solution was kept under magnetic stirring at 180 ºC for 72 hours. Then it was filtered and washed 3 times with DMF and methanol. Finally, the obtained product was dried in an oven at 80 ºC.

TiO$_2$/Cu-MOF-NH$_2$ synthesis. 0.7 g of TiO$_2$, 0.724 g of copper (II) nitrate trihydrate and 1.644 g of aminorephthalic acid were dissolved in a mixed solvent of DMF and methanol (36/4 ml) under magnetic stirring for 30 minutes. The solution was kept under magnetic stirring at 180 ºC for 72 hours. Then it was filtered and washed 3 times with DMF and methanol. Finally, the obtained product was dried in an oven at 80 ºC.

Synthetic dye reduction reaction experiment. Methylene blue (MB) was used in the reduction reaction experiment of synthetic dye. The reaction conditions are given in Table 1.

Table 1. Reaction conditions

Reaction conditions	
C$_{MB}$	10 ppm
V$_{reaction}$	25 mL
m$_{cat}$	0.05 g
W$_{UV}$	46 W
t$_{light}$	120 min
t$_{dark}$	120 min

The synthetic dye removal reaction was carried out both in the dark and in the light. For this, two 10 ppm 25 mL dye solutions were prepared at the same time. 0.05 g of photocatalyst was added to the

solutions. One of the solutions was left under UV light and the other in the dark for two hours. Then, the products were centrifuged at 3000 rpm for 4 minutes. Finally, measurements were made by UV-Vis spectroscopy (Shimadzu 1280) at 665 nm.

In order to determine the concentration of MB before and after reaction, a calibration curve was drawn by measuring the absorbance value at different concentrations of MB from 1 ppm to 16 ppm. The curve is given in Fig 1.
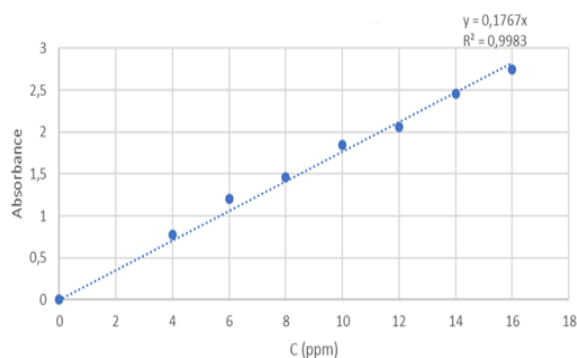
Fig. 1. Methylene blue (MB) calibration chart

The measured values were used in the yield calculation. The equation used to calculate the yield is given below:

$$\% \ Yield = \frac{Al - Ad}{Al} \ x \ 100 \qquad (1)$$

where A_l is the 'measured' value determined from the methylene blue calibration chart for the absorbance value under light. A_d is the 'measured' value determined from the methylene blue calibration chart for the absorbance value in the dark. Thus, the catalytic efficiency of the photocatalysts was calculated.

In the first stage of the study, the catalyst was prepared with and without TiO₂ and was characterized and compared.

The photocatalyst with TiO₂ was named TiO₂/Cu-MOF-NH₂ and the catalyst without TiO₂ was named Cu-MOF-NH₂. X-ray diffraction test (XRD), Fourier transform infrared spectroscopy (FTIR), and scanning electron microscopy (SEM) analysis were done. XRD was used to determine the phase structure of photocatalysts (TiO₂/Cu-MOF-NH₂ and Cu-MOF-NH₂), FTIR was used to identify organic functional groups, SEM was used to examine the material surface.

XRD analysis

XRD patterns of TiO₂/Cu-MOF-NH₂ and Cu-MOF-NH₂ photocatalysts are shown in Fig. 2. It is seen that MOF and TiO₂ MOF have crystalline structure and well match with the same family groups of MOFs in the literature. It can be observed that the XRD pattern of TiO₂/Cu-MOF-NH₂ shows diffraction peaks at around 10°, 20°, 24°, 26°, which are corresponding to the MOF structure. The peaks of anatase of TiO₂ are seen around 36°. According to the literature, the 10.30°, 11.84°, 16.82°, 20.67° and 24.73° diffraction peaks of the Cu-MOF-NH₂ photocatalyst at 2θ indicate a crystal structure [20]. Therefore, it can be said that Cu-MOF-NH₂ photocatalysts are in crystalline form. When the XRD pattern of Cu-MOF-NH₂ photocatalysts and TiO₂/Cu-MOF-NH₂ photocatalysts are compared, first large refractions occurred in the Cu-MOF-NH₂ XRD pattern and then the diffractions decreased to a large extent. In TiO₂/Cu-MOF-NH₂ XRD pattern although the diffractions decreased, they were still present. In addition, TiO₂/Cu-MOF-NH₂ photocatalyst has not been synthesized before in the literature. For this reason, there is no source that we can directly compare.

RESULTS AND DISCUSSION
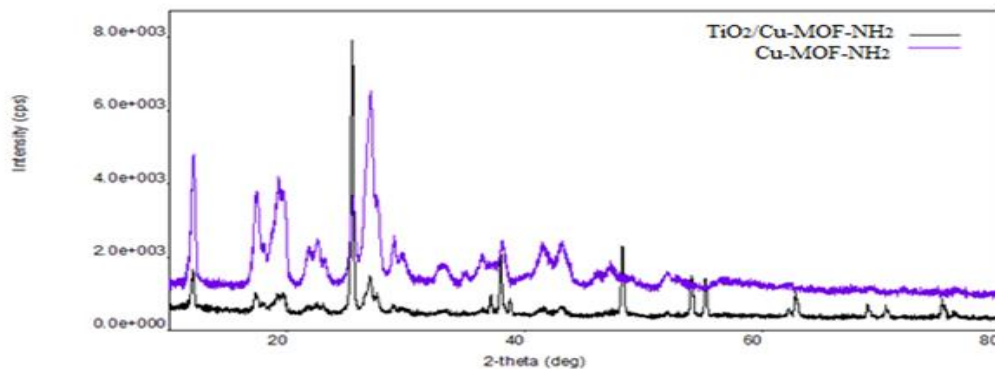
Fig. 2. XRD analysis of TiO₂/Cu-MOF-NH₂ and Cu-MOF-NH₂ photocatalysts.
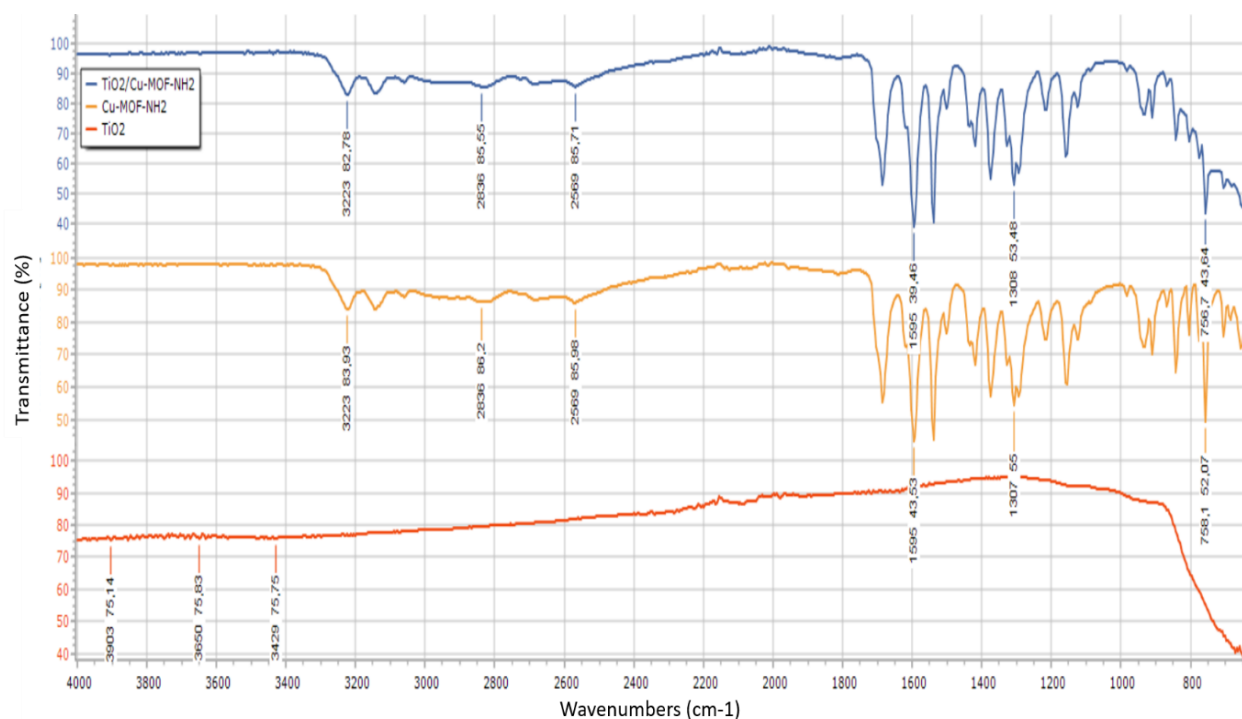
Fig. 3. FTIR analysis of TiO$_2$/Cu-MOF-NH$_2$, Cu-MOF-NH$_2$ and TiO$_2$.
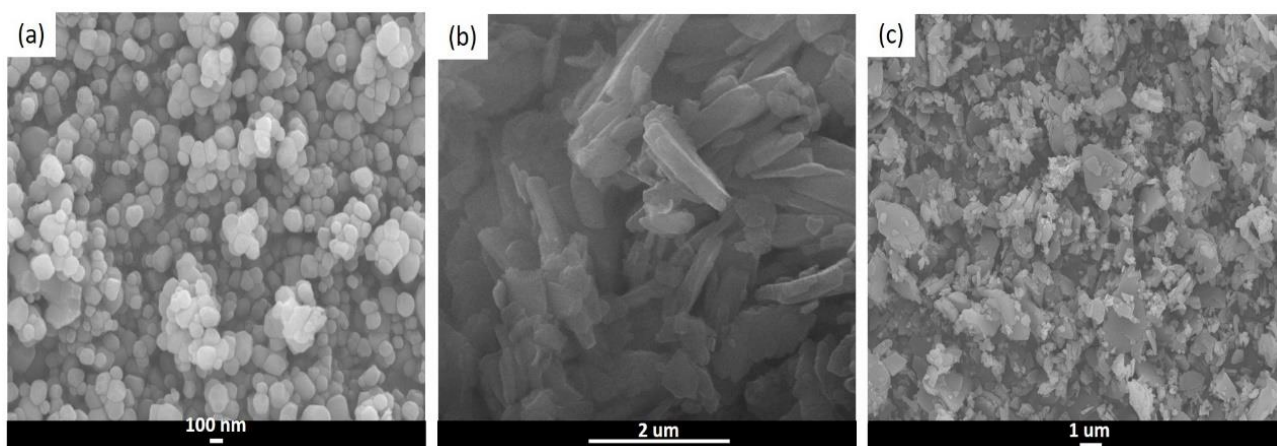
Fig. 4. SEM image**s** of TiO$_2$ (a), Cu-MOF-NH$_2$ (b) and TiO$_2$/Cu-MOF-NH$_2$ photocatalysts

Table 2. Results of synthetic dye reduction reactions for TiO$_2$/Cu-MOF-NH$_2$

	Absorbance value (abs)	Measured (ppm)	Absorbed in the Cat (ppm)	Removal (%)	Reaction yield (%)
TiO$_2$/Cu-MOF-NH$_2$ in the dark	1.467	8.30	1.70	17	
TiO$_2$/Cu-MOF-NH$_2$ under UV light	1.206	6.83	1.70	31.7	17.79
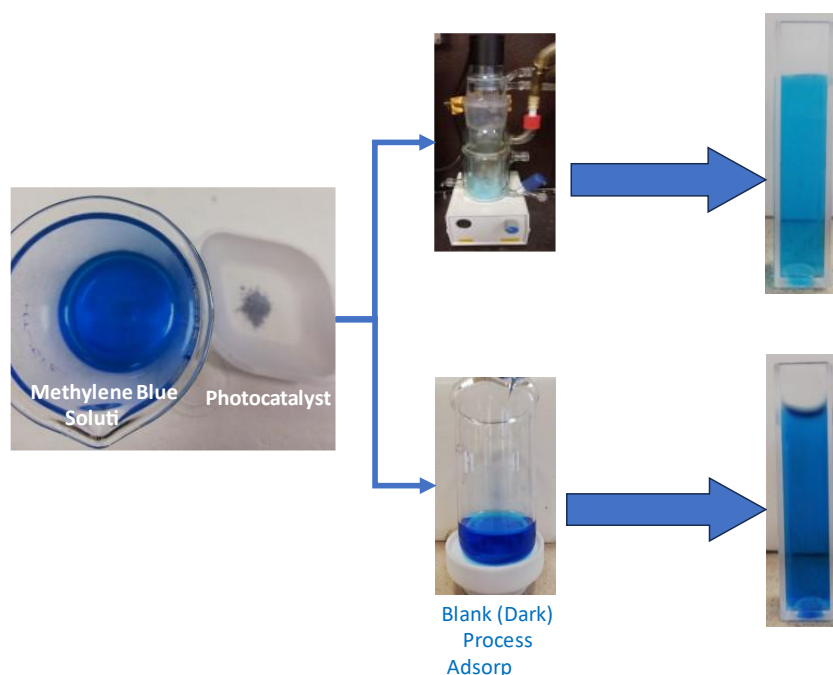
Scheme 1. Scheme of synthetic dye reduction reaction experiment.

FTIR analysis

FTIR results of TiO_2, Cu-MOF-NH_2 and TiO_2/Cu-MOF-NH_2 photocatalysts are shown in Fig. 3. There are several characteristic peaks of MOF materials in the first two lines. For example; the N-H stretching vibration gives peaks around 3223 cm^{-1} for both MOFs. The symmetric and asymmetric stretching vibrations of C-H are revealed in the range of 2836 cm^{-1} and 2569 cm^{-1}, respectively. The C=O stretching vibration peak is seen around 1595 cm^{-1}. The sharp peak at 1307 cm^{-1} is corresponding to the C-C vibration. The characteristic peak of Cu-O bonding can be seen at around 750 cm^{-1} for both MOF materials. Since the device used experimentally was ATR (Cary 630 FTIR spectrometer – Agilent), it can measure up to 600 cm^{-1}. TiO_2 bonds are seen below 500 cm^{-1}. Therefore, even if it is not possible to see the direct TiO_2 bonds, it is possible to see the effect below 700 cm^{-1}. A change was observed at the peaks below 700 cm^{-1} of and TiO_2/Cu-MOF-NH_2 material. In the literature, in MOFs that are directly treated with TiO_2 without modification, an O-H bond at around 3400 cm^{-1} is observed. In this study, TiO_2 was used after the thermal treatment, therefore, these bonds have disappeared.

SEM analysis

The morphological structures of TiO_2, Cu-MOF-NH_2, and TiO_2/Cu-MOF-NH_2 photocatalysts are seen in Fig. 4. As seen in Figure 4a, TiO_2 particles are completely spherical, homogeneous and nanosized. The structure of the Cu-MOF-NH_2 material has a layered arrangement. Geometric structures are mostly roughly quadrangular. However, there are also round structures. Their length and width are micro sized and their thickness is in the nanoscale (Figure 4b). TiO_2/Cu-MOF-NH_2 material appears as a mixture of TiO_2 and Cu-MOF-NH_2. Both structures can be seen. TiO_2 particles were found to adhere to MOFs throughout all particles. This is an important finding that shows that photocatalysis can do its task. Cu-MOF-NH_2 keeps carbon dioxide in its structure, while TiO_2 provides photocatalytic activity. In this way, it is seen that the catalyst-substrate contact can increase and this can significantly affect the reaction efficiency.

Results of synthetic dye reduction reactions

The photocatalytic activity of the synthesized samples was calculated by measuring the absorption value of methylene blue as it was decomposed by photocatalysts under UV light and the absorption value of the sample in the dark. Thus, the catalytic efficiency of the photocatalysts was found. The absorbance values and photocatalytic efficiency of the photocatalysts are shown in Table 2.

The table shows the results of the experiments carried out in both dark and light conditions. Since there is no photocatalytic reaction in the experiments carried out in the dark, the separation result depends on the adsorption ability of the photocatalyst, while the result seen in the light includes both adsorption and photoreaction. MOF is a microporous material with a very wide active adsorption area. In the BET analyzes performed, the surface area was found to be close to 480 m^2/g. This indicates that it is prone to

dye adsorption due to its large surface area. There are already many studies in the literature in which copper-based MOF materials are used as adsorbents [21-24].

In the experiments carried out in the light, both the adsorption and reaction results of the synthesized MOF are included. Since there is also a catalytic effect here, it is not possible to determine how much of the separation value obtained is adsorption. For this reason, 1.7 ppm, 17% separation, which is the value in the dark, was taken as the same type and used at the same rate. The rest of the total separation value of 31.7% was realized as a result of the photocatalytic reaction. This result can be seen in Scheme 1. The color of the dye solution obtained in the experiments performed under UV light is much lighter. As seen in the studies in the literature, the MOF-supported photocatalyst acts as a multifunctional material by performing simultaneously both adsorption and reaction [25-27]. As seen in the table, the photoreaction efficiency was calculated as 17.79%.

CONCLUSION

The accumulation of carbon dioxide (CO$_2$) creates serious problems in our environment. A solution is needed and one of the solutions developed is CO$_2$ reduction by a photocatalytic reduction method. Photocatalysis is a method based on the use of catalysts and light. Photocatalysts are very important for the photocatalysis method and new photocatalysts need to be developed. Therefore, we synthesized TiO$_2$/Cu-MOF-NH$_2$. The photocatalyst was characterized using FTIR, SEM and XRD tests. According to the results the TiO$_2$/Cu-MOF-NH$_2$ was successfully synthesized. The results of the synthetic dye reduction showed that the TiO$_2$/Cu-MOF-NH$_2$ photocatalyst has photocatalytic activity. Photocatalytic efficiency of the photocatalyst is 17.79%. Therefore, this study encourages the use and development of TiO$_2$/Cu-MOF-NH$_2$ as a photocatalyst.

REFERENCES

1. P. Prabhu, V. Jose, J. M. Lee, *Adv. Funct. Mater.*, **30**(24) (2020).
2. N. S. Sifat, Y. Haseli, *Energies*, **12**(21), 4143 (2019).
3. F. Nocito, A. Dibenedetto, *Curr. Opin. Green Sustain. Chem.*, **21**, 34 (2020).
4. S. Chakrabortty, J. Nayak, B. Ruj, P. Pal, R. Kumar, S. Banerjee, M. Sardar, P. Chakraborty, *J. Environ. Chem. Eng.*, **8** (2020).
5. A. Nikokavoura, C. Trapalis, *Appl. Surf. Sci.*, **391**, 149 (2017).
6. H. Abdullah, M. R. Khan, M. Pudukudy, Z. Yaakob, N.A. Ismail, *J. Rare Earths*, **33** (11), 1155 (2015).
7. X. Meng, T. Wang, L. Liu, S. Ouyang, P. Li, H. Hu, T. Kako, H. Iwai, A. Tanaka, J. Ye, *Angew. Chem.*, **53** (43), 11478 (2014).
8. M. Tahir, N. S. Amin, *Renew. Sust. Energ. Rev.*, **25**, 560 (2013).
9. M. R. Uddin, M. R. Khan, M. W. Rahman, A. Yousuf, C. K. Cheng, *React. Kinet. Mech. and Catal.*, **116**, 589 (2015).
10. J. Low, J. Yu, W. Ho, *J. Phys. Chem. Lett.*, **6** (21), 4244 (2015).
11. A. M., Idris, X. Jiang, J. Tan, Z. Cai, X. Lou, , J. Wang, Z. Li, *J. Colloid Interface Sci*, **607**, 1180 (2022).
12. X. Li, Q. L. Zhu, *Energy Chem.*, **2**(3), 100033 (2020).
13. Y. N. Gong, L. Jiao, Y. Qian, C. Y. Pan, L. Zheng, X. Cai, H. L. Jiang, *Angew. Chem.*, **132**(7), 2727 (2020).
14. D. Li, M. Kassymova, X. Cai, S. Q. Zang, H. L. Jiang, *Coord. Chem. Rev.*, **412**, 213262 (2020).
15. C. Liu, W. Wang, B. Liu, J. Qiao, L. Lv, X. Gao, F. Wang, *Catalysts*, **9**(8), 658 (2019).
16. L. Wang, P. Jin, S. Duan, H. She, J. Huang, Q. Wang, *Sci. Bull.,* 926 (2019).
17. J. Lu, S. Wang, Y. Zhao, K. Ge, J. Wang, H. Cui, Y. Yang, *Catal. Commun.*, 106613 (2023).
18. D. Sun, Y. Fu, W. Liu, L. Ye, D. Wang, L. Yang, Z. Li, *Chem. Eur. J.*, **19**(42), 14279 (2013).
19. L. Liu, J. Zhang, X. Cheng, M. Xu, X. Kang, Q. Wan, C. Ma, *Nano Res.*, **16**(1), 181 (2023).
20. B. C. de Silva, K. Irikura, J. B. S. Flor, R. M. M. dos Santos, A. Lachgar, R. C. G. Frem, M. V. B. Zanoni, *J. CO$_2$ Util.*, **42** (2020).
21. I. Mantasha, H. A. Saleh, K. M. Qasem, M. Shahid, M. Mehtab, M. Ahmad, *Inorganica Chim. Acta*, **511**, 119787 (2020).
22. Q. Fu, D. Shi, C. Mo, J. Lou, S. Zhou, L. Zha, J. Luo, *J. So*lid State Chem.*, **311**, 123100 (2022).
23. M. Ş. Eren, H. Arslanoğlu, H. Ciftci, *J. Environ. Chem. Eng.*, **8**(5), 104247 (2020).
24. S. Lin, Z. Song, G. Che, A. Ren, P. Li, C. Liu, J. Zhang, *Microporous Mesoporous Mater.*, **193,** 27 (2014).
25. Y. Pi, X. Li, Q. Xia, J. Wu, Y. Li, J. Xiao, Z. Li, *Chem. Eng. J.*, **337**, 351 (2018).
26. H. Wang, X. Yuan, Y. Wu, G. Zeng, X. Chen, L. Leng, H. Li, *Appl. Catal B*, **174,** 445 (2015).
27. M. S. Samuel, K. V. Savunthari, S. Ethiraj, *Environ. Sci. Pollut. Res.*, **28**, 40835 (2021).
28. Z. Li, J. Chu, D. Meng, Y. Wen, X. Xing, H. Miao, Y. Li, *ACS Catal.*, **9**(9), 8659 (2019).
29. A. D. Tjandra J. Huang, *Chin. Chem. Lett.,* **29**, 734 (2018).

Polysaccharide-based films for transdermal drug delivery systems

D. Ekşi, E. Akyol, I. Küçük*

Yildiz Technical University, Department of Chemical Engineering, Istanbul, Turkey

Polysaccharide-based materials are derived from plants and can be blended with other bioactive materials to enhance their properties, resulting in improved drug release, stability, bioavailability, and target specificity. Polysaccharides are known to exhibit delayed color development, reduced acidity, and increased firmness in drug materials. Therefore, it is necessary to study the mechanisms underlying their kinetics to understand their high activities, potencies, and specificities when used in pharmaceutical products.

The present study aims to investigate the potential of various polysaccharides as transdermal films to control the release of donepezil hydrochloride, a drug commonly used to treat Alzheimer's disease. For this purpose, pectin and guar gum were used as a polysaccharide-based polymer matrix for the transdermal films. The drug release kinetics was determined by analyzing samples taken at various time intervals using a UV spectrophotometer. *In vitro*, drug release studies were performed for donepezil hydrochloride by using a Franz diffusion cell which simulates human skin. To investigate release kinetics, data obtained from *in-vitro* drug release studies were plotted in various kinetic models which include zero order, first order, Higuchi and Korsmeyer-Peppas. The results in the present work confirm the controlled release of donepezil hydrochloride and the polysaccharide content of the transdermal patch can extend the release of donepezil hydrochloride. Therefore, the study's results suggest that pectin and guar gum have potential as new materials for developing treatments for Alzheimer's disease and other diseases that require continuous drug release.

Keywords: Drug delivery**,** Donepezil hydrochloride, Polysaccharide, Alzheimer

INTRODUCTION

Alzheimer's disease is a progressive neurodegenerative condition that predominantly affects the elderly population. While most of the treatment for Alzheimer's disease is administered orally, this treatment method has disadvantages for elderly patient groups with difficulties in memory and swallowing. Transdermal drug delivery systems offer advantages over oral dosage forms in the management of various diseases [1-4].

Transdermal drug delivery systems (TDDS) have emerged as a promising alternative to conventional methods of administering drugs due to their numerous advantages. Unlike oral administration, TDDS allow for controlled and sustained release of drugs through the skin over an extended period. This controlled release ensures a constant dosage, improves therapeutic efficacy, and minimizes fluctuations in drug concentration. Additionally, transdermal administration is non-invasive, eliminating the need for invasive procedures and reducing the risk of complications and infections associated with traditional methods [5, 6].

The convenience of transdermal patches or topical applications also enhances patient compliance by simplifying the drug regimen and reducing the frequency of dosing.

Moreover, transdermal administration enhances the bioavailability of the drug and improves therapeutic efficacy by bypassing the organs responsible for first-pass metabolism [7-9].

Transdermal drug delivery systems typically consist of three main components: a drug reservoir, a polymer matrix, and a skin adhesive layer. The polymers used in TDDS must possess biocompatibility, biodegradability, and suitable mechanical properties. Recently, polysaccharides like pectin and guar gum have gained attention as promising candidates for transdermal drug delivery systems. These polysaccharides exhibit desirable properties such as biocompatibility, biodegradability, and ability to form a gel-like matrix, facilitating sustained drug release and improved skin adhesion. The inclusion of other bioactive ingredients such as plasticizers, antimicrobial agents, or therapeutic drugs can further enhance the properties of transdermal drug delivery systems [10, 11].

The aim of the present study was to develop a transdermal drug delivery system for controlled release of donepezil hydrochloride which is mainly used in the treatment of Alzheimer's disease. For this purpose pectin, guar gum, glycerol, and boric acid were used in the formulation of transdermal patches. The *in vitro* drug release studies were carried out

---

* To whom all correspondence should be sent:
E-mail: kucuk@yildiz.edu.tr

using a Franz diffusion cell for donepezil hydrochloride loaded films at pH 7.4.

MATERIALS AND METHOD

Materials

Pectin and guar gum were purchased from Benosen Company. Glycerol, used as a plastizer, was purchased from Tekkim Kimya. Boric acid was supplied from Eti Maden and donepezil hydrochloride was supplied by Abdi İbrahim Medicine Company, Turkey.

Transdermal film preparation

Transdermal films were prepared by using the solvent casting technique. Guar gum and pectin were used as polysaccaharide-based polymers and they were weighed and then dissolved in distilled water under stirring using a magnetic stirrer for a duration of thirty minutes to ensure proper dissolution and uniformity. After this period, glycerol was added as a plastizer, boric asit as an antibacterial agent and donepezil hydrochloride as a drug. The formulation of the polysaccharide-based transdermal films is summarized in Table 1.The final solutions were kept at rest for another 2 h to eliminate the bubbles formed. To obtain the films, 14 g of the solution was poured onto circular Petri dishes (12 cm in diameter) and dried for 72 h at 37 ◦C. Schematic presentation of the experimental procedure can be seen in Figure 1.
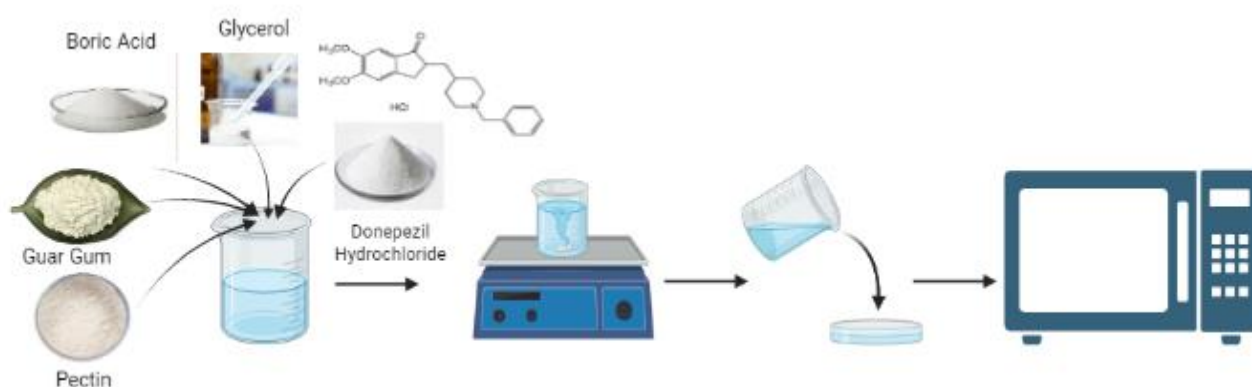
Figure 1. Schematic presentation of the experimental procedure for preparing transdermal films

Table 1. Formulation of transdermal films

Film code	2% Pectin (ml)	2% Guar gum (ml)	Glycerol (% w/v)	Boric acid (% w/v)	Donepezil - HCl (% w/v)
PGB-1	100	-	2	0.1	1.43
PGB-2	75	25	2	0.1	1.43
PGB-3	50	50	2	0.1	1.43
PGB-4	25	75	2	0.1	1.43
PGB-5	-	100	2	0.1	1.43
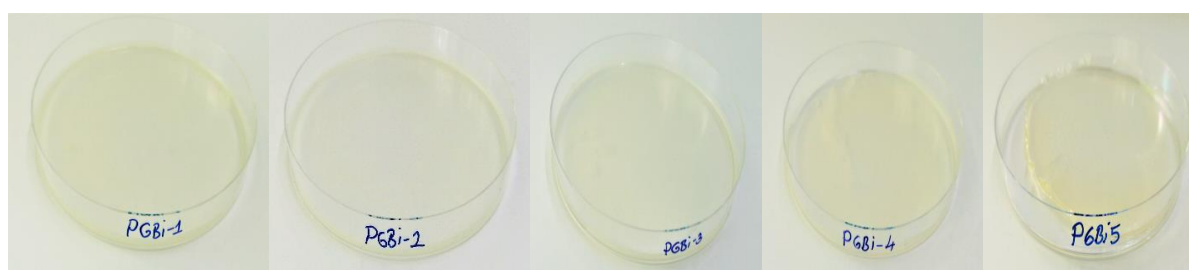
Figure 2. The dried state of the films

Table 2. Release kinetic models

Release kinetic modeling	
Zero-order model	$Q=Q_o+k*t$
First-order model	$Q/Q_o =1-e^{(-k*t)}$
Higuchi model	$Q=k*t^{1/2}$
Korsmeyer-Peppas model	$Q/Q_o =k*t^n$

RESULTS

Drug release experiments

In vitro, drug release studies were conducted with a vertical Franz diffusion cell shown in Figure 2. Transdermal film samples prepared by guar gum and pectin were placed in the membrane section of the Franz cell. Cellulose acetate membrane filters, with a diameter of 47 mm and a pore size of 0.45 µm, were prepared and placed in a pH 7.4 phosphate buffer (PBS) solution to mimic the skin. The prepared films were positioned on the cellulose acetate membrane filter, sandwiched between the diffusion cell cover and the receiver chamber. The top of the diffusion cell cover and the tip of the sampling tube were covered with parafilm to prevent evaporation. The diffusion cell was maintained at 36.8°C to represent body temperature by incubating under shaking at 100 rpm. Drug release was achieved in the diffusion cell for 8 hours. The hourly samples were collected and analyzed using a UV-vis spectrophotometer based on the absorbance at 270 nm. A linear calibration curve was constructed at a concentration range of approximately 0-40 mg/L with R^2 value of 0.9996.

Kinetic behavior of drug release

Drug release kinetic behavior graphs are used to understand the release of drugs from a formulation over time. These graphs typically plot the cumulative percentage of drug released *versus* time. The shape of the graph can provide information about the drug release mechanism and kinetics. Different models can be used to fit the experimental data and interpret the drug release kinetics. It includes first-order, zero-order, Korsmeyer-Peppas and Higuchi models. Factors that can affect drug release kinetics include the composition and morphology of the carrier, surface morphology, and molecular structures of the polymers. Understanding the drug release kinetics is important in formulating drugs with desired delivery and predicting the behavior of the formulated drug *in vivo*. Therefore, the kinetics of donepezil hydrochloride drug release during the pH 7.4 phosphate buffer permeability study were determined using the zero-order, first-order, Higuchi equation and Korsmeyer-Peppas equations. The equations for the release kinetic models are given in Table 3 below.

Q is the amount of drug dissolved in time, Q_0 is the initial amount of drug in the solution, k is the zero order release constant expressed in units of concentration/time [11-13].

R^2 regression coefficient values found by using the kinetic model equations are shown in Table 3. According to the table, the highest R^2 values were observed in Higuchi and Korsmeyer-Peppas release kinetics. As a result, it was seen that the films fit the Korsmeyer-Peppas model and the release mechanism was examined through this model. The results are shown in Table 3.

The controlled release behavior of the drug from polymer matrices was characterized by the Korsmeyer-Peppas equation. The values of the emission exponent (*n*) obtained from the slope of log t *versus* %log emission plot indicate that the release mechanism is working. Table 4 presents the *n* values of the five films obtained using the provided equation. The experimental findings indicate that the release of the drug from PGBI-5 film formulations adheres to the Fickian diffusion mechanism, as evidenced by the values of *n* being less than or equal to 0.45. Moreover, during instances of abnormal drug release, a combination of Fickian diffusion and polymer chain relaxation/erosion within the hydrated layers of the matrix is observed. The involvement of additives is believed to contribute to the overall release process by influencing these two mechanisms. In contrast, film formulations PGBI-1, PGBI-2, PGBI-3, and PGBI-4 exhibit a non-Fickian mechanism, as indicated by their *n* release exponent values falling within the range of $0.45<n<0.89$. Consequently, it can be inferred from these results that the drug release process is dependent on both drug diffusion and polymer relaxation, signifying the interplay between these factors.

Table 3. Regression coefficients according to release kinetic models

Film code	Zero-order kinetic model	First-order kinetic model	Higuchi kinetic model	Korsmeyer – Peppas kinetic model
PGB-1	0.5492	0.3234	0.7478	0.88829
PGB-2	0.5313	0.3339	0.7622	0.8656
PGB-3	0.6129	0.443	0.8149	0.9244
PGB-4	0.6898	0.462	0.884	0.9459
PGBİ-5	0.708	0.452	0.9139	0.911
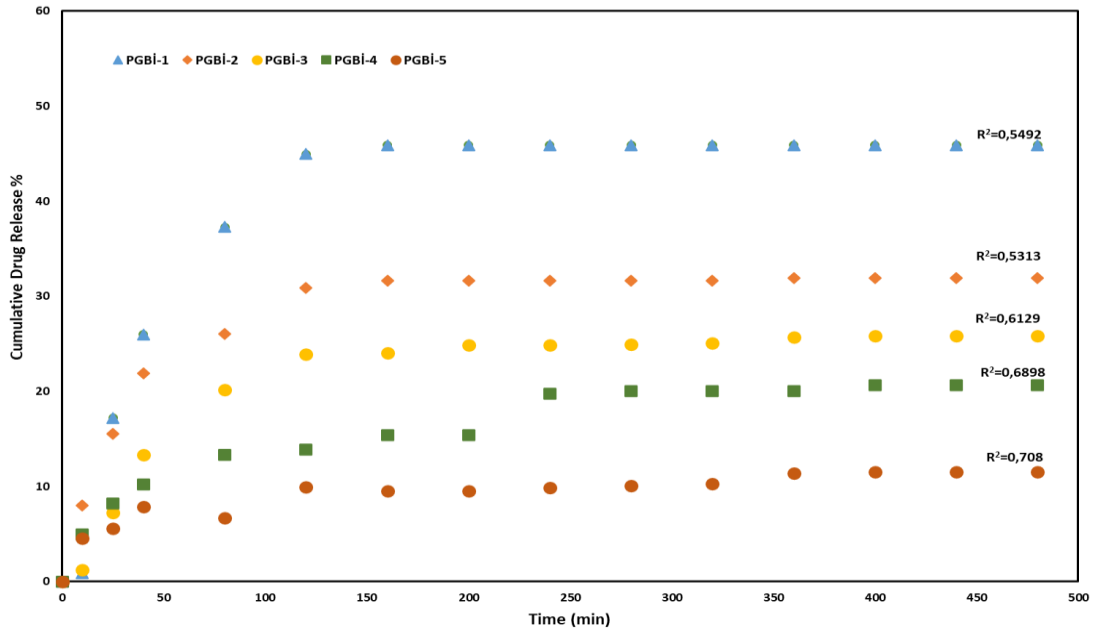
Figure 3. Zero-order kinetic model
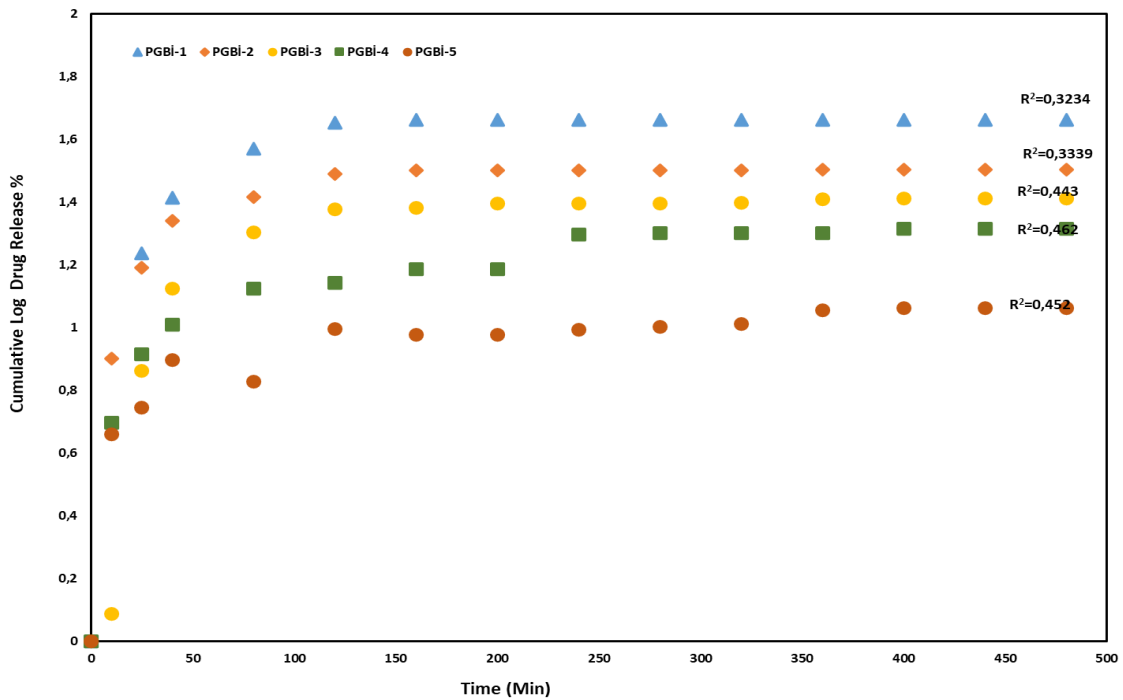
Figure 4. First-order kinetic model
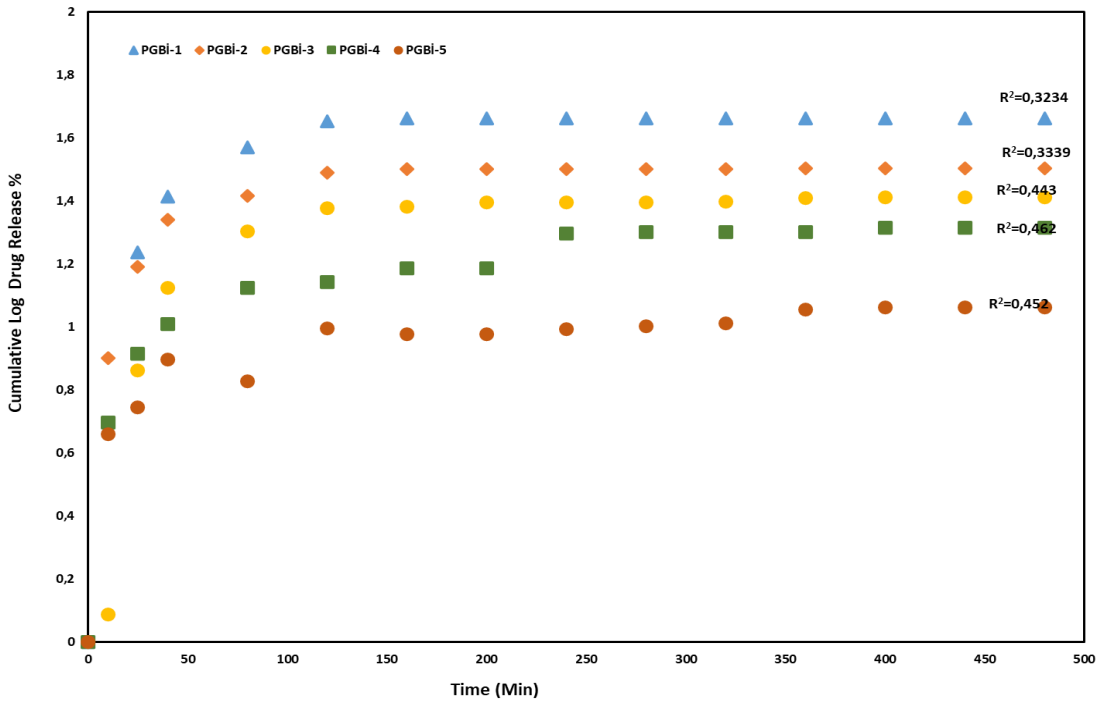
Figure 5. Higuchi kinetic model
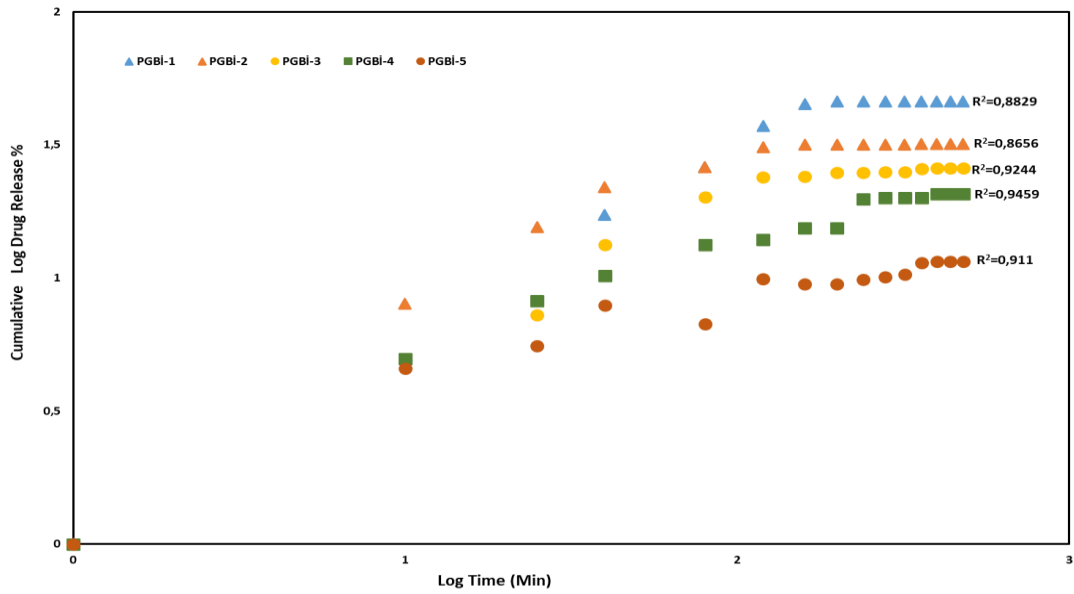
Figure 6. Korsmeyer - Peppas kinetic model

Table 4. Korsmeyer-Peppas release kinetic values

Film codes	n	k
PGBI-1	0.5842	0.2652
PGBI-2	0.5015	0.3107
PGBI-3	0.5193	0.1479
PGBI-4	0.4667	0.1686
PGBI-5	0.3476	0.1845

DISCUSSION

In this study, five different transdermal patches were successfully synthesized by incorporating varying ratios of substances and plasticizers. The introduction of different substances resulted in distinct release rates among the patches. To evaluate the drug release profiles, all patches were subjected to an 8-hour analysis in a pH 7.4 environment. Utilizing UV spectroscopy, the results revealed that the patch designated as PGBI-1 exhibited the highest release rate, measuring at 47.19%. Notably, the other patches demonstrated release rates of 33.54% for PGBI-2, 26.96% for PGBI-3, 20.68% for PGBI-4, and 10.67% for PGBI-5. These findings establish a clear correlation between the incorporated substances and the resulting drug release rates, underscoring the significance of formulation optimization for transdermal patches.

REFERENCES

1. N. Yadav, A. Mittal, J. Ali, J. Sahoo, *Current Protein and Peptide Science*, **22**(6), 458 (2021).
2. S. Sadab, S. Sahu, S. Patel, R. Khan, B. Khare, B. S. Thakur, P. K. Jain, *Asian Journal of Dental and Health Sciences*, **2**(4), 40 (2022).
3. K. Purushotham, K. A. Vijetha, *GSC Biological and Pharmaceutical Sciences*, **22**(2), 245 (2023).
4. K. A. Fratta, M. Ginder, D. A. H. Haggerty, *Journal of Emergency Medicine,* in press.
5. S. Chatterjee, P. C. L. Hui, C. W. Kan, *Polymers*, **10**(5), 480 (2018).
6. O.A. Al Hanbali, H.M.S. Khan, M. Sarfraz, M. Arafat, S. Ijaz, A. Hameed, *Acta Pharm.,* **69**(2), 197 (2019).
7. S. Chakraborty, N. V. Gupta, K. T. Sastri, M. Sharadha, P. Chand, H. Kumar, R.A.M. Osmani, D.V. Gowda, V. Jain, *Journal of Drug Delivery Science and Technology*, **73**(1), 103476 (2022).
8. X. Wang, in: SHS Web of Conferences, EDP Sciences, 2022, vol. 144, p. 01006.
9. D. Ramadon, M. T. McCrudden, A. J. Courtenay, R. F. Donnelly, *Drug Delivery and Translational Research*, 1 (2021).
10. S.E. Sanni, A.A. Adedamola, F. Ifi, E.E. Okoro, B.A. Oni, S. Bitire, R.E. Sadiku, Plant Polysaccharides as Pharmaceutical Excipients, Elsevier, 2023, p. 429.
11. Y. Acar, E. Akyol, *The Online Journal of Science and Technology*, **11**(1), 31 (2021).
12. L. Bartosova, J. Bajgar, *Current Medicinal Chemistry*, **19**(1), 4671 (2012).
13. S. Dash, P. N. Murthy, L. Nath, P. Chowdhury, *Acta Poloniae Pharmaceutica,* **67**(3), 217 (2010).

Investigation of poly(ethylene-alt-maleic-anhydride)-pregabalin (1:1) ratio controlled drug delivery system synthesized in catalyst-free media: stability and activity at different pHs

O. Eslek, D. Sakar[*]

Yildiz Technical University, Department of Chemistry, 34220, Esenler, Istanbul, Turkey

The controlled release of pregabalin drug active material covalently bound to poly(ethylene-alt-maleic anhydride) (PEAMA) copolymer was aimed in order to prevent the drug leaving the polymer matrix. Also, it was proposed to increase stability and activity of the drug, thus reducing frequent drug intake. Poly(ethylene-alt-maleic anhydride) (PEAMA) and pregabalin (PRG) at a (1:1) ratio copolymer-drug delitvery system (PEAMA-PRGI) was synthesized in catalyst-free media and was characterized by ^{1}H NMR and FTIR/ATR. The stability and activity of PEAMA-PRGI copolymer-drug delivery system were determined in different pH environments at 37 °C *via* zetasizer measurements and UV/VIS spectroscopy, respectively.

Keywords: Controlled drug delivery system, poly(ethylene-alt-maleic-anhydride), pregabalin, stability and activity

INTRODUCTION

The main purpose of controlled drug delivery systems is to release the drug to the target tissue or organ. The system offers a release with maximum therapeutic effect by controlling the amount of the drug and the duration of treatment. Maleic anhydride can be used in drug delivery systems *via* the maleic anhydride-copolymer formula. Amide, ester and carboxylic structures containing amino and hydroxyl groups can be bounded with a covalent bound to maleic anhydride group by ring-opening of the maleic anhydride [1-3]. Pregabalin is a medication commonly used to treat epilepsy, fibromyalgia, pain, and anxiety. Pregabalin has a half-life of approximately 6 hours. After oral intake of PRG, the drug reaches peak blood levels in 1.5 hours and it can be taken frequently. This reason can lead to the development of a controlled drug delivery system through conjugating with polymers [4-6].

To overcome halflife problem of PRG in body circulation, the PRG drug active substance was covalently bonded with PEAMA at (1:10) ratio. The synthesized PEAMA-PRGI copolymer-drug delivery system was structurally characterized and the stability (controlling polydispersity, particle size, mobility, zeta potential) and activity (checking maximum and minimum absorption) were determined at different pHs *via* zetasizer and UV/VIS, respectively.

EXPERIMENTAL AND INTRUMENTAL PART

Poly(ethylene-alt-maleic anhydride) (PEAMA) (Mw≃100,000-500,000, LOT: #MKCC4605) was purchased from Sigma-Aldrich. Pregabalin (PRG) was a gift from Bilim Phar- maceuticals, (purity 99.5 %). N,N-dimethylformamide (DMF) (≥99.8%) and dimethyl sulfoxide (DMSO) (≥99.9%) were purchased from Merck and used as solvents.

PEAMA-PRG controlled drug delivery system was synthesized by functionalization of PEAMA copolymer at (1:1) molar ratio with pregabalin in dimethylformamide (DMF) for 72 h at 60 °C [7]. The reaction mechanism is given in Scheme 1.
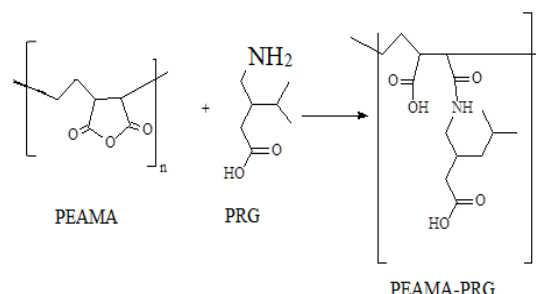
Scheme 1. Reaction mechanism of PEAMA-PRGI copolymer-drug delivery system [7].

Synthesized PEAMA-PRG controlled drug delivery system was characterized *via* FTIR-ATR (Thermo Fisher Scientific Nicolet iS10 FT-IR spectrometer which has an attenuated total reflection (ATR) apparatus) and ^{1}H NMR (Agilent Varian 400 MHz NMR spectrometer in DMSO-d6 at 25 °C). The results were discussed and details given in the master thesis of Ozge Eslek [7].

Particle size, polydispersity, mobility and zeta potential measurements for stability checking were done with Brookhaven Instruments Corporation 90Plus zetasizer. SR-542 probe was used for zeta

---

* To whom all correspondence should be sent:
E-mail: dsakar@yildiz.edu.tr

potential measurements. pH measurements were taken with Sentek P14/BNC electrode; Shimadzu UVmini-1240 spectrometer was used for controlling activity of samples using Hellma 100-QS cuvette at different pHs, at 37 °C.

RESULTS AND DISCUSSION

Structural characterization of the synthesized PEAMA-PRG (1:1) copolymer-drug delivery system was done by FT-IR/ATR and ^{1}H NMR [7].

In order to determine the stability and activity of the synthesized drug delivery systems in solution, aqueous sample solutions were prepared at different pH values, and measured with both zetasizer and UV/VIS spectrophotometer, respectively.

Zetasizer measurements of polydispersity, particle size, mobility and zeta potential of PEAMA, PRG and PEAMA-PRG (1:1) copolymer-drug delivery system gave information on the stability in aqueous solution and were done at different pH values.

The polydispersity index values of PEAMA, PRG and PEAMA-PRGI copolymer-drug delivery system at different pH values are given in Table 1.

Table 1. Polydispersity index values of PEAMA, PRG and PEAMA-PRGI copolymer-drug delivery system at different pHs

pH	PRG	PEAMA	PEAMA-PRG I
2	0.312	0.405	0.188
3	0.744	0.485	0.267
4	0.716	0.341	0.379
5	0.757	0.321	0.333
6	0.638	0.564	0.322
7	0.510	0.429	0.398
8	0.623	0.583	0.474
9	0.547	0.612	0.456
10	0.568	0.664	0.437
11	0.591	0.595	0.452

Polydispersity index (PDI index) defines the width or spread of particle size distribution. It is expressed as a dimensionless number extrapolated from the autocorrelation function in photon correlation spectroscopy. The value of polydispersity index may vary from 0.01 (mono dispersed particles) to 0.5-0.7, whereas, PDI index value > 0.7 indicated broad particle size distribution of the formulation [8].

The PDI values of PEAMA, PRG and PEAMA-PRG I at different pHs were smaller than 0.7 and these results implied that the sample particles at different pHs showed monodisperse particle size distributions. If comparing the distribution of PRG and PEAMA particles with the distribution of PEAMA-PRGI particles, we will see that PEAMA-PRGI particles have a narrower distribution and uniform particles at different pHs (PDI=0.2-0.4) than PEAMA and PRG particles.

The particle sizes of PEAMA, PRG and PEAMA-PRGI copolymer-drug delivery system at different pH values are given in Table 2.

Table 2. Particle sizes (nm) of PEAMA, PRG and PEAMA-PRGI copolymer-drug delivery system at different pHs

pH	PRG	PEAMA	PEAMA-PRGI
2	1690	300	190
3	1460	290	240
4	1700	250	390
5	1880	225	230
6	1560	330	380
7	470	320	630
8	590	340	860
9	650	385	860
10	680	440	830
11	700	360	855

PRG swelled and had larger particle size values at acidic pHs compared to basic pHs, whereas PEAMA particle sizes were unaffect by pH changes. The particle size change trend of PEAMA-PRGI copolymer-drug delivery system was different from yhst of PRG and PEAMA. With increasing pH, particles of PEAMA-PRGI were 4 times swollen at basic pHs, from 190 to 855 nm and large particles were obtained after pH 6.

The mobility of PEAMA, PRG and PEAMA-PRGI copolymer-drug delivery system at different pH values is given in Table 3.

It is seen from Table 3 that PRG, PEAMA and PEAMA-PRGI are negatively charged over the studied pH ranges.

The zeta potential of PEAMA, PRG and PEAMA-PRGI copolymer-drug delivery system at different pH values is given in Table 4.

Table 3. Mobility of PEAMA, PRG and PEAMA-PRGI copolymer-drug delivery system at different pHs

pH	PRG	PEAMA	PEAMA-PRG I
2	-0.28	-1.17	-1.58
3	-0.38	-1.87	-3.58
4	-1.93	-3.72	-4.03
5	-2.69	-4.13	-5.64
6	-2.80	-5.14	-5.57
7	-3.81	-5.61	-4.94
8	-4.35	-6.73	-6.54
9	-3.92	-7.16	-6.84
10	-5.10	-7.61	-6.12
11	-4.09	-7.34	-4.65

Table 4. Zeta potential (mV) of PEAMA, PRG and PEAMA-PRGI copolymer-drug delivery system at different pHs.

pH	PRG	PEAMA	PEAMA-PRG I
2	-2.87	-12.15	-16.96
3	-3.90	-19.07	-37.10
4	-19.93	-38.46	-41.47
5	-25.41	-42.79	-58.42
6	-28.98	-53.17	-57.63
7	-39.40	-58.05	-51.09
8	-45.06	-69.92	-67.72
9	-40.58	-74.06	-70.76
10	-52.77	-78.80	-63.34
11	-42.39	-75.92	-48.15

The stability of PRG, PEAMA and PEAMA-PRGI increased with increasing pH. They were more stable at basic pH than at acidic pH.

Absorption spectra for checking activity and cumulative release of PRG from PEAMA-PRGI at different pH values are given in Figure 1 for PRG, Figure 2 for PEAMA and Figure 3 for PEAMA-PRGI.

According to the absorption spectrum, Fig. 1, PRG shows maximum activity at pH 11 (A=0.68), minimum activity at pH 6 (A=0.4) at 235 nm and PRG activity decreased by 59% from pH 11 to pH 6.
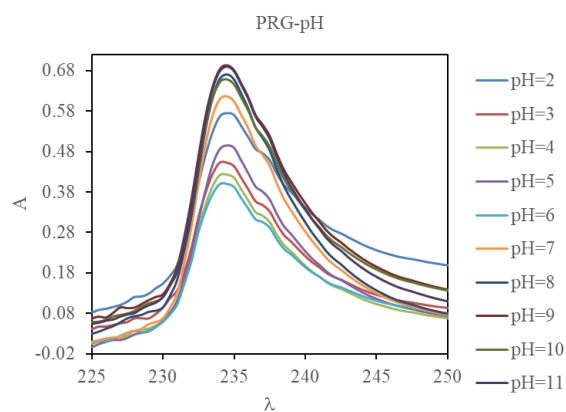
Figure 1. Absorption spectrum of PRG at different pHs
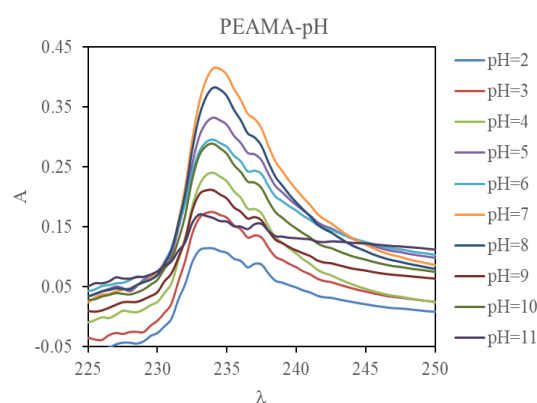
Figure 2. Absorption spectrum of PEAMA at different pHs

According to the absorption spectrum, Fig. 2, PEAMA shows maximum activity at pH 7 (A=0.4), minimum activity at pH 2 (A=0.11) at 234 nm and PEAMA activity decreased by 28% from pH 7 to pH 2.
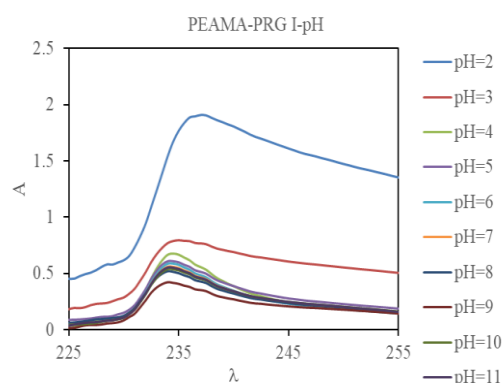
Figure 3. Absorption spectrum of PEAMA-PRGI at different pHs

According to Fig. 3, PEAMA-PRGI has maximum activity at pH 2 (A=1.9), minimum activity at pH 9 (A=0.4) at 234 nm and PEAMA-PRG I activity decreased by 21% from pH 2 to pH 9.

297

CONCLUSION

In the present study, the pH effect on the stability and activity of the synthesized PEAMA-PRGI copolymer-drug system was determined. The pH effect on the activity of PEAMA-PRGI was different from that on PRG and PEAMA. The activity of PEAMA-PRGI increased four times at acidic pH whereas maximum activity of PEAMA and PRG was obtained at pH 7, and pH 11, respectively. The maximum stability of PEAMA, PRG and PEAMA-PRGI was observed at basic pH 10, pH 10, and pH 9, respectively. PEAMA, PRG and PEAMA-PRGI were negatively charged over the studied pH ranges.

REFERENCES

1. A**.** Nagaraja, M. D. Jalageri, Y. M. Puttaiahgowda, K. Raghava Reddy, A. V. Raghu, *J. Microbiol. Methods,* **163**, 105650 (2019).
2. D. Şakar Daşdan, A. Dizdar, G. Karakus, *Bulg. Chem. Commun.*, **49**, 43 (2017)
3. H. Ringsdorf, *Journal of Polymer Science: Polymer Symposia*, 135 (1975).
4. K. Çakıral, D. Sakar, *Polymer Bulletin*, **80** (7), 7687 (2023).
5. B. M. Mishriky, N. H. Waldron, A. S. Habib, *Bras. J. Anaesth.,* **114**, 10 (2015).
6. R. Kavoussi, *Eur. Neuropsychopharmacol.,* **16**, Suppl. 2, S128 (2006).
7. O. Eslek, Yildiz Technical University, Master Thesis, Unpublished Results, 2023.
8. R. Raval, N. Maheshwari, D. Kalyane, S. R. Youngren-Ortiz, M. B. Chougule, R. K. Tekade, Advances in Pharmaceutical Product Development and Research, in book: Basic Fundamentals of Drug Delivery, Chapter 10 - Importance of Physicochemical Characterization of Nanoparticles in Pharmaceutical Product Development, R Tekade (ed.), Elsevier, 2019, p. 369.

Investigation of degradation products of secondary metabolites of Bupropion molecule by DFT methods

S. Kurumoglu[*], Y. Y. Gurkan

Tekirdag Namık Kemal University, Department of Chemistry, Tekirdag, Turkey

Every substance (food, drug, etc.) taken into the body is excreted from the body by enzymatic mechanisms and given to the natural environment it pollutes the nature. Data from the Ministry of Health show that the amount of antidepressant use has increased by about 70 percent in the 11 years until 2020. According to the latest health statistics of the Ministry for 2020, while 29 antidepressant drugs per 1000 people per day were registered in 2009, this rate increased to 49 in 2020. In addition to its use as an antidepressant, Bupropion is also used in the treatment of smoking cessation, methamphetamine and cocaine addiction, behavioral addictions such as pathological gambling, and attention deficit hyperactivity disorder.

Our aim is to optimize with DFT method the 3 secondary metabolites of Bupropion, which are formed because of enzymatic reactions after the drug is taken into the body. It is to theoretically explain the degradation pathways the secondary metabolites given to the natural environment with urine may be exposed to.

Keywords: Gaussian 09, DFT, Antidepressant, Bupropion.

INTRODUCTION

When the annual statistics of antidepressant use in Turkey by the World Health Organization are examined, a linear increase is observed [1]. Every product (food, beverage, drug, etc.) taken into the body undergoes biotransformation as a result of enzymatic reactions, turns into metabolites and is excreted from the body [2].

Due to the increasing environmental pollution and climate crisis in the world, the substances released out of the body must be planned and implemented in a way that will not harm the environment [3]. Qualitative and quantitative analyses should be made whether the drugs used are mixed with soil and water resources. It is important that the analysis results are within tolerance limits that will not adversely affect human health, and if it is above the tolerance limits, drugs should be removed from water and soil resources [4].

Behaviors of drugs in nature are: degradation by soil microorganisms, chemical degradation (e. g. hydrolysis), adsorption and binding by organic and mineral soil, uptake by plant roots, evaporation, diluting effects of water flow processes [5].

Bupropion belongs to the chemical class of aminoketones and it is also known with the generic name of amfebutamone hydrochloride. It is a second-generation antidepressant approved in US and in some European countries, but its exact mechanism of action is not completely clear. With respect to the first generation antidepressants which

different sites in the brain, second-generation drugs act at specific neurotransmitter receptor sites. In particular, Bupropion hydrochloride seems to act as a dopamine norepinephrine reuptake inhibitor and it is used also in smoking cessation and for treatment of seasonal affective disorders [6]. Bupropion is approved for use in major depression and seasonal affective disorder and has demonstrated comparable efficacy to other antidepressants in clinical trials. Bupropion is also useful in augmenting a partial response to selective serotonin reuptake inhibitor antidepressants, although Bupropion should not be combined with monoamine oxidase inhibitors [7].

S. Sevvanthi has analyzed the Bupropion molecule reactivity with various DFT methods such as local reactivity descriptors, Molecular electrostatic potential (MEP), Frontier Molecular orbitals (FMOs), Natural bond orbitals (NBO), etc. [8].

The stability in water of Bupropion was determined and the pH-degradation profile was obtained. The effects of hydrogen ion, solvent and hydroxide ion concentration were discussed with particular emphasis on the kinetics of degradation of Bupropion. Kinetics and degradation of Bupropion were determined by both HPLC-UV and LC-MS analysis utilizing high pH chromatographic methods. Degradation of Bupropion in aqueous solutions follows first-order reaction kinetics [9].

Although it is unlikely that any metabolite isomer is chiefly responsible for the stimulus actions of

---

* To whom all correspondence should be sent:
E-mail: skurumoglu@nku.edu.tr

Bupropion, some probably play a role in the complex actions of this agent [10].

The aim of this study is to computationally examine the degradation reactions of secondary metabolites of the drug molecule Bupropion to remove it from water sources and convert it into harmless molecules.

METHODOLOGY

Degradation reactions of molecules to be investigated will be examined by molecular modeling methods and theoretical approaches will be proposed for reaction pathways. For this purpose, possible reactions were calculated using Gaussian 09 package program. DFT method was used in the theoretical study. Quantum chemical methods are particularly significant in the study of electrochemistry and provide researchers with a relatively quick way of studying the structure and behavior of corrosion inhibitors [11].

In this study, possible reaction pathways of secondary metabolites of the Bupropion molecule were examined. For this purpose, the geometry of the molecules of secondary metabolites of Bupropion was optimized and the most appropriate quantum mechanical method was determined. Possible products were theoretically predicted and calculable examinations were carried out.

Calculations of the most durable conformers of secondary metabolites of the Bupropion molecule were carried out using DFT/B3LYP/6-31G(d) methods. All molecular orbital calculations were used in Gauss view5 molecular representation program and Gaussian 09W program [12].

The energy of the fragmentation reactions of all organic compounds in aqueous environment is affected by the water molecules. In addition, geometric stretching in the solution is induced by H_2O. However, the results obtained in many studies are that the geometry changes of the soluble substance for both open- and closed-shell structures have a trivial effect. Therefore, in order to explain the solvent effect of H_2O on Bupropion molecule $+\cdot OH$ reaction energy in this study; DFT/B3LYP/6-31G(d) method calculations were made and the COSMO (conductor-like screening solvation model) solvation model applied to the Gaussian package program was used [13].

RESULTS AND DISCUSSION

Fig. 1 shows the optimized geometric molecular structure of Bupropion in the drug molecule. Electronegative atoms attached to molecules O, N, Cl are shown in color. The bond lengths, bond angles

and Mulliken loads of the molecules in Table 1 give preliminary information about the fragmentation sites of molecules.

In Table 1 presenting the Mulliken loads of the molecules, the atoms with the highest electronegativity $C_1, O_{13}, N_{20}, C_{23}$ are written in bold.

Electrochemical calculations in gaseous and aqueous phase were performed for each molecule. The ΔE energy, ΔH enthalpy and ΔG Gibbs free energy values given in Tables 1, 4, 5, 7, 8, 10, 11 are given separately for each molecule. When the Gibbs free energy values of ΔG were examined, it was seen that the ΔG value of each fragmentation was negative. Thus, we list the drug molecules from the most stable to the most unstable.

The optimized geometric molecular structure of Bupropion is given in Figure 1.
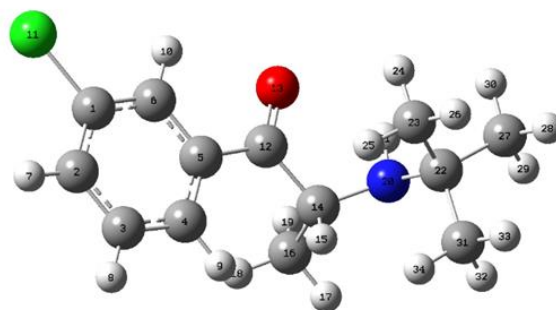
Figure 1. Optimized geometric structure of Bupropion with DFT method (grey: C; white: H; blue: N; red: O; green: Cl).

The ΔE energy, ΔH enthalpy, ΔG Gibbs free energy values and Mulliken loads of the Bupropion molecule are given in Table 1. When the Mulliken loads of the Bupropion molecule (Table 1) are analyzed, the electronegative atoms are $C_1, O_{13}, N_{20}, C_{23}$. As it can be seen in Figure 1, O_{13} of this atom forms a double bond with C_{12} atom. Since these bonds are stable, the bonds are not expected to break. C_1, N_{20}, C_{23} atoms are other electronegative atoms.

Bupropion's most durable geometric structure was optimized with DFT/B3LYP/6-31G(d) methods. As a result of DFT calculations, Bupropion 's total energy in the gaseous phase is -687692 kcal/mol, enthalpy -687691 kcal/mol, Gibbs free energy -687731 kcal/mol. The values of the total energy in the aqueous phase, enthalpy and Gibbs free energy are -687695.66 kcal/mol, -687695.06 kcal/mol, and -687734 kcal/mol, respectively. Optimized Bupropion 's geometric structure is shown in Figure 1 and geometric parameters; bond lengths, bond angles and Mulliken loads are shown in Table 2.

Table 1. Energy values of Bupropion in gaseous and aqueous phases, and their Mulliken loads in gaseous phase.
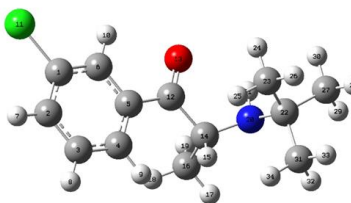
Bupropion ($C_{13}H_{18}O_1N_1Cl_1$)	Gaseous phase (kcal × mol^{-1})	Aqueous phase (kcal × mol^{-1})	Mulliken loads
	ΔE= -687692 ΔH= -687691 ΔG= -687731	-687695.66 -687695.06 -687734	**C_1 -0.249281** C_2 0.087099 C_3 0.009009 C_4 0.024974 C_5 0.041585 C_6 0.101939 Cl_{11} 0.078084 C_{12} 0.305184 **O_{13} -0.437718** C_{14} 0.071671 $C1_6$ 0.056567 **N_{20} -0.259149** C_{22} 0.157157 **C_{23} -0.004864** C_{27} 0.006372 C_{31} 0.011372

Table 2. Bond lengths and bond angles of atoms of Bupropion molecule.

Bupropion ($C_{13}H_{18}O_1N_1Cl_1$)	Bond length	(Å)	Bond length	(Å)	Bond angle	(º)
	$C_1 - Cl_{11}$	1.83	$C_{16} - C_{14}$	1.55	$C_5 - C_1 - Cl_{11}$	119.15
	$C_2 - H_7$	1.08	$N_{20} - C_{14}$	1.46	$C_{14} - C_{12} - O_{13}$	119.03
	$C_3 - H_8$	1.08	$C_{22} - N_{20}$	1.49	$C_{16} - C_{14} - C_{12}$	108.46
	$C_4 - H_9$	1.08	$C_{23} - C_{22}$	1.55	$C_{16} - C_{14} - N_{20}$	109.70
	$C_5 - C_{12}$	1.49	$C_{27} - H_{29}$	1.09	$H_{21} - N_{20} - C_{14}$	109.92
	$C_6 - H_{10}$	1.83	$C_{31} - C_{22}$	1.54	$C_{14} - N_{20} - C_{22}$	120.12
	$C_{12} - O_{13}$	1.25			$C_{31} - C_{23} - C_{22}$	34.87
	$C_{14} - C_{12}$	1.54			$C_{22} - C_{27} - H_{29}$	110.16

Bond lengths of $C_5–C_{12}$, $N_{20}–C_{14}$ and $C_{22}–N_{20}$ in Table 2 are 1.49 Å; 1.46 Å and 1.55 Å, respectively, and the bond angle of $C_{14}–N_{20}–C_{22}$ is 120.12^0, while the bond angle of $C_5–C_1–Cl_{11}$ is the second widest bond angle with 119.15^0. Based on this information, it is expected that the methyl groups of O_{13}, N_{20}, Cl_{11} atoms will break. So, it is understood that this is the first stage of degradation mechanism and O_{13} is the most electronegative atom. Looking at the area surrounded by this atom, in Table 2, $C_6–H_{10}$ has a bond length of 1.83 Å, although the O_{13} atom is the most electronegative atom. Since there are bonds longer than this bond length, it is predicted that if there is a bond break here, it will happen after the other bonds. Even the fact that $C_{14}–N_{20}–C_{22}$ and $C_5–C_1–Cl_{11}$ in Table 2 have the widest bond angles with 120.12^0 and 119.15^0 respectively, this will not change the situation. Degradation pathway and optimized structure of secondary metabolites of Bupropion and the numbering system are shown in Figures 1, 2.

Secondary metabolites (M: Bupropion, M.2.1: 4'-OH-Bupropion, M.2.2: treo-4'-OH-Bupropion,

M.2.3: eritro-4'-OH-Bupropion) of the Bupropion geometric structure and geometric parameters are shown in Tables 3, 4, 6, 7, 9, 10. Possible degradation pathways of the secondery metabolites were identified as breaking of N-C, C-O, Cl-C and aromatic ring bonds. The reaction sites were determined according to the Mulliken loads, bond lengths and bond angles distribution in the molecule. According to the values in the Mulliken loads, the nucleophilic site of the molecule is N_{20}. The hydroxyl radical, which is a very active species, has a strong electrophilic character. Therefore, it is willing to attack the molecule and form reaction intermediates. Degradation pathway and optimized structure of secondary metabolites of Bupropion are given in Figure 2.

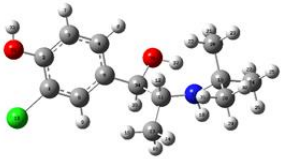Bond lengths, bond angles and Mulliken loads of atoms of M.2.1 molecule are given in Table 3.

The ΔE energy, ΔH enthalpy, and ΔG Gibbs free energy values of M.2.1 molecule are given in Table 4.

Degradation pathway of M.2.1 molecule and optimized structure of metabolites of M.2.1 are given in Figure 3.

The energy values in gaseous and aqueous phase of degradation fragments of M.2.1 molecule at ground state are given in Table 5.

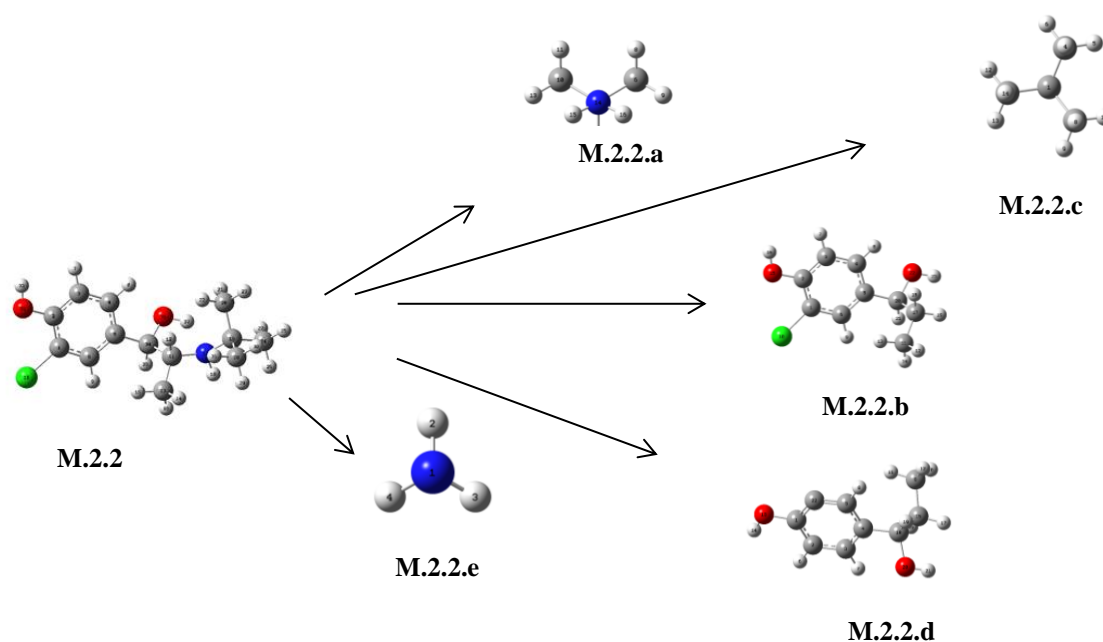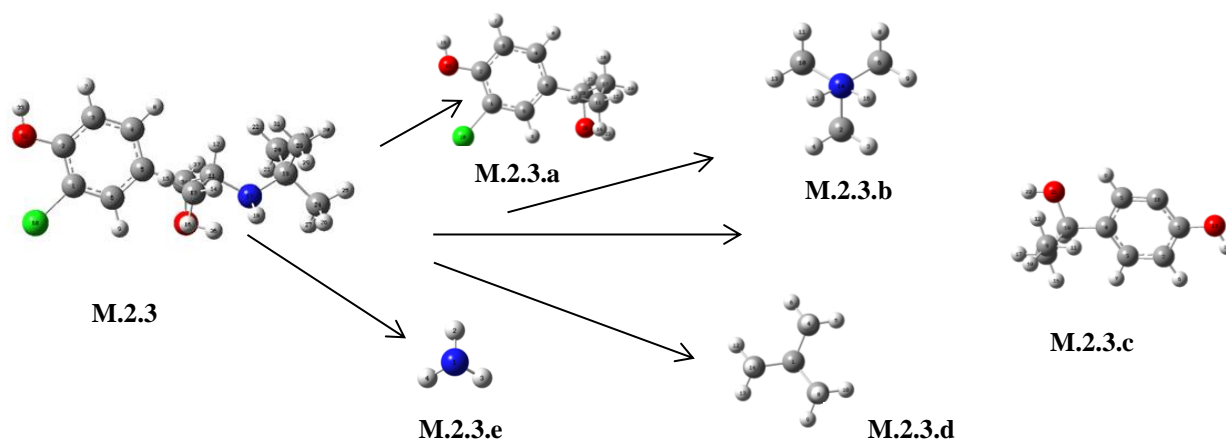**M.2.1**

M1

M.2.2

M.2.3
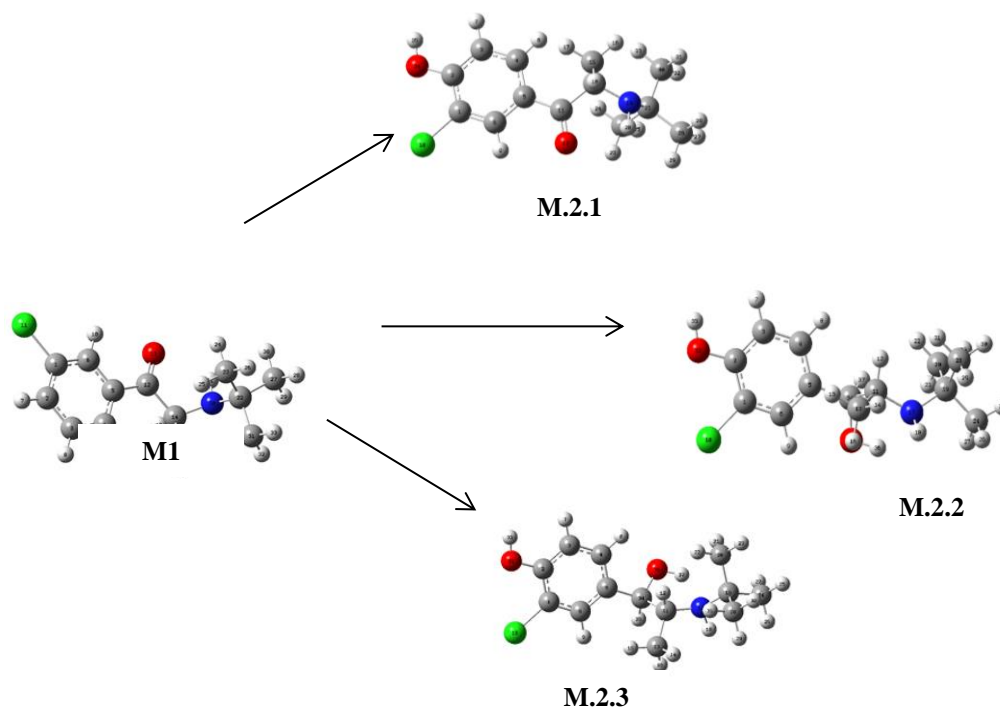
Fig. 2. Degradation pathway and optimized structure of secondary metabolites of Bupropion and the numbering system (grey: carbon; red: oxygen; blue: nitrogen; white: hydrogen; green: chlorine), (M: Bupropion, M.2.1: 4'-OH-Bupropion, M.2.2: treo-4'-OH- Bupropion, M.2.3: eritro-4'-OH- Bupropion)

Table 3. Bond lengths, bond angles and mulliken loads of atoms of M.2.1 molecule.

M.2.1

Bond angle	(°)	Bond length	(Å)			Mulliken loads	
$C_{10}- C_1 - C_2$	119.21	$Cl_{10} - C_1$	1.81	C_3	**-0.009240**	C_{15}	0.026049
$C_5- C_{11} - O_{12}$	32.71	$C_{11} - O_{12}$	1.25	C_4	**-0.003966**	N_{19}	**-0.224433**
$C_{13}- N_{19} - C_{21}$	120.02	$N_{19} - C_{21}$	1.49	C_5	0.057623	C_{21}	0.098541
$H_{35}- O_{34} - C_2$	112.13	$O_{34} - C_2$	1.38	C_6	0.075028	C_{22}	0.039640
				Cl_{10}	0.157489	C_{26}	0.011356
				C_{11}	0.334010	C_{30}	**-0.006674**
				O_{12}	**-0.405728**	O_{34}	-0.222987
				C_{13}	0.061775		

Table 4. Energy values in gaseous and aqueous phase of M.2.1 molecule at ground state.

	Phase	ΔE Energy (kcal/mol)	ΔH Enthalpy (kcal/mol)	ΔG Gibbs Free Energy (kcal/mol)
M.2.1	Gas	-734869.66	-734869.07	-734910.16
	Cosmo	-734877.14	-734876.54	-734917.65
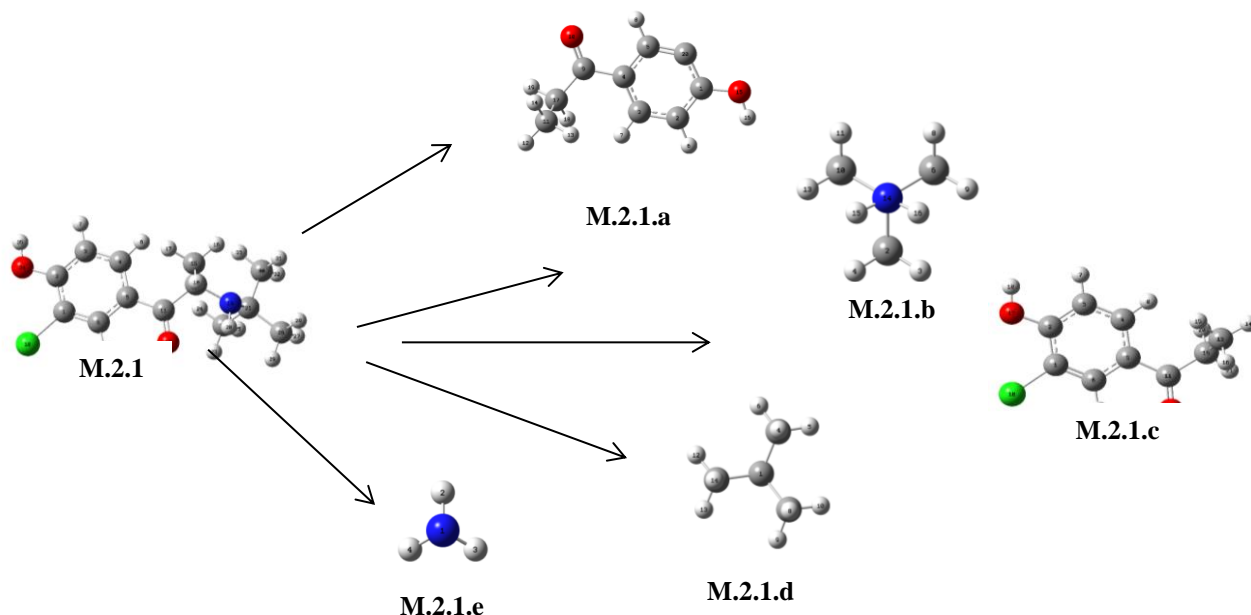
Fig. 3. Degradation pathway and optimized structures of M.2.1 metabolites and the numbering system (grey: carbon; red: oxygen; blue: nitrogen; white: hydrogen; green: chlorine).

Table 5. Energy values in gaseous and aqueous phase of degradation fragments of M.2.1 molecule at ground state.

Fragments	Phase	ΔE Energy (kcal/mol)	ΔH Enthalpy (kcal/mol)	ΔG Gibbs Free Energy (kcal/mol)
M.2.1.a	Gas	-60158542	-601584.83	-601616.49
M.2.1.a	*Cosmo*	*-601594.92*	*-601594.32*	*-601626.04*
M.2.1.b	Gas	-134030.38	-134029.79	-134052.88
M.2.1.b	*Cosmo*	*-134033.33*	*-134032.74*	*-134055.77*
M.2.1.c	Gas	-312768.98	-312768.39	-312798.40
M.2.1.c	*Cosmo*	*-312777.40*	*-312776.81*	*-312806.84*
M.2.1.d	Gas	-99347.68	-99347.08	-99368.58
M.2.1.d	*Cosmo*	*-99348.05*	*-99347.46*	*-99368.96*
M.2.1.e	Gas	-35460.88	-35460.29	-35474.00
M.2.1.e	*Cosmo*	*-35464.74*	*-35464.15*	*-35477.85*

Bond lengths, bond angles and Mulliken loads of atoms of M.2.2 molecule are given in Table 6.

The ΔE energy, ΔH enthalpy, ΔG Gibbs free energy values of M.2.2 molecule are given in Table 7.

The energy values in gaseous and aqueous phase of degradation fragments of M.2.2 molecule at ground state are given in Table 8.

Bond lengths, bond angles and Mulliken loads of atoms of M.2.3 molecule are given in Table 9.

The ΔE energy, ΔH enthalpy, ΔG Gibbs free energy values of M.2.3 molecule are given in Table 10.

The energy values in gaseous and aqueous phase of degradation fragments of M.2.3 molecule at ground state are given in Table 11.

Degradation pathway of M.2.3 molecule and optimized structure of metabolites of M.2.3 are given in Figure 5.

Table 6. Bond lengths, bond angles and Mulliken loads of atoms of M.2.2 molecule.

M.2.2

Bond angle	(°)	Bond length	(Å)		Mulliken loads		
Cl_{10} - C_1 – $6C_6$	119.31	Cl_{10} - C_1	1.82	C_5	0.030374	C_{24}	-0.000371
C_{11}- N_{17} - H_{18}	111.65	N_{17} - H_{18}	1.02	C_6	0.159715	C_{28}	-0.006498
O_{32} - C_2 – C_3	123.05	O_{32} - C_2	1.38	Cl_{10}	0.140668	O_{32}	-0.236589
H_{37}- C_{34} - O_{36}	103.31	C_{34} - O_{36}	1.44	C_{11}	0.140356	C_{34}	0.157115
				C_{13}	-0.000515		
				N_{17}	-0.274760		
				C_{19}	0.092619		
				C_{20}	0.058911		

Table 7. Energy values in gaseous and aqueous phase of M.2.2 molecule at ground state.

	Phase	ΔE Energy (kcal/mol)	ΔH Enthalpy (kcal/mol)	ΔG Gibbs Free Energy (kcal/mol)
M.2.2	Gas	-735609.60	-735609.01	-735650.43
	Cosmo	-735620.28	-735619.69	-735661.26

Fig. 4. Degradation pathway and optimized structures of M.2.2 metabolites and the numbering system (grey: carbon; red: oxygen; blue: nitrogen; white: hydrogen; green:chlorine).

Table 8. The energy values at gaseous and aqueous phase of degradation fragments of M.2.2 molecule at ground state.

Fragments	Phase	ΔE Energy (kcal/mol)	ΔH Enthalpy (kcal/mol)	ΔG Gibbs Free Energy (kcal/mol)
M.2.2.a	Gas	-602321.20	-602320.60	-602353.09
M.2.2.a	*Cosmo*	*-602330.69*	*-602330.10*	*-602362.60*
M.2.2.b	Gas	-134030.38	-134029.79	-134052.88
M.2.2.b	*Cosmo*	*-134033.33*	*-134032.74*	*-134055.77*
M.2.2.c	Gas	-313503.78	-313503.18	-313533.90
M.2.2.c	*Cosmo*	*-313512.32*	*-313511.72*	*-313542.62*
M.2.2.d	Gas	-99347.68	-99347.08	-99368.58
M.2.2.d	*Cosmo*	*-99348.05*	*-99347.46*	*-99368.96*
M.2.2.e	Gas	-35460.88	-35460.29	-35474.00
M.2.2.e	*Cosmo*	*-35464.74*	*-35464.15*	*-35477.85*

Table 9. Bond lengths, bond angles and Mulliken loads of atoms of M.2.3 molecule.

M.2.3

Bond angle	(°)	Bond length	(Å)	Mulliken loads			
Cl_{10} - C_1-C_6	119.31	Cl_{10} - C_1	1.82	C_5	0.141047	C_{24}	0.006455
C_{13}- C_{11} - H_{12}	42.31	Cl_1 - H_{12}	1.09	C_6	0.013921	C_{28}	-0.002651
H_{15}- C_{13} - H_{16}	107.79	C_{13} - H_{16}	1.09	Cl_{10}	0.143286	O_{32}	-0.234704
C_{19}-N_{17} - C_{11}	121.24	N_{17} - C_{11}	1.49	C_{11}	0.140635	C_{34}	0.131646
O_{32} - $2C_2$ – C_1	118.56	O_{32} - C_2	1.38	C_{13}	0.012155	O_{35}	-0.215447
C_{34} - O_{35} -H_{36}	104.07	C_{34} - O_{35}	1.45	N_{17}	-0.242171		
				C_{19}	0.102713		
				C_{20}	0.022138		

Table 10. Energy values in gaseous and aqueous phase of M.2.3 molecule at ground state.

	Phase	ΔE Energy (kcal/mol)	ΔH Enthalpy (kcal/mol)	ΔG Gibbs Free Energy (kcal/mol)
M.2.3	Gas	-735608.40	-735607.81	-735649.12
	Cosmo	-735607.81	-735618.20	-735659.40

Fig. 5. Degradation pathway and optimized structures of M.2.3 metabolites and the numbering system (grey: carbon; red: oxygen; blue: nitrogen; white: hydrogen; green: chlorine).

Table 11. Energy values in gaseous and aqueous phase of degradation fragments of M.2.3 molecule at ground state.

Fragments	Phase	ΔE Energy (kcal/mol)	ΔH Enthalpy (kcal/mol)	ΔG Gibbs Free Energy (kcal/mol)
M.2.3.a	Gas	-602321.15	-602320.56	-602353.10
M.2.3.a	*Cosmo*	-602330.71	-602330.11	-602362.69
M.2.3.b	Gas	-134030.38	-134029.79	-134052.88
M.2.3.b	*Cosmo*	-134033.33	-134032.74	-134055.77
M.2.3.c	Gas	-313503.86	-313503.27	-313534.11
M.2.3.c	*Cosmo*	-313512.23	-313511.64	-313542.41
M.2.3.d	Gas	-99347.68	-99347.08	-99368.58
M.2.3.d	*Cosmo*	-99348.05	-99347.46	-99368.96
M.2.3.e	Gas	-35460.88	-35460.29	-35474.00
M.2.3.a	*Cosmo*	-35464.74	-35464.15	-35477.85

The ΔE energy, ΔH enthalpy and ΔG Gibbs free energy values in Tables 1, 4, 5, 7, 8, 10, 11 are given separately for each molecule. Looking at the data in Tables 1, 4, 5, 7, 8, 10, 11, the fragment 4 (F4) of Bupropion has the lowest energy, in other words, it has the most stable structure. This fragment is formed by bond breaking from the ring to which the electronegative O atom is attached.

In this study, possible reaction paths in the reaction between secondary metabolites of Bupropion and OH radical were determined. The degradation reaction requires energy. OH radicals are used to degrade drug substances in water. As seen in the fragments obtained, secondary metabolites of Bupropion were reduced to total 15 fragments and became harmless to the environment. Our aim was to break down the drugs that are mixed with water down to the smallest harmless substances and remove their toxic effect from water. As can be seen from the results, this fragmentation took place theoretically.

For the fragments in Tables 4, 5, 7, 8, 10, 11 the energy values in the gaseous and aqueous phase were examined. The lowest energy level, in other words, the degradation path starting from the most stable fragment for secondary metabolites of Bupropion in Figure 2, was determined both in the light of the above mentioned predictions, and by the analysis of the energy values of each fragment in Tables 1, 4, 5, 7, 8, 10, 11.

CONCLUSIONS

In this study, the possible reaction paths between secondary metabolites of the drug Bupropion molecule and OH radicals were determined. For this purpose, geometry optimization of the molecules was made, then the most appropriate quantum mechanical method was determined and the possible products were theoretically predicted.

The fragmentation reaction requires energy. OH radicals are used to degrade drug molecules. Our goal was to break down drug molecules molecules down to the smallest harmless substances. As can be seen from the results, this fragmentation took place theoretically. These results will guide experimental studies and determine the fragmentation mechanism.

The geometrical parameters of bond length, bond angle, Mulliken loads, ΔE energy, ΔH enthalpy, ΔG Gibbs free energy were calculated using DFT analysis with Gaussian 09.

In these days the use of antidepressants has increased considerably, our aim is to determine the metabolites of the Bupropion drug molecule that may occur in wastewater. The aim of this theoretical study is to refine the wastewater matrix and guide experimental studies by determining the fragmentation mechanism.

After the Bupropion drug molecule is taken into the body, it is converted by enzymes into 3 main primary metabolites. However, studies have shown that only 24% of them are in this form in the urine. As a result of the studies, the presence of 3 secondary metabolites excreted in the urine was determined.

In this study, possible degradation pathways of 3 secondary metabolites given to the wastewater matrix with urine were predicted by molecular modeling. It is estimated that the treatment of these degradation products, which are likely to be found in wastewater, will affect the characterization of wastewater, which is a living matrix.

Optimized physicochemical parameters of each secondary metabolite using the DFT/B3LYP/6-31G(d) method: bond lengths, bond angles, Mulliken charges and ΔE energy, ΔH enthalpy, ΔG Gibbs free energy values were calculated. Based on these properties, it has been estimated by computational methods that the OH radical formed in wastewater has reduced to 5 molecules each secondary metabolite as a result of its effects on

secondary metabolites. The physicochemical properties of the 15 new fragments obtained: ΔE energy, ΔH enthalpy, ΔG Gibbs free energy values were calculated.

It is thought that these theoretical calculations made in this period when the importance of environmental pollution has much more increased can be of a quality that can give priority to the treatment of wastewater.

REFERENCES

1. https://stats.oecd.org/Index.aspx?ThemeTreeId=9# (Date of access 31.06.2023).
2. Zh. Zhang, W. Tang, *Acta Pharmaceutica Sinica B*, **8** (5), 721 (2018)
3. B. Sık, İ.Ö. Küçükçetin, T. Erkaymaz, G. Yıldız, *Akademik Gıda,* **10**(2), 89 (2012).
4. H. M.G. van der Werf, *Agriculture, Ecosystems and Environment,* **60**, 81 (1996).
5. J. E. Sager, J. R. Choiniere, J, Chang, A. Stephenson-Famy, W. L. Nelson, N. Isoherranen, *ACS Medicinal Chemistry Letters*, 791 (2016).
6. E. Maccaroni, L. Malpezzi, N. Masciocchi*, Journal of Pharmaceutical and Biomedical Analysis,* **50** (2009).
7. R. E. Kast, K. P. DeSanty, K, F. Foley, *Expert Review of Neurotherapeutics*, **6** (9), 1249 (2006).
8. S. Sevvanthi, S. Muthu, M. Raja, *Journal of Molecular Structure*, **1173**, 251 (2018).
9. P. M. O'Byrne, R. Williams, J. J. Walsh, J. F. Gilmer, *Journal of Pharmaceutıcal and Biomedical Analysis*, **53** (3), 376 (2010).
10. M. L. Bondarev, T. S. Bondareva, R. Young, R. A, Glennon, *European Journal of Pharmacology*, **474** (1), 85 (2003).
11. G. Gece, *Corrosion Science*, **50,** 11 (2008).
12. M. W. Hanna, Quantum mechanics in chemistry. Masachusetts,: Benjamin/Cummings Publ., 1981.
13. J. P. Lowe, Quantum Chemistry, 2nd edn., USA Academic Press, 1993.

2-(((3-Chlorophenyl) imino) methyl)-4-nitrophenol: synthesis, molecular and medicinal studies

S. Şahin[1]*, N. Dege[2]

[1]Faculty of Sciences, Department of Chemistry, Ondokuz Mayis University, Türkiye
[2]Faculty of Sciences, Department of Physics, Ondokuz Mayis University, Türkiye

In this study, an organic compound with Schiff base structure, 2-(((3-chlorophenyl) imino) methyl)-4-nitrophenol (ClSB) was synthesized, and its structure elucidation was performed by X-ray analysis. The molecular properties were investigated both structurally and electronically. The physicochemical properties and ADME parameters were investigated using a web server to evaluate the medicinal efficacy. The potential targets of the title compound were determined using the LigTMap server based on ligand similarity and binding similarity scores. We found potential targets in these enzyme classes: hydrolase, kinase, and transferase. Based on these results, the seven most potential targets were selected based on the docking scores obtained ($\Delta G \geq -7$ kcal mol^{-1}). Among all targets, thankyrase 2 was determined to be the most effective target for our compound with docking scores of -9.266 and -8.621 kcal mol^{-1}. Gastrointestinal absorption and blood-brain barrier permeability of the title compound were also determined.

Keywords: Chlorine compound, Schiff base, FMOs, ADME, docking.

INTRODUCTION

Schiff base compounds, also called imines or azomethines, are represented by the molecular formula $>$ C=N- and attract attention due to their applications in biological and medical fields [1]. These compounds gain importance due to the presence of CH = N- bond and unpaired electrons on the nitrogen atom in their molecular structure [2]. Both Schiff base ligands and their complexes are functional materials in many fields including agro/bio-chemistry, health and pharmaceutical applications, catalytic and therapeutic activity [3]. Chlorinated compounds are valuable chemicals in medicinal chemistry, and there are more than 250 FDA-approved drugs containing a chlorine atom [4]. Frontier molecular orbitals (FMOs) are commonly used to determine the chemical reactivity, electronic properties, and NLO functions of the materials under study [5].

In the current study, we synthesized a Schiff base molecule by a classical condensation method between an active carbonyl and amine compound. The molecular structure of the synthesized molecule was verified by X-ray analysis. The compound was studied both chemically and medically using software and *in silico* web tools.

EXPERIMENTAL

Chlorinated Schiff base (ClSB) was synthesized by refluxing the mixture of aromatic amine (0.039 mmol, 5.1 mg) and aldehyde (0.039 mmol, 6.6 mg) in an ethanol solution for 24 hours. A schematic representation of the synthesis is shown in Fig. 1. The obtained solution was slowly cooled to room temperature and remained for one week without further purification methods. The crystals formed were taken for X-ray analysis. $C_{13}H_9ClN_2O_3$, yield: 68%.

SMILES:
OC1=CC=C(C=C1\C=N\C1=CC(Cl)=CC=C1)[N+]([O-])=O
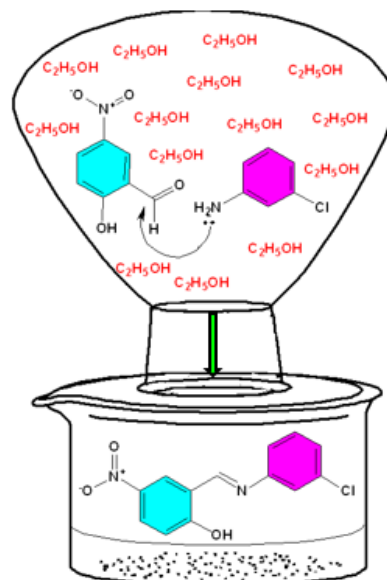
Fig. 1. Synthesis reaction of ClSB.

* To whom all correspondence should be sent:
E-mail: songul.sahin@omu.edu.tr

MATERIALS AND METHODS

Chemicals: 2-hydroxy-5-nitrobenzaldehyde, 3-chloroaniline, and ethanol were purchased from commercial suppliers.

X-ray diffraction: A STOE IPDS 2 instrument was used for X-ray data collection. SHELXTL [6] was used to solve and refine the structure. Mercury was used to create molecular graphics. PublCIF was used to prepare the CIF file of the ClSB.

ADME and target identification: in silico ADME studies were performed using the free web tool SwissADME [7]. LigTMap was used for target identification.

Docking studies: Docking experiments were performed using LigTMap [8].

RESULTS AND DISCUSSION

X-ray analysis and structural properties

A yellow stick-shaped crystal with the dimensions 0.52×0.23×0.05 mm³ was selected for X-ray data acquisition. A STOE IPDS 2 diffractometer was used for measurements. The measurements were performed at room temperature without using an extra cooling apparatus. The unit cell parameters were determined to be 14.77, 3.79, and 21.57 Å (a, b, and c, respectively) lengths and 90.00°, 90.00°, and 91.73° (α, γ, and β, respectively) angles. The crystal system and space group of ClSB were determined monoclinic and $P2_1/n$ in the above-mentioned order. A unit cell deposits four monomeric units in a volume of 1209.54 Å³ (Z=4). The calculated density of ClSB is 1.519 Mgm⁻³. The structure was refined by the method F^2 with 176 parameters. All atoms except hydrogen atoms were refined anisotropically. The solution was completed with the scores $wR(F^2)$ 0.281 and GooF 1.09. The other crystallographic parameters are listed in Table 1. Three hydrogen bonds were detected in the molecule, in which two of them (H6…O3/2.53 Å and H13…O3/2.65 Å) are intermolecular hydrogen bonds, and one of them intramolecular hydrogen (H1…N1/1.55 Å) bond (Table 2). The atom numbering style indicated in these interactions is shown in Fig. 2.
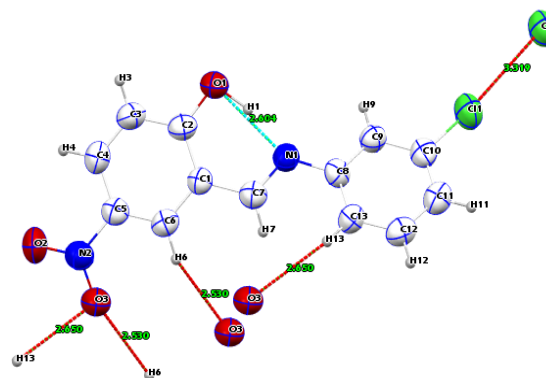
Fig. 2. Molecular representation of ClSB with the numbered scheme.

Table 1. Crystallographic data obtained by the CIF file of ClSB.

Crystal Data		Data Collection	
CCDC deposition number	2211897	Diffracto-meter	STOE IPDS 2
Chemical formula	$C_{13}H_9ClN_2O_3$	θ min-max for data collection (°)	1.7; 25.1
Formula weight	276.67	Index ranges; h, k, l	-17/15; -4/4; -25/25
Temperature (K)	293	Measurement method	Rotation method
Wavelength (Å)	0.71073	Measured reflections	6531
Crystal system	Monoclinic	Independent reflections	2153
Space group	$P2_1/n$	Reflections with I> 2σ(I)	1296
a ≠ b ≠c (Å)	14.77; 3.79; 21.57	Absorption correction	X-RED32 [9]
α = γ ≠ β (°)	90; 90; 91.73	$T_{min-max}$	0.913; 0.932
Crystal size (mm)	0.52; 0.23; 0.05	R_{int}	0.119
Z	4	Refinement method	
Volume, V (Å³)	1209.54	Refinement method	F^2
μ (mm⁻¹)	0.32	No of parameters	176
F (000)	568	R [F^2 > 2σ(F^2)]	0.095
θ (°)	1.4-39.1	$wR(F^2)$	0.281
Calculated density (Mgm⁻³)	1.519	GooF=S	1.09
Color and shape	Yellow; stick	Δρmin-max (e Å⁻³)	-0.28; 0.27

Table 2. Hydrogen bond geometry list for ClSB (Å)

D—H···A	D—H	H···A	D···A	D—H···A
C6—H6···O^{3i}	0.93	**2.53**	3.380 (8)	152
C13—H13···O^{3ii}	0.93	**2.65**	3.569 (8)	170
O1—H1···N1	1.08 (9)	**1.55 (9)**	2.602 (7)	163 (8)
Symmetry codes: (i)–x, −y–2, −z–1; (ii) −x, −y–1, −z–1.				

Molecular docking experiments

We searched potential druggable targets of ClSB *via* LigTMap and listed the docking parameters in Table 5 for top candidates. The search was performed in 17 target classes. Among them, hydrolase, kinase and transferases were determined as most potential candidates for our compound. We selected and listed them, if the docking score was equal to or lower than -7.00 kcal/mol. In this sense, cAMP and cAMP-inhibited cGMP 3',5'-cyclic phosphodiesterase 10A, serine/threonine-protein kinase pim-1, cell division protein kinase 2, cell division protein kinase 5, sulfotransferase 1A1, and thankyrase-2 were determined as potential biological targets. We listed in Table 5 the docking results and other parameters calculated. Top ranked target was found thankyrase 2 with the docking scores of -9.266 and -8.621 kcal/mol. Thankyrase 2 (TNKS 2) plays a role in fundamental cellular processes [10] and is connected with diseases such as cancer [11].

Frontier molecular orbitals (FMOs)

The FMOs obtained with the DFT/B3LYP 6-311 G ++ (d, p) basis set are shown in Fig. 3 for ClSB. We calculated HOMO and LUMO orbitals to predict electronic transitions in the molecule and to study its chemical reactivity parameters. The energy levels of HOMO and LUMO, which are the most important orbitals for chemical reactions, and the band gap were calculated to be -7.11 eV, -2.84 eV, and 4.27 eV, respectively. We also calculated reactivity descriptors including the chemical and ionization potentials, softness and hardness, electron affinity and electronegativity, electrophilicity and charge transfer index using the energy values of the HOMO and LUMO orbitals. These parameters, their formulas and calculated values are listed in Table 3.

BOILED-Egg model

Prediction of gastrointestinal absorption and BBB penetration was performed using a free web tool developed by Daine and Zoate [12].
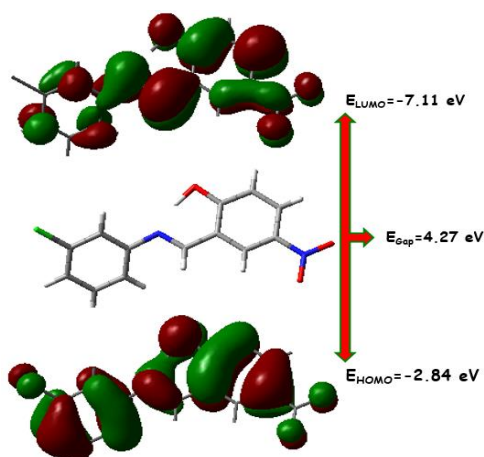
Fig. 3. HOMO and LUMO orbitals of ClSB

Table 3. Chemical reactivity descriptors of THSB

Parameters	Value (eV)
E_{HOMO}	-7.11
E_{LUMO}	-2.84
Energy band gap ($\Delta E = E_{LUMO} - E_{HOMO}$)	4.27
Ionization potential ($I = -E_{HOMO}$)	7.11
Electron affinity ($A = -E_{LUMO}$)	2.84
Chemical hardness ($\eta = (I-A)/2$)	2.13
Chemical softness ($S = 1/2\eta$)	0.23
Electronegativity ($\chi = (I+A)/2$)	4.97
Chemical potential ($\mu = -(I+A)/2$)	-4.97
Electrophilicity index ($\omega = \mu^2/2\eta$)	5.79
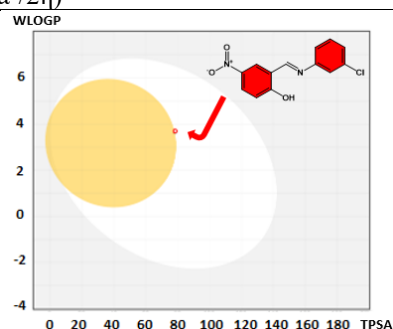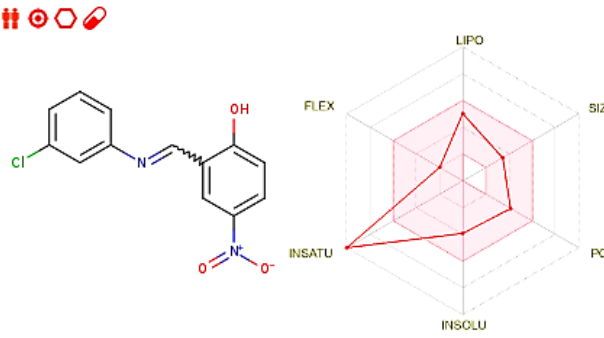
Fig. 4. BOILED-Egg model of the title compound for BBB permeation and GI absorption.

The Brain Or IntestinaL EstimateD permeation method (BOILED-Egg) places the studied molecules in an Egg model according to their octanol/water partition coefficient (WLOGP) and topological polar surface area (TPSA). It can be operated by uploading the simplified molecular-input line-entry system (SMILES) of the compounds under investigation. After the calculations, an output scheme was obtained as in Fig. 5 (for ClSB). In this figure, the yolk-colored and white regions represent

good brain access and gastrointestinal absorption, respectively. A molecule in the Egg-yolk area has access to the brain and can be absorbed by the gastrointestinal tract; in the other condition, the molecule is taken up only in the gastrointestinal tract. The grey area shows negative results in terms of both GI absorption and BBB penetration. The small red circle in Fig. 5 shows the location of ClSB. According to the above explanations, ClSB has no BBB permeation but it can be absorbed by the gastrointestinal tract.

Table 4. Physicochemical and pharmacokinetics properties of the title compound.

SMILES   Clc1cccc(c1)/N=C/c1cc(ccc1O)[N+](=O)[O-]

Physicochemical Properties	
Formula	C13H9ClN2O3
Molecular weight	276.68 g/mol
Num. heavy atoms	19
Num. arom. heavy atoms	12
Fraction Csp3	0.00
Num. rotatable bonds	3
Num. H-bond acceptors	4
Num. H-bond donors	1
Molar Refractivity	75.99
TPSA	78.41 Å²

Lipophilicity	
Log $P_{o/w}$ (iLOGP)	1.89
Log $P_{o/w}$ (XLOGP3)	3.32
Log $P_{o/w}$ (WLOGP)	3.70
Log $P_{o/w}$ (MLOGP)	2.05
Log $P_{o/w}$ (SILICOS-IT)	1.81
Consensus Log $P_{o/w}$	2.55

Water Solubility	
Log S (ESOL)	-3.92
Solubility	3.35e-02 mg/ml ; 1.21e-04 mol/l
Class	Soluble
Log S (Ali)	-4.64
Solubility	6.30e-03 mg/ml ; 2.28e-05 mol/l
Class	Moderately soluble
Log S (SILICOS-IT)	-4.43
Solubility	1.04e-02 mg/ml ; 3.74e-05 mol/l
Class	Moderately soluble

Pharmacokinetics	
GI absorption	High
BBB permeant	No
P-gp substrate	No
CYP1A2 inhibitor	Yes
CYP2C19 inhibitor	Yes
CYP2C9 inhibitor	Yes
CYP2D6 inhibitor	No
CYP3A4 inhibitor	Yes
Log K_p (skin permeation)	-5.63 cm/s

Druglikeness	
Lipinski	Yes; 0 violation
Ghose	Yes
Veber	Yes
Egan	Yes
Muegge	Yes
Bioavailability Score	0.55

Medicinal Chemistry	
PAINS	0 alert
Brenk	3 alerts: imine_1, nitro_group, oxygen-nitrogen_single_bond
Leadlikeness	Yes
Synthetic accessibility	2.51

Table 5. Docking parameters of ClSB with the targets predicted.

	Target Name	PDB ID	Target class	Ligand name	Ligand similarity score	Binding similarity score	LigT Map score	Predicted affinity (-logM)	Docking score (PSOVina2, kcal/mol)
1	cAMP and cAMP-inhibited cGMP 3',5'-cyclic phosphodiesterase 10A	4LM0	Hydrolase	5NI	0.41	0.4	0.407	5.14	-7.003
2	Serine/threonine-protein kinase pim-1	4ENX	Kinase	Z20	0.487	0.5	0.491	6.163	-7.435
3	Cell division protein kinase 2	3LE6	Kinase	2BZ	0.426	0.333	0.398	6.163	-7.292
4	Cell division protein kinase 5	3O0G	Kinase	3O0	0.44	0.182	0.363	6.163	-8.519
5	Sulfotransferase 1A1	3QVU	Transferase	NPO	0.544	0.2	0.441	6.29	-7.245
6	Thankyrase-2	4I0T	Transferase	1V0	0.425	0.25	0.373	6.29	-9.266
7	Thankyrase-2	4TKI	Transferase	33E	0.402	0.222	0.348	6.29	-8.621

CONCLUSION

In summary, a Schiff base molecule was synthesized and characterized. Its molecular structure was analyzed to determine its crystalline nature and secondary interactions. HOMO and LUMO orbitals were studied, and chemical reactivity descriptors were calculated. For medicinal chemistry evaluation, physicochemical properties, ADME descriptors, and drug-like properties were determined using SwissADME. Potential targets were screened in 17 enzyme classes and the top three classes (hydrolase, transferase, kinase) were selected for further docking evaluation. Seven enzymes within three enzyme classes achieved high docking scores (in this study, we reported the enzymes with docking scores equal to or lower than -7 kcal mol^{-1}). The best efficiency (docking scores of -9.266 and 8.621 kcal mol^{-1}) of the title compound was found against thankyrase 2, which belongs to the enzyme class of transferases. The title compound showed good absorption in the intestine, but unfavorable permeation through the BBB.

REFERENCES

1. 1. N. Manhas, P. Singh, N. A. Koorbanally, *Polycycl. Aromat. Compd.*, **42**(8), 5183 (2022).
2. 2. M. Hricovíni, M. Hricovíni, *Tetrahedron*, **73**(3), 252 (2017).
3. 3. Z. T. Omar, S. Jadhav, R. Pathrikar, S. Shejul, M. Rai, *Polycycl. Aromat. Compd.*, 1 (2021).
4. 4. W.-Y. Fang, L. Ravindar, K. P. Rakesh, H. M. Manukumar, C. S. Shantharam, N. S. Alharbi, H.-L. Qin, *Eur. J. Med. Chem.*, **173**, 117 (2019).
5. 5. M. Medimagh, C. Ben Mleh, N. Issaoui, A. S. Kazachenko, T. Roisnel, O. M. Al-Dossary, H. Marouani, L. G. Bousiakoug, *J. Mol. Liq.*, **120851**, (2022).
6. 6. G. M. Sheldrick, *Acta Crystallogr. A*, **71**(1), 3 (2015).
7. 7. A. Daina, O. Michielin, V. Zoete, *Sci. Rep.*, **7**(1), 42717, (2017).
8. 8. F. Shaikh, H. K. Tai, N. Desai, S. W. I. Siu, *J. Cheminform.*, **13**(1), 44 (2021).
9. 9. Stoe, X. Cie, X-AREA and X-RED32, Stoe & Cie, Darmstadt, Germany, 2002.
10. 10. T. Karlberg, N. Markova, I. Johansson, M. Hammarström, P. Schütz, J. Weigelt, H. Schüler, *J. Med. Chem.*, **53**(14), 5352 (2010).
11. 11. E. Zamudio-Martinez, A. B. Herrera-Campos, A. Muñoz, J. M. Rodríguez-Vargas, F. J. Oliver, *J. Exp. Clin. Cancer Res.*, **40**(1), 144 (2021).
12. 12. A. Daina, V. Zoete, *ChemMedChem*, **11**(11), 11171 (2016).

Removal of pyraclostrobin, pinoxaden, gammacyhalothrin pesticides from groundwater by DFT method

H. G. Yorulmaz[1], B. Gurkan[2], Y. Y. Gurkan[1*]

[1]Tekirdag Namık Kemal University, Department of Chemistry, Tekirdag, Turkey
[2]Gebze Technical University, Department of Physics, Kocaeli, Turkey

Today, there is a shortage of food due to the increase in the world population. For this reason, pesticides are used to remove plant pests in order not to cause product loss in agriculture. Especially in agriculture, synthetic pesticides created to achieve high efficiency are increasing day by day. The pesticides used get into the soil and then into the groundwater. In this study, ways of decomposition of the pesticides pyraclostrobin from the fungicide variety, pinoxaden from the herbicide variety, and gammacyhalothrin from the insecticide variety in groundwater were theoretically investigated. Optimized geometries were drawn with Gauss View 5.0, and then geometric optimization was carried out by the Gaussian 09W program using functional density theory (DFT) and Hartree-Fock methods. The geometrical structure (bond angles and bond lengths) of all three molecules and their possible degradation products were calculated at the level of B3LYP theory within the Hartre-Fock (HF) method and DFT in the basic set of 6-31G(d). Thus, the possible degradation mechanisms of these three pesticide molecules in water were determined. These results will guide experimental studies.

Keywords: Gaussian09, DFT, Pesticides, Pinoxaden

INTRODUCTION

Environmental pollution is increasing with industrialization and future developments. Pesticides, which are indispensable for modern agriculture, are used in many areas. Pesticides are substances used for the purpose of destroying, removing and reducing the damage of the pests that cause product deterioration during the production, orientation and maintenance of various agricultural products [1].

The usage areas of pesticides are quite wide. They are used in agricultural production, fish breeding, places where decorations such as parks and gardens are made, industry, storage, animal food, insect control and many other areas [2]. The concentration of synthetic pesticides and the use of these pesticides occur throughout the day in order to achieve higher yields in agriculture. Pesticides can reach groundwater or surface waters depending on the soil structure, vegetation, slope, by leaking from the soil or by currents from the soil. Pesticides reaching groundwater are decomposed at a lower rate due to the lack of light, temperature and oxygen [3, 4].

The use of pesticides, especially their ratio to water bodies, is an event that must be regularly examined. If the inspections are not done at certain intervals, the harms of pesticides may increase.

Fertilizers, which are used more than necessary, reach groundwater resources with rain water. In agricultural areas, pesticides should not be diluted and filled into containers; pesticide containers should not be placed near water sources. Also, pesticide containers should not be left in nature [2]. The treatment of contaminated groundwater is very difficult and expensive. Therefore, the best protection is not to pollute the groundwater at all. Pesticides can be released into the air by spraying or misting. Depending on the prospects of the particles and the weather conditions, pesticides may spread elsewhere. For this reason, if spraying will be done by air, attention should be paid to weather conditions and should be well evaluated.

Pesticides can reach quite a distance by being dragged by air. They can interact with other substances in the air and cause more effects on living things [2]. To prevent pesticides from being dragged along, the flour Henry Act constant, which better shows the evaporation temperatures of pests in many cases, should be considered, agents that controls drift while protecting the fillers, enlarging the droplet diameter, reducing the pressure (vapor pressure detecting the evaporation of pure pesticides) should be used. Provided facilities to detect, while choosing the nozzle, it is necessary to pay attention to its requirements.

---

* To whom all correspondence should be sent:
E-mail: yyalcin@nku.edu.tr

When removing it, it should be towards the air flow, and spraying should be done in suitable weather conditions [5, 6].

In this study, firstly, the initial geometries of the molecules were determined, and their geometric optimization was made on the basis of the DFT/B3LYP/6-31G(d) (Becke(B) 3 Lee-Yang-Parr (LYP)) method of density functional theory (DFT). For each molecule, possible disintegration reactions were proposed by using the calculated energy values. All calculations were performed both in the gas phase and in the water phase by modeling the solvent effect.

METHODOLOGY

The reaction model used in the computational part of this study is the reaction between the pyraclostrobin, pinoxaden, gammacyhalothrin molecules and the photo-generated •OH radicals [7]. Therefore, all the calculations were based on hydroxyl radical chemistry. Hydroxyl radicals can react with organic compounds by (i) hydrogen abstraction from single bonds, (ii) addition to double bonds, and (iii) one-electron oxidation, which is mostly loss of water from hydroxyl radical adducts. The reaction system under consideration consists of •OH radicals, in other words, of open-shell species. It is well known that open-shell molecules pose severe problems in quantum mechanical calculations. Hartree–Fock (HF) methods suffer from spin contamination, because they are wave function-based. In contrast to the HF methods, density functional theory (DFT) methods use the exact electron density instead of the wave function to calculate molecular properties and energies. Electron correlation, whose absence is the main drawback of HF methods, is accounted for in DFT methods. They suffer from spin contamination less than HF methods and this feature makes them suitable for calculations involving open-shell systems. Therefore, geometry optimizations of the reactants were performed with the DFT method. The

DFT calculations were carried out as implemented in GAUSSIAN 09 code [8], using the exchange-correlation functional B3LYP which combines HF and Becke exchange terms with the Lee–Yang–Parr correlation functional, together with the 6-31G* basis set. Vibrational frequencies were calculated for the determination of the structures as stationary points and true minima on the potential energy surfaces. All the possible stationary geometries located as minima were generated by free rotation around single bonds [9-11].

RESULTS AND DISCUSSION

In the search for a plausible mechanism for the photocatalytic degradation reaction of pyraclostrobin, pinoxaden, gammacyhalothrin molecules DFT reactivity descriptors were employed to have information about the most susceptible sites for hydroxyl radical attack. Fig. 1 shows the optimized structures of pyraclostrobin, pinoxaden, gammacyhalothrin molecules and the numbering system that is used throughout the calculations. Three main competing reaction pathways shown in Fig. 2 were determined by selecting the specific sites of pyraclostrobin molecule, on the basis of their softness values being close to that of the •OH radical.

Three main competing reaction pathways shown in Figs. 2-4 were determined by selecting the specific sites of pyraclostrobin, pinoxaden, gammacyhalothrin molecules, on the basis of their softness values being close to that of the •OH radical. The predicted mechanism was confirmed by comparison with the experimental results on simple structures reported in the literature, as explained below. The lowest-energy structure is the most stable structure. Statements in this fragmentation took place both experimentally and theoretically, as seen from the Gibbs free energy values of Tables 1-3 and support it.

Pinoxaden   Pyraclostrobin   Gamma-Cyhalothrin
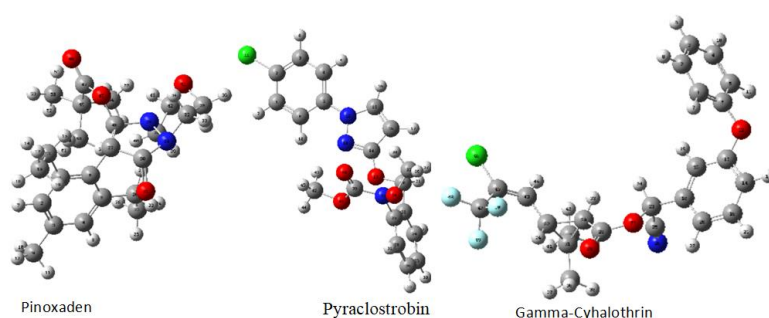
Fig. 1. The optimized geometric structure of pyraclostrobin, pinoxaden, gammacyhalothrin molecules *via* DFT method (grey: C; white: H; red: O; blue: N; green: Cl; light blue: F).
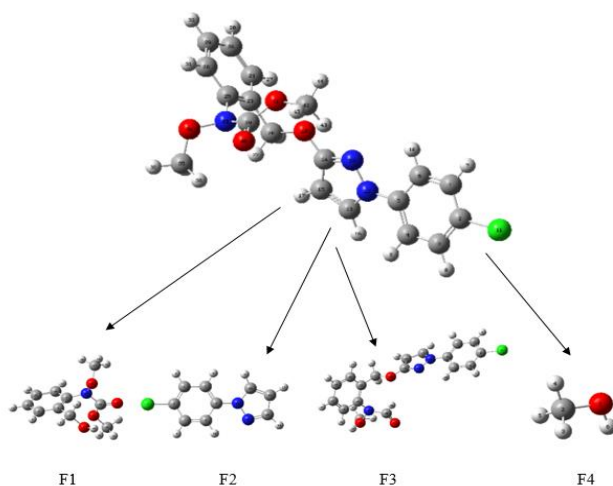
Fig. 2. Possible pathways for the photocatalytic degradation of pyraclostrobin (grey: C; white: H; red: O; blue: N; green: Cl).
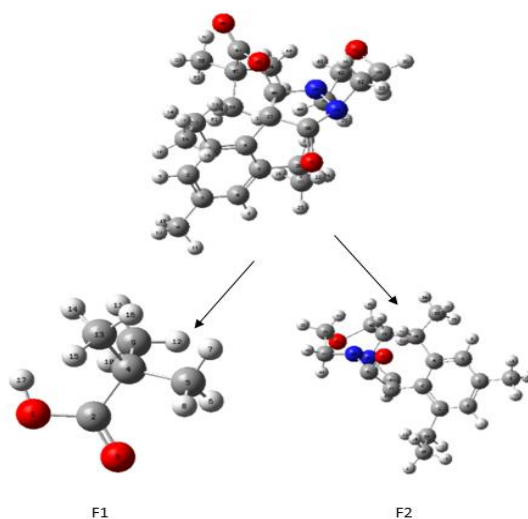
Fig. 3. Possible pathways for the photocatalytic degradation of pinoxaden (grey: C; white: H; red: O; blue: N).
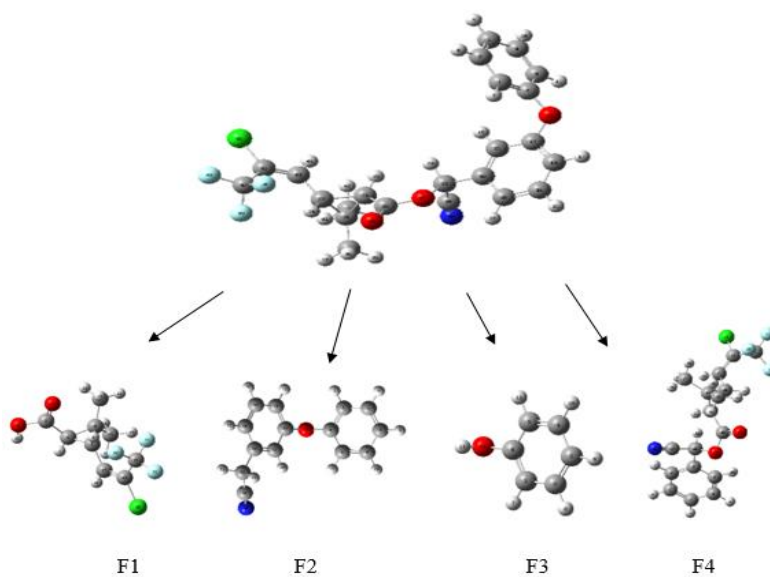
Fig. 4. Possible pathways for the photocatalytic degradation of gammacyhalothrin (grey: C; white: H; red; O; blue: N; green: Cl; light blue: F).

315

Table 1. Constant energy, enthalpy and Gibbs free energy values according to the DFT method.

Molecules	Phase	ΔE Energy (kcal mol⁻¹)	ΔH Enthalpy (kcal mol⁻¹)	ΔG Gibbs free energy (kcal mol⁻¹)
Pyraclostrobin	Gas	-1041505.427	-1041504.800	-1041558.326
	COSMO	*-1041517.036*	*-1041516.471*	*-1041570.123*
F1	Gas	-467005.689	-467005.124	-467043.277
	COSMO	*-467015.792*	*-467015.164*	*-467052.940*
F2	Gas	-575235.743	-575235.178	-575264.169
	COSMO	*-575237.374*	*-575236.810*	*-575264.671*
F3	Gas	-969651.128	-969650.563	-969699.948
	COSMO	*-969662.172*	*-969661.545*	*-969711.181*
F4	Gas	-72577.439	-72576.812	-72593.755
	COSMO	*-72580.64*	*-72580.075*	*-72597.018*

Table 2. Constant energy, enthalpy and Gibbs free energy values according to the DFT method.

Molecules	Phase	ΔE Energy (kcal mol⁻¹)	ΔH Enthalpy (kcal mol⁻¹)	ΔG Gibbs free energy (kcal mol⁻¹)
Pinoxaden	Gas	-819249.395	-819248.830	-819308.506
	COSMO	*-819260.250*	*-819259.623*	*-819319.362*
F1	Gas	-217656.767	-217656.203	-217682.432
	COSMO	*-217752.257*	*-217752.101*	*-217752.198*
F2	Gas	-602330.640	-602330.075	-602376.637
	COSMO	*-602340.053*	*-602339.488*	*-602386.237*

Table 3. Constant energy, enthalpy and Gibbs free energy values according to the DFT method.

Molecules	Phase	ΔE Energy (kcal mol⁻¹)	ΔH Enthalpy (kcal mol⁻¹)	ΔG Gibbs free energy (kcal mol⁻¹)
Gamma-cyhalothrin	Gas	-1209558.550	-1209557.922	-1209618.414
	COSMO	*-1209569.155*	*-1209568.590*	*-1209630.023*
F1	Gas	-789978.735	-789978.108	-790017.139
	COSMO	*-789987.332*	*-789986.705*	*-790025.171*
F2	Gas	-420330.503	-420329.938	-420366.145
	COSMO	*-420337.405*	*-420336.840*	*-420372.859*
F3	Gas	-192867.777	-192867.150	-192889.364
	COSMO	*-192871.856*	*-192871.291*	*-192893.505*
F4	Gas	-1017432.174	-1017431.546	-1017483.818
	COSMO	*-1017441.649*	*-1017441.085*	*-1017492.540*

CONCLUSIONS

The degradation system was determined for these three effective molecules. The energy values caused by the fragmentation and the electronegative atoms in it, bond lengths and angles were examined and explained. In the study, possible reaction routes were used in the reaction between pesticide active ingredients and water. It functions as an energy for a reaction to disintegration. So, the OH radicals in water break down these chemicals. The most focal structure of a group is its lowest energy state. Accordingly, when we rank the pesticide agents from the most stable to the most unstable, the order is: gammacyhalostrobin -1209558.550 kcal/mol, pyraclostrobin -1041505.427 kcal/mol, pinoxaden -819249.395 kcal/mol. Pesticide agents' purpose was to break down products down to the smallest harmless substances. As a result, when we list the 4 fragments which are the degradation products of the 1st molecule, the pyraclostrobin fragment, as the most unstable, the order is: F3 - 969651.129 kcal/mol, F2 -575235.743 kcal/mol, F1 -467005.689 kcal/mol, F4 -72577.439 kcal/mol. When we order the 2 fragments, which are the fragmentation products of the 2nd molecule pinoxaden, from the most stable to unstable, F2 is -602330.640 kcal/mol, F1 is -217656.767 kcal/mol. When we rank the 4 fragments, degradation products of the 3rd molecule, gammacyhalothrin, from the most unstable, F4 -1017441.649 kcal/mol, F1 -789978.735 kcal/mol, F2 -420330.503 kcal/mol, F3 -192867.777 kcal/mol. As can be seen from the results, the fragmentation occurred theoretically. These results will guide experimental workers and determine the fragmentation mechanism.

REFERENCES

1. H. H. Tok, Environmental pollution, Trakya University, Tekirdag Faculty of Agriculture, 1997.
2. C. Guler, Z. Cobanoglu, Pesticides, Ministry of Health Environmental Health Basic Source Series, Ankara, 1997.
3. U. Yucel, Effects of pesticides on humans and the environment, Ankara Nuclear Research and Training Center, Department of Nuclear Chemistry, 2007.
4. A. Altıkat, T. Turan, F. Ekmekyapar Torun, Z. Bingul, *Atatürk Ziraat University Journal*, **40** (2), 87 (2013).
5. D. C. Young, Computational chemistry a practical guide for applying techniques to real-world problems (electronics), New York, John Wiley and Sons, 2001, p. 381.
6. W. Zhang, *Proceedings of the International Academy of Ecology Environmental Sciences*, **8**(1), 1 (2018).
7. N. San, M. Kilic, Z. Cinar, *J. Adv. Oxid. Technol.* **10**(1), 51 (2007).
8. Gaussian 09, Revision B.04, in: Gaussian, Inc., 2009.
9. J .P. Stewart, *J. Comput. Chem.,* **10**, 221 (1989).
10. J. P Lowe, Quantum Chemistry, 2nd edn., Academic Press, USA, 1993.
11. I. N. Levine, Quantum Chemistry, Boston, Alloy and Bacon Inc., 1983.

Physico-mechanical characteristics of materials and methods for provisional non-removable prosthetic constructions - Part 1. Contemporary literature review

M. Dimova-Gabrovska[1]*, S. Rangelov[1], E. Kirilova[2], K. Kirilov[3,4]

[1]Department of Prosthetic Dental Medicine, Faculty of Dental Medicine, Medical University – Sofia, Sv. Georgi Sofiysk, Str., 1, Sofia 1431, Bulgaria

[2]Institute of Chemical Engineering, Bulgarian Academy of Sciences, Acad. G. Bonchev Str., Bl.103, Sofia 1113, Bulgaria

[3]Institute of Molecular Biology, Bulgarian Academy of Sciences, Acad. G. Bonchev Str., Bl. 21, Sofia 1113, Bulgaria
[4]Department of Natural Sciences, New Bulgarian University, Montevideo Str., 21, Sofia 1618, Bulgaria

In prosthetic dental medicine rehabilitation prior to definitive prosthesis placement there is an important step in clinical treatment plans. Different materials and methods for fabrications have been developed over the years, with still no universal solution for all cases. The knowledge of contemporary available options for dental provisionalization, all of which have their pros and cons regarding different clinical scenarios is crucial for any dental medic practicing prosthetic dentistry.

Keywords: Preliminary dental prosthetics, mechanical characteristics, dental polymers, preliminary non-removable prosthetics, interim dental materials

INTRODUCTION

According to several contemporary authors, interim fixed prostheses are essential in fixed prosthetic treatment, because for a certain period they provide protection and healing of dental, periodontal, and mucous tissues, improvement of aesthetic and phonetic functions, disclosure of data for assessment of hygiene control, stabilization of position of teeth [1-3], restoration of occlusal function [4-6].

It is considered that when making interim fixed prostheses, the clinician and dental technician should take into account the physical and mechanical characteristics of the materials used [1-3, 7] as well as whether they are biocompatible with all oral tissues [3, 8-10].

Rosenstiel *et al*. summarize their understanding that depending on their chemical composition, the materials used to make interim prostheses can generally be divided into four groups: polymethyl methacrylate (PMMA), polyethyl or butyl methacrylate, microfilled bisphenol A-glycidyl dimethacrylate (Bis-GMA) composite resin, and urethane dimethacrylate (light-polymerizing resins) [11, 12]. The primary monomer determines many of the material's properties such as polymerization shrinkage, strength, and exothermic heat of reaction [8, 11]. There is no material used to make interim prosthesis that meets all requirements of the patients and the clinicians [13-15]. Typically, clinicians

select materials based on factors such as ease of manipulation, cost effectiveness, aesthetics, strength, and marginal accuracy.

The production of interim prostheses is carried out by applying the following basic techniques: (1) direct provisionalization in the mouth, on the abutments, or on the prepared teeth; (2) provisionals made indirectly; and (3) a mixed technique of indirect-direct provisionalization [16]. One of the most popular and frequently used techniques for making prostheses, which belongs to the group of indirect techniques, is CAD/CAM (computer-aided design–computer-aided manufacture) technology. The latter overcomes many of the problems of direct techniques associated with dosage, mixing, and material states. With CAD/CAM workflow systems, a high-quality interim prosthesis is obtained [17]. CAD/CAM applies two types of techniques - subtractive and additive to make interim prostheses. In subtractive methods, prostheses are obtained from a monolithic block of a certain material by applying milling and grinding processes. In additive methods, the final product is obtained by successively accumulating layers of material, a.k.a. the 3D printing method [18, 19]. In recent years, the 3D printing method has gained popularity, being applied with a variety of polymer materials [20].

It has been found that the success of prosthetic treatment performed with digital technology depends to a large extent on the choice of material

---

* To whom all correspondence should be sent:
E-mail: marianadimova@abv.bg

for making the prostheses. Most often, polymer-based materials, such as PMMA, are used in the CAD/CAM workflow [20].

When performing prosthetic treatment, interim fixed prostheses have a limited life. Some complex cases of oral rehabilitation, prosthetic treatments dedicated to children, adolescents or the elderly, the presence of some systemic diseases that require the termination or postponement of dental procedures, as well as the extension of the sequence of provisionalization require their prolonged use, in which this period increases significantly [11, 16, 21-23].

The latter requires the achievement of in-depth knowledge of mechanical properties of materials such as flexural strength, stiffness, impact resistance and stability [24-26] to be used for the development of new materials with higher strength properties to withstand the high functional loads.

AIM

The aim of the article is to present contemporary terminological positions and systematize contemporary materials and methods for preliminary non-removable prosthetics in prosthetic dental medicine.

Definition and essence of contemporary preliminary non-removable prosthetics

The definition of a preliminary (interim) prosthesis, as stated in The Glossary of Prosthodontic Terms [27], is as follows:

"...a fixed or removable dental prosthesis, or maxillofacial prosthesis, designed to enhance esthetics, stabilization, and/or function for a limited period of time, after which it is to be replaced by a definitive dental or maxillofacial prosthesis; often such prostheses are used to assist in determination of the therapeutic effectiveness of a specific treatment plan or the form and function of the planned for definitive prosthesis…"

As synonyms of an interim prosthesis are presented [27]: provisional prosthesis, provisional restoration.

In 2003, M. Dimova [28] introduced the term "preliminary constructions" for the first time in our country. She argued that these constructions should not only be temporary (remaining in the mouth for a specific short period) but also serve as prototypes for the final prosthetic constructions. The clinical stage of preliminary prosthesis plays an important role for the dental practitioner, as it has periodontal

prophylactic and caries prophylactic significance, prevents tooth migration, and significantly contributes to determining the design of the permanent construction. The definition provided by M. Dimova for preliminary constructions is as follows:

"Preliminary constructions are prototypes of the final constructions in terms of the three medical-biological parameters (MBP) - preventive, functional, and aesthetic. They serve as the material carrier of the mutual informed consent between the dental practitioner and the patients regarding the type of final construction. They are planned in advance and fabricated in the laboratory prior to preparing the prosthetic field in the patient's mouth and long before the fabrication of the final constructions. They retain the potential for unlimited additional adjustments."

This definition of preliminary constructions was proposed and supported by M. Dimova [28]. It is based on the analyzed theoretical frameworks and requirements presented in her dissertation work, which outline the criteria that these constructions should meet.

In his textbook from 1992, Acad. N. Popov [29] proposes a classification of preliminary constructions in implant prosthodontics based on their fabrication technique. This classification based on the protocol used for their fabrication is generally applicable even in non-implant prosthodontics.

"... - fabricated in clinical conditions (direct technique) using the techniques of conventional prosthodontics,

- fabricated in the laboratory on working models (indirect technique), and

- fabricated in a combined manner - using a direct-indirect technique, where pre-made shell crowns are fabricated, significantly reducing the clinical working time..."

Preliminary prosthetic constructions, whether supported by natural teeth or implants, are preferred as a method for restoring missing teeth and dental tissues, satisfying both aesthetics and function. In the past, interim fixed prosthetic constructions were perceived as a substitute for the final construction during its fabrication in the dental laboratory. Preliminary prosthetics during the course of prosthetic treatment, intended to be completed with a fixed construction, are considered by many authors [1, 25, 28, 30-37] as an essential stage and should fulfill multiple tasks - preventive, functional, and aesthetic.

MATERIALS AND METHODS FOR FABRICATING PRELIMINARY NON-REMOVABLE PROSTHESES

Materials

The classification of conventional materials used for fabricating interim fixed prosthetic constructions (IFPC) can be divided into materials that are individually preformed, according to a report by Burns *et al.* for the Committee on Scientific Development in Fixed Prosthodontics of the Academy of Fixed Prosthodontics in 2003 [38].

I. *The materials for custom made* preliminary non-removable prosthetic constructions can be categorized based on their polymerization mechanism [38]:

1) Chemically activated self-polymerizing plastics;

2) Heat-activated plastics;

3) Light-activated plastics;

4) Dual-curing plastics;

5) Others (alloys and hybrid materials).

The most commonly used conventional materials for interim constructions are acrylic plastics [28, 34, 39]. According to some authors [25, 38, 40, 41], a disadvantage of acrylic plastics is their susceptibility to fracture [42]. However, they offer the advantage of adjustability through addition and subtraction [43, 44].

Burns *et al.* [38] divide acrylic resins into several types for provisional prosthesis materials:

A. Polymethyl methacrylate (PMMA) - first introduced in the 1940s, it still is the most widely used material for provisional restorations [34]. Iy possesses strength, affordability, and is easily polished, but its monomers are cytotoxic [45], and the polymerization reaction in self-polymerizing acrylics is highly exothermic, which carries the risk of sensitizing or devitalizing prepared vital teeth [28]. Therefore, in the literature, they are recommended as materials for indirect or direct-indirect methods of fabricating provisional restorations.

B. Polyethyl methacrylates (PEMA) - this category includes vinyl, ethyl, and butyl methacrylates which have similar chemical behavior. They are characterized by lower toxicity and exothermicity compared to PMMA, but they have inferior mechanical properties. They are recommended for short-term provisional restorations and rebase procedures in the indirect-direct technique [32].

C. Other acrylic resins or combinations of methacrylates without fillers - urethane dimethacrylate (UDMA) and others.

D. Composite materials - Representatives of this group commonly contain a polymer resin called bisphenol A glycidyl methacrylate (Bis-GMA) and inorganic fillers such as alumino-silicate, quartz, or acrylic particles. Depending on their polymerization mode, they can be:

- Self-polymerizing;
- Light-cured;
- Dual-cured (light- and self-polymerizing).

They are characterized by affordability, strength, ease of use in clinical conditions, good polish ability, and color stability. They have low toxicity, sensitizing potential, and allergenic potential compared to PMMA [28].

Most composite materials are supplied with a dispensing gun and mixing tips, similar to those used for addition of silicone corrections. This makes them significantly faster and more convenient for clinical use (direct and direct-indirect methods), although the cost of the materials is slightly higher [15].

II. *Preformed options* for preliminary non-removable prosthetic constructions - this category includes pre-made crowns, which are most commonly used in pediatric dentistry [46-49]. They can be made of metal, composite, zirconium dioxide, and other materials. This category also includes blanks for subtractive CAD/CAM milling - discs and blocks made of polymerized materials under ideal conditions [50].

In 2021, Benli *et al.* [51] tested and compared the mechanical properties of twenty subtractive manufactured crowns made of polylactic acid (PLA) - an organic, biodegradable material that is increasingly being used as a substitute for non-biodegradable industrial polymers and in the production of prototypes through thermoplastic extrusion printing. The other materials used in the study were the same number of subtractive manufactured crowns made of PMMA and polyetheretherketone (PEEK). Despite showing the lowest fracture strength, the PLA material exhibited similar values of marginal fit, which, combined with its ability to degrade in the environment without causing harm, ranks it among the materials suitable for provisional prosthetic crowns.

Methods

1) Conventional (analog) methods

Conventional methods for fabricating provisional prosthetic constructions involve taking an impression of the patient's dentition, creating a prototype of the future provisional restoration, and fabrication.

Laboratory methods refer to the techniques used to fabricate provisional restorations on a model. This

includes waxing up a prototype, investing, pressing, and thermocycling in flasks or a polymerizer using heat-polymerizing resin [52]. It also involves injecting thermoplastic polymers into molds or direct modeling using self-polymerizing resin and thermocycling in a polymerizer.

On the other hand, *clinical methods* involve fabricating provisional restorations directly in the patient's mouth or using direct-indirect techniques with the help of matrices prepared in the laboratory on diagnostic wax patterns [53].

A *combined method* for fabricating thin-walled precise provisional restorations: In order to meet the three objectives of prevention, function, and aesthetics (PFA) in our country, Dimova [28] introduced a combined method for fabricating precise preliminary restorations with thin-walled frameworks. The laboratory preparation for fabricating the frameworks of provisional restorations precedes the preparation of the abutment teeth.

2)   Digital methods

Digital technologies (CAD/CAM) for provisional prosthetic constructions have significantly entered everyday practice and have greatly reduced the fabrication time in the clinic and laboratory. They can be divided into two main types of methods:

I.   Subtractive methods: These methods involve obtaining the desired construction by subtracting material from prefabricated CAD/CAM blocks.

II. Additive methods: These methods involve creating the desired construction by adding material for CAD/CAM purposes.

In terms of historical development, initially, the methods of fabricating provisional restorations through subtracting (milling) material from prefabricated blocks, which were polymerized under ideal conditions, found wide application in dental medicine [54]. The predominant material used was PMMA, with some manufacturers offering products with enhanced mechanical properties achieved through additional cross-linking in the polymer network, known as cross-linked polymers [55].

The more recent method is the additive method, which allows for the fabrication of constructions with more complex geometry but has a more sensitive workflow protocol [56]. In 2015, Rayyan *et al.* [57] conducted a comparative study on the color stability, imbibition, wear resistance, surface hardness, fracture strength, and microindentation between crowns fabricated on identical replicas of the upper first premolar using epoxy resin. The materials included in the study were PMMA CAD/CAM blocks, self-polymerizing PMMA, self-

polymerizing Bis-GMA, and thermoplastic resin for provisional restorations. The conclusion of the study was that CAD/CAM-fabricated provisional crowns using PMMA outperformed the other constructions made from different materials in terms of their color [10], mechanical, and physical characteristics [57].

The results of the study conducted by Alt *et al.* [25] in 2011 comparing the mechanical properties of materials for direct and indirect fabrication of FPDs are similar. The authors note the superior qualities of the experimental specimens fabricated using the subtractive CAD/CAM method and highlight the absence of composite materials (discs or blocks) for this fabrication technique, despite their advantages.

In another study by Yao *et al.* [58], the compressive strength and marginal fit between Bis-GMA materials for direct (clinical) fabrication of FPDs and PMMA materials for subtractive CAD/CAM fabrication method were compared after thermocycling for 5000 thermal cycles (from 5°C to 55°C). Once again, the results favored the experimental specimens fabricated using the subtractive method, particularly after undergoing thermocycling.

In a study by Al-Dwairi *et al.* in 2020 [30], the flexural strength, fracture toughness, and modulus of elasticity (E) of two PMMA materials (AvaDent and Tizian) for subtractive CAD/CAM technology and one heat-polymerized PMMA material (Meliodent by Heraeus Kulzer) were investigated. Each group of 15 specimens was stored in distilled water at $37 \pm 1°C$ for 7 days. The results demonstrated better mechanical properties for materials used in the subtractive fabrication method, although there was some variation among different brands.

In a laboratory study published in 2019, Alp *et al.* [20] investigated three groups of CAD/CAM PMMA polymer blanks for the subtractive manufacturing method (Telio CAD [T]; M-PM-Disc [M]; Polident-PMMA [P]), one Bis-GMA clinical composite material (Protemp 4 [PT]), and one cold-polymerizing clinical PMMA material (ArtConcept Artegral Dentine [C]). The test specimens were prepared with dimensions of $2 \times 2 \times 25$ mm according to ISO 10477:2004 standard (Dentistry - Polymer-based crown and veneering materials). Test specimens (N=15 of each type) were subjected to 10,000 thermal cycles (5 to 55°C). A three-point bending test was conducted on a universal testing machine at a crosshead speed of 1.0 mm/min. The results showed the highest values for the subtractive manufacturing materials, intermediate values for the Bis-GMA clinical material, and the lowest values for the self-polymerizing PMMA clinical material for dental prostheses.

Milled PMMA disc preliminary structures are not characterized by the toxicity, heating, and shrinkage described [8, 28, 40] with self-polymerizing and dual-polymerizing plastics for clinical use. Other advantages include increased mechanical resistance [20, 25, 30, 57, 58] fit [57, 58], and color stability [57].

3D printing setups are becoming increasingly accessible, where manufacturing after digital design is accomplished through material addition (additive method), allowing for material savings and reduced production time compared to subtractive methods (milling) [59-61]. According to several studies, printed preliminary structures are not inferior to milled ones in terms of accuracy and strength [62].

Reinforcing preliminary non-removable prosthetic constructions

Reinforcing preliminary non-removable prosthetic structures is a method aimed at increasing mechanical resistance and reducing the likelihood of fracture, which is a common issue in clinical practice, especially in bridge constructions. The reinforcement method can be applied during the fabrication of the prosthesis or after intraoral use, when repairing a fractured structure.

In 1991, Larson *et al.* [63] conducted an experimental study on specimens made of three types of polymers for fixed dental prostheses: one methyl methacrylate (PMMA) and two polyether methacrylate (PEMA) materials, with and without carbon fiber reinforcement. The groups were further divided based on the storage medium, with half of the specimens being immersed in water. The results showed a significant increase in the elastic modulus of the specimens in the reinforced groups, regardless of the storage condition. Immersion in water did not cause statistically significant changes in the results.

In a study conducted in 2003 by Pfeiffer and Grube [64], the fracture resistance of fixed dental prostheses made from various materials with and without reinforcement was compared. The experiments involved identical long-span bridge structures with 2 abutments and varying numbers and lengths of pontics (3-unit: 12 mm, 4-unit: 19 mm, and 5-unit: 30 mm), and the central part of the pontics in the occlusal region was subjected to loading. The researchers found that reinforcement with impregnated fibers significantly increased the fracture resistance for different lengths of pontics.

In 2004, Kim and Watts [65] investigated the influence of glass fiber reinforcement on polymers for fixed dental prostheses. They compared three dimethacrylate-based materials and one methyl methacrylate material, and also examined the effect of water storage on the specimens. The study revealed a significant increase in the flexural strength values for the groups reinforced with glass fibers and lower values for specimens stored in water, although the differences were not statistically significant.

In a similar study conducted in 2004, Hamza *et al.* [66] compared the mechanical properties of three types of materials for fixed dental prostheses (PMMA, PEMA, and composite), reinforced with two types of glass fibers and four types of polyethylene fibers (Kevlar). The authors examined the fracture strength and flexural strength of the specimens according to ASTM no. E 399-83 and ISO 14077, respectively. For both tests, they used non-reinforced specimens as a control group.

DISCUSSION

A brief discussion of the new trends in materials and methods and their practical significance is presented.

Reinforcement of polymer materials for FPDs is a method used to create medium-term (1 to 6 months) and long-term (6 months to 2 years) provisional prosthetic restorations [67] in cases where their use is necessary within complex, multidisciplinary treatment plans. The methods for their fabrication can be direct (clinical), indirect (laboratory), direct-indirect (clinical-laboratory), or indirect-direct (laboratory-clinical).

Clinical methods

Clinical or direct methods save time and resources for both the clinician and the patient. For their fabrication, factory-made or individual matrices (external formers of provisional restorations) are most commonly used, thus avoiding the time-consuming direct modeling of tooth forms. However, direct methods have some drawbacks. These include the allergenic potential of unpolymerized provisional restorative materials placed on oral tissues, thermal trauma and sensitization of vital prepared teeth [28, 68], poorer marginal adaptation of the restorations due to the need for removal during the impression phase from the prepared abutments to prevent blockage in potential subgingival spaces, the need for training of the dental practice staff in the fabrication, finishing, and polishing of the restorations [15]. Reinforcement of such restorations can be achieved through the use of polyethylene or glass fibers adapted intraorally onto the preparations and subsequently placed in the individual matrix along with the provisional restorative material, as described by Hammond and Hodd in an article from 2016 [69], or they can be

fixed without bonding using a liquid composite on dried abutments before placing the matrix with the provisional material, similar to the fiber-splinting technique often used in the fabrication of a retentive splint following orthodontic treatment or in cases of periodontal mobility [70].

Laboratory methods

In laboratory methods of provisional prosthetics, reinforcement can be achieved using all known materials directly onto the prepared tooth abutments, with the polymerization of the plastic materials under ideal conditions, better finishing and polishing of the restorations [15]. The only drawback can be the period between preparation and fabrication of the provisional restorations when the patient has to be either with clinically fabricated restorations or without any [53].

Clinical-laboratory methods

Reinforcement of provisional restorations fabricated in clinical conditions in the laboratory is achieved by integrating fibers into prepared channels in the restoration, filling them with polymers [40], and performing finishing and polishing. We believe that this technique combines the drawbacks of both clinical and laboratory methods.

Laboratory-clinical method. This method involves the fabrication of preliminary laboratory "shells" based on preliminary models, diagnostic modeling, and laboratory pre-conservative preparation of the tooth abutments on the model intended for prosthetic treatment in the mouth [8, 67]. In the clinical phase, the teeth are prepared, the reinforcing fibers are adapted to the preparations, and the restorations are reseated along with them. These restorations possess all the advantages of laboratory methods but also avoid some of the drawbacks of clinical methods, such as compromised marginal adaptation and exposure of the preparations to elevated temperatures during polymerization and the cytotoxicity of unpolymerized provisional restorative materials [28].

CONCLUSION

The presented variety of modern materials and methods for preliminary (provisional) non-removable prosthetics in dental medicine, as well as the options for reinforcement through armament, require a thorough analysis and a wide range of *in vitro* and *in vivo* studies to provide recommendations for daily dental practice. They are also the subject of detailed scientific research in a dissertation entitled "Reinforcement of preliminary restorations - a laboratory and clinical study."

REFERENCES

1. M. Patras, O. Naka, S. Doukoudakis, A. Pissiotis, *J. Esthet. Restor. Dent.*, **24**(1), 26 (2012).
2. S. Miura, M. Fujisawa, F. Komine, T. Maseki, T. Ogawa, J. Takebe, Y. Nara, *J. Oral Sci.,* **61**(2), 195 (2019).
3. N.D. Ruse, M.J. Sadoun, *J. Dent. Res.,* **93**(12), 1232 (2014).
4. D. G. Gratton, S.A. Aquilino, *Dent. Clin. North Am.*, **48**(2), 487 (2004).
5. S. Hahnel, S. Krifka, M. Behr, C. Kolbeck, R. Lang, M. Rosentritt, *J. Oral Sci.*, **61**(2), 270 (2019).
6. Z. Valcheva, H. Arnautska, G. Ivanova, I. Atanasova, S. Yaneva, *J. Union Sci.-Varna Med. Ecol. Ser.,* **22**(2), 42 (2017).
7. A. Skorulska, P. Piszko, Z. Rybak, M. Szymonowicz, M. Dobrzyński, *Materials*, **14**(7), 1592 (2021).
8. M. Dimova, I. Stoeva, *Scientific works of the Union of Scientists - Plovdiv, 2007, Series B. Medicine, pharmacy and dental medicine,* **9**, 171 (2008) (in Bulgarian).
9. J. H. Koumjian, A. Nimmo, *J. Prosthet. Dent.*, **64**(6), 654 (1990).
10. D. R. Haselton, A. M. Diaz-Arnold, D. V. Dawson, *J. Prosthet. Dent.,* **93**(1), 70 (2005).
11. S. F. Rosenstiel, M. F. Land, J. Fujimoto, Contemporary Fixed Prosthodontics, 4th edn. St. Louis: Mosby, 2006, *pp.* 96, 466.
12. F. Nejatidanesh, H.R. Lotfi, O. Savabi, *J. Prosthet. Dent.*, **95**(5), 364 (2006).
13. F. B. Robinson, S. Hovijitra, *J. Prosthet. Dent.*, 47(4), 390 (1982).
14. R. L. Wang, B. K. Moore, C. J. Goodacre, M. L. Swartz, C. J. Andres, *Int. J. Prosthodont.*, **2**(2), 173 (1989).
15. S. F. Rosenstiel, M. F. Land, J. Fujimoto, Contemporary Fixed Prosthodontics, Fifth edn., St. Louis, Missouri, Elsevier, 2016, p. 401.
16. C. Abad-Coronel, E. Carrera, N. Mena Córdova, J. I. Fajardo, P. Aliaga, *Materials*, **14**(24), 7791 (2021).
17. H. Lambert, J. C. Durand, B. Jacquot, M. Fages, *J. Adv. Prosthodont.*, **9**(6), 486 (2017).
18. K. M. Regish, D. Sharma, D. R. Prithviraj, *Int. J. Dent.*, 134659 (2011).
19. S. Digholkar, V.N.V. Madhav, J. Palaskar, *J. Indian Prosthodont. Soc.*, **16**(4), 328 (2016).
20. G. Alp, S. Murat, B. Yilmaz, *J. Prosthodont.*, **28**(2), e491 (2019).
21. Z. Mousavi Nejad, A. Zamanian, M. Saeidifar, H. R. Vanaei, M. Salar Amoli, *Polymers*, **13**(24), 4442 (2021).
22. M. Y. Song, J. M. Park, E. J. Park, *J. Adv. Prosthodont.,* **2**(3), 106 (2010).

23. G. Maille, E. Loyer, *J. Prosthet. Dent.,* **121**(2), 358 (2019).
24. F. Beuer, J. Schweiger, D. Edelhoff, *Bras. Dent. J.,* **204**(9), 505 (2008).
25. V. Alt, M. Hannig, B. Wostmann, M. Balkenhol, *Official Publication of the Academy of Dental Materials*, **27**(4), 339 (2011).
26. S. Taufall, M. Eichberger, P. R. Schmidlin, B. Stawarczyk, *Clin. Oral Investig*., **20**(9), 2493 (2016).
27. K. J. Ferro, S. M. Morgano, C. F. Driscoll, M. A. Freilich, A. D. Guckes, K. L. Knoernschild, M. Twain, The glossary of prosthodontic terms, 2017.
28. M. Dimova, Preliminary constructions in permanent dentures, PhD Thesis, Sofia, 2003 (in Bulgarian).
29. N. Popov, *Med. and Phys. J*., 1992 (in Bulgarian).
30. Z. N. Al-Dwairi, K. Y. Tahboub, N. Z. Baba, C. J. Goodacre, *J. Prosthodont*., **29**(4), 341 (2020).
31. M. Balkenhol, H. Köhler, K. Orbach, B. Wöstmann, *Official Publication of the Academy of Dental Materials,* **25**(7), 917 (2009).
32. G. J. Christensen, *Journal of the American Dental Association (1939),* **127**(2), 249 (1996).
33. G. J. Christensen, *Journal of the American Dental Association (1939),* **128**(3), 353 (1997).
34. R. S. Jamel, E. M. Yahya, *Al-Rafidain Dental Journal*, **22**(1), 203 (2022).
35. D. A. Kaiser, E Jr. Cavazos, *Dent. Clin. North Am.,* **29**(2), 403 (1985).
36. J. L. Lui, J. C. Setcos, R. W. Phillips*, Operative Dentistry,* **11**(3), 103 (1986).
37. S. Rangelov, *Problems of Dental Medicine*, **47**(2021/1), 13 (2021).
38. D. R. Burns, D. A. Beck, S. K. Nelson, *J. Prosthet. Dent*., **90**(5), 474 (2003).
39. M. F. Ireland, D. L. Dixon, L. C. Breeding, M. H. Ramp, *J. Prosthet. Dent*., 80(2), 158 (1998).
40. N. Milanov, Photopolymerizable plastic for repairs - a clinical and experimental study, PhD Thesis, Sofia, 2022 (in Bulgarian).
41. M. Yankova, Clinical and experimental study of elastic materials for lining full prostheses, PhD Thesis, Sofia, 2018 (in Bulgarian).
42. A. G. Gegauff, J. J. Wilkerson, *The International Journal of Prosthodontics,* **8**(1), 62 (1995).
43. F. Vahidi, *Dent. Clin. North Am*., **3**(3), 363 (1987).
44. H. M. Skurow, M. Nevins, *The International Journal of Periodontics & Restorative Dentistry,* **8**(1), 8 (1988).
45. N. S. Đorđević, D. Tričković-Vukić, M. G. Šehalić, D. D. Marjanović, D. D. Lazić, R. D. Radosavljević, et al., *Journal of Oral Science*, **64**(3), 228 (2022).
46. K. Sztyler, R.J. Wiglusz, M. Dobrzynski, *Materials* (Basel), **15**(6), 2081 (2022).
47. M. Hristozova, S. Zlatev, A. Vlahova, A Fully Digital Approach in Aesthetic Rehabilitation, Case report, Oral presentation, Science and Youth Conference, MU-Plovdiv, 11.04.2021.
48. Z. Valcheva, H. Arnautska, J. *Union Sci.-Varna Med. Ecol. Ser.*, **27**(1), 37 (2022).
49. Z. Valcheva, H. Arnautska, M. Rushid, J. *Union Sci.-Varna Med. Ser.,* **27**(2), 41 (2022).
50. T.A. Sulaiman, J. *Esthet. Restor. Dent*., **32**, 171 (2020).
51. M. Benli, B. Eker-Gümüş, Y. Kahraman, O. Huck, M. Özcan, *Dental Materials Journal*, **40**(3), 772, (2021).
52. B. Yordanov, I. Yoncheva, Manual of Prosthetic Dentistry Propaedeutics, Sofia, 2000 (in Bulgarian).
53. Filchev, Prosthetic dentistry – clinic, Sofia, Mind Print, 2014 (in Bulgarian).
54. M. Vlahova, *Balk. J. Dent. Med*., **20**(2), 122 (2016).
55. N. P. C. Cheremisinoff, in: N. P. Cheremisinoff (ed.) Condensed Encyclopedia of Polymer Engineering Terms, Boston, Butterworth-Heinemann, 2001, p. 39.
56. I. Taneva, T. Uzunov, *Journal of Physics: Conference Series,* IOP Publishing, **1492** (1), 012018.
57. M. M. Rayyan, M. Aboushelib, N.M. Sayed, A. Ibrahim, R. Jimbo, *J. Prosthet. Dent*., **114**(3), 414 (2015).
58. J. Yao, J. Li, Y. Wang, H. Huang, *J. Prosthet. Dent*., **112**(3), 649 (2014).
59. A. Barazanchi, K. C. Li, B. Al-Amleh, K. Lyons, J. N. Waddell, *J. Prosthodont.,* **26**(2), 156 (2017).
60. M. Revilla-León, M. Meyers, A. Zandinejad, M. Özcan, *Journal of Esthetic and Restorative Dentistry,* 31 (2018).
61. M. Javaid, A. Haleem, *Journal of Oral Biology and Craniofacial Research,* **9**(3), 179 (2019).
62. E. J. Bae, I. D. Jeong, W. C. Kim, J. H. Kim, *J. Prosthet. .Dent.*, **118**(2), 187 (2017).
63. W. R. Larson, D. L. Dixon, S. A. Aquilino, J. M. Clancy, *J. Prosthet. Dent*., **66**(6), 816 (1991).
64. P. Pfeiffer, L. Grube, *The Journal of Prosthetic Dentistry,* **89**(2), 170 (2003).
65. S. H. Kim, D. C. Watts, *The International Journal of Prosthodontics,* **17**(3), 318 (2004).
66. T. A. Hamza, S. F. Rosenstiel, M. M. Elhosary, R. M. Ibraheem, *J. Prosthet. Dent*., **91**(3), 258 (2004).
67. N. Pietrobon, C. R. Lehner, P. Schärer, *Schweizer Monatsschrift fur Zahnmedizin = Revue mensuelle Suisse d'odonto-stomatologie = Rivista mensile Svizzera di odontologia e stomatologia,* **106**(3), 236 (1996).
68. M. B. Moulding, P. E. Teplitsky, *The International Journal of Prosthodontics,* **3**(3), 299 (1990).
69. B. D. Hammond, J. A. Hodd, *J. Prosthet. Dent,* **116**(4), 496 (2016).
70. D. Filchev, E. Yoncheva, *Dental Medicine*, **94**(3), 91 (2012).

Strength qualities of test specimens of materials for preliminary non-removable prosthetic constructions - Part 2. Principal component analysis

S. Rangelov[1]*, M. Dimova-Gabrovska[1], E. Kirilova[2], K. Kirilov[3,4]

[1]Department of Prosthetic Dental Medicine, Faculty of Dental Medicine, Medical University – Sofia, Sv. Georgi Sofiyski, Str., 1, Sofia 1431, Bulgaria
[2]Institute of Chemical Engineering, Bulgarian Academy of Sciences, Acad. G. Bonchev Str., Bl.103, Sofia 1113, Bulgaria
[3]Institute of Molecular Biology, Bulgarian Academy of Sciences, Akad. G. Bonchev Str., Bl. 21, Sofia 1113, Bulgaria
[4]Department of Natural Sciences, New Bulgarian University, Montevideo Str., 21, Sofia 1618, Bulgaria

Prosthetic rehabilitation prior to definitive prosthesis placement is an important stage in dental prosthetic treatment. Fracture of provisional bridge constructions is a common problem in practice, and reinforcement with different materials is an approach for prevention and repair in such cases. Investigating the strength properties of materials for provisional prosthesis through in vitro studies is crucial for making informed choices regarding material and reinforcement in treatment plans. For this purpose, investigation of the physico-mechanical characteristics (maximum force before fracture, flexural strength, and modulus of elasticity) of combinations between six types of polymeric materials and five types of reinforcing fibers was conducted. Comparative analysis of such a large dataset (1260 test specimens) was performed using Principal Component Analysis (PCA). The results are promising for the qualities of provisional non-removable prostheses fabricated using digital methods with or without reinforcement, and they allow for the systematization of the studied materials. The test specimens made of CAD/CAM resin for 3D printing, specifically Temporary CB resin (FormLabs, USA), demonstrated the most optimal strength qualities.

Keywords: Principal component analysis, mechanical characteristics, dental polymers, preliminary non-removable prosthetics, interim dental materials

INTRODUCTION

The theoretical study of the mechanical properties of materials is extremely important for predicting their behavior under applied loads of various types [1] as well as for achieving a better understanding of failure mechanics [2]. This applies to the greatest extent when considering materials that are used in medicine and specifically in dentistry. The mechanical properties of materials for preliminary non-removable prosthetic constructions (PNRPC) are an important factor in determining the clinical application [3] of different materials and methods and are crucial for the long-term success and effectiveness of this mandatory stage prior to final prosthetic treatment, as well as for patient satisfaction and motivation towards the proposed therapeutic approach. In preliminary bridge constructions, the investigation [4] and interpretation of flexural strength, maximum force before fracture, and modulus of elasticity [5] under laboratory in vitro conditions, play a crucial role in clinical approval and selection of materials and reinforcements in treatment plans. In 2004, Kim and Watts [6] examined the influence of glass fiber reinforcement on polymers for PNRPC - three dimethacrylate materials and one monomethacrylate. The effect of water storage on the test specimens was also compared. The study found a significant increase in flexural strength values for the fiber-reinforced groups and lower values for the specimens stored in a water environment, but without statistical significance.

In a similar study, again in 2004, Hamza *et al.* [7] compared the mechanical properties of three types of PNRPC materials (poly(methyl methacrylate) (PMMA), poly(ethyl methacrylate) (PEMA) and composite), reinforced with two types of glass fibers and four types of polyethylene fibers (Kevlar). The authors investigated fracture strength and flexural strength of the test specimens, according to ASTM no. E 399-83 and ISO 14077, respectively, using non-reinforced specimens as a control group.

In a comparative study from 2022, Pantea *et al.* [8] performed testing on polymer materials for the fabrication of preliminary constructions - two using conventional methods and two using digital methods.

---

* To whom all correspondence should be sent:
E-mail: s.rangelov@fdm.mu-sofia.bg

Their results were better for the polymer materials for 3D printing, which they attributed to the homogeneity of the specimens produced using this method.

In data analysis, a contemporary statistical method called principal component analysis (PCA) is used [9]. The capabilities of PCA in processing large volumes of data make it a preferred method in many cases. PCA is performed by transforming the observations of correlated variables into a set of linearly uncorrelated variables through orthogonal transformation. These new transformed variables are called principal components. They are arranged in a way that the preservation of variation in the original variables decreases along the order. Thus, the first principal component retains the maximum variation (maximum possible information) present in the original components, followed by the second principal component retaining the remaining maximum information, and so on.

For the purposes of studying the mechanical characteristics of polymer dental composites for preliminary non-removable prostheses with or without reinforcing fibers, (PCA) was used. Six types of experimental specimens were fabricated according to ISO 10477 standard, employing both laboratory conventional methods and digital methods such as CAD/CAM milling and 3D printing. Some of them were reinforced with five types of fibers - metal (with and without aesthetic coating), glass (with and without polymer coating), and polypropylene fibers. Several mechanical properties of the dental samples were measured, including flexural strength, maximum force before fracturing, and modulus of elasticity. The results obtained for these properties were further analyzed using PCA.

The objective of this study is to evaluate the strength qualities of test specimens made from materials for PNRPC based on in vitro data using PCA analysis.

MATERIALS AND METHODS

The strength properties of experimental specimens made from three types of laboratory dental polymers for PNRPC are studied and compared. The specimens are made from thermopolymerizing material, factory-polymerized material for subtractive fabrication using CAD/CAM, and light-polymerizing material for additive fabrication using CAD/CAM, based on the type of polymerization activation. The specimens were categorized as unreinforced or reinforced with

fibers, including dental glass fibers - Fiber Splint One Layer (Polydentia, Switzerland), polyethylene fibers - Ribbond Regular 4.0 mm (Ribbond Inc., USA), braided multi-strand orthodontic wire for splinting - 015" Leone (Leone S.p.a., Italy), esthetically coated chrome-cobalt ligature wire - 012" Leone (Leone S.p.a., Italy), and glass fiber thread coated with light-polymerizing resin for dental use - Interlig 8.5 ×0.2 mm (Angelus, Brazil). The details are presented in Tables 1 and 2.

The specimens were fabricated (Fig. 1) *in vitro* using a device that is registered as a protected subject of industrial property (utility model) in the Patent Office of the Republic of Bulgaria under No. 4383 U1 with the following title: "Device for fabricating specimens from polymer materials for crowns and veneers with reinforcement capability"

For the three-point bending flexural test an universal testing system MultiTest single-column force tester 2.5-i (Mecmesin Ltd., United Kingdom) was used. The testing was conducted following the instructions given in ISO 10477:2021 'Dentistry – Polymer-based crown and veneering materials':

"…Flexural strength test apparatus, appropriately calibrated, to provide a constant cross-head speed of $(1,0 \pm 0,3)$ mm/min. The apparatus consists of two rods (2 mm in diameter), mounted parallel with 20 mm between centres, and a third rod (2 mm in diameter) centred between, and parallel to the other two, so that the three rods in combination can be used to give a three-point loading to the specimen..."

All data from specimens tested was collected by the Emperor™ Force software (Mecmesin Ltd., United Kingdom) and exported in table format to Excel (Microsoft, USA).

The obtained statistical data on the physical-mechanical characteristics of the laboratory and clinical experimental specimens, with and without reinforcement, were subjected to a comprehensive analysis using the Principal Component Analysis (PCA) method included in the software package OriginPro 7.5.

The principal components are the eigenvectors of the covariance matrix, and they are orthogonal or perpendicular to each other. The first two principal components have been used to plot the data in two dimensions and visually identify clusters of closely related data points.

The PCA method was performed in several main steps [10]:

Step 1: Data normalization

The PCA method is sensitive to the variations of the initial variables. When the variables vary on different scales with large deviations from each other, varables with larger ranges of variation may dominate those with smaller ranges. To normalize the variables in the current sample, the values of the variables with greater variation are subtracted. After normalization, the variables are transformed to equal scales.

Step 2: Calculation of the covariance matrix

The covariance matrix consists of the covariances between all possible pairs of variables. The (i,j) element represents the covariance between the i-th and j-th variable. The covariance matrix is of size p x p, where p represents the number of variables. Since the covariance of a variable with itself is its variance, the elements on the main diagonal of the covariance matrix represent the variances of each variable. Covariance is commutative, and the elements of the covariance matrix are symmetric with respect to the main diagonal, which means that the upper and lower parts are equal.

This matrix shows how the variables in the input dataset vary from their mean values relative to each other or indicates the presence of correlations between them. Correlation, in turn, denotes the relationship between two variables. The correlation value varies from -1 to +1.

The presence of a positive value in an element of the covariance matrix indicates that increasing the value of one variable in the considered pair of variables leads to an increase in the value of the other variable.

The presence of a negative value in an element of this matrix indicates that increasing the value of one variable leads to a decrease in the value of the other variable.

The presence of an element in the matrix with a value of 0 indicates that the variables are orthogonal or have no correlation between them.

On the other hand, the absolute value of each element of the covariance matrix indicates the strength of the relationship between the variables.

Table 1. Distribution of the investigated non-reinforced test specimens.

Group	Code	NS[1]	Subgroup Material/Supplier	Code	N	Storage conditions	Code	NS[1]
Solid laboratory specimens	3.1	180	HP – PMMA[3] Superpont C+B (Spofa Dental, Czech Republic)	3.1.1	60	Dry DW[2]	3.1.1.A 3.1.1.B	30 30
			CAD-CAM pre-polymerized PMMA DD temp MED (Dental Direkt GmbH, Germany)	3.1.2	60	Dry DW	3.1.2.A 3.1.2.B	30 30
			CAD-CAM printing resin Temporary CB Resin (FormLabs, USA)	3.1.3	60	Dry DW	3.1.3.A 3.1.3.B	30 30
Solid clinical specimens	3.2	180	Self-polymerizing PEMA DENTALON plus (Kulzer, Germany)	3.2.1	60	Dry DW	3.2.1.A 3.2.1.B	30 30
			Light-curing composite Revotek LC (GC, Japan)	3.2.2	60	Dry DW	3.2.2.A 3.2.2.B	30 30
			Dual-curing composite TempSpan (Pentron, USA)	3.2.3	60	Dry DW	3.2.3.A 3.2.3.B	30 30

[1]Number of specimens;
[2]Distilled water;
[3]Heat polymerizing PMMA Superpont C+B (Spofa Dental, Czech Republic).

Table 2. Distribution of tested reinforced specimens.

Reinforcement	Code	NS[1]	Subgroup Material/Supplier	Code	N	Storage conditions	Code	NS[1]
Fiber glass thread Fiber Splint One Layer (Polydentia, Switzerland)	4.1	180	HP – PMMA[3]	4.1.1	60	Dry	4.1.1.A	30
						DW[2]	4.1.1.B	30
			CAD-CAM PMMA[4]	4.1.2	60	Dry	4.1.2.A	30
						DW	4.1.2.B	30
			CAD-CAM resin[5]	4.1.3	60	Dry	4.1.3.A	30
						DW	4.1.3.B	30
Polyethylene thread Ribbond Regular 4.0 mm (Ribbond Inc., USA)	4.2	180	HP - PMMA	4.2.1	60	Dry	4.2.1.A	30
						DW	4.2.1.B	30
			CAD-CAM PMMA	4.2.2	60	Dry	4.2.2.A	30
						DW	4.2.2.B	30
			CAD-CAM resin	4.2.3	60	Dry	4.2.3.A	30
						DW	4.2.3.B	30
Metal triple-braided wire for splinting 015" Leone (Leone S.p.a., Italy)	4.3	180	HP - PMMA	4.3.1	60	Dry	4.3.1.A	30
						DW	4.3.1.B	30
			CAD-CAM PMMA	4.3.2	60	Dry	4.3.2.A	30
						DW	4.3.2.B	30
			CAD-CAM resin	4.3.3	60	Dry	4.3.3.A	30
						DW	4.3.3.B	30
Aesthetically coated ligature wire 012" Leone (Leone S.p.a., Italy)	4.4	180	HP - PMMA	4.4.1	60	Dry	4.4.1.A	30
						DW	4.4.1.B	30
			CAD-CAM PMMA	4.4.2	60	Dry	4.4.2.A	30
						DW	4.4.2.B	30
			CAD-CAM resin	4.4.3	60	Dry	4.4.3.A	30
						DW	4.4.3.B	30
Glass fiber threads coated with light-curing resin Interlig 8,5 x 0,2 mm (Angelus, Brazil)	4.5	180	HP - PMMA	4.5.1	60	Dry	4.5.1.A	30
						DW	4.5.1.B	30
			CAD-CAM PMMA	4.5.2	60	Dry	4.5.2.A	30
						DW	4.5.2.B	30
			CAD-CAM resin	4.5.3	60	Dry	4.5.3.A	30
						DW	4.5.3.B	30

[1]Number of specimens;
[2]Distilled water;
[3]Heat polymerizing PMMA Superpont C+B (Spofa Dental, Czech Republic);
[4]CAD-CAM factory pre-polymerized PMMA DD temp MED (Dental Direkt GmbH, Germany);
[5]CAD-CAM printing resin Temporary CB Resin (FormLabs, USA).
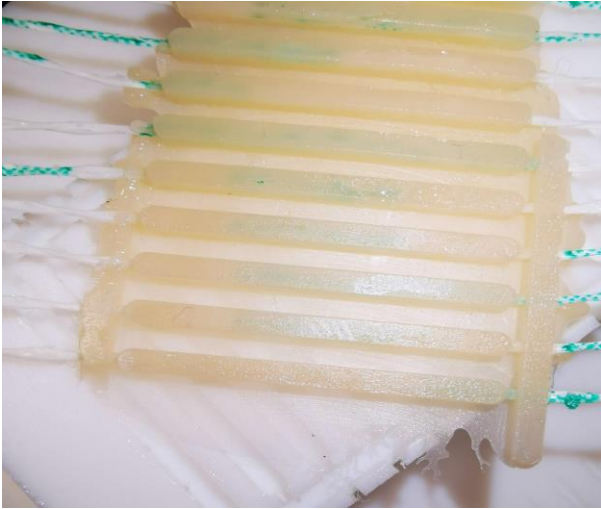
Fig. 1. Test series of specimens with a dual-curing clinical material for PNRPC reinforced with glass fibers for industrial use.

Step 3: Calculation of eigenvectors and eigenvalues of the covariance matrix

The eigenvalues are the coefficients in the eigenvectors. They indicate the amount of variance carried in each principal component. By arranging the eigenvectors in order of their eigenvalues, from highest to lowest, the principal components are obtained in order of significance.

Step 4: Calculation of principal components

Principal components are constructed in such a way that the first principal component captures the largest possible variation (variance) in the dataset. The second principal component captures the next largest variance, and so on until the last component. The number of principal components is equal to the original number of variables. Organizing the information into principal components allows for dimensionality reduction of the data array with minimal loss of information and the removal of components that carry little information. After determining the principal components, the percentage of variance (information) accounted for by each component is calculated by dividing the eigenvalue of each component by the sum of all eigenvalues.

Step 5: Determination of feature vectors

At this step, the decision is made regarding which principal components (with larger values and eigenvalues) should be retained and which ones should be discarded (those with smaller values and eigenvalues). The principal components that are retained form a matrix of vectors called the feature vector. The feature vector is a matrix whose columns

represent the eigenvectors of the components that have been chosen to be preserved. This process reduces the dimensionality of the data.

Step 6: Data transformation along the principal components

In the final step, the data is transformed from the original axes (variables) to those represented by the principal components by multiplying the transpose of the original dataset by the transpose of the feature vector.

RESULTS

The PCA method was applied for statistical analysis of the experimental data obtained from testing 1260 specimens of the three physico-mechanical characteristics: bending strength (FS) in MPa; maximum force before fracture (Fmax) in N, and modulus of elasticity (E) in MPa, using the aforementioned materials, their reinforcements, and storage conditions. As a result, the values of two principal components, PC1 and PC2, were determined, which account for 87.56% and 12.43% of the variance in the experimental data, respectively.

The results obtained from applying PCA are presented in tables below. Table 3 displays the results of the covariance analysis. There is a high degree of correlation (r = 0.999) between FS and Fmax.

Table 3. Correlation matrix containing correlation coefficients.

Variables	FS (MPa)	Fmax (N)	E (MPa)
FS (MPa)	1	0.999	0.713
Fmax (N)	0.999	1	0.714
E (MPa)	0.713	0.714	1

In Table 3, FS (MPa) represents the bending strength, Fmax (N) represents the maximum force before fracturing, and E (MPa) represents the modulus of elasticity.

In Table 4, the summarized contribution of the dependent variables to the statistical model is presented. The highest percentage, 87.56%, is associated with the bending strength FS (MPa), followed by a contribution of 12.43% from the maximum force before fracturing Fmax (N). The eigenvalues of the matrix are shown in Table 4.

From the results presented in Tables 3, 4, and 5, it can be observed that there is a very strong correlation between the two variables FS and Fmax, indicating a close relationship between them. This means that an increase in one variable will inevitably lead to an increase in the other. The observed relationship is

directly proportional, corresponding to a correlation coefficient of approximately +1. This provides a basis to consider that one of the two variables, FS or Fmax, can be chosen for further analysis while excluding the other variable from subsequent consideration. In this case, the variable Fmax is selected. A weaker correlation is observed between the variables E and FS.

Table 4. Eigenvalues of the correlation matrix.

Component	Eigenvalue	Variance	Cumulative Probability
FS (MPa)	2.626	87.56%	87.56%
Fmax (N)	0.372	12.43%	99.98%
E (MPa)	$5.39.10^{-4}$	0.02%	100%

Table 5. Extracted eigenvectors.

Vectors	Coefficients of PC1	Coefficients of PC2
FS (MPa)	0.600	-0.374
Fmax (N)	0.600	-0.372
E (MPa)	0.527	0.849

Fig. 2. Plot of the two principal components in two dimensions and visual identification of clusters of closely related data points.

Table 6. Obtained optimal results for the investigated polymer materials, reinforcements, and storage conditions after applying the PCA method.

Exp.	Sample Code	Reinforcement	Polymer	Storage conditions	F max/N	FS/MPa	E/MPa
Cluster with the highest modulus of elasticity E (MPa)
484	4.1.3.A	Glass fibers - Fiber Splint One Layer (Polydentia, Switzerland)	CAD-CAM resin for printing Temporary CB Resin, (FormLabs, USA)	at room temperature	24.2	91.5	10894.8
492					24.8	92.1	10895.4
Cluster of data points with the highest modulus of elasticity E (MPa) and good flexural strength FS (MPa)
154	3.1.3.B	Laboratory plain without reinforcement	CAD-CAM resin for printing Temporary CB Resin, (FormLabs, USA)	in distilled water at room temperature	26.4	99.9	11205.4
157					26.5	100	11205.5
164					26.6	100.1	11205.6
174					26.9	100.4	11205.9
181					26.8	100.3	11205.8
Cluster of data points with the highest flexural strength FS (MPa) and good modulus of elasticity E (MPa)
785	4.3.2.B	Braided orthodontic wire for splinting - 015" Leone (Leone S.p.a., Italy)	CAD-CAM prefabricated PMMA DD temp MED (Dental Direkt GmbH, Germany)	in distilled water at room temperature	32.2	121.7	10893.6
789					32.3	121.8	10893.7
795					32.4	121.9	10893.8
804					32.8	122.3	10894.2
807					32.7	122.2	10894.1
810					32.6	122.1	10894
Cluster of data points with the highest flexural strength FS (MPa)
786	4.3.2.B	Braided orthodontic wire for splinting - 015" Leone (Leone S.p.a., Italy)	CAD-CAM prefabricated PMMA DD temp MED (Dental Direkt GmbH, Germany)	in distilled water at room temperature	28.8	108.8	9337.8
793					28.9	108.9	9337.9
797					29	109	9338
799					29.4	109.4	9338.4
801					29.3	109.3	9338.3
805					29.2	109.2	9338.2

Figure 2 represents the distribution of data in two dimensions - the two principal components. Based on this visualization, clusters of closely related data points have been identified. In Table 6 are systematized the clusters of data points corresponding to the optimal results obtained for the two variables: modulus of elasticity E (MPa) and flexural strength FS (MPa), which determine more durable dental polymer materials.

DISCUSSION

In the present study, the PCA method was applied to investigate the physico-mechanical characteristics (maximum force before fracture, flexural strength, and modulus of elasticity) of polymer dental composites, used for preformed non-removable prostheses with or without reinforcing fibers.

Principal component analysis is a statistical method applied to process large datasets that contain a high number of measurements/observational features. Its application aims to reduce the dimensionality of the data while increasing interpretability and minimizing information loss. This is achieved by creating new uncorrelated variables, known as principal components, which sequentially maximize the variance. Finding such new variables involves solving an eigenvalue/eigenvector problem, where the new variables are defined based on the available dataset. In most cases, the analysis focuses on identifying the first two principal components, representing the data in two dimensions and visually identifying clusters of closely related data points.

When applying PCA, a strong correlation was found between two of the investigated mechanical properties - flexural strength and maximum force before fracture. The results obtained from the analysis of the experimental data for the remaining two properties - flexural strength and elastic modulus, allowed the identification of the three types of test specimens made of polymer materials with and without reinforcement, which exhibited the highest values for these properties. They are:

1) Plain test specimens made of CAD-CAM resin for 3D printing, specifically Temporary CB Resin from (FormLabs, USA).

2) Test specimens made of CAD-CAM resin for 3D printing, specifically Temporary CB Resin from (FormLabs, USA), reinforced with a single layer of glass fiber splint (Fiber Splint One Layer) from Polydentia (Switzerland).

3) Test specimens made of CAD-CAM factory PMMA (polymethyl methacrylate) material, specifically DD temp MED from Dental Direkt GmbH (Germany), reinforced with a triple-braided chrome-cobalt wire for splinting, specifically 0.015" wire from Leone (Italy).

CONCLUSIONS

The presented sequence of materials and reinforcements, determined based on PCA as the materials and combinations with the highest strength qualities, directs clinical thinking towards the need for validation of these data in a clinical experiment. This, along with the presented in vitro study, is the subject of scientific research in a dissertation titled "Reinforcement of materials for preliminary constructions - laboratory and clinical investigation".

REFERENCES

1. J. Ivanova, V. Valeva, T. Petrova, W. Becker, *Mechanics of Advanced Materials and Structures*, **22**(10), 813 (2015).
2. J. Ivanova, V. Valeva, T. Petrova, W. Becker, Piezo health monitoring of adhesive joints, in: Proceedings of the 9th Conference on Sustainable Development of Energy, Water and Environment Systems SDEWES, September 20 - 27, 2014, Venice-Istanbul, article 0194.
3. S. F. Rosenstiel Land, M. F. Fujimoto, J. Contemporary Fixed Prosthodontics, Fifth edn. St. Louis, Missouri, Elsevier, 2016.
4. P. Pfeiffer, L. Grube, *The Journal of Prosthetic Dentistry*, **89**(2), 170 (2003).
5. Z. N. Al-Dwairi, K. Y. Tahboub, N. Z. Baba, C. J. Goodacre, *J. Prosthodont.*, **29**(
6. *The International Journal of Prosthodontics*, **17**(3), 318 (2004).
7. T. A. Hamza, S. F. Rosenstiel, M. M. Elhosary, R. M. Ibraheem, *J. Prosthet. Dent.*, **91**(3), 258 (2004).
8. M. Pantea, R. C. Ciocoiu, M. Greabu, A. Ripszky Totan, M. Imre, A. M. C. Țâncu,... A. E. Petre, *Materials*, **15**(9) 3075 (2022).
9. L. I. Smith, A Tutorial on Principal Components Analysis, 2002. https://ourarchive.otago.ac.nz/bitstream/handle/10523/7534/OUCS-2002-12.pdf
10. https://builtin.com/data-science/step-step-explanation-principal-component-analysis

Joule heating effect in carbon-based epoxy resin: an experimental and numerical study

G. Spinelli[1,2], R. Guarini[2], R. Kotsilkova[2], E. Ivanov[2,3]*, L. Vertuccio[4], V. Romano[5], L. Guadagno[5]

[1]*University of Study "Giustino Fortunato", Via Raffaele Delcogliano 12, 82100, Benevento, Italy*
[2]*Institute of Mechanics, Bulgarian Academy of Sciences, Acad. G. Bonchev Str., Bl. 4, 1113, Sofia, Bulgaria*
[3]*Research and Development of Nanomaterials and Nanotechnologies, NanoTech Lab Ltd., Acad. G. Bonchev Str., Bl. 4, 1113 Sofia, Bulgaria*
[4]*Department of Engineering, University of Campania "Luigi Vanvitelli", Via Roma 29, 81031 Aversa, Italy*
[5]*Department of Industrial Engineering, University of Salerno, Via Giovanni Paolo II, 84084 Fisciano (SA) Italy*

Extruded metals are the most common materials used for the production of heat sinks for thermal management. Nowadays, in the structural design phase, reduction of mass with consequent savings in materials and costs is one of the main aspects to consider. More recently, polymer-based nanocomposites with improved electrical and thermal properties are increasingly assessed for heat transport applications. The present study is focused on nanocomposites based on a structural epoxy resin filled with multi-walled carbon nanotubes (MWCNTs) which are prepared and then experimentally characterized. More specifically, after a preliminary investigation in terms of electrical conductivity, the temperature increase over time, due to the Joule heating effect is analyzed in response to different voltage values (70V, 80V, and 90V) applied to the test samples with a filler concentration of 3 wt%. These experimental results are used to validate a 3-dimensional numerical simulation carried out by using a commercial software (COMSOL Multiphysics®). A very positive agreement between experimental and modeling data is found. Once the model was validated, a number of physical properties of such nanocomposites related to the Joule heating were numerically explored for testing their potential practical use as heat exchangers. The aim of this study is to encourage the application of modern computational methods in conjunction with experimental techniques for adding knowledge in materials science. With this approach, new materials can be discovered or those already existing can be better investigated.

Keywords: carbon-based epoxy nanocomposites, thermal transport properties, multiphysics simulations, Joule-heating, electrical properties

INTRODUCTION

Low thermal and electrical properties are limitations not yet completely overcome when it comes to polymer-based composites, which are therefore classically recognized as insulating materials. Nevertheless, the use of polymers in thermal applications like heat exchangers is increasingly investigated for a series of benefits. Lightness, easy workability, cost reduction are just some of the remarkable properties compared to similar devices classically made by extrusion of metals, primarily aluminum and copper, which are high-density materials and, in particular, non-biodegradable [1, 2]. Recently, to achieve these goals, academic and industrial research efforts have been successfully focused to improve the overall electrical, mechanical and thermal properties of nanocomposites through the use of nanoscale fillers [3-6]. Among these nanonfillers, carbon-based particles such as graphene and its derivatives, as well as carbon nanofibers (CNFs) and carbon nanotubes (CNTs), have attracted great attention, owing to their excellent intrinsical physical properties and their strong interfacial interactions, when dispersed in the host polymer matrices [7]. In particular, since the discovery of their existence, CNTs have been widely considered as promising fillers for developing new advanced polymer nanocomposites due to their chemical stability (their carbon atoms form sp2 covalent bonds with honeycomb structure), their unique 1-dimension geometry and their large aspect ratio. All these peculiar characteristics are suitable to form percolation paths which support the electrical and thermal transport within the polymer, thus enhancing the general physical properties of the resulting materials. Smoleń *et al.* have investigated the effect of multiwalled carbon nanotubes produced by catalytic chemical vapor deposition and then subjected to covalent functionalization, on the mechanical and electrical properties of epoxy-based composites in which the percolation threshold was obtained with 1 wt% addition of filler [8]. The use of a surfactant (Triton X-100) to enhance the dispersion state of carbon nanotubes in epoxy polymers for improving the thermomechanical, mechanical and

* To whom all correspondence should be sent:
E-mail: ivanov_evgeni@yahoo.com

electrical properties of the resulting nanocomposites was evaluated by Geng *et al.* [9].

Moreover, mechanical processing methods based on a high-pressure homogenizer and a three-roll calendaring mill in combination [10], were proposed to achieve a well dispersed nanofiller thus enhancing the toughness and electrical properties of the CNT-based epoxy composites which exibit a low percolation threshold (about 0.01 wt%).

The adoption of carbon-based nanofillers for the development of epoxy-based vinyl ester composites with improved mechanical and electromagnetic properties were also considered in view to their potential use in aerospace applications as radar absorbing materials [11].

Thermally and electrically conductive epoxy nanocomposites including carbon nanotubes have been proposed for practical applications in electronics, automotive, and aerospace industries to dissipate heat or to avoid static charge [12].

In the present study, samples based on an epoxy resin filled with different filler content (0.3, 0.5, 1, 2 and 3 wt%) of multiwall carbon nanotubes (MWCNTs) were produced and then experimentally characterized. Based on the results of a preliminary electrical investigation, the electrically most conductive composite (epoxy containing 3 wt% of MWNTs) was selected for thermo-electric insights on the Joule effect due to different voltage values (70 V, 80 V and 90 V) applied to the samples. Joule heating was explored not only experimentally but also through a simulation study carried out with a commercial software (COMSOL Multiphysics®). A good match between experimental and numerical results was found. This means that computational studies are welcomed in materials science to discover new materials and their properties, to better investigate the existing ones, to explain experimental results, to determine material behavior under specific conditions, mechanisms, theories and much more.

MATERIALS AND METHODS

In the present study, the nanocomposites for the experimental tests were manufactured by mixing up, in accordance with a procedure already described in Spinelli *et al.* [13], the following phases: i) an epoxy matrix 3,4-epoxycyclohexylmethyl-3',4'-epoxycyclohexane carboxylate (ECC) which serves as a precursor; ii) a curing agent based on methyl hexahydrophthalic anhydride (MHHPA); iii) multiwall carbon nanotubes (commercial name: Arkema Graphistrength® C100) as a conductive nanofiller. The above-mentioned constituents were suitably combined to obtain samples with different concentrations, i.e. [0.3, 0.5, 1, 2 and 3] wt%. The crucial physical and chemical characteristics of precursor, hardener agent and filler, as well as the size of the parallelepiped-shaped test specimens, are briefly summarized in Figure 1. More information can be found in Guadagno *et al.* [14].
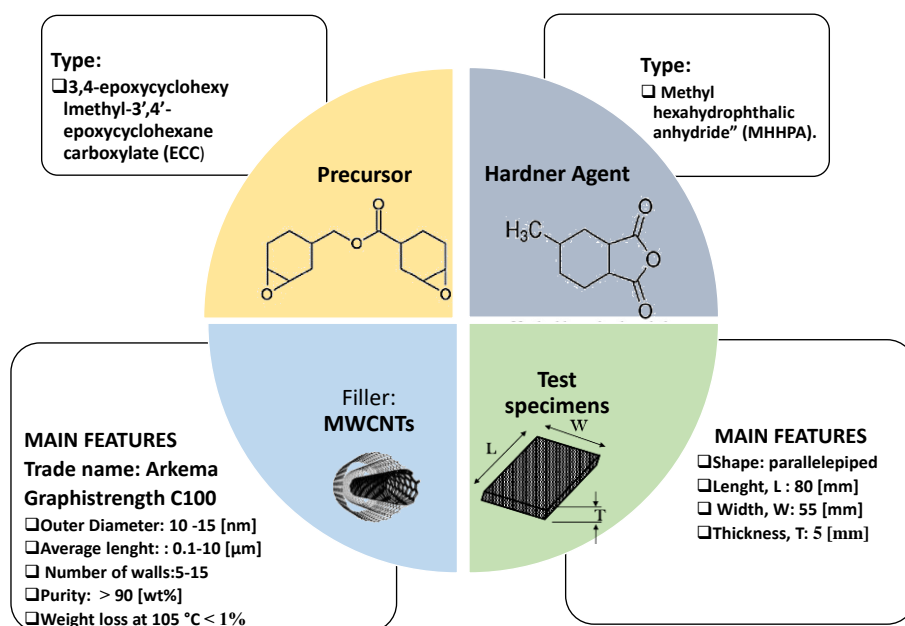
Figure 1. Principal characteristics of the phases of compounds and test samples.
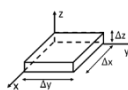
Since the test specimen resistance is of the order of several kΩ, its electrical conductivity was evaluated with a two-probe measurement by assuming the contact resistance negligible, as successfully adopted in literature and in our previous studies [15-18]. On the basis of the results of this preliminary electrical characterization, the electrically most conductive composites containing 3 wt% CNTs have been selected for the experimental and numerical investigation of Joule heating effect.

For this aim, silver paint (commercial name: RS 196-3600) was placed on the short sides of the test samples to provide ohmic contacts between the power supply EA-PSI 8360-10T (Elektro-Automatik, 0–360 V, 0–10 A, 1 kW max) and the HP34401A ammeter (min current 0.1 μA). In particular, the variation over time of the top surface temperature of the specimens, due to Joule heating generated by different values of applied voltage (70V, 80V and 90V) was experimentally observed. These thermal profiles were monitored by means of a thermocouple from which the data were directly acquired by a data acquisition board (Data Logger TC-08 supplied by Pico Technology) managed with the respective software PicoLog. A schematically represention of this thermo-electric measurement setup is shown in Figure 2.

A numerical investigation of the Joule heating effect has been carried out through the software COMSOL Multiphysics®, which is based on Finite Element Method (FEM). The results of the simulation study were then compared with the experimental ones. A schematic representation of the case study addressed in the present work and the main model definitions is reported in Figures 3a) and b), respectively.

With a reference to a differential volume $\Delta x \Delta y \Delta z$, the governing equation for heat transfer in a solid (at constant pressure) used in the numerical simulations can be expressed in cartesian coordinates, according to the following expression:

$$\frac{\partial}{\partial x}\left(\lambda \frac{\partial T}{\partial x}\right) + \frac{\partial}{\partial y}\left(\lambda \frac{\partial T}{\partial y}\right) + \frac{\partial}{\partial z}\left(\lambda \frac{\partial T}{\partial z}\right) + Q|_{Joule\ heating} = \rho c_p \frac{\partial T}{\partial t}$$

(1)

where λ, ρ and c_p are the thermal conductivity [Wm^{-1}K^{-1}], the density [kgm^{-3}] and the specific heat [Jkg^{-1}K^{-1}] of the material, respectivley, whereas $Q=J \cdot E$ is the source term [Wm^{-3}] of the Joule heating related to the electric current. More in details, *J* represents the current density [Am^{-2}] and *E* is the electric field strength [WA^{-1}m^{-1}] generated by the different voltage values (70V, 80V, 90V). Table 1 summarizes the initial and boundary conditions for uniquely resolving the thermal balance of eq. (1).
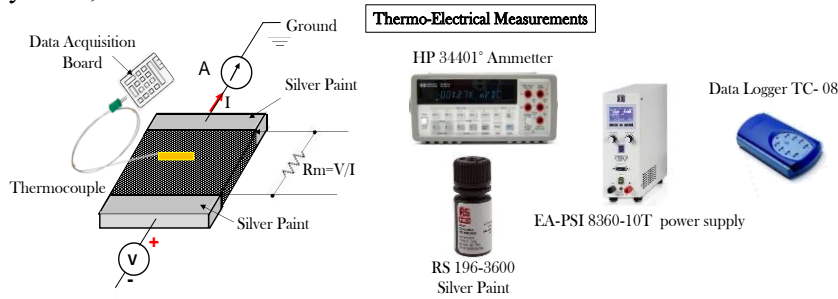
Figure 2. Schematic representation of the thermo-electric and Joule heating tests with the main adopted laboratory apparatus.

Figure 3. a) Case study addressed in the present study; b) Main model definitions for the numerical investigation adopted in COMSOL Multiphysics

Table 1. Initial and boundary conditions (I.C. and B.C., respectively) for resolving equation 1.

Initial (I.C.) and boundary (B.C.) conditions		Equations	Validity
I. C.	t=0	T=Room Temperature (T_0)	$\forall x, \forall y, \forall z$
B. C.	*Upper and Lower Surfaces* $z=0$ $z=5$	$-\lambda\dfrac{\partial T}{\partial z} = h \cdot (T - T_\infty)$	$(\forall x, \forall y, t > 0)$
B. C.	*Lateral Surfaces* $y=0$ $y=55$	$-\lambda\dfrac{\partial T}{\partial y} = h \cdot (T - T_\infty)$	$(\forall x, \forall z, t > 0)$
B. C.	*Back and Front Surfaces* $x=0$ $x=80$	$-\lambda\dfrac{\partial T}{\partial x} = h \cdot (T - T_\infty)$	$(\forall y, \forall z, t > 0)$

RESULTS AND DISCUSSION

DC electrical characterization

As it is espected by the percolation theory, the trend of the electrical conductivity (σ_{DC}) exhibits a power law dependence, which is classically described by the following equation:

$$\sigma_{DC} = \sigma_0 \cdot (v - E.P.T.)^t \quad (2)$$
$$for \ v > E.P.T.$$

where the preexponential factor σ_0, represents the intrinsic electrical conductivity of the nanofillers, v is the instantaneous filler concentration and t is a critical exponent, which depends on the dispersion state of the filler within the matrix [19]. The term *E.P.T.* accounts for the well-known electrical percolation threshold, i.e. the minimum filler loading, at which the electrical behavior of the polymeric matrix changes from insulator to conductive, due to at least one established percolation path. Due to the good dispersion of the nanotubes and their ability to form the percolation network, this electrical threshold is achieved, in our case, with the modest concentration of 0.3 wt%. With this amount of MWCNTs, the overall macroscopic electrical conductivity of the resulting nanocomposites is equal to $6.5 \cdot 10^{-3}$ S/m, whereas at the concentration of 3 wt% it is about $6.8 \cdot 10^{-2}$ S/m.

The latter formulation (epoxy+3wt% of MWCNTs), being the most conductive among those investigated in the present study, is therefore adopted to both experimental and numerical analysis of the thermal properties due to Joule heating effect.

Figure 4 a) shows the so-called percolation curve, i.e. the variation of the electrical conductivity as function of the filler concentration, for the nanocomposites investigated in the present study. Moreover, as commonly verified in literature [20-22] and as shown in Fig. 4b), a theoretical investigation, confirming that the tunneling effect is the main electrical conduction mechanism in composite materials is the existence of a linear correlation between the electrical conductivity (expressed in natural logarithmic) as function of $v^{-1/3}$. The value of the coefficient of determination R^2 close to 1 confirms the validity of this assumption.
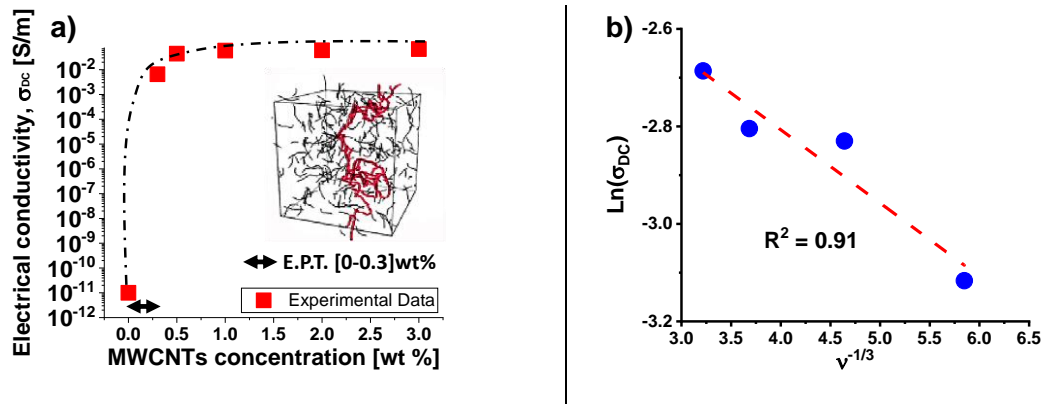
Figure 4. a) Percolation-curve for the epoxy-based nanocomposites filled with different filler concentrations; b) Statistical approach, confirming the role of electron tunneling as the main conduction mechanism in composite materials.

Experimental results on Joule heating effect

Figure 5 a) presents the experimental trend of the upper surface temperature over the time (up to 3600 s), when three different voltage values (70, 80 and 90 V) are applied to the test specimens including 3 wt% of MWCNTs.

From a physical point of view, it is possible to note how the heat transfer begins as transient and then reaches a steady-state, when a thermal equilibrium is reached. More in details, during the transient heat transfer, when the heat flow rate keeps changing, the temperature of the medium is a function of time, $T = T(t)$ for a short duration (t* denoted in the figure). It rises quickly and exponentially tends toward constant steady-state values (indicatively 324K, 331K and 338K, at 70V, 80V, 90V, respectively). A magnification of such time windows is reported in Figure 5b).

During the steady-state transfer which is characterized by a constant and specific rate of heat transfer, the temperature is constant throughout time. This is because the total amount of heat transfer due to the Joule heating is equal to that dissipated with the surrounding area through natural convection. In particular, as shown in Figure 5c), these steady-state values (at t=3600 s) are linearly proportional (the coefficient of determination R^2 is strictly close to 1) to the applied voltage values.

This result is in line with the theoretical prediction since the Joule effect, analytically equivalent to a thermal power dissipation *P,* depends linearly on the voltage *V,* according to the relation $P=V \cdot I$ where *I* is the electrical current. Differently, as shown in Figure 5 d), a near-perfect exponential fit (otherwise, a coefficient of determination equal to 0.973 is found with a linear fit or equal to 0.981 with a power-law fit) is found for the experimental data concerning the heat rate, HR [Kmin[-1]] as a function of the applied voltage. For reasons of clarity, the heat rates are calculated as slopes of the corresponding curves (S_{90V}, S_{80V} and S_{70V}) of Figure 5b) during the first instants of the transient phase.

Numerical study on Joule heating effect

Computational studies involving simulations, modeling and theoretical approaches are increasingly used for developing new materials and to better explain the properties of existing ones.

Figure 6 illustrates the electric potential distribution (left part) and the 3D temperature profiles (right part) by simulating, in a finite element software, the nanocomposites based on 3 wt% of MWCNTs, when subjected to the three different voltage values, as it was the case for the experimental measurements (70, 80 and 90 V in Figs. 6 a), b) and c), respectively).
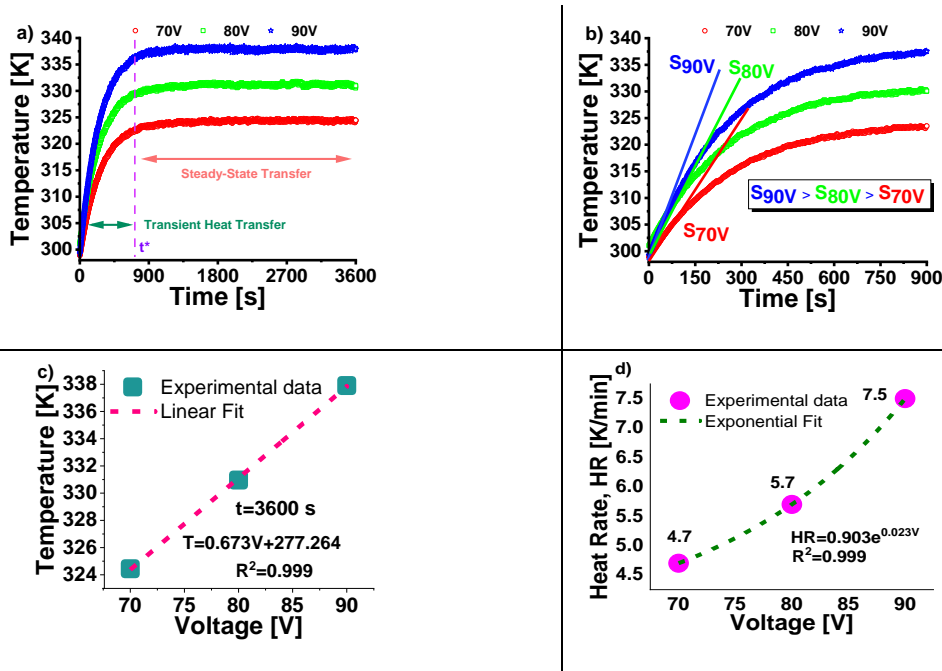
Figure 5. a) Temperature profiles due to Joule heating at different applied voltage values (70, 80 and 90 V); b) Magnification of the transient heat transfer time windows; experimental and curve fitting of the steady-state temperature values and heat rate as function of the voltage levels in c) and d), respectively.

It is worth noting that the electrical potential linearly increases along the increasing x- axis and therefore, it was found that the position of the minimum and maximum electric potential strength occurred at the position 0 mm and 8 mm, respectively, along the direction to which the voltage is applied. As it is expected, it assumes constant values in each transversal cross-section.

Even more interestingly is that almost the same steady-state values for the surface temperatures are numerically found (see the color bars: 323K, 331K and 339K at 70V, 80V, 90V, respectively) by means the multiphysics simulations, thus confirming an interesting agreement between experimental and numerical results.

The use of a 3D software representation allows to graphically explore the temperature distribution on the solid and identify the hottest areas (central parts), compared to those less heated (edges and corners).

In order to deepen this investigation, Figure 7 shows the simulated convective heat flux (at t= 3600 s) for the simulated nanocomposite, always distinguished according to the voltage level applied (70, 80 and 90 V in a), b) and c), respectively). First of all, as evident from the analysis of these figures, the convective flux is visibly greater on the larger surfaces of the sample, than on the lateral ones, since this main mode of thermal energy transport directly depends on the exchange area (and also on the higher temperature achieved in this region) in agreement with Newton's law of cooling, analytically expressed by the following relation:

$$Q = h \cdot S \cdot \Delta T \qquad (3)$$

where h [W/m^{-2}·K^{-1}] is the heat transfer coefficient by natural convection, that denotes the proportionality term between the heat flow Q [W] and the temperature difference ΔT [K], which origins the convective transport between a hot solid surface S [m^2] and the surrounding air. Moreover, by referring to such graphics with their relative color bars it is also possible not only to quantify these heat fluxes but also to evaluate the different rates (the greater the applied voltage, the greater is the temperature difference and consequently the convective flux).

To conclude such numerical investigation, Figure 8 shows the 3D views of the total internal energy U (at t=3600 s) for the nanocomposite, when it undergoes a voltage test of 70, 80 and 90V, in a), b) and c), left part, respectively. Instead, in the corresponding right-hand parts of the same Figure 8 are shown the two-dimensional graphics of this state variable U, as a function of the length [mm] in corrispondence of the symmetry axis along the x-direction. The choice to report the view of some selected cross-section of the sample is driven by the opportunity to show a visual inspection of its change in all spatial directions.

Before discussion of the numerical results, it is important to recall that the internal energy of a solid depends on temperature, i.e. $U=U(T)$ and in particular that its variations ΔU can be expressed in the simple form:

$$\Delta U = U(T_f) - U(T_i) \qquad (4)$$

where T_f and T_i indicate the initial and final temperature of the solid, respectively.

By convention it is assumed that if ΔU >0, the solid absorbs heat from the outside: this implies that, consequently, the thermal agitation of the constituent atoms increases. Otherwise, if ΔU <0, the solid transfers its heat outside by cooling thus reducing its atomic vibrations. As is clearly visible from Figure 8, our simulation study is in agreement with such theoretical aspects. First of all, the internal energy is positive since the sample is warming up due to the Joule effect, i.e. due to the current that flows in it, as a consequence of the applied voltage which in turn affects the rate of this internal energy variation (higher the voltage, greater the rate). Moreover, due to the key role that the temperature plays in determing such changes, the internal energy U appears visibly uneven throughout the sample given its non-uniform local heating. As is better evident from the bidimensional graphics, the total internal energy varies parabolically along the length in the x-axis direction (as is the case of the temperature profile, unless a scaling factor corresponds to the specific heat), to reach a maximum at the center of the sample (at x=40 mm) and minimum values in the terminal parts (x=0 mm and x= 80 mm), which are decisively colder, as previously discussed.
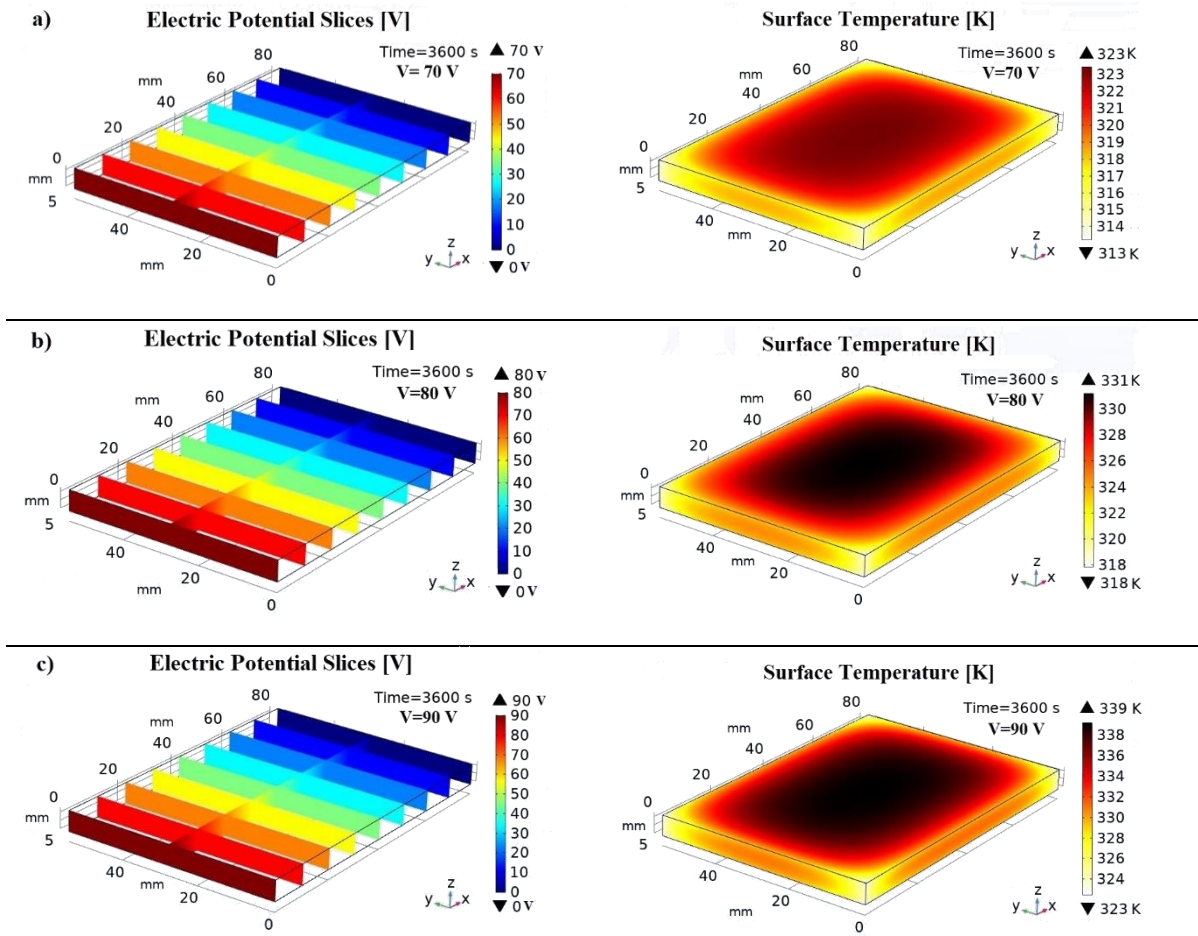
Figure 6. Electric potential distribution (left part) at t=3600 s along the direction to which the different voltage (70V, 80V and 90V, in a), b) and c), respectively) is applied. In the right part, the graphics show the 3D views of the corresponding surface temperature reached by Joule effect.
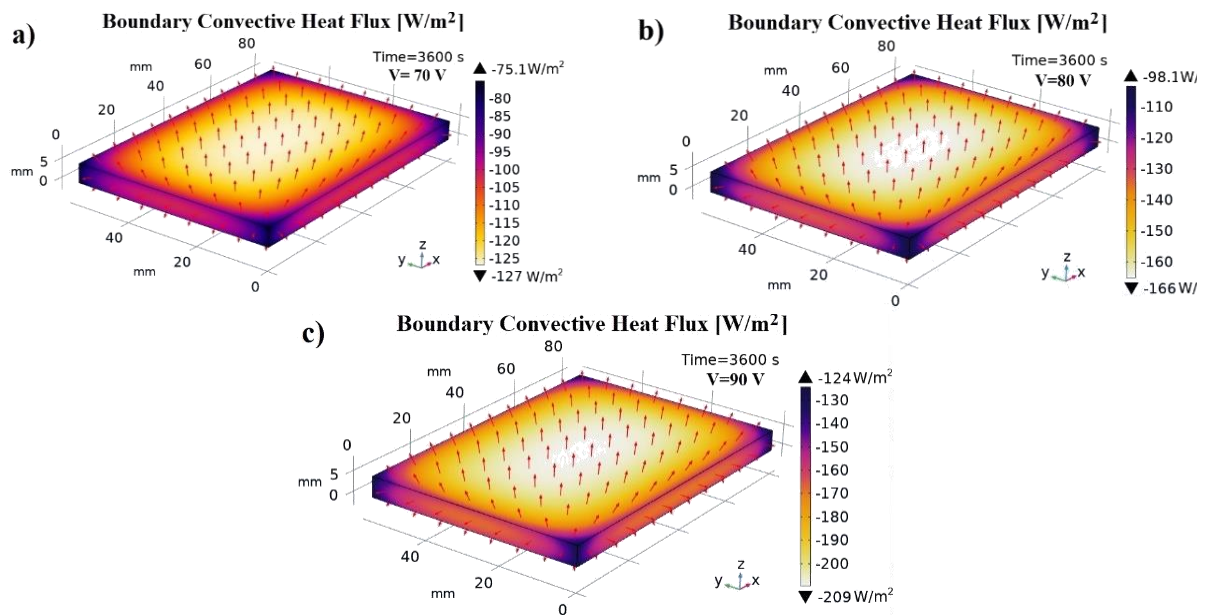
Figure 7. Convective flux at t=3600 s in case of applied voltage of 70, 80 and 90V in a), b) and c), respectively.
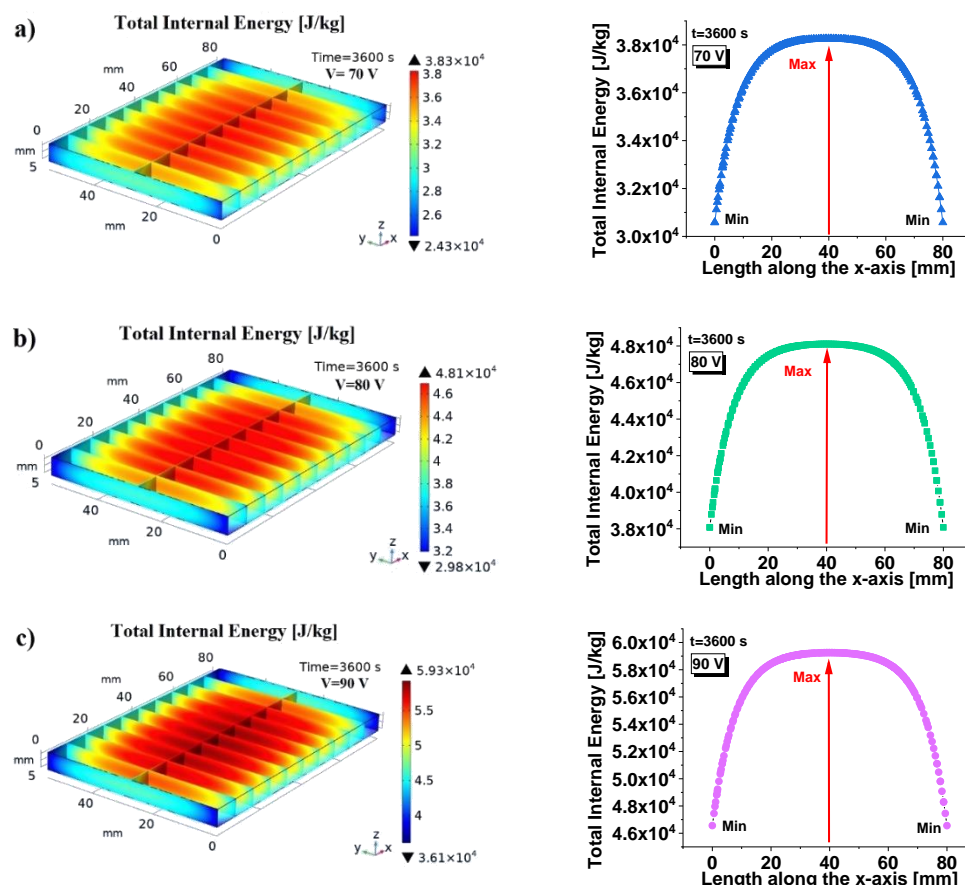
Figure 8. 3D-views (left part) of the total internal energy at t=3600 s due to the Joule heating effect, as a consequence of the different voltage values, 70V, 80V and 90V, applied to the sample in a) b) and c), respectively. In the right part, the graphics show the corresponding total internal energy as a function of the length in the x-axis direction.

CONCLUSION

Thermoelectric behavior of epoxy resin filled with 3 wt% of MWCNTs, due to Joule heating effect, was experimentally and numerically investigated. In particular, different thermal aspects, due to the Joule heating effect, when different voltage values (70 V, 80 V and 90 V) were applied to the samples, were numerically analyzed by means of a simulation study performed with a commercial software (COMSOL Multiphysics®). Given the good agreement found between experimental and simulation results, numerical studies by application of innovative computational approaches are encouraged in material science to design and to manufacture new advanced materials or to better investigate and optimize the existing ones. Further thermal aspects will be investigated in a future paper to explore the potential use of electrically and thermally conductive polymers in practical thermal applications such as heat exchangers.

REFERENCES

1. J. Mark, K. Ngai, W. Graessley, L. Mandelkern, E. Samulski, G. Wignall, J. Koenig, Physical properties of polymers, Cambridge University Press, Cambridge, 2004.
2. H. Zhang, T. Shi, A. Ma, *Polymers*, **13**, 2797 (2021).
3. G. Spinelli, R. Guarini, R. Kotsilkova, E. Ivanov, V. Romano, *Nanomaterials,* **11**, 1511 (2021).
4. G. Spinelli, R. Guarini, R. Kotsilkova, T. Batakliev, E. Ivanov, V. Romano, *Materials,* **5**, 986 (2022).
5. R. Kotsilkova, E. Ivanov, V. Georgiev, R. Ivanova, D. Menseidov, T. Batakliev, V. Angelov, H. Xia, Y. Chen, D. Bychanok, P. Kuzhir, R. Di Maio, C. Silvestre, S. Cimmino, *Polymers*, **12**, 1208 (2020).
6. E. Ivanov, R. Kotsilkova, H. Xia, Y. Chen, R. K. Donato, K. Donato, A.P. Godoy, R. Di Maio, C. Silvestre, S. Cimmino, V. Angelov, *Appl. Sci.,* **9**, 1209 (2019).
7. C. I. Idumah, C. M. Obele, *Surf. Interfaces*, **22**, 100879 (2021).

8. P. Smoleń, T. Czujko, Z. Komorek, D. Grochala, A. Rutkowska, M. Osiewicz-Powęzka, *Materials*, **14**, 3325 (2021).
9. Y. Geng, M. Y. Liu, J. Li, X. M. Shi, J. K. Kim. *Compos. Part A Appl.,* **39**, 1876 (2008).
10. R. Hollertz, S. Chatterjee, H. Gutmann, T. Geiger, F. A. Nüesch, B.T.T. Chu, *Nanotechnology*, **22**, 125702 (2011).
11. F. Marra, A.G. D'Aloia, A. Tamburrano, I.M. Ochando, G. De Bellis, G. Ellis, M.S. Sarto. *Polymers, 8*, 272 (2016).
12. A. Moisala, Q. Li, I. A. Kinloch, A. H. Windle, *Compos. Sci. Techn.,* **66**, 1285 (2006).
13. G. Spinelli, P. Lamberti, V. Tucci, L. Guadagno, L. Vertuccio, *Nanomaterials*, **10**, 434 (2020).
14. L. Guadagno, R. Longo, F. Aliberti, P. Lamberti, V. Tucci, R. Pantani, G. Spinelli, M. Catauro, L. Vertuccio, *Nanomaterials*, **13**, 495 (2023).
15. G. Spinelli, R. Kotsilkova, E. Ivanov, V. Georgiev, R. Ivanova, C. Naddeo, V. Romano, *Polymers*, **12**, 2414 (2020).
16. L. Vertuccio, L. Guadagno, G. Spinelli, P. Lamberti, V. Tucci, S. Russo, *Compos. B. Eng*., **107**, 192 (2016).
17. J. Ku-Herrera, F. Avilésù, *Carbon*, **50**, 2592 (2012).
18. A. Oliva-Avilés, F. Avilés, V. Sosa, *Carbon*, **49**, 2989 (2011).
19. C. W. Nan, Y. Shen, J. Ma, *Annu. Rev. Mater. Res*., **40**, 131 (2010).
20. M. T. Connor, S. Roy, T. A. Ezquerra, F. J. B. Calleja, *Phys. Rev. B*, **57**, 2286 (1998).
21. A. Mdarhri, F. Carmona, C. Brosseau, P. Delhaes, *J. Appl. Phys*., **103**, 054303 (2008).
22. B. E. Kilbride, J. Coleman, J. Fraysse, P. Fournet, M. Cadek, A. Drury, S. Hutzler, S. Roth, J. W. Blau, *J. Appl. Phys.,* **92**, 4024 (2002).

Preparation and characterization of NGO/Al$_2$O$_3$ composite ceramic materials

M. A. Georgieva, A. A. Georgieva[*], K. Z. Panayotova, F. S. Yovkova,

I. G. Markovska

Prof. Dr. Assen Zlatarov University Burgas, Department of Chemical Technology, 8000, Burgas, Bulgaria

The present paper reports on the application of a two-stage technology for the preparation of composite ceramic material of the graphene/ceramic matrix type. Firstly, finely porous corundum ceramic material was obtained using the solid-state sintering method at comparatively low temperatures for corundum materials - 1500°C - by adding graphene at a concentration of 2 mass %, as well as 3 mass % TiO$_2$. In the second stage of the experiment, graphene oxide was obtained in nano colloid form (2 mg/ml, dispersed in H$_2$O) which was impregnated into the solid porous corundum samples synthesized to obtain a composite ceramic material of the NGO/Al$_2$O$_3$ type. In the characterization of the ceramic samples, mainly infrared spectroscopy, X-ray phase analysis, scanning and transmission electron microscopy, and light microscopy were used. Some important physicochemical properties of the synthesized samples were determined: water absorption (WA, %), apparent density (ρ_{app}, g/cm^3), and apparent (open) porosity (P$_{app}$, %). The samples were found to have homogeneous, fine-grain, and finely porous structure.

Keywords: porous ceramics, graphene nanoplates, graphene oxide nano colloid, composite ceramic materials

INTRODUCTION

Worldwide, intense work is done to obtain new ceramic materials which combine the unique functional (e.g. electric, magnetic, conducting or mechanic) properties of the nanocomposite material with the properties of the traditional ceramic materials [1-4].

The development of polymeric and ceramic composites reinforced with carbon nano-fillers like carbon nanotubes (CNT), graphene nanoplates (GNP), etc., became a rapidly developing research field. Due to the improved functionality and physical properties of these materials, the implementation of the composites in various industrial branches can be significantly widened. By varying the length and shape of the carbon nanofillers, and incorporating them in small quantities, the overall performance characteristics of the matrix can be significantly improved [3-5].

It has been found from the literary survey carried out that the combination of the advantages of the nanotechnology and the classic methods of silicate technology is an innovative approach to the preparation of new composite materials which combine the unique functional properties of the nanomaterials with the properties of the ceramic materials [1-11].

The aim of the present work is to obtain composite ceramic material of the type NGO/Al$_2$O$_3$ by applying a two-stage technology. The first stage involves preparation of finely porous corundum ceramic samples with added 2 mass % graphene nanostructures and 3 mass % TiO$_2$ using low-temperature synthesis. On the second stage, graphene oxide - NGO is obtained in nano colloid form and impregnated into the solid porous corundum samples synthesized.

MATERIALS AND METHODS

Materials

Initially, a finely porous corundum ceramic material containing 2 mass % graphene nanostructures and 3 mass % TiO$_2$ was obtained by the method of solid-state sintering at relatively low temperatures of about 1500°C.

For the synthesis of the porous ceramic samples from blend C0, the initial raw materials used were highly dispersed powder of Al$_2$O$_3$ (Sigma Aldrich) and one graphene source - Gn (graphene nanoplatelets (Sigma Aldrich)). In the blending process, an additive of 3 mass% TiO$_2$ (Sigma Aldrich, purity of $\geq$ 99%) was introduced in the mixture. This additive significantly decreases the sintering temperature usually used in such process.

The preparation of the corundum ceramics was carried out as follows: 4% polyvinyl alcohol was added to the powders obtained as a plasticizer and the samples were dry-formed using hydraulic press at a pressure of 40 MPa. The regime of drying the samples was: 120°C - 70 min, 180°C - 50 min. The regime of sintering of the samples prepared from blend C0 was: isothermal period of 20 min at 200°C, at 300°C - 20 min, at 400°C - 20 min, at 500°C - 30 min, at 800°C - 30 min, at 1100°C - 30 min, at

* To whom all correspondence should be sent:
 E-mail: adriana_georgieva79@yahoo.com

1300°C - 30 min, and at the maximal temperature of 1500°C - isothermal period of 60 min. The aim was to achieve the highest possible densification on the basis of solid-state sintering and to obtain finely porous materials with good mechanical characteristics. After the sintering, the samples were allowed to cool freely.

In the second stage of the experiment, graphene oxide was synthesized in the form of a nano colloid. Here, the initial graphite (Graphite, synthetic powder, < 20 mum (Sigma Aldrich)) was oxidized by the method of Hummer with addition of MnO_4 [5, 12]. The graphene oxide - GO was added to deionized water and the pH of the solution was corrected with NaOH to 11.0. The suspension obtained was treated with high power ultrasound at intensity about 200 W for 2 hours. The aim of this treatment was to obtain colloidal dispersed system: water-dispersed solution of GO with well dispersed nanostructures. The concentration of the graphene oxide nano colloid prepared by this method was estimated to be 2 mg/ml, dispersion in H_2O.

One of the advantages of graphene oxide is that it is easily dispersible in water and other organic solvents, as well as in various matrices, due to the presence of oxygen-containing functional groups. This property is certainly important for effectively mixing material with ceramic or polymeric matrices when the aim is to improve their electrical and mechanical properties [5].

Bearing in mind the considerations above, during the next stage of the experiment the colloid particles of graphene oxide - NGO were impregnated into the solid porous corundum samples synthesized aiming to obtain composite ceramic material of the type NGO/Al₂O₃. The resulting composites obtained from blend C1 were dried in a desiccator at 120°C for 60 min.

Methods

Infrared spectroscopy. The FT-IR studies were performed on a Tensor 27 Fourier infrared spectrophotometer FT-IR (Bruker, Germany) in the interval 400 - 4000 cm^{-1} at a resolution of 1 cm^{-1}. The measurements were taken at room temperature. For each analysis, a sample weighing 0.3 mg was pressed with 100 mg of KBr at a pressure of 2 to 4 atm.

X-ray powder analysis. The registration of an X-ray powder diffraction pattern was carried out using automated computer-controlled X-ray diffractometric system D500 Siemens (Germany) under the following regime: 40 kV, 30 mA, monochromatic copper radiation.

SEM. The SEM analysis of the ceramic materials obtained was carried out with a Tabletop SEM

HIROX SH-4000M scanning electron microscope, 30× - 60000×, SE&BSE detector, voltage 5 kV - 30 kV, resolution 15 nm. The samples were preliminarily pre-wired with gold.

TEM. The corundum ceramic materials synthesized were studied by TEM EDS analysis carried out using a transmission electron microscope JEOL - JEM 2100 with EDS detector Oxford X-max 80T, at accelerating voltage of 200 kV.

Light microscopy. Light microscopy observations were performed with a Celestron 5 MP LCD Deluxe digital microscope.

RESULTS AND DISCUSSION

The following more important properties of the corundum ceramic samples synthesized (C0) were determined: water absorption (WA, %), apparent density (ρ_{app}, g/cm³) and apparent (open) porosity (P_{app}, %). The results obtained indicated that the introduction of 2 mass% of graphene - Gn in the initial blends followed by high temperature sintering gave ceramic samples with sufficient density - 3.26 g/cm³, water absorption - 10.43 % and substantial apparent porosity - 33.46 %. Hence, even at small quantities, the introduced graphene nanostructures serve as pore-forming agents.

Basically, the following methods were used to characterize the composite material obtained: infrared spectroscopy, X-ray powder analysis, scanning and transmission electron microscopy, light microscopy.

The initial blends and the sintered ceramic samples were studied by infrared spectroscopy (*FT-IR*). The result for the sintered corundum samples obtained from blend C0 are presented graphically in Fig. 1. The absorption bands and the corresponding functional groups present in the composition of the sintered corundum ceramic samples containing 2 mass % of graphene nanoplates can be interpreted as follows.
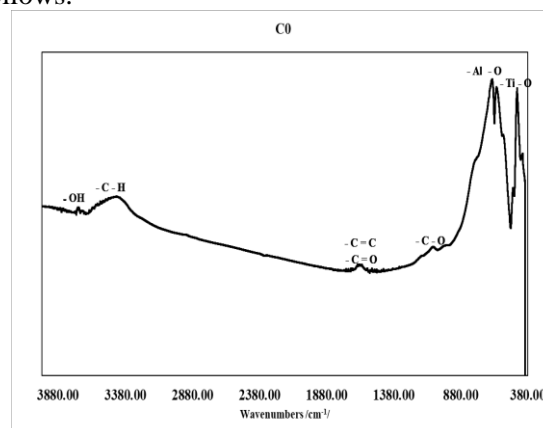
Figure 1. FT-IR spectrum of corundum samples prepared from blend C0 and sintered at 1500ºC

The absorptions at ~3780 cm⁻¹ are characteristic for the vibrations of the O-H bond. The vibrations observed at ~1631.49 cm⁻¹ can be attributed to the C=C bond [13, 14] which means that part of the carbon structures is preserved after the high temperature sintering and remain within the corundum ceramics while the others are burned. The latter process imparts certain porosity to the ceramic material obtained. The peaks appearing at ~1085.09 cm⁻¹ are characteristic for the vibrations of the C-O bond [13, 14]. The FT-IR spectra obtained contain high peaks in the frequency range from ~500 cm⁻¹ to ~900 cm⁻¹. They are characteristic for the vibrations of the Al-O bonds in Al₂O₃ [13, 14]. Major part of the absorption bands observed for the sintered ceramic samples were attributed to the vibrations of the Al-O bonds in the high temperature α-modification of Al₂O₃ (corundum). The absorption band at ~460.08 cm⁻¹ is characteristic for the vibrations of the Ti-O bond.

XRD analysis. The XRD analysis proved that the main crystalline phases in the ceramic materials synthesized are three: Al₂O₃, Al₂TiO₅ and TiO₂ (Figure 2), with the main phase being corundum. The presence of these phases was proved also by the FT-IR analysis.
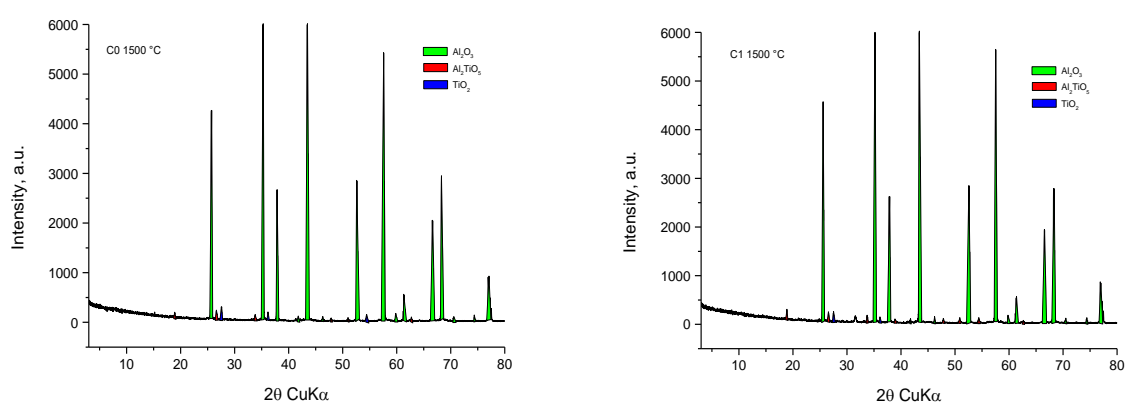
Figure 2. Powder X-ray diffraction patterns of sample with composition C0 and ceramic composite with composition C1
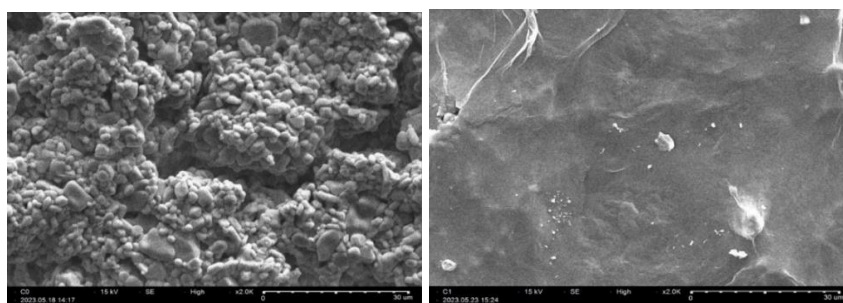
a)	b)
SEM of sample with composition C0 - ×2.0K	SEM of composite NGO/Al₂O₃ C1 - ×2.0K
c)	d)
SEM of sample with composition C0 - ×6.0K	SEM of composite NGO/Al₂O₃ C1 - ×6.0K
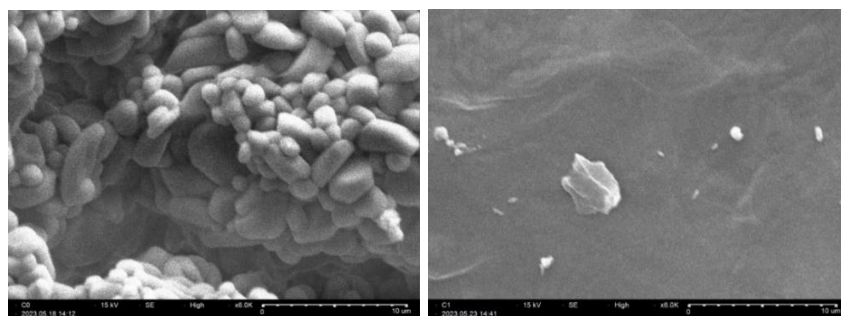
Figure 3. SEM images of sintered ceramic materials - samples with composition C0 a composite NGO/Al₂O₃ - composition C1

The decreased sintering temperature of the ceramics was due to the addition of TiO_2 (3 mass %) introduced in the initial blend. Part of it forms a solid solution with corundum, thus increasing the defects of the lattice and, respectively, easing the sintering of the ceramics at lower temperature.

The morphology of the objects studied was analyzed by electron microscope observations using SEM, TEM (Figures 3 and 4) and light microscopy (Figure 5).

SEM analysis. The microphotographs of the sintered at 1500°C corundum samples without (composition C0) and with impregnated NGO (composition C1) are shown in Figure 3.

The electron microscopy images presented in Figures 3a and 3c show fine-grain fine-pore structure of the ceramic samples with corundum grain sizes from 0.5 to 3 μm. Therefore, they confirm the conclusion stated above that the addition of graphene nanostructures to the initial blends in concentration of 2 mass % followed by high temperature sintering, leads to burning of part of the graphene which results in formation of porosity in the ceramics obtained.

The images of the composite material - Figures 3b and 3c indicate that the graphene oxide nano colloid was distributed throughout the sample and, to great extent, occupied the pores of the ceramic matrix.

TEM analysis. STEM images of the sintered sample with composition C0 (2 mass % of Gn) and ceramic composite C1 (NGO/Al₂O₃) are shown in Figures 4a and 4b. The map spectra indicate for the presence of the main elements Al, Ti, O and C.

Light microscopy. The surfaces of the corundum ceramic samples containing 2 mass % of graphene Gn (C0) sintered at 1500°C, as well as these of the ceramic matrices impregnated with nano colloid graphene oxide NGO (C1) were studied by light microscopy (Figures 5a and 5b).

As can be seen from the photographs presented in Figure 5, the surface of the ceramic materials synthesized was homogeneous and finely grained. In the impregnated ceramic matrices (C1), the nano colloid graphene oxide has not only spread across the surface but has also penetrated into material's pores, as verified by the earlier-discussed SEM analysis.

a)   b)
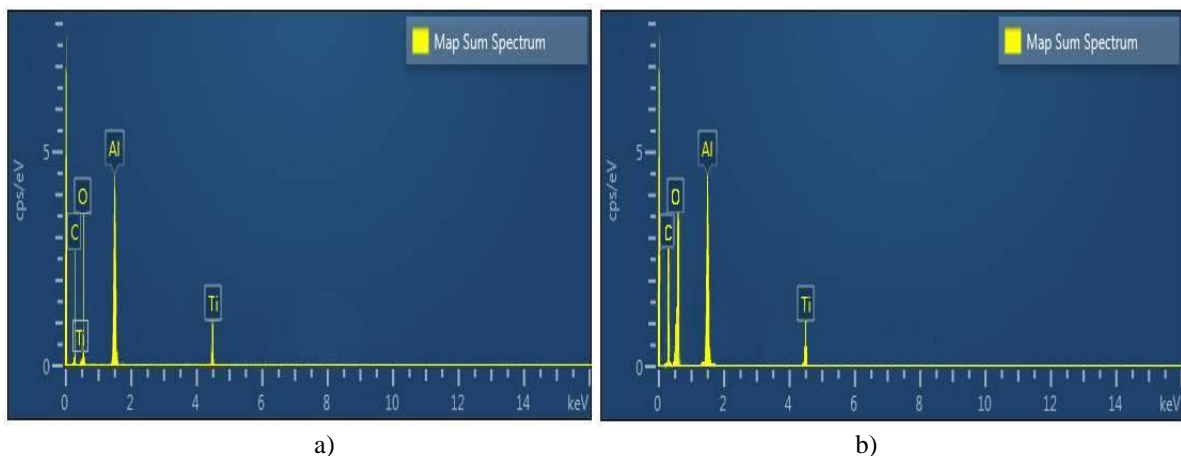
Figure 4. (a, b) STEM images of samples with compositions C0 and C1

a)   b)
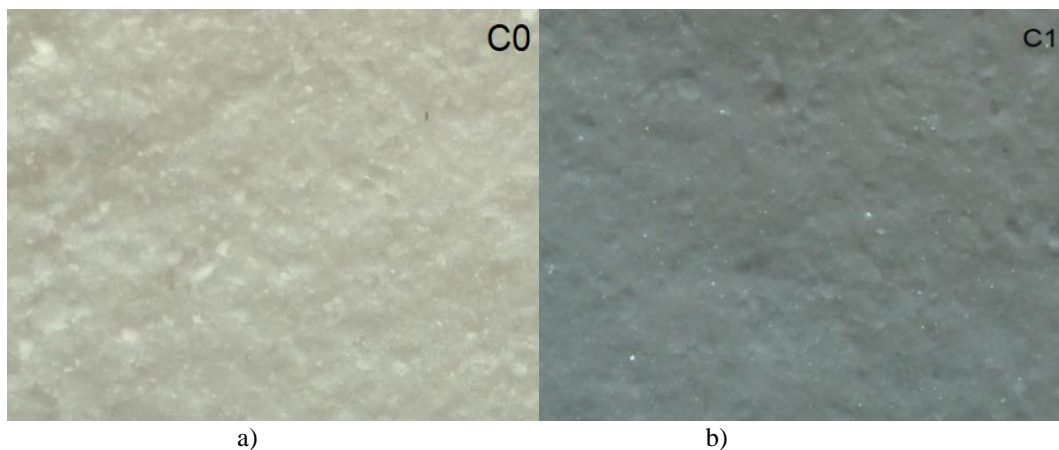
Figure 5. Photographs of the surface of: 5a) corundum ceramic samples with composition C0 and 5b) ceramic composite NGO/Al₂O₃ - composition C1

CONCLUSION

A two-stage technology was applied to prepare a composite ceramic material of the type graphene/ceramic matrix - NGO/Al$_2$O$_3$. Finely porous corundum ceramic material was obtained by the method of solid-state sintering at a temperature of 1500°C which is relatively low for corundum materials and this was achieved by adding 2 mass % of graphene and 3 mass % of TiO$_2$. By introducing of 2 mass % of graphene nanoplates Gn in the initial blends followed by high temperature sintering, part of the graphene added burned out, thus imparting porosity to the ceramics obtained. The ceramic samples synthesized were found to have sufficient density - 3.26 g/cm^3, water absorption - 10.43 % and significant apparent porosity - 33.46 %.

During the next stage of the experiment, graphene oxide was obtained in nano colloid form (2 mg/ml, dispersion in H$_2$O) which was impregnated into the solid porous corundum samples synthesized aiming to obtain composite ceramic material of the type NGO/Al$_2$O$_3$. The SEM analysis confirmed that the graphene added initiated the formation of well-shaped fine corundum grains with sizes in the range 0.5-3 μm. The electron microscopy images of the composite material showed that the impregnated graphene oxide nano colloid was distributed not only on the surface but had also penetrated into the pores of the ceramic matrix. The results obtained from TEM EDS analysis confirmed the existence of carbon originating from the graphene. This carbon content most probably enhances the effect of the TiO$_2$ addition and accelerates the recrystallization processes. The surface of the corundum based ceramic materials was studied by light microscopy and it was found that the samples are characterized by comparatively homogeneous and fine-grain surface.

REFERENCES

1. A. Georgieva, F. Yovkova, K. Panayotova, M. Georgieva, M. Minova, 61st Annual Scientific Conference - University of Ruse and Union of Scientists, Razgrad, Bulgaria, *Reports Awarded with BEST References Crystal Prize'22*, 167 (2022).
2. J. Zhu, B. Jia, Y. Di, B. Liu, X. Wan, W. Wang, R. Tang, S. Liao, X. Chen, *Frontiers in Materials,* **1,** 1 (2022).
3. B. Yazdani, Y. Xia, I. Ahmad, Y. Zhu, *Journal of the European Ceramic Society*, **35**, 179 (2015).
4. A. Centeno, V.G. Rocha, B. Alonso, A. Fernandez, C.F. Gutierrez-Gonzalez, R. Torrecillas, A. Zurutuza, *Journal of the European Ceramic Society*, **33**, 3201 (2013).
5. A. Jirickova, O. Jankovsky, Z. Sofer, D. Sedmidubsky, *Materials*, **15**, 920 (2022).
6. X. Wang, J. Zhao, E. Cui, X. Tian, Z. Sun, *Nanomaterials*, 11, 1374 (2021).
7. Z. Sun, J. Zhao, X. Wang, E. Cui, H. Yu, *Nanomaterials*, 10, 1815 (2020).
8. H. Abdel Dayem, B. Salib, F. El-Hosiny, *Fuel*, **227**, 1 (2020).
9. P. Rutkowski, P. Klimczyk, L. Jaworska, L. Stobierski, A. Dubeil, *J. Therm Anal Calorim*, **122**, 105 (2015).
10. K. Broniszewski, J. Wozniak, M. Kostecki, A. Olszyna, *Mater. Today Proc.*, **2**, 370 (2015).
11. S. Wang, S. Kang, T. Fang, Y. Hsiao, *Sci. Adv. Mater.*, **6**, 1951 (2014).
12. D. Markano, D. Kosynkin, J. Berlin, A. Sinitskii, Z. Sun, A. Slesarev, *ACS Nano*, **4**, 4806 (2010).
13. L. Zhang, Y. Li, H. Guo, H. Zhang, N. Zhang, T. Hayat, Y. Sun, *Environmental Pollution*, **248**, 332 (2019).
14. http://www.ioffe.ru/LNEPS/abstracts/rabchinskii. pdf

Analytical modeling of stresses and strains in layered nanocomposite structures - opportunities and challenges

T. St. Petrova

Institute of Chemical Engineering, Bulgarian Academy of Sciences,
Laboratory of transfer processes in multiphase media
Acad. Georgi Bonchev Str., Bl. 103, 1113 Sofia, Bulgaria

This review aims to analyze and summarize the achievements to date, including some authors' results, in the field of analytical modeling of stresses and strains in layered nanocomposite structures, as well as the conditions under which delamination is observed in such structures. The work is organized as follows: Section 1: Brief review on papers for analytical modeling of nanocomposites (2000-2023): Section 2: Examples of analytical solutions applications to nanocomposites, Section 3: 2D analytical solutions for nanocomposites, and Conclusions.

BRIEF REVIEW ON PAPERS ABOUT ANALYTICAL MODELING OF NANOCOMPOSITES

During the last two decades a boom in publications - 193,409 publications selected from Web of Science Core Collection, dedicated to nanocomposites [1] (Fig. 1 (a)) has been seen. It can easily be verified that the largest share is occupied by the works that are mainly experimental and investigate the methods of synthesis of new, mainly polymer nanocomposites. A significant part is devoted to the study of their properties and characteristics (mechanical, optical, electrical and thermal conductivity, etc.). Another reference shows that only 392 out of 16,152 articles include modeling in addition to the experiment [2]. Given the increasingly wide application of nanocomposites in various industrial areas, the number of publications concerning modeling of the behavior of nanocomposites is also increasing - 21,776 according to Web of Science, 570 of which are review articles [3]. In most cases, commercial software products such as ANSYS, Abaqus, COSMOS, etc., are used in the modeling of nanocomposites, as complex geometries can be simulated under different types of loads on the nanocomposite; the disadvantages of this type of modeling are the time for mesh preparation and execution, sometimes the convergence of the chosen

numerical method in the software; modeling a so-called "jump" in any of the sought-after quantities in a given cell/s of the mesh also creates a problem. From a total of 1,326 published articles matching the keywords "nanocomposites" and "finite element modeling" [4], 27 are review articles.

In contrast to numerical methods, analytical methods for obtaining solutions for stresses, strains and other characteristics in nanocomposites are much faster, easier and convenient to use. Their disadvantages are usually the low dimensionality of the solutions, as well as the simplification of the geometry of the considered nanocomposite and the types of loads.

As far as the author's of the present work knowledge, there is no published review specifically dedicated to analytical methods for stress/strain modeling in nanocomposite structures, especially those in which the nanomaterial is considered as a separate layer. Given the rapid pace of research in the field and the ever-widening application of nanocomposites in industry, such a summary, accompanied by relevant analysis, would be helpful in future applications of layered nanocomposite structures, especially under specific loads.

A search was made in the available literature sources on the internet with keywords "analytical solution+nanocomposite" and "shear-lag+nanocomposites". The result after 2004 to the present (by year) is graphically displayed in Fig. 1 (b).

---

* To whom all correspondence should be sent:
E-mail: t.petrova@iche.bas.bg

(a)   (b)
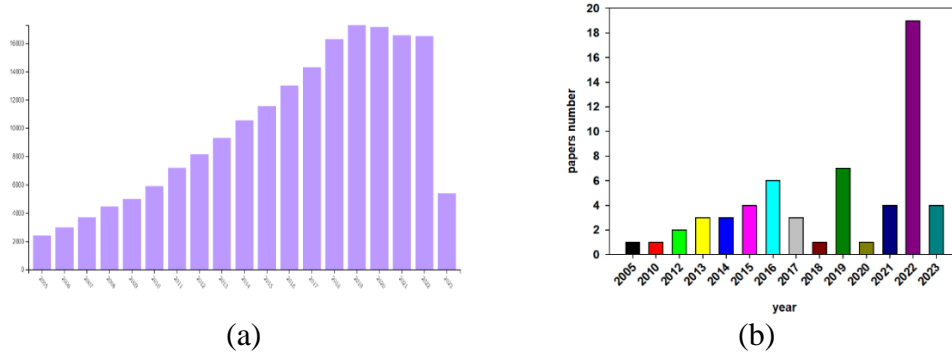
Fig. 1. Number of articles found by keywords: (a) "nanocomposites", (b) "analytical solution+nanocomposites+shear-lag" during 2005-2023.

In Fig. 1 (b) the articles with results of the author of the present work (co-authored with colleagues) during the considered period are also included. From the figure it can be seen that the interest in this type of modeling systematically increased from the discovery of graphene until 2016, followed by a slight decline and the interest resumed again in the last 4-5 years. Along with graphene and the created nanocomposite structures based on graphene, whose applications are numerous and in various fields such as electronics, medicine, automotive, construction, energy, optics, etc., new 2D nanomaterials are also entering the scene - such as black phosphorus (2014), borophene (2015), MoS_2, WS_2, as well as hybrid combinations thereof like graphene/MoS_2 [5], which have yet to be extensively studied and modeled.

The classification of the types of analytical models covered in the reference can be done in several ways. If they are grouped by the dimensionality of the model, one-dimensional, two-dimensional and three-dimensional models can be distinguished. If they are grouped according to the applicability in different zones –elastic and plastic for changes in stresses and deformations - the models can be divided into linear-elastic and cohesive (plastic).

According to the dimensionality classification of the models covered in the reference, one-dimensional analytical models occupy a major share, and they are also those that refer to modeling primarily in the field of elasticity. A previous publication asset with the participation of the author of the present work contributes to this by using analytical one-dimensional model solutions to describe the behavior of two-layer composites subjected to static/dynamic loads under conditions of varying temperature, humidity and electric field [6-17]. Especially for nanocomposites, the developments with the author's participation cover one-dimensional solutions of a cohesion model for statically loaded graphene nanocomposites [13, 17] , 350

as well as two-dimensional solutions obtained by the 2D stress-function variational method [18-24] for statically loaded nanocomposites incorporating graphene, WS_2, MoS_2 to different polymer matrices. The obtained solutions were studied by parametric analysis regarding the influence of different factors on delamination in the different types of composites and nanocomposites.

The models that give an analytical solution for higher dimensionality and/or outside the elastic region are very few, which is explainable due to the complexity in the formulation of the boundary value problems and in the computations in deriving the solutions, for example [25-28]. With the exception of [29], no other publications were found offering analytical solutions for the stresses/strains in nanocomposites under combined (mechanical and temperature) loading. An example of the joint use of analytical and/or numerical solutions for more than 1D in elastodynamics can be seen in [30-33].

In the present review, the emphasis is placed on the one- and two-dimensional analytical solutions derived for the stresses and strains in statically loaded nanocomposites. In the following sections, various examples of the available analytical models – 1D and 2D, in both the elastic and cohesive domains – will be reviewed and discussed.

EXAMPLES OF ANALYTICAL SOLUTIONS APPLIED TO NANOCOMPOSITES

The most common used one-dimensional and linear elastic model for both composite and nanocomposite structures is the so-called shear-lag model or method. Its first appearance in the literature was the work of Volkersen [34], who gave an analytical description of the stress transfer σ in a joint-type structure (single-lap joint) loaded on both sides as follows (Fig. 2).

Here, the main idea is that the connecting adhesion layer serves to transfer the load to the individual parts (arms) of the structure, and this

happens at the expense of the shear stresses τ, which distribute the load along the length of the arm connecting part *l* (Fig. 2).
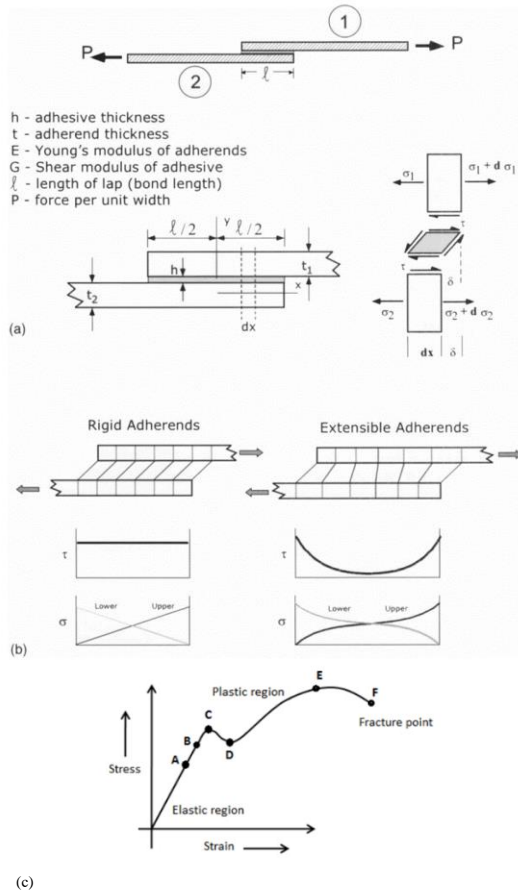
Fig. 2. Illustrative scheme of (a, b) Volkersen's shear-lag model, and (c) the stress-strain diagram [35].

In the scheme of Fig. 2 (a) and (b), it is graphically shown how the predictions of this model look analytically for the stress σ in the two arms of the structure, as well as the interfacial shear stress τ in the cases of materials with different flexibility. Volkersen offers the following analytical solution for the interphase shear stress τ for the joint structure (Fig. 2):

$$\tau(x) = \frac{P\omega}{2\sinh(\omega l/2)}\cosh\omega l +$$
$$+ \frac{P\omega}{2\cosh(\omega l/2)}\left(\frac{E_2 t_2 - E_1 t_1}{E_1 t_1 + E_2 t_2}\right)\sinh\omega l \tag{1}$$

where $\omega = \sqrt{\dfrac{G}{h}\left(\dfrac{E_1 t_1 + E_2 t_2}{E_1 t_1 E_2 t_2}\right)}$

As can be seen, the one-dimensional analytical solution (1) depends only on x, but it also depends nonlinearly on the material characteristics of the structure - Young's modulus *E*, the shear modulus *G*, and also on the geometry of the structure - the thicknesses of the two arms t_1, t_2 and the connecting part *h*, the length of the connecting (total) part *l*, as well as on the magnitude of the applied force *P*. This solution is derived under specific assumptions – neglecting torsion and bending, as well as normal stresses in the structure, also the effects of shrinkage due to different values of Poisson's number, as well as assuming perfect fit in *l* and linear-elastic properties for the materials in the structure. Despite the idealized formulation, this solution has its place in hundreds of publications and has been successfully validated with other models and, most notably, with experimental data in the elastic domain of applied loads [35].

Later, Cox [36], based on Volkersen's solution, revised and derived the shear-lag model and, accordingly, an analytical solution for σ and τ for fiber-matrix composite structures (composite materials containing threads or fibers, with in order to increase their resistance and strength). From Fig. 3 it can be seen that the solutions for σ and τ again depend on the applied external deformation ε_1, on the material properties of the thread and the matrix (substrate) E_f, G_m, as well as on the geometry of the object – length *L*, radius of the thread *a* and the substrate *R* (a cylindrical representative volume of the composite was considered), the thread size ratio *s=L/a*. This model obeys the same assumptions as the previous one and has been used just as widely, especially in composite structures [35]. After the emergence of nanocomposites with embedded nano-threads/fibers, especially the embedding of carbon nano-tubes in various matrices, we can trace the use of the Cox model in the following several works [37-40]. In [37], Fig. 4, left, the solutions for the stresses σ and τ are in cylindrical coordinates and in exponents, with respect to the carbon nanotube length (along the z-axis), which is mathematically similar to Cox (Fig. 3), since as hyperbolic sines and cosines are expressed with exponents, which is also confirmed by the graphical representation of σ and τ in both figures. In the work [38], to the analytical solution for the interfacial shear stress $\tau=\mu(q_0-q_1+q_2)$ the effects of additional residual stresses q_0, q_1 and q_2, arising respectively due to the different coefficients of thermal expansion of the two materials, are added, from the difference in Poisson numbers, and from the action of cohesive Van der Waals (WdW) forces (Fig. 4, right). In both examples, the solutions contain the geometric and material characteristics of the materials making up the nanocomposites, as well as the external load, and in [38] other characteristics such as thermal expansion coefficients, Poisson's ratios and cohesive forces are also considered. It is worth to note, that in [38] an external influence other than mechanical is

considered and accounted for in the model solution. The use of a simpler basic model to which analytical solutions can be added/ quantifying additional effects is a well-known mathematical approach that gives great results, but is unfortunately too rarely used, mostly due to difficulties in finding data on additional effects and quantifying them. Kundalwal *et al.* [39] presented a three-phase (three types of materials) shear-lag model for a polyamide nanocomposite containing a carbon filament to which carbon nanotubes were attached in a brush-like manner; the nanocomposite is subjected to a three-dimensional static load (Fig. 5, left). Here the solutions for the stresses σ and τ are again expressed as a combination of hyperbolic sines and cosines and integration constants. In the same work, a comparison of the results obtained by the authors with results of the finite element method (FEM) is made; the agreement is more than good, confirming the use of analytical solutions in modeling even for three-phase nanotube/matrix nanocomposites.

In the publication of Hu *et al.* [40], one can again observe the addition of additional modeling of the interfacial shear stress τ to the basic shear-lag solutions. In particular, the interphase boundary is modeled by a spring layer model with its own stiffness coefficient K, which is reflected in the coefficient α of the exponents in the solutions (Fig. 5, right).

In practice, this means that the interphase shear stress does not transmit the transfer of the applied external stress directly and proportionally, but is limited by the value of the coefficient K.

After the discovery of the stable two-dimensional form of graphene (2004, although its existence is known since 1930), attempts were made to model the behavior of graphene nanocomposites, where the nanomaterial is a 2D two-dimensional lattice/flake with an atomic thickness of 0.35 nm, incorporated or deposited in/on other material/s. The beginning of the modeling of graphene and other nanocomposites by the application of the shear-lag model to analytically describe the behavior of σ and τ was laid with the pioneering works of Nobel Price Laureates Novoselov and Geim. In their works [41, 42], shear-lag was applied for the first time to a Graphene/SU-8/PMMA nanocomposite subjected to static axial external deformation (Fig. 6).

The solutions for the interfacial tension τ and for the strain in the graphene layer e_f are again described by hyperbolic sines and cosines for external loading up to 0.4% successfully with the shear-lag model. At an external strain of 0.6%, however, the graphene begins to wrinkle, that is, the behavior becomes non-linear and the model cannot correctly describe the experimental data.

$$\sigma_f = E_f \varepsilon_i [1 - \cosh(nx/r)/\cosh(ns)]$$

$$\tau_i = \frac{1}{2} n E_f \varepsilon_1 \sinh(nx/r)/\cosh(ns)$$

$$n^2 = \frac{2G_m}{E_f \ln(R/a)}$$
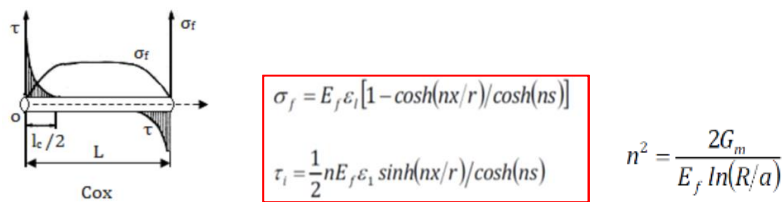
Fig. 3. Cox model and solution for fiber/filament-incorporated composites [35].

Fig. 4. Application of the Cox model to fiber nanocomposites: left [37], right [38].
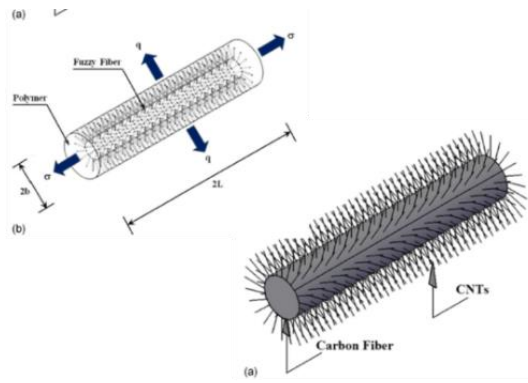
$$\left(w_i^m - w_i^f\right) K = \tau_i^f,$$

$$\overline{\sigma_{zz}^f} = c_1 e^{\alpha z} + c_2 e^{-\alpha z} + \frac{R^2}{a^2 + (R^2 - a^2)\frac{E^m}{E^f}}\sigma,$$

$$\tau_{rz}^f = -\frac{\alpha}{2}r\left(c_1 e^{\alpha z} - c_2 e^{-\alpha z}\right),$$

$$\sigma_{zz}^m = \frac{R^2}{R^2 + a^2\left(\frac{E^f}{E^m} - 1\right)}\sigma + \left(c_1 e^{\alpha z} + c_2 e^{-\alpha z}\right)$$
$$\times \left\{[1 - \beta(R^2 - a^2)]\left(\frac{E^m}{E^f} - \frac{aE^m}{2K}\alpha^2\right) - \beta a^2\right\}$$

$$\tau_1 = -\frac{a}{2}[A_{36}\alpha\cosh(\alpha x) + A_{37}\alpha\sinh(\alpha x) + A_{38}\beta\cosh(\beta x)$$
$$+ A_{39}\beta\sinh(\beta x)]$$

$$\overline{\sigma_x^f} = A_{36}\sinh(\alpha x) + A_{37}\cosh(\alpha x) + A_{38}\sinh(\beta x) + A_{39}\cosh(\beta x)$$
$$+ (A_{33}/A_{32})\sigma - (A_{34}/A_{32})q - (A_{35}/A_{32})\tau \qquad (38)$$

α depends now on the parameter K – interface spring stiffness parameter

Fig. 5. Application of the Cox model to fiber nanocomposites: left [39], right [40].
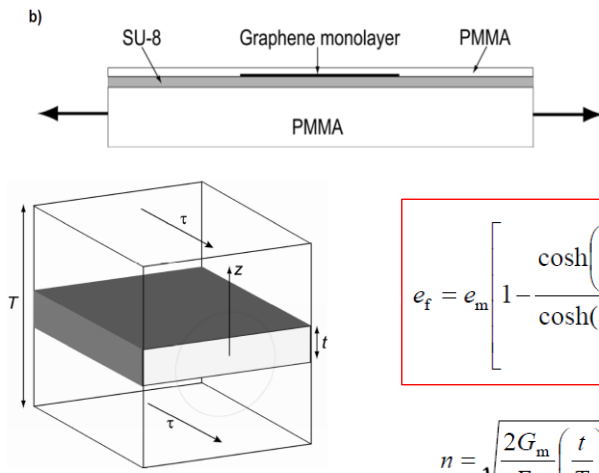
$$e_f = e_m\left[1 - \frac{\cosh\left(ns\frac{x}{l}\right)}{\cosh(ns/2)}\right]$$

$$n = \sqrt{\frac{2G_m}{E_f}\left(\frac{t}{T}\right)}$$

$$\tau_i = nE_f e_m \frac{\sinh\left(ns\frac{x}{l}\right)}{\cosh(ns/2)}$$
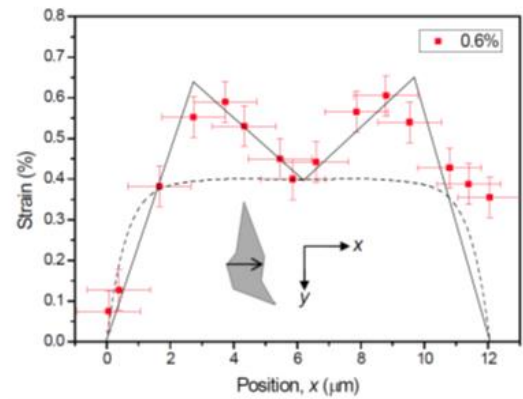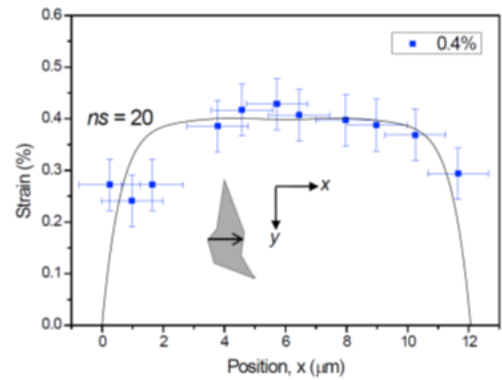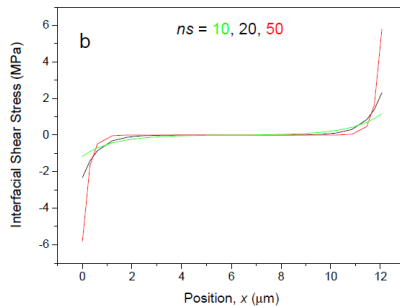
Fig. 6. Illustrative scheme of σ and τ solutions and nanocomposite–shear-lag [41,42].
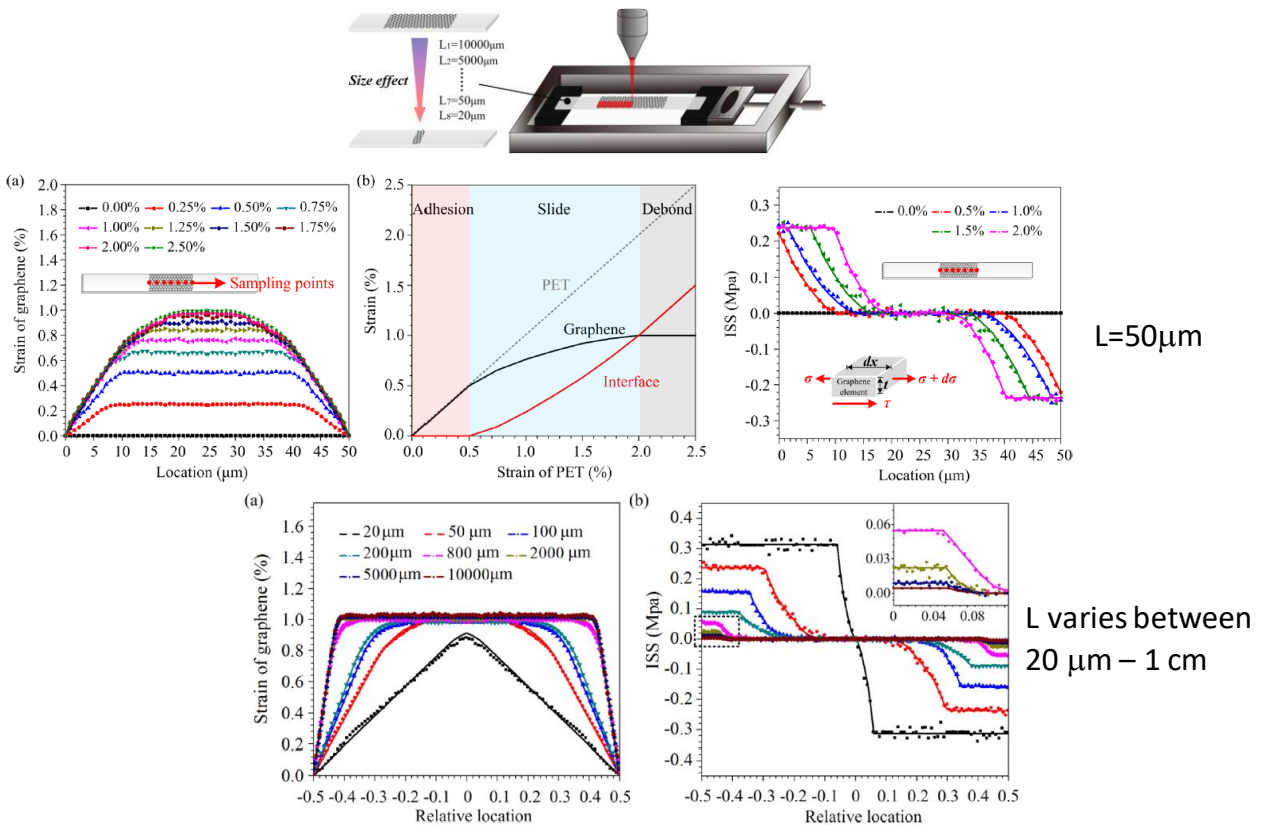
Fig. 7. Illustrative scheme of ε and τ solutions and graphics - shear-lag [43].

Shortly thereafter, Xu *et al.* [43] investigated the influence of the length of the graphene flake/layer on the value of the interfacial shear stress and on the strain in the layer, again with shear-lag (Fig. 7). They found with parametric analysis that the length of the graphene layer significantly affects the stress transfer between the layers of the nanocomposite and specifically, τ and the strain in graphene ε. As the loading in the PET substrate increases, the strain ε in the graphene linearly increases until reaching a sliding mode and a retention plateau, after which exfoliation of the graphene flake/layer follows. As the length of the graphene flake/layer increases from 20 to 10000 μm, the interfacial tension τ decreases until complete exfoliation occurs. The interfacial mechanical properties of graphene less than 20 μm long are extremely sensitive to its length, while for graphene longer than 1000 μm they are no longer size dependent. After Gong's breakthrough, more researchers are still successfully using the shear-lag model to describe the behavior of σ and τ in nanocomposites with a combination of different 2D nanomaterials and polymer matrices (PET, PMMA): tungsten disulfide WS$_2$ [44], hybrid nanocomposites – a combination of MoS$_2$ and graphene [5], boron nitride hBN [45], as well as the titanium carbide Ti$_3$C$_2$ known in the literature as Mxene [46]. An overview of the obtained results can be briefly followed in Figs. 8 ÷10. As can be seen from the

354

figures, the solutions of the shear-lag model for the deformations in the nanomaterial layer successfully describe the experimentally measured data in the elastic region of the externally applied mechanical loads. Given the different mechanical properties of the investigated nanocomposites, and in particular, the choice of materials in the nanocomposite, the applicability limits of the model will also depend on this. It also turns out that the thickness of the nanomaterial layer is significant – for example, in [44] for the same applied external strain of 0.55%, the model solution for the strain in the WS$_2$ monolayer well describes the experimental data, but with several WS$_2$ layers this is no longer so, as a tendency to form wrinkles in the middle of the layer appears (Fig. 8, right, (d)), because of the interactions between the nanomaterial layers.

In Fig. 9 the effect of the interaction of two different nanomaterials – graphene and molybdenum disulfide – on the transfer of stress from the PET polymer layer to the upper two layers is observed. It can be seen that in sample I of Fig. 9 the transfer is 100% from polymer to MoS$_2$ for loadings up to 1.2%, while in sample II with two nanolayers, the transfer drops to 75% from MoS$_2$ to graphene even at 1% external loading; as the external load increases, the stress transfer between the layers continues to decrease. This effect, found experimentally, is due to the presence of a second

interphase layer in sample II [5]. Du *et al.* [5] confirmed their experimental observations with simple model, based on the force balance equations and superposition of solutions. In Fig. 10, top, it can be seen for the Ti_3C_2M-XENE/PMMA nanocomposite that the model deformation in the Ti_3C_2 layer matches well with the experimental data for 0.2% external loading; at 0.4%, however, more

substantial differences begin to appear in the plateau region for ε [46]. When modeling the deformation in a 50-layer (17 nm) boron nitride nanocomposite hBN /PMMA (Fig. 10, bottom), the limits of the external load, up to which the model well describes the experiment, are even lower - up to 0.15% external load [45].

$$\varepsilon_f = \varepsilon_m \left[1 - \frac{\cosh\left(ns\frac{x}{l}\right)}{\cosh(ns/2)} \right]$$

$$\tau_i = nE_f\varepsilon_m \frac{\sinh\left(ns\frac{x}{l}\right)}{\cosh(ns/2)}$$
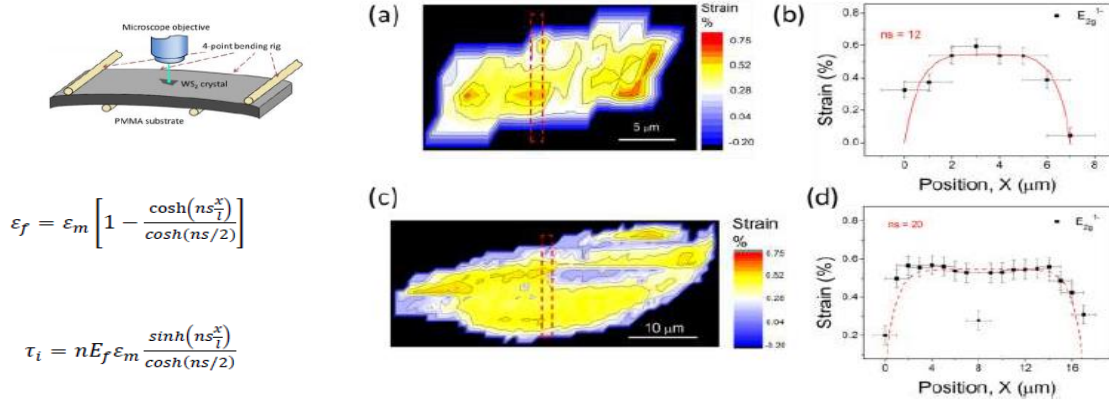
Fig. 8. Illustrative scheme of ε and τ solutions and graphics - shear-lag [44].
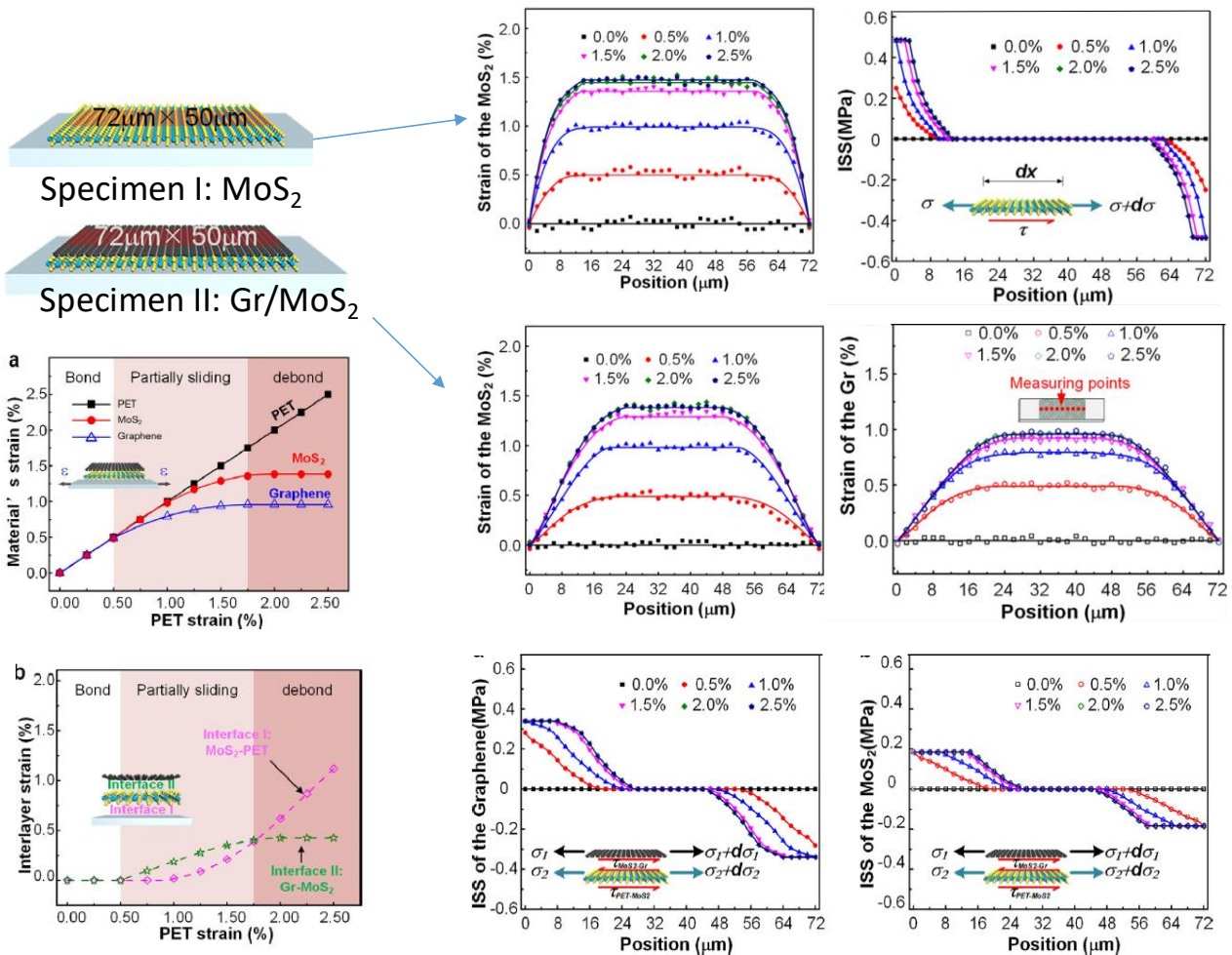
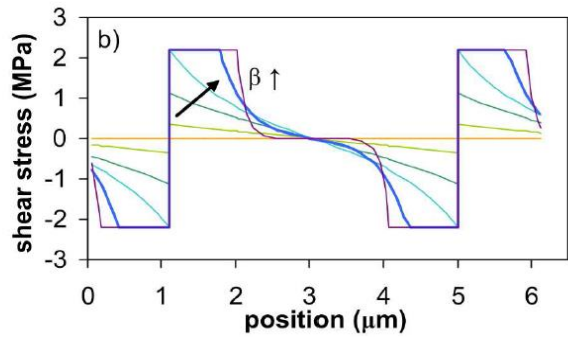**Fig. 9.** Illustrative scheme of ε and τ solutions and graphics - shear-lag [5].
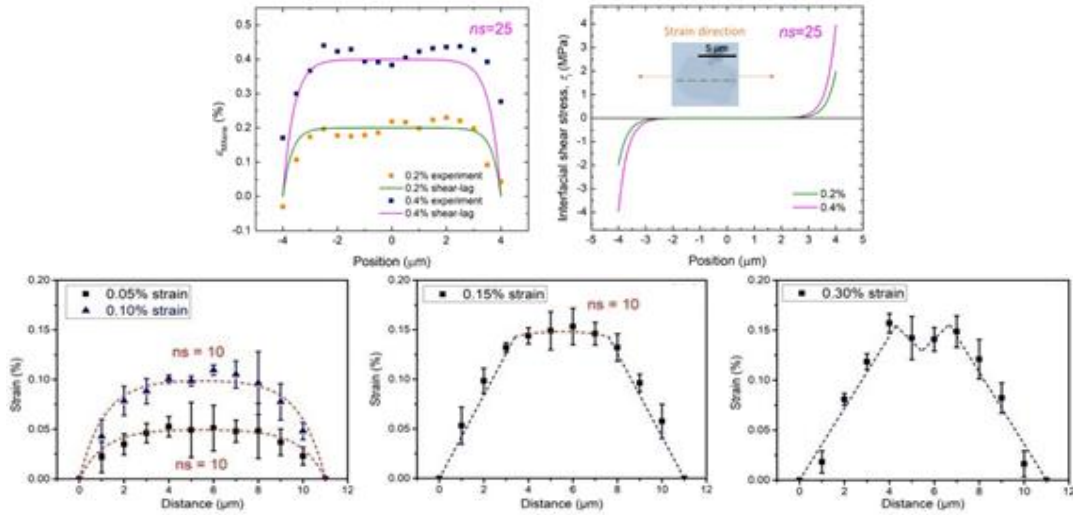
Fig. 10. Illustrative scheme of ε and τ solutions and graphics - shear-lag, (top - [46], bottom – [45]).

As mentioned, the shear-lag model and its variations considered so far give solutions valid in the elastic region of external loads. When loading above this zone (up to $0.2 \div 0.4\%$, depends on the material) a different behavior is observed - the materials begin to slip and slide and the relationship between stresses and deformations is no longer linear (Fig. 2 (c), stress-strain diagram [47]). After this yield point, the stresses again non-linearly increase until the so-called fracture mode of the respective material/structure is reached. In order to analytically describe the stresses and strains outside the elastic zone, one-dimensional models operating in the yield zone were created. These are the so-called partial debonding model and total debonding model [48]. These models were developed to describe the stresses in fiber/matrix reinforced composites and were later used for nanocomposites [49]. In the partial debonding model, debonding is assumed to start at a distance $ml/2$ from the matrix ends, where m is a number between 0 and 1, and represents the dimensionless length of the debonded portion. Perfect adhesion is assumed in the central part of the thread. The stresses - axial σ_f and shear τ, are determined by equations (2), and are graphically presented in Fig. 11.

$$\sigma_f = 4\tau_i \left(\frac{l}{2} - x \right) / d, \quad \tau = \tau_i$$

$$m = \frac{E_f \varepsilon - 2 \frac{\tau_{deb}}{n} \coth\left(ns(1-m)\right)}{2\tau_i s} \quad (2)$$

In the total debonding model, when the fiber is detached from the supporting matrix along its entire

length, i.e., m=1, and if s is the quotient of the length and diameter of the fiber, we will have the following expressions for σ and τ , and respectively the graphs (Fig. 11):

$$\sigma_{f,\max} = 2\tau_i s \quad (3)$$
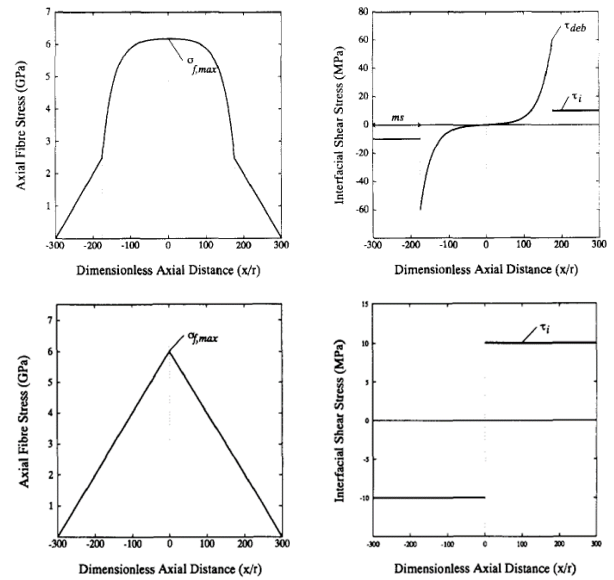
Fig. 11. Illustrative scheme of σ and τ solutions for the partial debonding (top) and total debonding models (bottom) [48].

In cases where we are between the yield and failure limits, other models are applied to predict the stresses and strains in nanocomposites - the so-called cohesive or plastic models, also nonlinear shear lag type, which also provide analytical solutions in these areas [50-54]. The next few figures illustrate the results obtained by the aforementioned researchers. Given the rather voluminous output of solutions for these models, they are presented schematically here.

Jiang et al., 2013 – Graphene/PET
Non-linear shear-lag
- Take into account interfacial sliding when the interfacial shear stress exceeds a critical value

Monolayer graphene
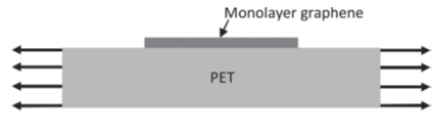
$$\tau(x) = -\beta E_{2D}\varepsilon_m \frac{\sinh(\beta x)}{\cosh(\beta L/2)}$$

$$\varepsilon_f(x) = \varepsilon_m\left[1 - \frac{\cosh(\beta x)}{\cosh(\beta L)2)}\right]$$

$$\beta = \sqrt{k_m/E_{2D}}$$

where k_m is the effective surface stiffness of the elastomer (assumed to be a constant).
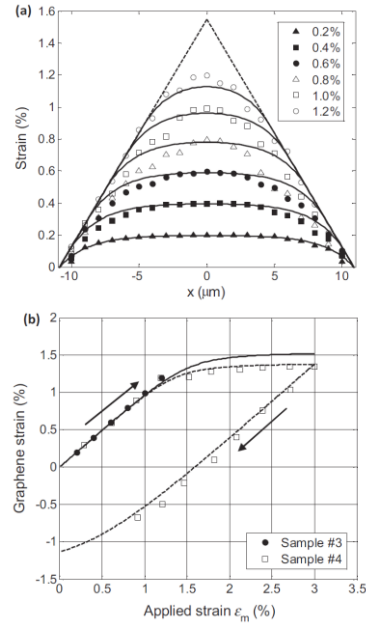
Fig. 12. Illustrative scheme of ε and τ solutions and graphics – non-linear shear-lag for graphene/PET, [50].

As can be seen from Fig. 12, the solutions for ε and τ closely resemble those of ordinary shear-lag as combinations of hyperbolic sines and cosines. The difference is in the value of the *β* parameter in the *x* argument. Here, an additional constant k_m is also included in the parameter, which represents the effective stiffness of the polymer surface. The analogous parameter *ns* in shear-lag (see Fig. 6) does not take into account this effect, and here the sliding of the interfacial boundary is also taken into account when the interfacial tension exceeds a certain critical value (for the considered nanocomposite it is at 1.2% external load). The graphs for the deformations in the graphene layer above the elastic zone are described very well by the nonlinear shear-lag at values of the external strain up to 3%. A similar result was achieved with the same nonlinear model in [51] for a graphene/cobalt nanocomposite (Fig. 13). In this work, the parameter *β* is again used, but in it, in addition to the k_m-like constant *C*, the material characteristics of the substrate (cobalt) are also included. This model accounts for the onset of sliding and, accordingly, the formation of wrinkles in graphene after a rather low level of external loading of 0.2%, due to the poor adhesion between graphene and cobalt. An application of two nonlinear models, as well as the finite element method to describe the deformations in graphene above the yield zone can be seen in the work [52] (Fig. 14). A cohesive model with shear-lag analysis was combined, and 5 behavior modes were established for the strain distribution for an external load of up to 3.3%. Applying this modeling approach

allows determining important characteristics for the nanocomposite above the elastic limit such as interface stiffness, shear strength, and fracture toughness. A parametric analysis was also performed, which showed that higher interface stiffness and/or shear strength lead to higher stress transfer efficiency, while higher fracture toughness can delay debonding (delamination).

As can be seen from the graphical comparison of the solutions in Figs. 15 and 16 with the experimental data or with the FEM, the analytical solutions created to model the deformations and interfacial stresses in different types of nanocomposites outside the elastic zone do very well. As can be seen from Fig. 12, the solutions for ε and τ closely resemble those of ordinary shear-lag as combinations of hyperbolic sines and cosines. The difference is in the value of the *β* parameter in the *x* argument.

2D ANALYTICAL SOLUTIONS FOR NANOCOMPOSITES

In contrast to the variety of 1D models and analytical solutions, described in the preceding section, the 2D models offering analytical solutions for layered nanocomposite structures are counted on the fingers. There are a lot of two-dimensional analytical solutions, offered by continuum mechanics, plate theory, etc., used for describing the behavior in layered composite structures (single lap-joint, double lap-joint) [55-57] at mechanical and/or temperature loading, but not for those incorporating 2D nanoadditives as layers.

There is a critical strain level of 0.2% beyond which sliding will occur, $\beta = 1\cdot106$ m^{-1}.
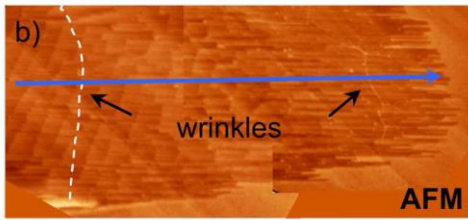
The interfacial shear strength critical τ_c of 2.2±0.3 MPa

$$\beta = \sqrt{\frac{2}{C}\frac{G_s}{t_s}}$$

G_s - the shear modulus of the substrate, t_s - the thickness of the substrate =50 μm
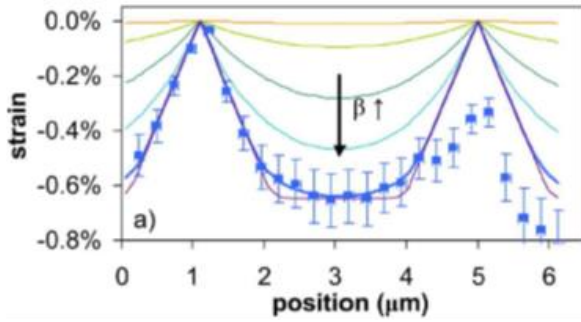
Fig. 13. Illustrative scheme of ε and τ solutions and graphics – non-linear shear-lag for graphene/cobalt [51].
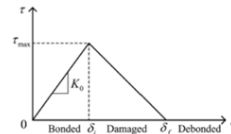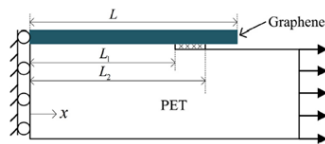
$\beta = \sqrt{K_0/E_g h}$ is the shear-lag parameter.

constant stiffness K_0

$$\varepsilon = \varepsilon_m\left(1 - \frac{\cosh(\beta x)}{\cosh(\beta L)}\right)$$

$\varepsilon_m = 0.2\%$ (Bonded)

$$\varepsilon = \varepsilon_m - \delta_i\beta\frac{\cosh(\beta x)}{\sinh(\beta L_1)}$$

$\varepsilon_m = 0.4\%$ (Damaged)

$$\varepsilon = \varepsilon_m + A\alpha\sin(\alpha(x - L_1)) - B\alpha\cos(\alpha(x - L_1))$$

$\varepsilon_m = 3.3\%$ (Debonded)
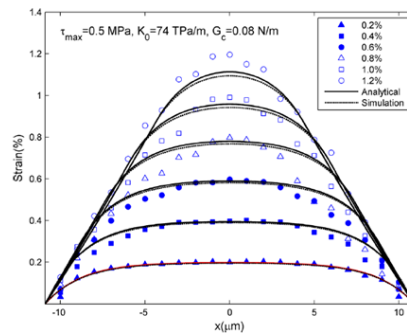
Fig. 14. Illustrative scheme of ε solutions and graphics – cohesive model, shear-lag and FEM for graphene/PET [52].
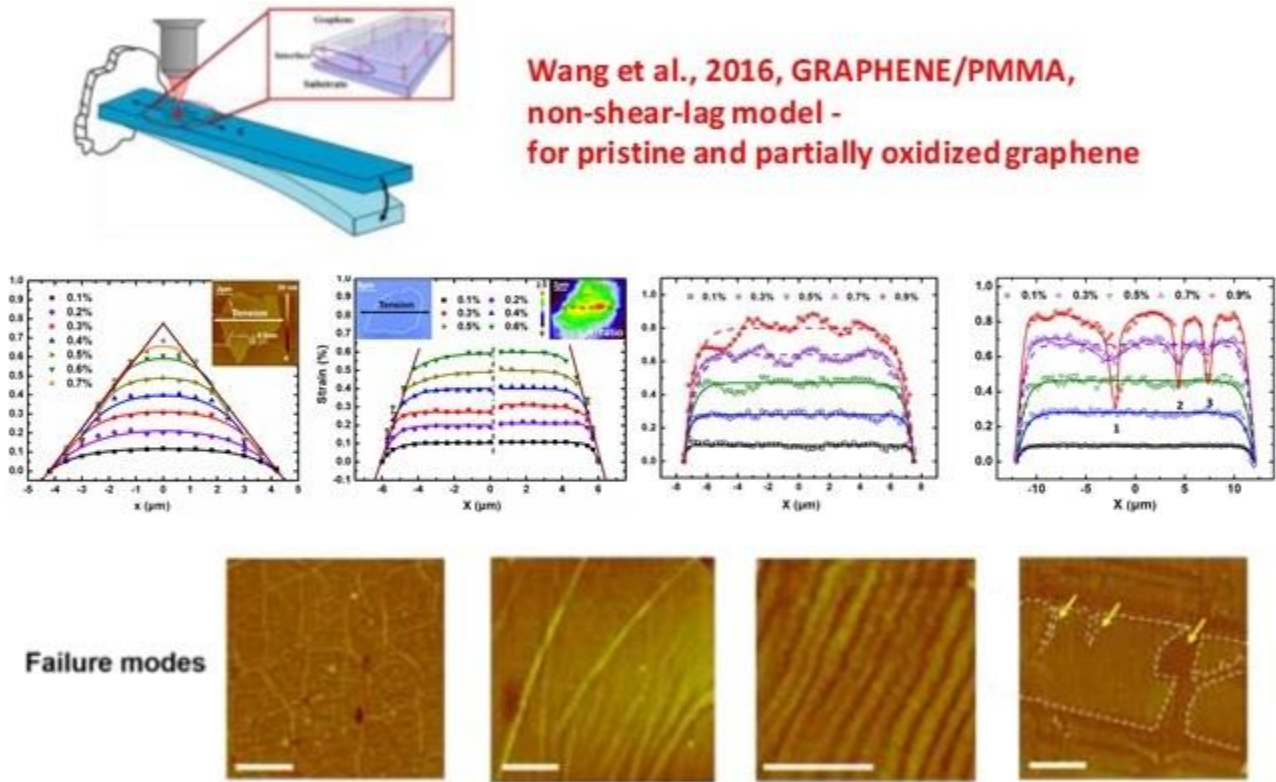
Fig. 15. Illustrative scheme of ε solutions and graphics – non-linear shear-lag for Graphene/PMMA [53].
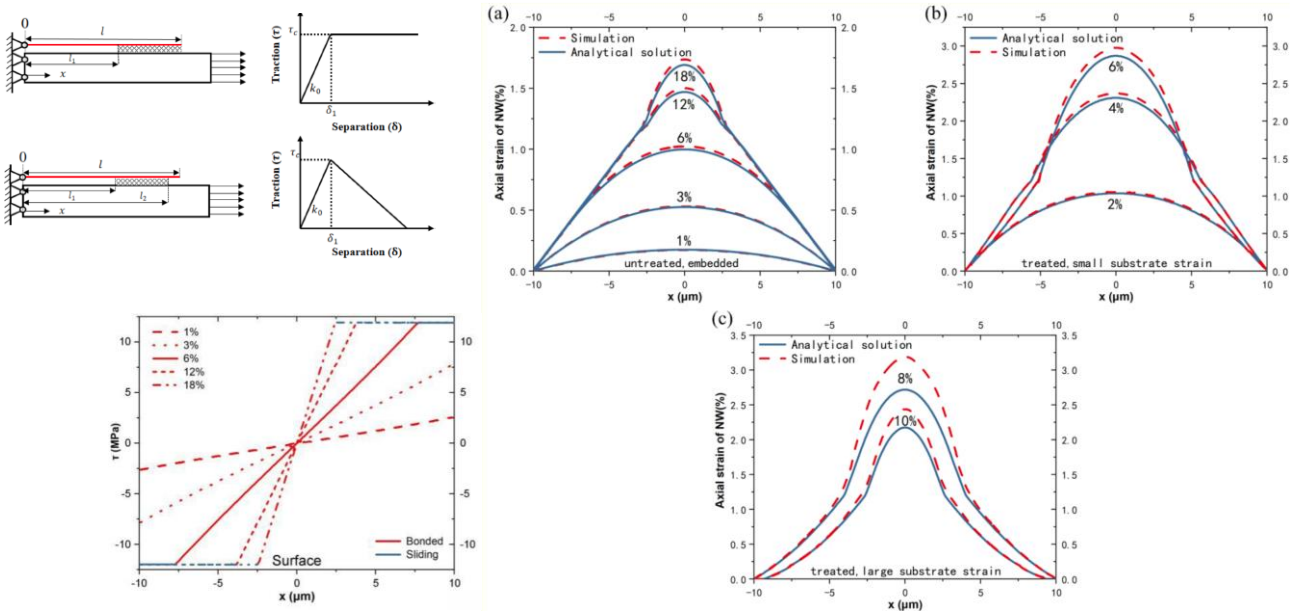
Fig. 16. Illustrative scheme of ε and τ solutions and graphics – non-linear shear-lag, bi-linear shear-lag , FEM, for elastoplastic nano-fiber AgNW/PDMS [54].

Several works were also found on so-called nano-adhesives (nanoclays), nano-additions of graphene and other 2D nanomaterials to various adhesives, in order to strengthen single-lap joint structures [58-60]. For some biological materials such as bone or nacre (generic nanocomposite structure with staggered alignment of mineral platelets in protein matrix) [61] a perturbation method was applied for analytically solving the 2D displacement and stress fields of such type of nanocomposite structure under uniaxial tension. The disadvantage of all these models is that interface layer between matrix and nano-layer are not taken into account. In 1D models like shear-lag the interface is represented as a line without considering its thickness and material properties. Meanwhile, it is proved that this interface

layer exists and should not be ignored when modeling layered nanocomposites, analytically or numerically [62-64].

From 2019, our team started to work trying to fill this gap and our contribution to the 2D analytical modeling of stresses and strain fields in layered nanocomposites with interface layer is expressed by the publications [19-24]. A detailed description of the 2D method (stress-function variational method) used to obtain analytical solutions for the two-dimensional stresses and strains in three-layer nanocomposite structures is given therein. In short, the applied method allows to obtain and solve an analytical differential equation of 4th order with respect to the unknown axial stress in the first layer (nanolayer). All other stresses in the layers are expressed by this solution/s and its derivatives. Two types of model solutions for the axial stress in the nanolayer are derived, depending on the geometry of the three-layer nanocomposite and its material properties:

$$\sigma_1 = C_1 \exp(\lambda_1 x) + C_2 \exp(\lambda_2 x)$$
$$+C_3 \exp(\lambda_3 x) + C_4 \exp(\lambda_4 x) - A \quad (4)$$

$$\sigma_1 = \exp(-\alpha x)[M_1 \cos(\beta x) + M_2 \sin(\beta x)]$$
$$+\exp(\alpha x).[(M_3 \cos(\beta x) + M_4 \sin(\beta x)] - A \quad (5)$$

All other stresses in the layers are expressed by one of the abovementioned solutions and its derivatives, as:

$$\sigma_{xx}^{(1)} = \sigma_1(x) = \sigma_1,$$

$$\sigma_{yy}^{(1)} = \frac{1}{2}(y - y_t)^2 \sigma_1^{"},$$

$$\sigma_{xy}^{(1)} = (y_t - y)\sigma_1^{'}$$

$$\sigma_{xx}^{(a)} \equiv 0$$

$$\sigma_{yy}^{(a)} = \left[\frac{h_1^2}{2} + h_1(c - y)\right]\sigma_1^{"},$$

$$\sigma_{xx}^{(2)} = \sigma_0 - \rho\sigma_1, \quad (6)$$

$$\sigma_{yy}^{(2)} = \frac{-\rho}{2}\left[y^2 - y(y_t + h_a)\right]\sigma_1^{"},$$

$$\sigma_{xy}^{(2)} = \rho y \sigma_1^{'}, \quad where \quad \rho = h_1/h_2$$

The 2D strains in each layer are expresses by equations (4)÷(6) as:

$$\varepsilon_{xy}^{(i)} = \frac{(1+\nu^{(i)})\sigma_{xy}^{(i)}}{E^{(i)}} \quad (7)$$

$$\varepsilon_{xx}^{(i)} = \frac{\sigma_{xx}^{(i)}}{E^{(i)}} - \frac{\nu^{(i)}\sigma_{yy}^{(i)}}{E^{(i)}}$$

$$\varepsilon_{yy}^{(i)} = -\frac{\nu^{(i)}\sigma_{xx}^{(i)}}{E^{(i)}} + \frac{\sigma_{yy}^{(i)}}{E^{(i)}}$$

For convenience, only the main results and the validation of our model solutions with literature experimental and model data will be given below. The results of the parametric analysis are also presented, which, based on the study of the sensitivity of the model solutions, makes it possible to determine the factors affecting the delamination in the investigated nanocomposite structures, given their wide application in various industrial sectors.

Validation

The validation of the model results obtained by us for the stresses and strains, with data from literature, is performed for the following nanocomposite structures: graphene/SU-8/PMMA – Gong [42], WS₂/SU-8/PMMA – Wang [44], 3-layered graphene/SU-8/PMMA - Androulidakis *et al.* [65] and Du *et al.* [5] for MoS₂/interface/PET and graphene/MoS₂/ PET. The results of the comparison of the obtained solutions can be seen below in Figs. 17 ÷21.

The validity of the proposed method and analytical solutions is only within the elastic region. It is worth mentioning that this region varies for different types of 2D nanomaterial. At 0.6% external load (Fig. 17 (b)) both model solutions - ours and the shear-lag one used in [42] cannot describe Gong's experimental data for graphene strain sufficiently accurately. The explanation for this is Gong's experimental observation that when the external load varies in the range of 0.4% to 0.7%, a creep and relaxation zone is recorded in the graphene, which is the cause of the drop (approximately in the middle of the flake, to 0.4%) in the distribution of the measured axial strain in graphene. According to Gong, it seems that the interface between the graphene and the polymer is not efficient enough and the transfer of the applied external load occurs through interfacial friction in this range. The strain in the graphene does not drop to zero in the middle of the flake, however, indicating that the flake remains unbounded. Further evidence to support this claim can be found in Polyzos *et al.* [66]. They experimentally investigated the behavior of stresses and strains in a suspended graphene flake between two PMMA layers subjected to an axial external load. It is reported that up to 0.8% external load "there is evidence that axial loading of graphene is always accompanied by the formation of orthogonal wrinkles/folds, similar to what is observed in a thin macroscopic membrane subjected to axial tension". In [66] they also emphasize that the limitations in their research method require a linear relationship between stress and strain, that is, within the elastic zone.

From Fig. 18 it is seen, that for WS_2 this depends not only on external load magnitude, but on the thickness of the +nano layer, too. As is illustrated on Fig. 19, both solutions for axial stress in WS_2 are in good agreement with shear-lag predictions, especially Case 2, may be because both shear-lag and Case 2 are expressed by hyperbolic sines and cosines. The similar dependence is observed for multi-layer graphene when external load is out of elastic range (Fig. 20). Here the main deviations are in the right end of the flakes for both external loads considered. Probably, this is due to the defect in the flake itself or to an error in measurement method in [65].

Our latter model strain predictions for hybrid nanocomposite structure with 2 interfaces (graphene/MoS$_2$/PET) at external load 0.5% are in good accordance with experimental data (Fig. 21 (b)). For nanocomposite sample with one interface (MoS$_2$/interface/PET) the coincidence is quite good (Fig. 21 (a)); probably, the existence of two interfaces in the first sample between both nanomaterials (graphene and MoS$_2$) and (MoS$_2$ and PET) did not positively influence the stress transfer efficiency in this sample.
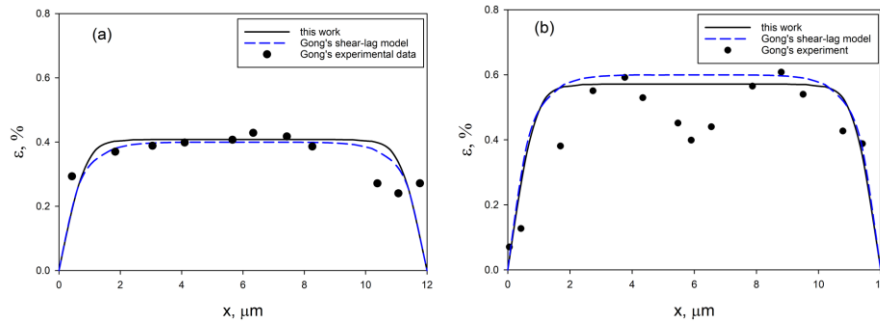
Fig. 17. Comparison of model predictions [19] for the ε in graphene with shear-lag model data and experimental data [42]; (a) at external load 0.4%, (b) – at 0.6%.

(a) (b) (c)
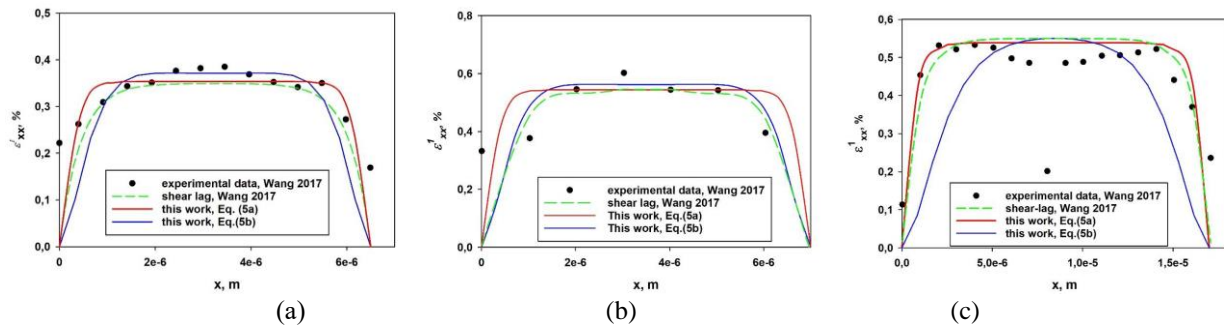
Fig. 18. Comparison of the two model solutions for ε in monolayer WS_2, according to equations (4) and (5) and (7) [21], with experimental and model shear-lag data of [44] at (a) external load 0.35%, (b) same at 0.55%, (c) multilayer WS_2 at 0.55%.
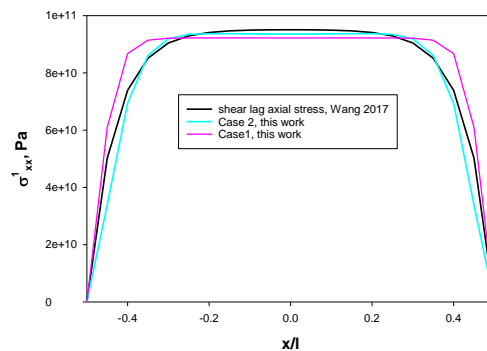
Fig. 19. Comparison of model σ solutions [24] in layer WS_2, with shear-lag model results of [44], for 0.35% external load.
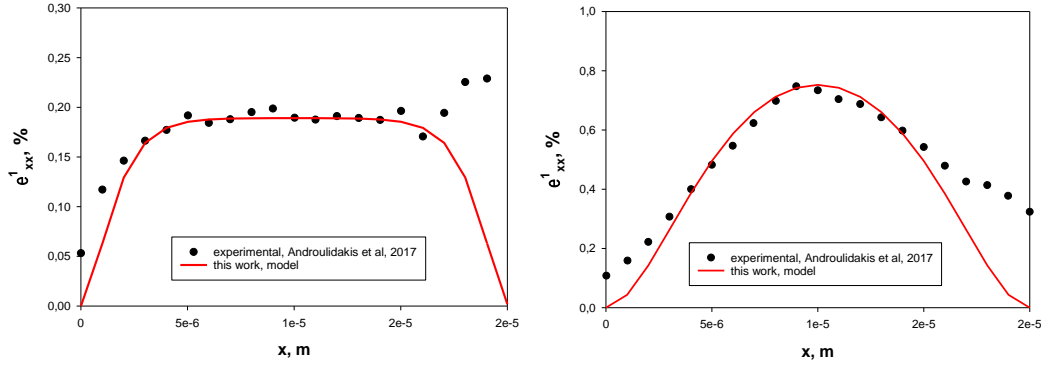
Fig. 20. Comparison of the model axial deformations [22] in 3-layer graphene with experimental data of [65], at external mechanical loading of 0.3% and 0.8 %.

| (a) | (b) |
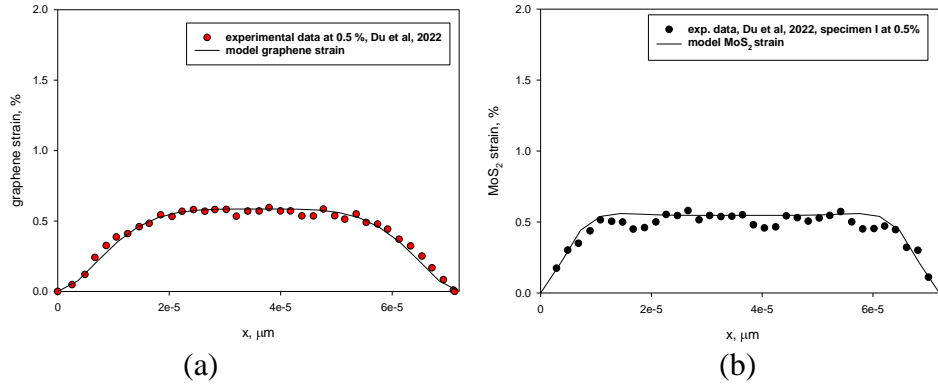
Fig. 21. Comparison of the model axial ε in the graphene layer (a), and in the MoS$_2$ layer (b), with experimental data of [5] at an external mechanical load of 0.5%.

Our future goal is to create a two-dimensional model for a three-layer nanocomposite with two interfacial layers.

Parametric analysis

For the nanostructures considered in the previous sub-section, a parametric analysis was made to determine which factors influence the delamination in them. The criterion for delamination is that the interface shear stress (ISS) calculated by the model in the second layer exceeds the critical value of the shear stress at tension (ultimate tensile shear strength), $\sigma_{xy}^{(a)} \geq USS^{(a)}$.

For each of the structures in the previous sub-section, a parametric analysis of $\sigma_{xy}^{(a)}$ for both two solutions was performed, since each of them corresponds to a combination of different thicknesses of the layers. Thus, in addition to the influence of the length, the influence of the layer thickness on the delamination was also investigated. As can be seen from the figures below, the geometry of the nanocomposite is a significant factor in debonding.

Graphene/SU-8/PMMA

The two solutions (4) and (5) for the axial stress were considered, respectively, with the help of equation (6) the shear stress $\sigma_{xy}^{(a)}$ in the second layer was calculated, as well as the abovementioned delamination criterion. For convenience, depending on the solution used, they are referred to as Case 1 (4) and Case 2 (5) in the following text. It was found that in the thinner layers (Case 1) of considered nanocomposite graphene/SU-8/PMMA, delamination can be observed at values of the external load $\sigma_0 \geq 350 MPa$, while in the thicker layers (Case 2) it occurs for $\sigma_0 \geq 750 MPa$, at a fixed value of the length l (Fig. 22). As the length increases and other parameters are fixed, delamination starts at lower values of the external load (Table 1). Also, the magnitude of σ_0 affects strongly the value of the debond length. The latter one is the solution of the equation $\sigma_{xy}^{(a)}(x) = \sigma_{USS}^{(a)}$ with the ultimate shear strength of the SU-8 adhesive (USS) on the right $\tau_{cr} = \sigma_{USS}^{(a)} = 30 MPa$. The delamination starts simultaneously from both ends of the structure and graphically its length corresponds to the intersection of the model $\sigma_{xy}^{(a)}$ with the critical value (red line). The obtained data

362

for the distance of the maximum value of $\sigma_{xy}^{(a)}$ from the edges of the layer are respectively 1.5 μm and 3.5 μm for Case 1 and Case 2 at maximum load, which values agree very well with the experimentally obtained data in [67] for the same structure – about 2 μm.

For the WS$_2$/SU-8/PMMA nanocomposite, the parametric analysis follows the same algorithm, again using both solutions, and the results are given in Figs. 23 and 24. Results were also obtained for the delamination length at different geometries (Fig. 24). As the length of the structure increases, so does the delamination length.

WS$_2$/SU-8/PMMA

Table 1

Case	l =6 μm	l = 12 μm	l = 20 μm	l = 30 μm
Case 1	$\sigma_0 \geq 2.5 \times 10^8$ Pa	$\sigma_0 \geq 3.5 \times 10^8$ Pa	$\sigma_0 \geq 8.5 \times 10^8$ Pa	$\sigma_0 \geq 3.3 \times 10^9$ Pa
Case 2	$\sigma_0 \geq 7.5 \times 10^8$ Pa	$\sigma_0 \geq 7.5 \times 10^8$ Pa	$\sigma_0 \geq 7.2 \times 10^8$ Pa	$\sigma_0 \geq 8 \times 10^8$ Pa
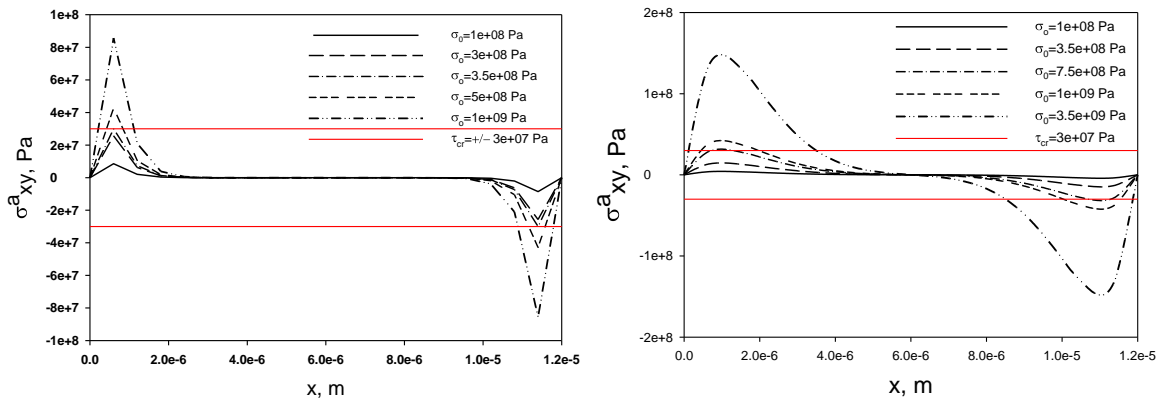
Fig. 22. Influence of the magnitude of the external load on the ISS for two different geometries (solutions) [20]; left, Case 1, right, Case 2, for monolayer graphene/SU-8/PMMA.
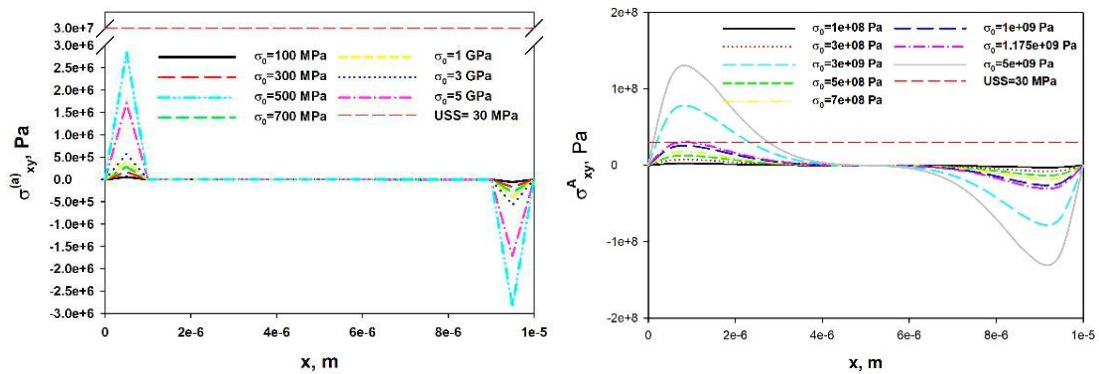
Fig. 23. Influence of the magnitude of the external load on the ISS at two different geometries (solutions) [23]; left, Case 1, right, Case 2, for the monolayer WS$_2$/SU-8/PMMA nanocomposite structure.

A similar result was also observed by Wang *et al.* [68] for the delamination length – 2 μm, for a WS$_2$/PVA nanocomposite structure.
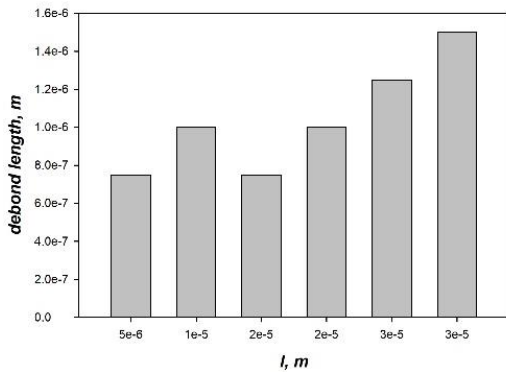
Fig. 24. Relationship between the debond length and the length l at a fixed load of 3 GPa, for Case 2, monolayer WS$_2$/SU-8/PMMA [23].

3-layered graphene/SU-8/PMMA

The main emphasis in [22] is the comparison between the model solutions for the deformations (strains) in the layers of considered 3-layered graphene/SU-8/PMMA nanocomposite, under different types of external loads, as can be seen from Fig. 25. In the case of a purely thermal effect (the red line), the deformations are nearly three times smaller than in the case of a purely mechanical effect (the black line). In the thermomechanical (green line), a superposition effect is observed in the amplitudes of the two loads, or in other words, the behavior is the same as in the mechanical load, but stronger, with the addition of the temperature effect, and this is best seen in the axial and the normal stress. Also, the effect of temperature is more clearly visible for deformations in the polymer layer than in graphene.

A similar observation is also found in the model results of Banaronei [29] obtained with finite elements. The work [29] is the first (to the best of our knowledge) to report results related to the distribution of stresses and longitudinal strains in graphene at different external temperatures. Since

the simulation used in [29] is FEM, no direct quantitative comparison is possible, only a qualitative assessment.

CONCLUSIONS

After this review on the analytical models for layered nanocomposites in the literature, the following conclusions and remarks could be proposed:

✓ Analytical "shear-lag" type models give simple 1D solutions, validated by experiments and FEM, for prediction of stresses and strains in composite and nanocomposites structures, subjected generally in tension loading.

✓ Analytical models allow adding of different effects to the stresses, especially to ISS, like interface spring stiffness constant, effects of residual stresses, due to the thermal and Poisson contraction, effect of WdW forces, effect of sliding, etc., and obtain analytical solutions to describe a complex combination of external and internal factors, acting on the stress transfer in nanocomposites.

✓ The correct application of shear-lag models for matrix-fiber nanocomposites is constrained - firstly in the elastic zone only, secondly by the volume of added fibers, and also, by the fiber length and interaction between fibers. Different models are derived to cover these gaps.

✓ Partial and total debonding models, as well as non-linear shear-lag create the "bridge" between predictions of stress transfer in elastic and plastic zone (cohesive shear-lag models and FEM simulations).

✓ 2D analytical stress-function method allows deriving of 2D solutions for three-layer nanocomposite structure, subjected to mechanical (axial tension) and thermo-mechanical static loading. These solutions are successfully validated in elastic zone by experimental and shear lag data for different nanocomposite structures.

(a)   (b)   (c)
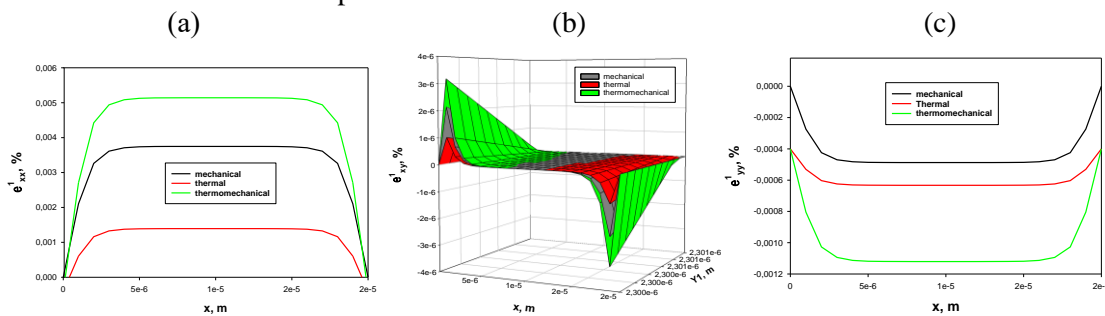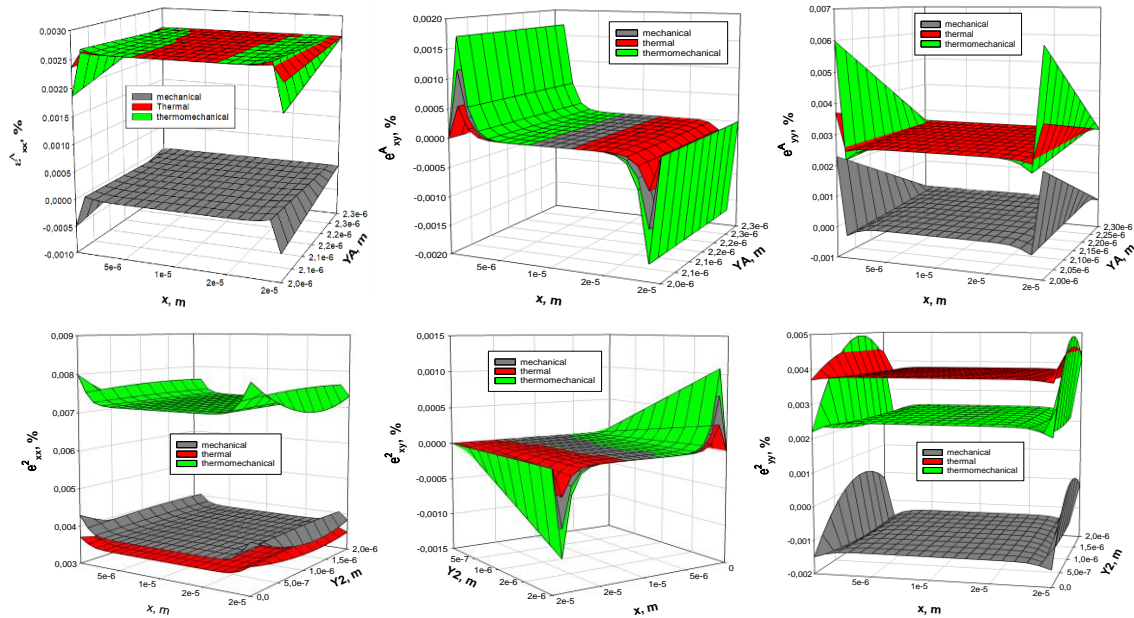
Fig. 25. Comparison of axial (a), shear (b) and peel strains (c) in graphene/SU-8/PMMA layers, under different types of loading [22].

REFERENCES

1. https://www.webofscience.com/wos/woscc/analyze-results/c956e875-4c9b-4d86-bd77-4ec87361bb63-91512fea, Assessed 26.06.2023.
2. https://www.webofscience.com/wos/woscc/summary/31c88f67-3965-4d38-8085-1e8a776b8d9c-9153a127/relevance/1, Assessed 26.06.2023.
3. https://www.webofscience.com/wos/woscc/summary/7a2f8a88-c322-4465-8e51-f594f1d9e179-9153d409/relevance/1, Assessed 26.06.2023.
4. https://www.webofscience.com/wos/woscc/summary/d8b0db8c-a5a0-4a07-9d8d-9413902b8ff1-9152f4f4/relevance/1, Assessed 26.06.2023.
5. H. Du, Y. Kang, C. Xu, T. Xue, W. Qiu, H. Xie, *Optics and Lasers in Engineering*, **149**, article 106825 (2022).
6. V. Valeva, T. Petrova, J. Ivanova, W. Becker, in: Proc. of Int. Conf. on Civil Engineering, Design and Constructions, 13 ÷ 15 September 2012, Varna, Bulgaria, 412.
7. J. Ivanova, V. Valeva, T. Petrova, W. Becker, in: Proc. of 8-th Conference on Sustainable Development of Energy, Water and Environmental Systems, September 22-27, (2013), Dubrovnik, Croatia, 0929-1.
8. J. Ivanova, V. Valeva, T. Petrova, W. Becker, *Mechanics of Advanced Materials and Structures*, **22** (10), 813 (2015).
9. J. Ivanova, V. Valeva, A. Yanakieva, T. Petrova, W. Becker, *Journal of Sustainable Development of Energy, Water and Environment Systems*, **4** (1), 23 (2016).
10. J. Ivanova, T. Petrova, E. Kirilova, W. Becker, *Engineering Transactions*, **65** (1), 97 (2017).
11. W. Becker, V. Valeva, T. Petrova, J. Ivanova, *Chemical Engineering Transactions*, **42**, 91 (2014).
12. E. Kirilova, T. Petrova, W. Becker, J. Ivanova, *ZAMM*, **97** (9), 1136 (2017).
13. E. Kirilova, T. Petrova, W. Becker, J. Ivanova, *IOP Conference Series: Materials Science and Engineering (MSE)*, **461** (1), 012029-1 (2018).
14. T. Petrova, E. Kirilova, W. Becker, J. Ivanova, *Pliska Studia Matematica*, **25**, 119 (2015).
15. T. Petrova, E. Kirilova, W. Becker, N. Vaklieva-Bancheva, J. Ivanova, *ZAMM*, **96**, 11, 1280 (2016).
16. T. Petrova, W. Becker, E. Kirilova, J. Ivanova, *CE/papers*, **1** (4), 487 (2017).
17. T. Petrova, E. Kirilova, W. Becker, J. Ivanova, J., *IOP Conference Series: Materials Science and Engineering (MSE)*, **461** (1), 012067-1 (2018).
18. E. Kirilova, T. Petrova, W. Becker, J. Ivanova, in: *2019 IEEE 14th Nanotechnology Materials and Devices Conference*, Stockholm, 27-30 October 2019.
19. T. Petrova, E. Kirilova, W. Becker, J. Ivanova, *J. Appl. Comput. Mech.*, **8**(3), 1065 (2022).
20. A. Apostolov, E. Kirilova, R. Vladova, N. Vaklieva-Bancheva, Ts. Rangelov, *Chemical Engineering Transactions*, **94**, 463 (2022).
21. T. Petrova, E. Kirilova, R. Vladova, B. Boyadjiev, W. Becker, P. Dineva-Vladikova, *U. Porto Journal of Engineering*, **8** (6), 160 (2022).
22. R. K. Vladova, T. S. Petrova, E. G. Kirilova, A.G. Apostolov, B. Ch. Boyadjiev, *Bulgarian Chemical Communications*, **54** (4), 349 (2022).

23. E. Kirilova, T. Petrova, N. Vaklieva-Bancheva, R. Vladova, Ts. Rangelov, A. Apostolov, *Procedia Structural Integrity*, **43**, 282 (2023).

24. T. Petrova, E. Kirilova, W. Becker, N. Vaklieva-Bancheva, R. Vladova, P. Dineva-Vladikova, *Procedia Structural Integrity*, **43**, 83 (2023).

25. Y. Zhang, J. Zhao, Y. Jia, T. Mabrouki, Y. Gong, N. Wei, T. Rabczuk, *Composite Structures*, **104**, 261 (2013).

26. M. Amirpour, R. Das, E.I. Saavedra Flores, *Composites Part B: Engineering*, **94**, 109 (2016).

27. D. Askari, M.N. Ghasemi-Nejhad, *Journal of Sandwich Structures & Materials,* **22**(7), 2330 (2020).

28. M. Tapia, Y. Espinosa-Almeyda, R. Rodríguez-Ramos, J. A. Otero, *Appl. Sci.,* **11**(4), article 1867 (2021).

29. S. A. Banarouei, Master thesis, York University, Toronto, Ontario, Canada (2021).

30. Ts. V. Rangelov, Y. D. Stoynov, P. S. Dineva, *Journal of Theoretical and Applied Mechanics*, **52**, 335 (2022).

31. Ts. Rangelov, P. Dineva, *Springer Proceedings in Mathematics & Statistics*, **412**, 117 (2023).

32. S. Parvanova, P. Dineva, *ZAMM*, e202200445, (2023) https://doi.org/10.1002/zamm.202200445 (in press).

33. G. D. Manolis, P. S. Dineva, Ts. V. Rangelov, G. I. Dadoulis, *Engineering Analysis with Boundary Elements*, **153**, 251 (2023).

34. O. Volkersen, *Luftfahrtforschung*, **15,** 41 (1938).

35. D.A. Dillard, A.V. Pocius, Chapter 1, Fundamentals of stress transfer in bonded systems, D.A. Dillard (ed.), Adhes. Sci. Eng. Mech. Adhes., Elsevier Science B.V., Amsterdam, 2002.

36. H. L. Cox, *Br. J. Appl. Phys.,* **3** (3), 72 (1952).

37. X.-L. Gao, K. Li, *International Journal of Solids and Structures*, **42**, 1649 (2005).

38. K. K. Ang, K. S. Ahmed, *Composites: Part B*, **50**, 7 (2013).

39. S. I. Kundalwal, M. C. Ray, S. A. Meguid, *Journal of Applied Mechanics*, **81**, 091001-1 (2014).

40. Y.-G. Hu, Y. F. Li, J. Han, C. P. Hu, Zh. H. Chen, S. T. Gu, *Acta Mech.* **230**, 2771 (2019).

41. L. Gong, I. A. Kinloch, R. J. Young, I. Riaz, R. Jalil, K. S. Novoselov, *Advanced materials*, **22** (24), 2694 (2010).

42. L. Gong, Ph.D. Thesis, Faculty of Engineering and Physical Sciences, The University of Manchester, Manchester, UK, 2012.

43. C. Xu, T. Xue, W. Qiu, Y.Kang, *ACS Appl. Mater. Interfaces*, **8**, 27099 (2016).

44. F. Wang, PhD thesis, The University of Manchester, Faculty of Science and Engineering, 2017, UK.

45. W. Wang, Z. Li, A. J. Marsden, M. A. Bissett, R. J. Young, *2D Mater.,* **8**, article 035058 (2021).

46. M. Liu, Y. Zhuo, A. Sarycheva, Y. Gogotsi, M. A. Bissett, R. J. Young, I. A. Kinloch, *ACS Appl. Mater. Interfaces*, **14**, 10681 (2022).

47. https://fhart.files.wordpress.com/2009/04/sapromat.pdf, fig.3.13, Assessed 26.06.23

48. Th. Lacroix, B. Tiimans, R. Keunings, M. Desaeger, I. Verpoest, *Composites Science and Technology*, **43**, 379 (1992).

49. M. Dong, R. J. Young, D. J. Dunstan, D. G. Papageorgiou, *Composites Science and Technology,* **233**, article 109892 (2023).

50. T. Jiang, R. Huang, Y. Zhu, *Adv. Funct. Mater.,* **24**, 396 (2014).

51. M. S. Bronsgeest, N. Bendiab, S. Mathur, A. Kimouche, H. T. Johnson, J. Coraux, P. Pochet, *Nano Lett.*, **15** (8), 5098 (2015).

52. G. Guo, Y. Zhu, *Journal of Applied Mechanics,* **82** (3), 031005-1 (2015).

53. G. Wang, Z. Dai, L. Liu, H. Hu, Q. Dai, Zh. Zhang, *ACS Appl. Mater. Interfaces,* **8,** 22554 (2016).

54. L.-H. Shao, X. Qu, T. Wang, Z. Cui, Y. Liu, Y. Zhu, *J. Mech. Phys. Solids,* **173**, article 105218 (2023).

55. Y. Zhang, Z. Zhou, Z. Tan, *Symmetry*, **11**, 1437 (2019).

56. B. Zhao, Z-H. Lu, *Mechanics of Advanced Materials and Structures,* **16**, 130 (2009).

57. B. Zhao, Z.-H. Lu, Y.-N. Lu, *International Journal of Adhesion & Adhesives,* **49**, 115 (2014).

58. S.K. Gupta, D.K. Shukla, A. Bharti, in: Proc. 2017 International Conference on Advances in Mechanical, Industrial, Automation and Management Systems, 3-5 February 2017, Allahabad, India, 307.

59. E.A. Akpinar, K. Gültekin, S. Akpinar, H. Akbulut, A. Ozel, *Composites Part B*, **98**, 362 (2016).

60. P. Jojibabu, Y.X. Zhang, G. Prusty, *International Journal of Adhesion and Adhesives*, **96**, article 102454 (2020).

61. G. Liu, B. Ji, K.-C. Hwang, B. C. Khoo, *Composites Science and Technology*, **71,** 1190 (2011).

62. G. Wang, L. Liu, Zh. Zhang, *Composites Part A: Applied Science and Manufacturing,* **141**, article 106212, (2021).

63. J. Huang, J. Zhou, M. Liu, *JACS Au*, **2**(2), 280 (2022).

64. X. Lu, F. Detrez, J. Yvonnet, J. Bai, *Composites Science and Technology*, **213**, article 108943, (2021).

65. Ch. Androulidakis, E.N. Koukaras, J. Rahova, K. Sampathkumar, J. Parthenios, K. Papagelis, O. Frank, C. Galiotis, *Appl. Mater. Interfaces,* **9** (31), 26593 (2017).

66. I. Polyzos, M. Bianchi, L. Rizzi, E.N. Koukaras, J. Parthenios, K. Papagelis, R. Sordan, C. Galiotis, *Nanoscale*, **7**(30), 13033 (2015).

67. G. Anagnostopoulos, C. Androulidakis, E. N. Koukaras, G. Tsoukleri, I. Polyzos, J. Parthenios, K. Papagelis, C. Galiotis, *ACS Appl. Mater. Interfaces*, **7**, 4216 (2015).

68. F. Wang, S. Li, M. A. Bissett, I. A. Kinloch, Z. Li, R. J. Young, *2D Materials*, **7**(4), Article number 045022 (2020).

Time-harmonic nano-cracks interaction in functionally graded piezoelectric half-plane

Ts. Rangelov[1]*, P. Dineva[2]

[1]Institute of Mathematics and Informatics, BAS, Acad. G. Bonchev Str., Bl. 8, 1113 Sofia, Bulgaria
[2]Institute of Mechanics, BAS, Acad. G. Bonchev Str., Bl. 4, 1113 Sofia, Bulgaria

A system of two nano-cracks situated in an exponentially graded in depth piezoelectric material (PEM) half-plane under time-harmonic anti-plane load is studied. The mechanical model is in the frame of 2D elastodynamics for graded continua and surface elasticity theory of Gurtin and Murdoch (GM). Mathematical model is defined by a system of integro-differential equations along the crack lines. The computational tool is an efficient nonhypersingular traction boundary integral equation method (BIEM) based on the analytically derived Green's function for the graded half-plane. The obtained results are with important application in computational nano-mechanics and in engineering practice concerning the reliability of the micro-electro-mechanical-systems emerged to meet the requirements of miniaturization and integration of different types of electronic components.

Keywords: Graded PEM half-plane; Nano-cracks; Anti-plane wave; GM surface elasticity; BIEM; Stress concentration

INTRODUCTION

There is a general agreement concluded from the experiments that the properties of piezoelectric nano-materials are size-dependent. For example: (a) as the nano-wire diameter decreases from 80 nm to 20 nm, the Young's modulus of ZnO nano-wire increases from 140 to 160 GPa (Agrawal *et al.* [1]); (b) the fracture strength of ZnO nano-wires increases as the nano-wire diameter decreases (Xu *et al.* [2]); (c) the piezoelectric constants of GaN nano-wires were reported up to six times more than that of the bulk values (Minary-Jolandan *et al.* [3]). The classical continuum mechanics is incapable to capture the size-dependence of solids behavior as the intrinsic length scale is not present in the constitutive laws. As a result, many non-classical theories were developed to study the size-dependent mechanical problems. A categorization of the nano-mechanical models depending on the link between material microstructure and intrinsic length scale h is presented by Manolis *et al.* [4]. Continuum mechanics-based models ($h \approx 10^{-2} m$) for nano-objects are non-local elasticity, strain gradient theory and surface elasticity model (Gurtin-Murdoch [5]). In the latter model, the surface is regarded as a thin layer with negligible thickness adhered to the underlying bulk material without slipping. The surface properties and constitutive relations are different from those of the bulk. Despite its zero thickness, the surface layer S is otherwise elastic, isotropic with its own surface Lame constants λ^S, μ^S and local constitutive law written in tangential direction l such as $\sigma_{ll}^S = \left(\lambda^S + 2\mu^S \right) \varepsilon_{ll}^S$, where σ_{ll}^S and ε_{ll}^S are the tangential stress and strain, correspondingly. Thus, under the Gurtin-Murdoch theory, the traditional boundary conditions along the surface layer S are replaced by non-classical ones that account for the unconventional surface elasticity conditions, while the bulk materials can still be described by classical continuum theory.

The main aim of the current work is to model the dynamic behavior of two nano-cracks in an exponentially graded in depth PEM half-plane under time-harmonic SH-wave. For numerical results we proceed with non-hypersingular traction BIEM using the half-plane Green's function analytically derived in [6].

MECHANICAL MODEL
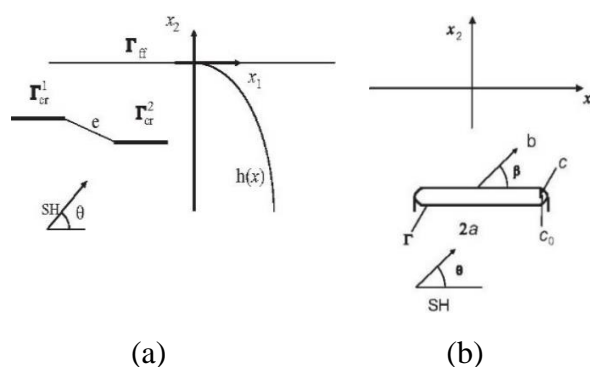
Fig. 1. a) Two nano-cracks in functionally graded half-plane; b) Reference model of a single blunt nano-crack.

In a Cartesian coordinate system $Ox_1x_2x_3$ a piezoelectric half-plane $R_-^2 = \{x = (x_1, x_2), x_2 < 0\}$ is considered poled in x_3 - direction and subjected

* To whom all correspondence should be sent:
E-mail: rangelov@math.bas.bg

to time-harmonic incident SH-wave with frequency ω. The only non-vanishing displacements are the anti-plane mechanical displacement $u_3(x, \omega)$ and the in-plane electrical displacements $D_i(x, \omega)$, $i = 1, 2$.

Let us introduce the notations for the generalized displacements, stresses and density as follows:

$$u_K(x, \omega) = \big(u_3(x, \omega), \phi(x, \omega)\big),$$
$$\sigma_{iJ}(x, \omega) = C_{iJKl}(x)u_{K,l}(x, \omega)$$
$$\rho_{JK}(x) = \rho(x),$$

where $\rho(x) = \rho^0 h(x)$ is the variable density for $J = K = 3$ and $\rho_{JK}(x) = 0$ for $J = 4$ or $K = 4$; $\phi(x, \omega)$ is the electric potential.

The equation of motion in the absence of body forces and free volume charges is:

$$\sigma_{iJ,i}(x, \omega) + \rho_{JK}(x)\omega^2 u_K(x, \omega) = 0 \qquad (1)$$

where:

$C_{i33l}(x) = c_{44}(x)$, $\quad C_{i34l}(x) = e_{15}(x)$ and $C_{i44l}(x) = -\varepsilon_{11}(x)$ in the case of $i = l$ and all three generalized material characteristics are zero at $i \neq l$.

Note that $c_{44}(x) = c_{44}^0 h(x)$, $e_{15}(x) = e_{15}^0 h(x)$ and $\varepsilon_{11}(x) = \varepsilon_{11}^0 h(x)$ are the shear stiffness, piezoelectric and dielectric permittivity of the graded PEM. The exponential inhomogeneity function $h(x) = e^{2bx_2}$ is with coefficient b and $c_{44}^0, e_{15}^0, \varepsilon_{11}^0, \rho^0$ are the reference constants.

The boundary condition along the free surface is:

$$t_J = \sigma_{iJ}(x, \omega)n_i(x) = 0 \qquad (2)$$

where $n_i(x)$ is the outward normal vector.

Following the Gurtin-Murdoch model [5], the boundary condition for the mechanical stresses along the crack's line l is:

$$t_3(x, \omega) = -\mu^S \frac{\partial^2 u_3}{\partial l^2}, \qquad (3)$$

where μ^S is the shear modulus of the infinitely thin surface layer S between the crack and matrix. Both nano-cracks are electrically impermeable, i.e., $D_n(x, \omega) = 0$ for $x \in S$.

The total wave field in the graded PEM half-plane is a sum of the free-field wave motion displacements u_K^{ff} and tractions t_K^{ff} and the scattered by the cracks ones u_K^{sc}, t_K^{sc}. The free-field wave displacement and traction in the graded half-plane is the wave motion in the cracks' free half-plane. It is a sum of the incident waves and the reflected ones by the traction-free half-plane boundary. Analytically derived solution for the free-field wave motion is presented in [6].

The mechanical model is presented by the governing equation (1) and the boundary conditions discussed above.

The aim is to obtain solutions for frequency-dependent displacements, strains and stresses in the

graded PEM half-plane. In addition, stress concentration fields near the nano-cracks are evaluated. The computational tool used for solution of this boundary-value problem (BVP) is an efficient non-hypersingular traction BIEM based on analytically derived Green's function for exponentially graded piezoelectric half-plane. The applied BIEM based on the fundamental solution for graded PEM full plane is described and verified in [7]. The innovative element here is the solution of dynamic fracture problem for multiple nano-cracks in a graded PEM half-plane with BIEM based on the Green's function.

NUMERICAL RESULTS

The numerical scheme for solution of the BVP under consideration is based on discretization and collocation technique. The mesh employed for each nano-crack with half-length $a = 2.5 \times 10^{-9} m$ and curvature radius $c = 0.375\,a$ consists of 10 quadratic boundary elements (BEs), 8 BEs along the flat part of the crack's boundary Γ denoted by $\Gamma^+ \cup \Gamma^-$ and 2 BEs along the semi-elliptic left and right parts of Γ denoted as Γ^l and Γ^r correspondingly. Quarter-point BEs for correctly modelling the crack-tip zones where the asymptotic generalized displacement behavior as O($\sqrt{r}$) at r → 0 are used.

After discretization of the system of non-hypersingular traction BIEs an algebraic system of equations with respect to the generalized displacements along the cracks' surfaces is obtained and solved. The displacements and strain-stress state at any point of the graded half-plane can be determined by the usage of the well-known integral representation formulae, see [7]. The numerical scheme is realized by the verified code basing on Mathematica software, see [8]. The following dimensionless parameters are introduced:

(a) Surface parameter $s = \mu^S / 2c_{44}^0 cc_s$, where $\mu^S = \pm 6.091 N/m$ is taken from [9]. The notation c_s is used in order to decrease or increase the fixed value of the curvature radius c of the semi-elliptic nano-crack root. The value of the surface parameter decreases/increases with increase/decrease of the curvature radius c. In the case $\mu^S = 0$, the surface parameter $s = 0$ and the non-classical boundary conditions recover the classical ones;

(b) Dimensionless frequency defined as:

$$\Omega = a\omega \sqrt{\frac{\rho^0}{c_{44}^0 + \frac{(e_{15}^0)^2}{\varepsilon_{11}^0}}} \; ;$$

(c) Dimensionless inhomogeneity magnitude defined as $\beta = 2a|b|$. The reference material is PZT-4 with the following material properties:

$c_{44}^0 = 2.5 \times 10^{10}\,N/m^2$; $e_{15}^0 = 12.7\,C/m^2$; $\varepsilon_{11}^0 = 64.6 \times 10^{-10}\,C/V.m$; $\rho^0 = 7500\,kg/m^3$.

The normalized stress concentration factor (SCF) F_{III}^* and electrical field concentration factor (EFCF) F_E^* close to the blunt nano-crack-tip at the point $(\pm x_1, 0)$ are evaluated by the formulae:

$$F_{III}^*\big((\pm x_1, 0), \omega\big) = \frac{\sigma_{23}((\pm x_1, 0), \omega)}{\sigma\sqrt{\pi a}}\sqrt{2\pi(x_1 \mp a)},$$
$|x_1| > a;$ (4)

$$F_E^*\big((\pm x_1, 0), \omega\big) =$$
$$e_{15}^0 \frac{E_3((\pm x_1, 0), \omega)}{\sigma\sqrt{\pi a}}\sqrt{2\pi(x_1 \mp a)},\ |x_1| > a.$$ (5)

where:

$$E_3 = \frac{\sigma_{24}((\pm x_1, 0), \omega)c_{44}^0 - \sigma_{23}((\pm x_1, 0), \omega)e_{15}^0}{c_{44}^0\varepsilon_{11}^0 + (e_{15}^0)^2};$$

$$\sigma = \underbrace{max}_{S}\sqrt{(\sigma_{23}^{in})^2 + (\sigma_{24}^{in})^2}.$$

What follows is a parametric study shown by Figures 2-6. All the figures illustrate the sensitivity of both the mechanical and electrical concentration fields near the nano-cracks on the following factors:

(a) The frequency of the incident wave and the value of the resonance frequency;

(b) The geometry of the nano-cracks configuration - collinear, parallel or shifted cracks;

(c) The influence of the half-plane boundary when compare Figs. 2a, 3a and Figs. 2b, 3b;

(d) The surface elasticity phenomenon: the dynamic response decreases with increase of the positive surface elasticity parameter and increases with the negative surface elasticity parameter. This happens because of destruction and reorganization of the atom symmetry along the interfaces at nano-level.

The size of the crack has strong influence on the scattered and diffraction wave field and also on the local zones of stress and electrical field concentrations. With decreasing of the crack size, surface elasticity phenomena arise and *vice versa* - cracks with size at macro-level do not show surface elasticity properties. Normalized displacement amplitude $|u_3|$ along the free surface of the PEM graded half-plane is presented in Fig. 6 for the following fixed data: inhomogeneity magnitude is $\beta = 0.2$, surface elasticity parameter is $s = 0.02$, separate distance between both nano-cracks is $e = 0.5a$, embedded depth is $d = a$, normalized frequencies of the incident normal SH wave are $\Omega = 1.1; 1.3; 1.7$.

Two different crack configuration geometries were studied, namely: (a) two collinear nano-cracks; (b) two shifted nano-cracks.

(a)

(b)
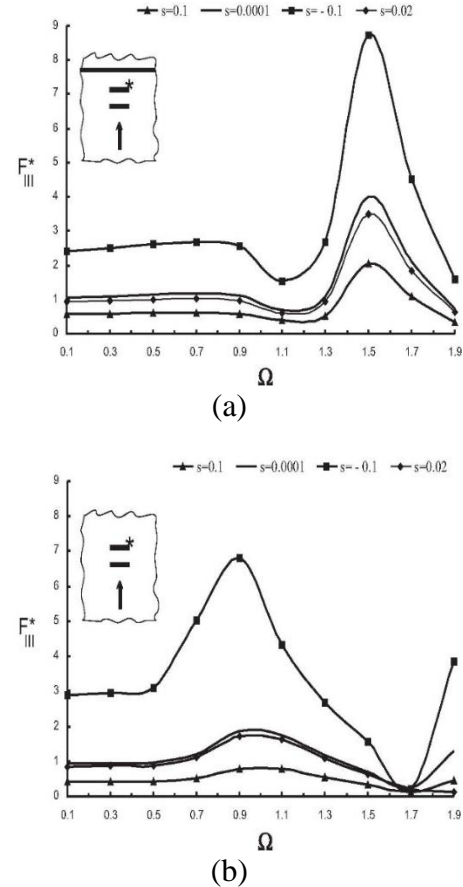
Fig. 2. Normalized SCF F_{III}^* *versus* Ω at upper nano-crack with embedded depth $d = a$ and separate distance $e = 0.5a$ from the lower nano-crack due to incident normal SH wave propagating in: (a) graded PEM half-plane with inhomogeneity magnitude $\beta = 0.2$; (b) graded PEM full plane with inhomogeneity magnitude $\beta = 0.2$. Different surface parameters s are used.

Figures 6a-6b clearly demonstrate that the scattered wave displacement along the traction-free surface of a graded PEM half-plane is strongly sensitive to the dynamic nano-cracks interaction and mutual nano-cracks configuration.

The obtained results have the potential to be used as a base for solution of inverse problems for identification of nano-cracks existence and their position in the functionally graded piezoelectric half-plane. All presented figures show surface elasticity effects. They appear due to the following solids state at nano-level. The number of atoms at the surface increases in respect to that in the bulk as the structural size reduces to the nanoscale. Since the surface atoms are more unstable (broken atomic bonds) than the bulk ones, they may induce the unique properties of nanomaterials.

(a)

(b)
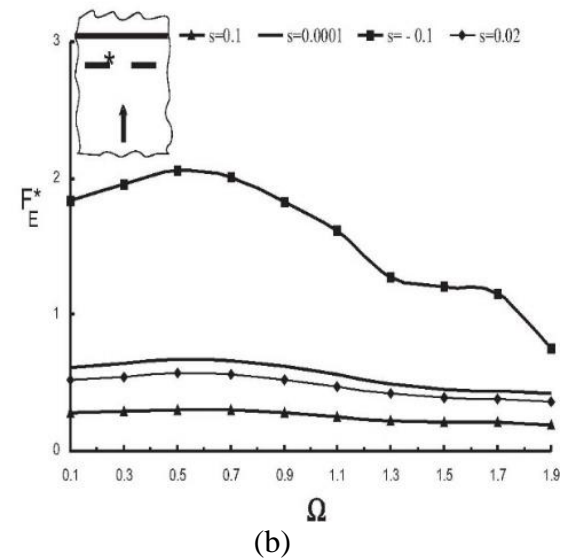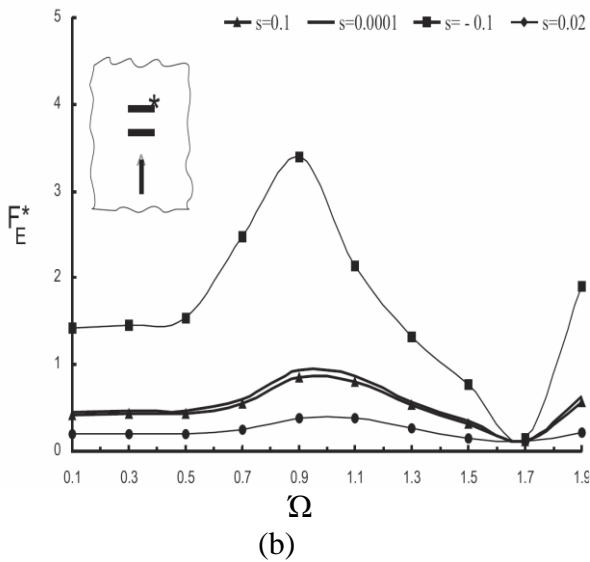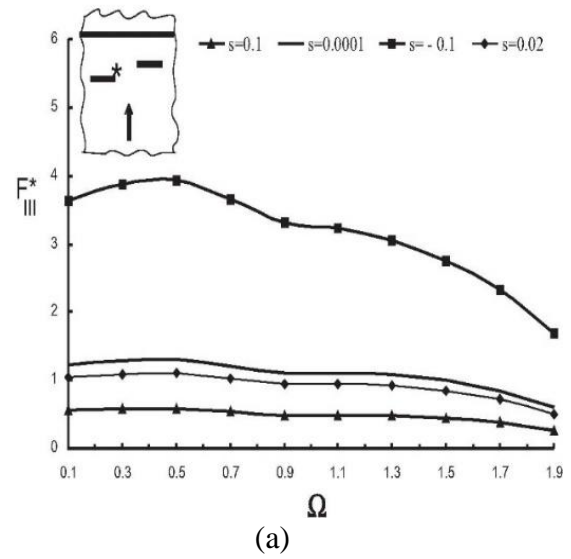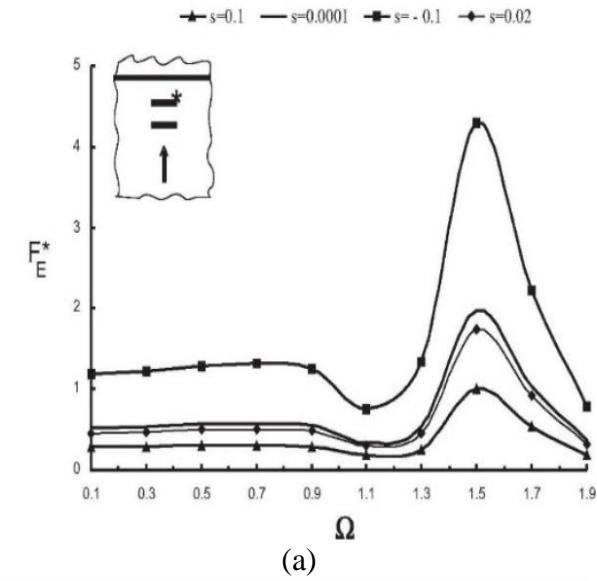
Fig. 3. Normalized EFCF F_E^* *versus* Ω at upper nano-crack with embedded depth $d = a$ and separate distance $e = 0.5a$ from the lower nano-crack due to incident normal SH wave propagating in: (a) graded PEM half-plane with inhomogeneity magnitude $\beta = 0.2$; (b) graded PEM full plane with inhomogeneity magnitude $\beta = 0.2$. Different surface parameters s are used.

At the nano scale, the atomic structures in the vicinity of the piezoelectric surface are far from steady. Because of the broken symmetry, they automatically modulate to be a self-equilibrated state different from those in the underlying piezoelectric bulk. The creation of an additional surface leads to excess of free energy E in the solid, i.e., the surface free energy, which is the origin of the surface effects.

(a)

(b)

Fig. 4. Normalized mechanical F_{III}^* (a) and electrical F_E^* (b) intensity factors *versus* Ω at left nano-crack with embedded depth $d = a$ and separate distance $e = 0.5a$ from the second collinear nano-crack due to incident normal SH wave propagating in a graded PEM half-plane with inhomogeneity magnitude $\beta = 0.2$. Different surface parameters s are used.

CONCLUSIONS

An exponentially graded piezoelectric half-plane with two nano-cracks situated in an arbitrary mutual disposition and subjected to incident time-harmonic SH wave is studied. The computational tool is non-hypersingular traction BIEM developed in the frame of Gurtin-Murdoch model, which established the mathematical framework for incorporating surface stresses into continuum mechanics formulations.

This theory was motivated in part by empirical observations pointing to the presence of a compressive surface stress in certain types of crystals. In the Gurtin-Murdoch model, the interfaces between nano-heterogeneities and the bulk matrix are regarded as infinitely thin surfaces that possess their own deformation and surface tension characteristics. A linearized surface stress–strain constitutive relation was proposed to characterize this surface/interface effect. More specifically, the equilibrium and constitutive equations of the bulk solid are the same as those in classical elasticity, but the presence of a surface/interface stress gives rise to non-classical boundary conditions. The surface stress tensor is associated with both the bulk stress tensor and the external load by means of a force balance equation established at the solid's surface. A strong contribution is insertion of the analytically derived Green's function in the traction non- hypersingular boundary integral equations. The Green's function obeys the Sommerfeld's radiation condition and thus infinitely extended boundaries are automatically accounted for without resorting to special types of viscous boundaries as is in the domain methods such as finite difference method and finite element method. In addition, when the half-plane Green's function is used, the discretization along the free surface is avoided and as a result the size of the algebraic system is significantly reduced. The simulations conducted here illustrate that the non-uniform dynamic stress and electrical field distribution depends on the following key model factors:

(a) The incident wave characteristics;

(b) The geometry of the crack configuration and the graded half-plane boundary;

(c) The type, magnitude and properties of the material gradient;

(d) The reference material properties;

(e) The coupled material properties of piezoelectric composite materials;

(f) The surface elasticity phenomenon and the nano-crack size.

The proposed, developed and verified numerical tool has a direct application in nanomechanics and in non-destruction testing of nanomaterials.

(a)

(b)
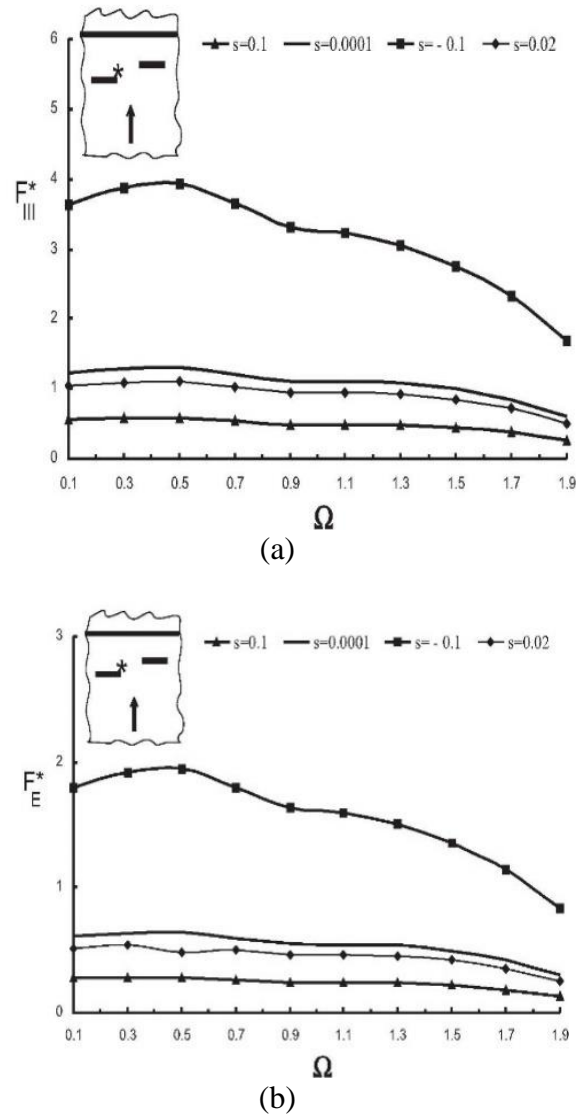
Fig. 5. Normalized mechanical F_{III}^* (a) and electrical F_E^* (b) intensity factors *versus* Ω at left nano-crack with embedded depth $d = a$ and separate distance $e = 0.5a$ from the second shifted nano-crack due to incident normal SH wave propagating in a graded PEM half-plane with inhomogeneity magnitude $\beta = 0.2$. Different surface parameters s are used.

(a)

(b)
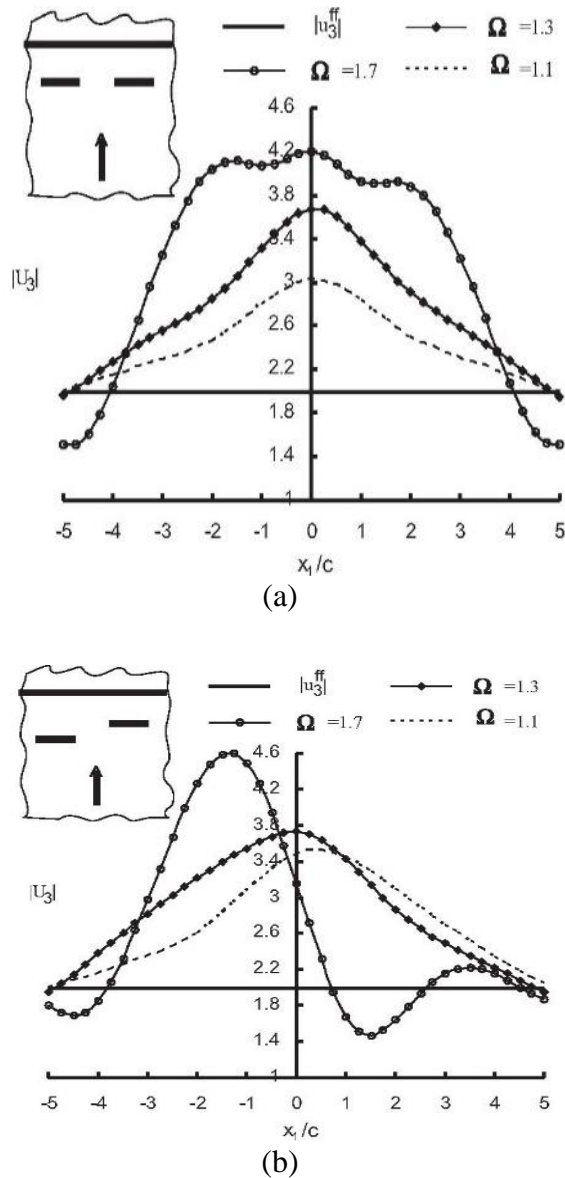
Fig. 6. Normalized displacement amplitude $|u_3|$ along the free surface of the PEM graded half-plane with the following fixed data: inhomogeneity magnitude $\beta = 0.2$, surface parameter $s = 0.02$, separate distance between both nano-cracks $e = 0.5a$, embedded depth $d = a$, frequencies of the incident normal SH wave Ω=1.1; 1.3; 1.7 for two different cracks configuration geometries: (a) two collinear nano-cracks; (b) two shifted nano-cracks.

REFERENCES

1. R. Agrawal, B. Peng, E. Gdoutos, H. Espinosa, *Nano Lett.*, **8**, 3668 (2008).
2. F. Xu, Q. Qin, A. Mishra, Y. Gu, Y. Zhu, *Nano Res.*, **3**, 271 (2010).
3. M. Minary-Jolandan, R.A. Bernal, I. Kuljanishvili, V. Parpoil, H.D. Espinosa, *Nano Lett.*, **12**, 970 (2012).
4. G. Manolis, P. Dineva, T. Rangelov, D. Sfyris, *Engineering Analysis with Boundary Elements (EABE),* **128**, 149 (2021).
5. M.E. Gurtin, A.L. Murdoch, *Archives for Rational Mechanics and Analysis,* **57,** 291 (1975).
6. T. Rangelov, P. Dineva, in: A. Slavova (ed.), NTADES, 2022, Springer PROMS, v. **412**, Springer Nature, 2023, p. 117.
7. P. Dineva, D. Gross, R. Muller, T. Rangelov, Dynamic Fracture of Piezoelectric Materials. Solutions of Time-harmonic problems via BIEM. Solid Mechanics and its Applications, v. 212, Springer Int. Publ., Switzerland, 2014.
8. Mathematica 6.0 for MS Windows. Champaign, Illinois, 2007.
9. V. B. Shenoy, *Int. J. Solids Struct.*, **39**, 4039 (2002).

Instructions about Preparation of Manuscripts

General remarks: Manuscripts are submitted in English by e-mail. The text must be prepared in A4 format sheets using Times New Roman font size 11, normal character spacing. The manuscript should not exceed 15 pages (about 3500 words), including photographs, tables, drawings, formulae, etc. Authors are requested to use margins of 2 cm on all sides.

Manuscripts should be subdivided into labelled sections, e.g. INTRODUCTION, EXPERIMENTAL, RESULTS AND DISCUSSION, *etc*. **The title page** comprises headline, author(s)' names and affiliations, abstract and key words. Attention is drawn to the following:

a) **The title** of the manuscript should reflect concisely the purpose and findings of the work. Abbreviations, symbols, chemical formulae, references and footnotes should be avoided. If indispensable, abbreviations and formulae should be given in parentheses immediately after the respective full form.

b) **The author(s)**' first and middle name initials and family name in full should be given, followed by the address (or addresses) of the contributing laboratory (laboratories). **The affiliation** of the author(s) should be listed in detail (no abbreviations!). The author to whom correspondence and/or inquiries should be sent should be indicated by an asterisk (*) with e-mail address.

The abstract should be self-explanatory and intelligible without any references to the text and containing up to 250 words. It should be followed by keywords (up to six).

References should be numbered sequentially in the order, in which they are cited in the text. The numbers in the text should be enclosed in brackets [2], [5, 6], [9−12], etc., set on the text line. References are to be listed in numerical order on a separate sheet. All references are to be given in Latin letters. The names of the authors are given without inversion. Titles of journals must be abbreviated according to Chemical Abstracts and given in italics, the volume is typed in bold, the initial page is given and the year in parentheses. Attention is drawn to the following conventions: a) The names of all authors of a certain publications should be given. The use of "*et al*." in the list of references is not acceptable; b) Only the initials of the first and middle names should be given. In the manuscripts, the reference to author(s) of cited works should be made without giving initials, e.g. "Bush and Smith [7] pioneered...". If the reference carries the names of three or more authors it should be quoted as "Bush *et al*. [7]", if Bush is the first author, or as "Bush and co-workers [7]", if Bush is the senior author.

Footnotes should be reduced to a minimum. Each footnote should be typed double-spaced at the bottom of the page, on which its subject is first mentioned. **Tables** are numbered with Arabic numerals on the left-hand top. Each table should be referred to in the text. Column headings should be as short as possible but they must define units unambiguously. The units are to be separated from the preceding symbols by a comma or brackets. Note: The following format should be used when figures, equations, *etc*. are referred to the text (followed by the respective numbers): Fig., Eqns., Table, Scheme.

Schemes and figures. Each manuscript should contain or be accompanied by the respective illustrative material, as well as by the respective figure captions in a separate file. As far as presentation of units is concerned, SI units are to be used. However, some non-SI units are also acceptable, such as °C, ml, l, etc. Avoid using more than 6 (12 for review articles) figures in the manuscript. Since most of the illustrative materials are to be presented as 8-cm wide pictures, attention should be paid that all axis titles, numerals, legend(s) and texts are legible.

The authors are required to submit the text with a list of three individuals and their e-mail addresses that can be considered by the Editors as potential reviewers. Please note that the reviewers should be outside the authors' own institution or organization. The Editorial Board of the journal is not obliged to accept these proposals.

The authors are asked to submit **the final text** (after the manuscript has been accepted for publication) in electronic form by e-mail. The main text, list of references, tables and figure captions should be saved in separate files (as *.rtf or *.doc) with clearly identifiable file names. It is essential that the name and version of the word-processing program and the format of the text files is clearly indicated. It is recommended that the pictures are presented in *.tif, *.jpg, *.cdr or *.bmp format.

The equations are written using "Equation Editor" and chemical reaction schemes are written using ISIS Draw or ChemDraw programme.

EXAMPLES FOR PRESENTATION OF REFERENCES

REFERENCES

1. D. S. Newsome, *Catal. Rev.–Sci. Eng*., **21**, 275 (1980).
2. C.-H. Lin, C.-Y. Hsu, *J. Chem. Soc. Chem. Commun*., 1479 (1992).
3. R. G. Parr, W. Yang, Density Functional Theory of Atoms and Molecules, Oxford Univ. Press, New York, 1989.
4. V. Ponec, G. C. Bond, Catalysis by Metals and Alloys (Stud. Surf. Sci. Catal., vol. 95), Elsevier, Amsterdam, 1995.
5. G. Kadinov, S. Todorova, A. Palazov, in: New Frontiers in Catalysis (Proc. 10th Int. Congr. Catal., Budapest (1992), L. Guczi, F. Solymosi, P. Tetenyi (eds.), Akademiai Kiado, Budapest, 1993, Part C, p. 2817.
6. G. L. C. Maire, F. Garin, in: Catalysis. Science and Technology, J. R. Anderson, M. Boudart (eds.), vol. 6, Springer Verlag, Berlin, 1984, p. 161.
7. D. Pocknell, *GB Patent* 2 207 355 (1949).
8. G. Angelov, PhD Thesis, UCTM, Sofia, 2001, pp. 121-126.
9. JCPDS International Center for Diffraction Data, Power Diffraction File, Swarthmore, PA, 1991.
10. CA **127**, 184 762q (1998).
11. P. Hou, H. Wise, *J. Catal.*, in press.
12. M. Sinev, private communication.
13. http://www.chemweb.com/alchem/articles/1051611477211.html.

Texts with references which do not match these requirements will not be considered for publication!!!

CONTENTS

Selected papers from the 1ˢᵗ Seminar on Investigations and Modeling of Nanocomposite Structures, held in Sofia, Bulgaria on April 25, 2023